

DEVELOPING ANODE-FREE LITHIUM METAL CELLS  
WITH LIQUID ELECTROLYTES

by

Alex Louli

Submitted in partial fulfillment of the requirements  
for the degree of Doctor of Philosophy

at

Dalhousie University,  
Halifax, Nova Scotia  
August 2021

© Copyright by Alex Louli, 2021

*For Baba,*

## Table of Contents

List of Tables .....	viii
List of Figures .....	ix
Abstract .....	xxiii
List of Abbreviations and Symbols Used .....	xxiv
Acknowledgements .....	xxviii
Chapter 1: Introduction.....	1
1.1 Motivation .....	1
1.2 Lithium-ion, Lithium Metal and Anode-Free Cells .....	4
1.3 Thesis Outline .....	13
Chapter 2: A Brief History of Lithium Metal.....	15
2.1 Lithium Metal Cell Design.....	24
2.2 Degradation of the Lithium Metal Anode .....	26
2.3 Strategies to Stabilize Lithium Metal.....	30
2.2.1 Mechanical Pressure .....	30
2.2.2 Electrolyte Chemistry .....	32
2.2.3 Plating Substrate .....	35
2.2.4 Solid Electrolytes.....	36
2.2.5 Current Commercial Efforts .....	39

Chapter 3: Experimental Methods .....	41
3.1 Cell Chemistry.....	41
3.1.1 Pouch Cells.....	41
3.1.2 Electrolyte.....	45
3.1.3 Coin Cells and Symmetric Cells.....	48
3.2 Cycling Experiments.....	49
3.2.1 Electrochemical Testing.....	49
3.2.2 Temperature.....	50
3.2.3 Pressure.....	50
3.3 Data Management .....	53
3.3.1 Cell Database.....	53
3.3.2 Universal Exporter.....	55
3.3.3 Universal Viewer.....	57
3.4 Nuclear Magnetic Resonance Spectroscopy .....	61
3.5 Scanning Electron Microscopy Imaging .....	63
3.6 X-ray Computed Tomography .....	63
3.7 Ultrasonic Transmission Mapping .....	64
3.8 Electrochemical Impedance Spectroscopy.....	65
3.9 Smart Nail Safety Testing .....	70



Chapter 4: Anode-Free Cells with NMC532 Positive Electrodes .....	72
4.1 Increasing Lifetime from 1 to 100 Cycles.....	72
4.1.1 Mechanical Pressure .....	75
4.1.2 Electrolyte Formulation .....	82
4.2 LiDFOB/LiBF <sub>4</sub> Dual-Salt Electrolyte.....	90
4.2.1 Electrochemical Analysis .....	90
4.2.2 Electrolyte Degradation.....	93
4.2.3 Morphology Degradation .....	96
4.2.4 Diagnosing & Treating Failure.....	102
4.3 Safety.....	111
Chapter 5: Effects of Different Cycling Conditions .....	118
5.1 Temperature .....	118
5.1.1 Room Temperature Operation.....	118
5.1.2 Hot Formation.....	121
5.2 Charge-Discharge Rates.....	125
5.2.1 Cycling Behaviour.....	126
5.2.2 Lithium Morphology .....	132
5.3 Depth of Discharge & Lithium Utilization .....	136
5.3.1 Depth of Discharge.....	137

5.3.2 Lithium Utilization .....	142
5.4 Optimized Cycling Conditions.....	144
5.4.1 Intermittent High DoD Protocol.....	144
5.4.2 Concluding Remarks .....	147
Chapter 6: Different Positive Electrodes for Anode-Free Cells.....	150
6.1 Comparison of NMC532, NMC811, LCO, & LFP Anode-Free Cells .....	151
6.1.1 Energy Density .....	151
6.1.2 Cycling with Different Voltage Limits.....	152
6.1.3 80% Depth of Discharge Analysis.....	158
6.1.4 Safety .....	165
6.2 Degradation Analysis .....	167
6.2.1 Impedance Growth .....	167
6.2.2 Salt Depletion .....	172
6.3 Additional Cycling Results .....	174
6.3.1 Different Electrolytes & Optimized Cycling Conditions .....	175
6.3.2 Cycle-Store .....	182
6.3.3 Concluding Remarks .....	185
Chapter 7: Hybrid Lithium-Ion/Lithium Metal Cells.....	187
7.1 Hybrid Graphite/Lithium Metal Electrodes .....	188

7.2 Performance of Hybrid Cells.....	190
7.2.1 Conventional Cycling.....	190
7.2.2 Specialized Cycling.....	194
7.2.3 Concluding Remarks.....	199
Chapter 8: Conclusions.....	200
8.1 Future Work.....	200
8.1.1 Natural Next Steps.....	200
8.1.2 Tangential Efforts.....	204
8.2 Outlooks.....	207
Appendix A Additional Data.....	210
A.1 Chapter 4 Supplementary Data.....	210
A.2 Chapter 5 Supplementary Data.....	226
A.3 Chapter 6 Supplementary Data.....	229
A.4 Chapter 7 Supplementary Data.....	243
Appendix B Rights and Permissions.....	246
References.....	266

## List of Tables

<b>Table 2.1:</b> Summary of anode-free research reviewed by Nanda <i>et al.</i> <sup>26</sup> and Salvatierra <i>et al.</i> <sup>30</sup> .....	21
<b>Table 3.1:</b> Specifications of pouch cells used in this work.....	44
<b>Table 3.2:</b> Inactive pouch cell component specifications. ....	45
<b>Table 3.3:</b> List of solvents used in electrolytes in this work.....	46
<b>Table 3.4:</b> List of lithium salts used in electrolytes in this work. ....	47
<b>Table 4.1:</b> Force and pressure loading experiments. Cells were constrained in normal boats (NB) for low pressure tests and in superboats (SB) for high pressure tests. The force at the bottom of the discharge (BOD), top of the initial charge (TOC) and the initial average pressures are listed. ....	76
<b>Table 5.1:</b> List of charge-discharge rates tested. C = charge, D = discharge. 1C = 1D = 230 mA → 2.66 mA/cm <sup>2</sup> . ....	126
<b>Table 5.2:</b> Parameters of the depth of discharge experiment.....	139
<b>Table 6.1:</b> Different depth of discharge cycling conditions for the NMC532, NMC811, LCO, and LFP anode-free cells tested in this work.....	155

## List of Figures

<b>Figure 1.1   Electric vehicle range.</b> List of electric vehicle models and their range and price as of September 2020.....	2
<b>Figure 1.2   Li-ion cell formats.</b> Diagrams of wound cylindrical, flat wound, and stacked lithium-ion cells. ....	5
<b>Figure 1.3   Li-ion cell stack. a,</b> The electrochemical unit cell called the “cell stack” which consists of a double sided positive electrode (cathode), a double sided negative electrode (anode), and two separators. ....	6
<b>Figure 1.4   Lithium-ion cell schematic.</b> The operation of a Li-ion cell during charge (red arrows) and discharge (blue arrows).....	10
<b>Figure 1.5   Lithium metal cell schematic.</b> The operation of a lithium metal cell during charge (red arrows) and discharge (blue arrows).....	10
<b>Figure 1.6   Li-ion, lithium metal and anode-free cells. a-c,</b> Cell schematics of a Li-ion (a), lithium metal (b), and anode-free (c) cell in the discharged state. <b>d-e,</b> Picture of a Li-ion (d) and an anode-free (e) pouch cell used in this work. ....	11
<b>Figure 2.1   First commercial lithium metal cells. a,</b> Exxon 25 mAh Li-Al/TiS <sub>2</sub> cell spec sheet from 1978, reproduced from Ref. <sup>34</sup> <b>b,</b> Moli Energy Canada 600 mAh Li/MoS <sub>2</sub> cell spec sheet, reproduced from Dr. Jeff Dahn.....	16
<b>Figure 2.2   Improvement of Li-ion cell energy density.</b> Volumetric energy density (red, left axis) and specific energy density (blue, right axis) vs year of commercialized 18650-format lithium-ion cells as reproduced from Ref. <sup>12</sup> .....	17
<b>Figure 2.3   Anode-free cell development. a,</b> Capacity retention vs cycle and <b>b,</b> Efficiency vs cycle of anode-free lithium metal cells. ....	20

**Figure 2.4 | Energy density dependence on cell parameters. a,** Energy density for cell stacks with different amounts of excess lithium (top) and their respective stack diagrams (bottom)..... 25

**Figure 2.5 | Lithium metal degradation mechanisms. a,** The “circle of death”—a diagram which lists the degradation mechanisms of a lithium metal anode, as retrieved from Ref.<sup>15</sup> ..... 28

**Figure 2.6 | Solid electrolyte comparison.** Spider plot comparing the important characteristics of solid electrolytes for polymer (blue), oxide (green), and sulfide (orange) chemistries. .... 37

**Figure 2.7 | Landscape of commercial Li metal efforts.** List of companies working to commercialize lithium metal cells based on solid-state and liquid electrolyte chemistries. .... 40

**Figure 3.1 | Pouch cell. a,** Picture of the small format ~0.25 Ah wound prismatic pouch cell used in this work. .... 41

**Figure 3.2 | Coin cell hardware. a,** The hardware for constructing coin cells including a bottom casing, the electrode stack, a spacer and spring on top of the stack, and the top casing and gasket. A picture of a built coin cell is included on the right. **b,** Coin cell testing fixture..... 48

**Figure 3.3 | Pouch cell testing fixtures. a,** A plastic fixture which constrains cells under low pressure (< 200 kPa) using rubber blocks, referred to as a normal boat (NB). .... 51

**Figure 3.4 | Superboat pressure measurement.** Picture (left) and schematic representation (right) of the superboat cell testing setup..... 52

**Figure 3.5 | Cell database. a,** Subset of the spreadsheet used to store the dry-cell information for the different pouch cell types used in this work. **b,** Subset of the spreadsheet used to store the experimental parameters of every cell tested..... 54

<b>Figure 3.6   Mobile app interface.</b> Screenshot of the cell tracking sheet as viewed from the mobile app. Beyond storing experimental parameters, this sheet also includes the location (channel and temperature box) of cells as well as notes for what to do with cells after testing.....	54
<b>Figure 3.7   Universal Exporter.</b> Interface for the Universal Exporter, used to generate universal cycling data files paired with cell metadata stored in the cell database.....	55
<b>Figure 3.8   Universal Exporter output file.</b> Example output from the Universal Exporter. The file name (shown on the top bar) includes cell metadata information.....	56
<b>Figure 3.9   Universal Viewer data selection window.</b> Interface window of the Universal Viewer for data selection. ....	58
<b>Figure 3.10   Universal Viewer graph window.</b> Interface window of the Universal Viewer for data visualization. ....	59
<b>Figure 3.11   Universal Viewer data selection.</b> A subset of data from selecting the desired experimental parameters (highlighted in blue). The top panel lists all data that shares the selected parameters. ....	60
<b>Figure 3.12   Universal Viewer graph example.</b> The output graph resulting from selecting a subset of data.....	60
<b>Figure 3.13   Fluorine NMR spectra.</b> <sup>19</sup> F absorption vs chemical shift NMR spectra for various electrolyte samples tested in this work measured with a Bruker AV500 spectrometer.....	62
<b>Figure 3.14   Ultrasonic transmission mapping. a,</b> Ultrasonic transmission maps of Li-ion cells filled with different volumes of electrolyte.....	65
<b>Figure 3.15   Impedance through an interface a-b,</b> Circuit models for impedance through an interface.....	67

<b>Figure 3.16   Circuit models. a,</b> A resistor used to model solution resistance ( $R_s$ ), in series with a R-CPE circuit used to model charge transfer and charge transfer resistance ( $R_{ct}$ ). .....	68
<b>Figure 3.17   Smart nail setup. a,</b> Schematic of the smart nail used for nail penetration tests adapted from Ref. <sup>131</sup> .....	71
<b>Figure 4.1   Increasing lifetime of anode-free cells. a,</b> Stack volumetric energy density vs cycle of anode-free cells compared to an optimized Li-ion cell. ....	73
<b>Figure 4.2   Operando pressure data. a-d,</b> Pressure data for cells containing FEC:DEC ( <b>a,b</b> ) and FEC:TFEC ( <b>c,d</b> ) electrolyte constrained at initial average pressures of 485 kPa ( <b>a,c</b> ) and 795 kPa ( <b>b,d</b> ). ....	77
<b>Figure 4.3   Pressure test. a-d,</b> Cycling data for cells containing FEC:DEC ( <b>a,c</b> ) and FEC:TFEC electrolyte ( <b>b,d</b> ) constrained under different pressures between 200-2205 kPa. .....	79
<b>Figure 4.4   Dual-salt pressure test. a,</b> Capacity retention of cells constrained under different pressures and testing fixtures (low pressure = 200 kPa in a NB, high pressure ~1200 kPa in an AB).....	82
<b>Figure 4.5   Effect of CO<sub>2</sub>. a,</b> Dry ice pellets used to introduce CO <sub>2</sub> to pouch cells. <b>b,</b> Pouch cell with added CO <sub>2</sub> (left) and without added CO <sub>2</sub> (right).....	83
<b>Figure 4.6   LiPF<sub>6</sub> concentration and volume. a-b,</b> Normalized capacity vs cycle of anode-free cells tested with different concentrations ( <b>a</b> ) and different volumes ( <b>b</b> ) of LiPF <sub>6</sub> FEC:DEC 1:2 electrolyte. ....	85
<b>Figure 4.7   Dual-salt solvent test. a-b,</b> Normalized capacity (a) and stack volumetric energy density (b) vs cycle of anode-free cells with 0.6 M LiDFOB 0.6 M LiBF <sub>4</sub> tested with different solvent blends.....	87



<b>Figure 4.8   Electrolyte evaluation. a-b,</b> Normalized capacity (a) and stack volumetric energy density (b) vs cycle of anode-free cells with various electrolyte formulations from the literature. ....	88
<b>Figure 4.9   Dual-salt electrochemical analysis. a-d,</b> Normalized capacity (a), delta V (b), coulombic efficiency (CE, c), and charge endpoint slippage (d) vs cycle of anode-free cells with 0.6 M LiDFOB 0.6 M LiBF <sub>4</sub> FEC:DEC 1:2 electrolyte.....	91
<b>Figure 4.10   Dual-salt electrochemical impedance spectroscopy. a,</b> -Imaginary vs real impedance Nyquist plots measured for dual-salt cells during cycling. ....	93
<b>Figure 4.11   Electrolyte degradation. a-c,</b> Change in salt concentration vs cycle for anode-free NMC532 full cells (a), negative Li-Li symmetric cells (b), and positive NMC532-NMC532 symmetric cells with 0.6 M LiDFOB 0.6 M LiBF <sub>4</sub> FEC:DEC 1:2 electrolyte.....	94
<b>Figure 4.12   Morphology degradation. a-d,</b> SEM and optical images (insets) of fully plated lithium (4.5 V).....	97
<b>Figure 4.13   Crude lithium cross-section.</b> SEM image of a lithium cross section with a glancing view. This cross section was generated by cutting the lithium sample with a knife at room temperature. ....	98
<b>Figure 4.14   Thickening of the lithium electrode. a-c,</b> X-ray computed tomography images of cycled anode-free cells with dual-salt electrolyte after one (a), 50 (b), and 80 (c) cycles.....	100
<b>Figure 4.15   Electrolyte dry-out. a-d,</b> Ultrasonic transmission mapping of anode-free pouch cells with dual-salt electrolyte cycled under low pressure (200 kPa). ....	101
<b>Figure 4.16   Diagnosing Failure.</b> Schematic representations of anode-free failure modes. ....	102

<b>Figure 4.17   Dual-salt electrolyte volume. a-c,</b> Cycling data for anode-free cells with different volumes of 0.6 M LiDFOB 0.6 M LiBF <sub>4</sub> FEC:DEC 1:2 electrolyte.....	105
<b>Figure 4.18   High concentration dual-salt. a-i,</b> Cycling data for anode-free cells with different dual-salt concentrations.....	106
<b>Figure 4.19   High concentration lithium morphology. a-c,</b> Optical (a) and SEM (b,c) images of lithium plated in 0.6 M LiDFOB 0.6 M LiBF <sub>4</sub> FEC:DEC 1:2 electrolyte after 100 cycles.....	109
<b>Figure 4.20   Best effort electrolyte. a-b,</b> Stack volumetric energy density vs cycle of various anode-free cells with lifetimes below 100 cycles (a) and above 100 cycles (b) compared to a Li-ion cell. ....	110
<b>Figure 4.21   Goblet of fire. a,</b> Charged graphite submerged in water. <b>b-e,</b> Plated lithium submerged in water (top) and respective morphology of lithium sample submerged (bottom).....	112
<b>Figure 4.22   Localized high concentration safety issues. a-b,</b> Pictured anode-free cell with 1.73 M LiFSI DME:TTE 1:4 electrolyte which had spontaneously exploded after 200 cycle testing. ....	114
<b>Figure 4.23   Smart-nail testing. a-c,</b> Anode-free cells aged to 50 cycles pictured during nail penetration.....	115
<b>Figure 4.24   Smart-nail electrolyte tests. a-f,</b> Temperature vs time during nail tests of cells with different electrolytes.....	116
<b>Figure 5.1   Effect of temperature.</b> Normalized capacity vs cycle for anode-free cells tested at different temperatures.....	119
<b>Figure 5.2   Temperature &amp; pressure.</b> Normalized capacity vs cycle for anode-free cells tested at different temperatures and pressures. ....	120

<b>Figure 5.3   Temperature impact on lithium morphology. a-b,</b> SEM images of lithium plated after two cycles at 20 °C (a) and 40 °C (b). .....	121
<b>Figure 5.4   Hot formation.</b> Normalized capacity vs cycle for anode-free cells tested at different temperatures, pressures, and with hot formation. ....	122
<b>Figure 5.5   Hot formation impact on lithium morphology. a-b,</b> SEM images of lithium plated after 20 cycles at 20 °C (a) and 20 °C after hot formation (b). .....	123
<b>Figure 5.6   Best effort hot formation. a-b,</b> Normalized capacity (a) and stack volumetric energy density (b) vs cycle for anode-free cells tested with high-concentration dual-salt electrolyte and hot formation compared to Li-ion cells. ....	125
<b>Figure 5.7   Charge-discharge rate test. a,</b> Voltage vs time profiles for the three types of charge-discharge protocols tested: symmetric charge-discharge, asymmetric faster charge (AFC), and asymmetric slower charge (ASC). .....	127
<b>Figure 5.8   Rate test comparisons. a,</b> Normalized capacity vs cycle number for all charge-discharge rate tests; cells tested with a symmetric charge-discharge protocol (blue), an asymmetric protocol with faster charge (AFC, green), and an asymmetric protocol with a slower charge (ASC, orange). .....	129
<b>Figure 5.9   Impedance growth and inventory loss. a-c,</b> Delta V vs cycle for cells tested with a symmetric charge-discharge protocol (a), an asymmetric protocol with faster charge (b), and an asymmetric protocol with a slower charge (c). .....	131
<b>Figure 5.10   Lithium morphology from different charge-discharge rates. a,</b> Lithium morphology generated in a cell cycled with a symmetric charge-discharge protocol of C/5 D/5 .....	133
<b>Figure 5.11   Proposed plating and stripping mechanisms.</b> .....	134

**Figure 5.12 | Creating a lithium reservoir with a limited depth of discharge. a-b,** Voltage vs specific capacity (bottom axis) and areal capacity (top axis) of the first charge-discharge of a NMC532 anode-free cell. .... 138

**Figure 5.13 | Depth of discharge test. a,** Areal capacity vs cycle and volumetric stack energy density vs cycle (inset) for cells cycled from 4.5 V down to different lower cut-off voltages and corresponding depths of discharge as indicated in the legend. .... 140

**Figure 5.14 | Impact of areal capacity vs lithium reservoir size. a,** Areal capacity vs cycle for cells cycled with different areal capacities under a fixed 90% DoD (small lithium reservoir, in red) and with limited DoDs (larger lithium reservoirs, in blue). .... 143

**Figure 5.15 | Specialized intermittent high DoD protocol. a-b,** Stack energy density vs cycle (a) and stack energy density vs equivalent full cycled and capacity throughput (b) for cells cycled with an intermittent high depth of discharge protocol. .... 146

**Figure 6.1 | Energy Density Comparison. a-b,** Stack energy density calculated by volume (a) and by mass (b) for anode-free lithium metal cells with  $\text{LiFePO}_4$  (LFP),  $\text{LiNi}_{0.5}\text{Mn}_{0.3}\text{Co}_{0.2}\text{O}_2$  (NMC532),  $\text{LiCoO}_2$  (LCO), and  $\text{LiNi}_{0.8}\text{Mn}_{0.1}\text{Co}_{0.1}\text{O}_2$  (NMC811) positive electrodes compared to a conventional Li-ion cell with an NMC532 positive electrode. .... 151

**Figure 6.2 | Voltage profiles. a-d,** First charge-discharge voltage vs areal capacity (top axes, black) and specific capacity (bottom axes, grey) for anode-free cells with NMC532 (a), NMC811 (b), LCO (c) and LFP (d) positive electrodes. .... 154

**Figure 6.3 | Voltage range and depth of discharge performance. a-c,** NMC532; **d-f,** NMC811; **g-i,** LCO; **j-l,** LFP anode-free cycling data plotted as normalized capacity (first row), stack volumetric energy density (second row), and  $\Delta V$  (third row) vs cycle for different voltage ranges and depths of discharges. .... 156

<b>Figure 6.4   80% DoD lithium inventory loss. a-b, NMC532; c-d, LCO; e-f, NMC811; g-h, LFP anode-free cycling data. The first and third columns show capacity vs cycle (left axes) and delta V (right axis).</b> .....	160
<b>Figure 6.5   Positive electrode cycling comparison. a-f, Cycling data for anode-free NMC532, NMC811, LCO, and LFP cells.</b> .....	163
<b>Figure 6.6   Positive electrode safety. a-b, Smart nail penetration tests of anode-free cells with different positive electrodes performed after 20 cycles (a) and 50 cycles (b).</b> .....	166
<b>Figure 6.7   Positive electrode EIS. a-b, NMC532; c-d, NMC811; e-f, LCO; g-h, LFP anode-free EIS spectra as a function of cycle.</b> .....	168
<b>Figure 6.8   EIS fit parameters. a-e, Equivalent circuit fit parameters vs cycle for EIS measurements of aged anode-free cells with different positive electrodes.</b> .....	170
<b>Figure 6.9   Positive electrode salt depletion. a-b, LiDFOB (a) and LiBF<sub>4</sub> (b) salt concentration vs equivalent full cycle as measured via liquid NMR of extracted electrolyte from cycled anode-free cells.</b> .....	173
<b>Figure 6.10   NMC532 electrolyte study. a-d, Cycling performance of NMC532 anode-free cells at 40 °C (a,b) and 20 °C after hot formation (c,d) compared with NMC532 Li-ion cells.</b> .....	176
<b>Figure 6.11   NMC811 electrolyte study. a-d, Cycling performance of NMC811 anode-free cells at 40 °C (a,b) and 20 °C after hot formation (c,d) compared with NMC532 Li-ion cells.</b> .....	178
<b>Figure 6.12   LCO electrolyte study. a-d, Cycling performance of LCO anode-free cells at 40 °C (a-c) and 20 °C after hot formation (d) compared with NMC532 Li-ion cells.</b>	180
<b>Figure 6.13   LFP electrolyte study. a-d, Cycling performance of LFP anode-free cells at 40 °C (a-c) and 20 °C after hot formation (d).</b> .....	182

**Figure 6.14 | Cycle-store testing. a-f**, Normalized capacity vs cycle (a-c) and normalized capacity vs time (d-c) for NMC532, NMC811, and LCO anode-free cells tested with a cycle-store protocol..... 184

**Figure 7.1 | Hybrid lithium-ion/lithium metal cells.** Comparison of cell stacks for anode-free (AF, left), lithium-ion (center), and hybrid lithium-ion/lithium metal (right) cells. 189

**Figure 7.2 | Differential voltage analysis. a**, Voltage (left axis) and  $dV/dQ$  (right axis) vs capacity for the second charge to 4.4 V of a hybrid cell..... 190

**Figure 7.3 | Hybrid cell electrolyte test.** Capacity vs cycle for hybrid cells tested with different electrolytes optimized for Li-ion cells (2VC, 2F1L) and lithium metal cells (LDBF)..... 191

**Figure 7.4 | Hybrid cell lithium morphology. a-d**, Optical picture (a) and SEM images (b-d) of lithium metal plated on top of graphite retrieved from hybrid lithium-ion/lithium metal cells after one charge to 4.4 V..... 193

**Figure 7.5 | Differential voltage analysis of aged cells. a**, Voltage (left axis) and  $dV/dQ$  (right axis) vs capacity for the 50<sup>th</sup> charge to 4.4 V of a hybrid cell. .... 194

**Figure 7.6 | Dual mode operation of hybrid cells.** Voltage vs capacity for the first charge of a hybrid cell and the constituent graphite negative and NMC532 positive electrodes. .... 195

**Figure 7.7 | Specialized hybrid cycling protocol.** Capacity vs cycle for hybrid cells tested with a protocol that cycled most of the time between 3.0-4.0 V in Li-ion mode (~140 mAh) with intermittent 3.0-4.4 V Li metal mode (~220 mAh) cycles. .... 197

**Figure 7.8 | Lithium metal electrolyte in a Li-ion cell.** Normalized capacity vs cycle for conventional Li-ion cells tested with an optimized Li-ion electrolyte ..... 198

**Figure 8.1 | Current collector modification. a-b**, Normalized capacity vs cycle of anode-free cells with modified copper current collectors..... 205

<b>Figure 8.2   Anode-free vs Li-ion cells.</b> Comparison of the lifetime of our best anode-free cell results with optimized lithium-ion cells.....	208
<b>Figure A.1   Comparison of lithium morphology.</b> SEM images of plated lithium images of plated lithium in a variety of electrolytes reported in the literature. ....	211
<b>Figure A.2   Pressure impact on lithium morphology.</b> SEM images of plated lithium after one charge (a-d) and after 50 cycles (A-D).....	212
<b>Figure A.3   Electrolyte conductivity.</b> Conductivity vs temperature measurements for electrolyte containing 1 M LiPF <sub>6</sub> salt with FEC:DEC 1:2 solvent (blue circles), FEC:TFEC 1:2 solvent (green squares) and EC:EMC 3:7 solvent (red stars).....	214
<b>Figure A.4   Dual-salt ether solvent test. a-b,</b> Normalized capacity (a) and stack volumetric energy density (b) vs cycle of anode-free cells with 0.6 M LiDFOB 0.6 M LiBF <sub>4</sub> tested with different ether solvent blends. ....	215
<b>Figure A.5   Localized high concentration electrolyte evaluation. a-b,</b> Normalized capacity (a) and stack volumetric energy density (b) vs cycle of anode-free cells with various localized high concentration electrolyte formulations from the literature. ....	216
<b>Figure A.6   4.3 V electrochemical analysis. a-d,</b> Normalized capacity (a), delta V (b), coulombic efficiency (CE, c), and charge endpoint slippage (d) vs cycle of anode-free cells with 0.6 M LiDFOB 0.6 M LiBF <sub>4</sub> FEC:DEC 1:2 electrolyte.....	217
<b>Figure A.7   Voltage-dependant electrolyte degradation.</b> Change in salt concentration molarity vs cycle for anode-free NMC532 full cells with 0.6 M LiDFOB 0.6 M LiBF <sub>4</sub> FEC:DEC 1:2 electrolyte. ....	218
<b>Figure A.8   Dual-salt symmetric cell cycling. a-b,</b> Voltage vs time of lithium-lithium (a) and positive-positive (b) symmetric cells with dual-salt electrolyte. ....	219
<b>Figure A.9   Low voltage positive symmetric cell cycling. a,</b> Voltage vs time of positive-positive symmetric cells with dual-salt electrolyte.....	220

**Figure A.10 | Single-salt electrolyte degradation. a-c,** Change in salt concentration molarity vs cycle for anode-free NMC532 full cells (a), negative Li-Li symmetric cells (b), and positive NMC532-NMC532 symmetric cells with 1.2 M LiDFOB FEC:DEC 1:2 electrolyte..... 221

**Figure A.11 | Single-salt positive symmetric cell cycling. a,** Voltage vs time of positive-positive symmetric cells with single-salt electrolyte. .... 222

**Figure A.12 | Low pressure morphology degradation. a-d,** SEM and optical pictures (insets) of fully plated lithium (4.5 V)..... 223

**Figure A.13 | EDS analysis. a,** SEM image of plated lithium from a cell cycled with 0.6 M LiDFOB 0.6 M LiBF<sub>4</sub> FEC:DEC 1:2 electrolyte under high pressure after 80 cycles. .... 224

**Figure A.14 | Best effort electrolyte. a-c,** Cycling data of various anode-free cells compared to a Li-ion cell. Normalized capacity (a), stack volumetric energy density (b), and delta V (c) vs cycle..... 225

**Figure A.15 | Charge-discharge rate test. a,** Capacity in mAh vs cycle for all charge-discharge rate tests with the inset showing a zoomed in view of the first 8 cycles to clearly show the initial difference in capacity. .... 226

**Figure A.16 | Energy Density of the charge-discharge rate test. a-c,** Stack volumetric energy density vs cycle for cells tested with a symmetric charge-discharge protocol (a), an asymmetric protocol with faster charge (b), and an asymmetric protocol with a slower charge (c). .... 227

**Figure A.17 | Depth of discharge impedance growth.  $\Delta V$  vs cycle** for cells cycled with different depths of discharge. Cells were cycled at C/5 D/2 at 40°C under high pressure. The electrolyte used was 1.4 M LiDFOB 0.4 M LiBF<sub>4</sub> FEC:DEC (1:2)..... 228

**Figure A.18 | 100 cycle thickness change.** Percentage change in cell thickness after 100 cycles vs equivalent full cycle. .... 229



<b>Figure A.19   Positive electrode rate test. a-c, Stack volumetric energy density vs cycle for anode-free NMC532 (a), NMC811 (b), and LCO (c) cells.</b> .....	230
<b>Figure A.20   Positive electrode FRA cycling.</b> Cycling data for anode-free cells with different positive electrodes tested with an FRA protocol for EIS measurements every 10 cycles.....	231
<b>Figure A.21   NMC532 EIS fits.</b> EIS spectra (blue circles) and fits (solid lines) for anode-free NMC532 cells as a function of cycle.....	232
<b>Figure A.22   NMC811 EIS fits.</b> EIS spectra (blue circles) and fits (solid lines) for anode-free NMC811 cells as a function of cycle.....	233
<b>Figure A.23   LCO EIS fits.</b> EIS spectra (blue circles) and fits (solid lines) for anode-free LCO cells as a function of cycle. ....	234
<b>Figure A.24   LFP EIS fits.</b> EIS spectra (blue circles) and fits (solid lines) for anode-free LFP cells as a function of cycle. ....	235
<b>Figure A.25   NMC811 emergent high frequency EIS hump.</b> EIS spectra for an aged anode-free NMC811 cell measured <i>in-situ</i> during FRA cycling at 40 °C from 50 kHz to 10 mHz (purple) and measured <i>ex-situ</i> at 10 °C from 700 kHz to 10 mHz (green).....	237
<b>Figure A.26   EIS fit parameters. a-e,</b> Equivalent circuit fit parameters vs equivalent full cycle for EIS measurements of aged anode-free cells with different positive electrodes. ....	238
<b>Figure A.27   NMC532 symmetric cells. a-c,</b> EIS spectra for symmetric cells built from electrodes retrieved from an NMC532 anode-free cell after 1 cycle.....	240
<b>Figure A.28   Positive electrode salt depletion. a-b,</b> LiDFOB (a) and LiBF <sub>4</sub> (b) salt concentration vs cycle as measured via liquid NMR of extracted electrolyte from cycled anode-free cells. ....	241

**Figure A.29 | NMC811 electrolyte study. a-b,** Cycling performance of NMC811 anode-free cells at 40 °C with NMC532 Li-ion cells. .... 242

**Figure A.30 | Hot formation for hybrid cells. a-b,** Capacity vs cycle for hybrid cells with 1 M LiDFOB 0.4 M LiBF<sub>4</sub> FEC:DEC 1:2 (LDBF) electrolyte tested at 40 °C and 20 °C with hot formation with conventional cycling (a) and a dual Li-ion mode/Li metal mode protocol (b)..... 243

**Figure A.31 | Depth of discharge impedance growth.** Capacity vs cycle of the Li metal mode cycles from the intermittent cycling protocols (10/5 and 10/1 Li-ion mode/Li metal mode cycles) plotted with the standard cycling results. .... 244

**Figure A.32 | Extended Li-ion mode operation.** Capacity vs cycle for hybrid cells aged for 60 cycles in Li metal mode and then subsequently in Li-ion mode for a further 440 cycles..... 245

## Abstract

Anode-free lithium metal cells store 60% more energy than lithium-ion cells. Such high energy density can increase the range of electric vehicles by over 200 km and will be critical for enabling electrified urban aviation. This is made possible by discarding the conventional graphite anode and harnessing the capacity delivered by the positive electrode in the form of a lithium metal anode formed *in-situ*. Using this cell design with a liquid electrolyte, anode-free cells are a drop-in solution compatible with today's manufacturing infrastructure.

However, anode-free cells are plagued with short lifetime. Inefficient lithium plating and stripping results in rapid capacity loss—lifetimes fewer than 20 cycles are typical. This is mostly a result of the lithium microstructure which usually forms in liquid electrolytes. Instead of plating as a flat metal sheet, lithium tends to deposit in a wild mossy structure. Unwanted reactions which deplete lithium capacity are exacerbated by this mossy structure, and high surface area lithium is also more volatile and less safe.

In this work, we investigate the degradation modes of anode-free cells that are necessary to overcome: microstructural degradation via scanning electron microscopy and x-ray tomography, resistance growth via electrochemical impedance spectroscopy, and electrolyte degradation via nuclear magnetic resonance spectroscopy. We also characterize the safety of anode-free cells with nail penetration tests. We show how cell chemistry affects performance using different electrolytes and different positive electrode materials (NMC532, NMC811, LCO and LFP). The impact of different cycling conditions—temperature, mechanical pressure, depth of discharge, and cycling rate are also studied. Finally, we use the insights gained in this work to extend the lifetime of anode-free cells to 200 cycles. Although cycle life must still be increased, we believe anode-free lithium metal cells with liquid electrolyte present one of the most straightforward paths toward unlocking the highest energy density cells for the next generation of energy storage.

## List of Abbreviations and Symbols Used

2F1L	2% FEC 1 LFO
2VC	2% VC
a.k.a.	also known as
AB	airboat
AF	anode-free
AFC	asymmetric faster charge
Ag-C	silver-carbon
Al	aluminum
ASC	asymmetric slower charge
BET	Brunauer-Emmett-Teller
BOD	bottom of discharge
BTFE	bis(2,2,2-trifluoroethyl) ether
CE	coulombic efficiency
CO <sub>2</sub>	carbon dioxide
CPE	constant phase element
CT	computed tomography
Cu	copper
DEC	diethyl carbonate
DEC	diethyl carbonate
DMC	dimethyl carbonate
DME	1,2-dimethoxyethane
DMSO	dimethyl sulfoxide
DoD	depth of discharge
DTD	1,3,2-Dioxathiolane-2,2-dioxide
dV/dQ	differential voltage
EC	ethylene carbonate
EC	ethylene carbonate
EDS	energy dispersive x-ray spectroscopy
EIS	electrochemical impedance spectroscopy
EM	electromagnetic
EMC	ethylmethyl carbonate
EV	electric vehicle
eVTOL	electric vertical take off and landing
FDMB	fluorinated 1,4-dimethoxybutane
FEC	fluoroethylene carbonate
FIB	focused ion beam
FRA	frequency response analyzer
GUI	graphical user interface
HCE	high concentration electrolyte
LCO	LiCoO <sub>2</sub>
LCV	lower cut-off voltage

LDBF	1 M LiDFOB 0.4 M LiBF <sub>4</sub> FEC:DEC 1:2
LFO	lithium difluorophosphate
LFP	LiFePO <sub>4</sub>
LHC	localized high concentration
Li	lithium
Li <sup>+</sup>	lithium ion (as in the charge carrying cation)
Li <sub>2</sub> O	lithium oxalate
LiBF <sub>4</sub>	lithium tetrafluoroborate
LiDFDOP	lithium difluoro(dioxalato) phosphate
LiDFOB	lithium difluoro(oxalato)borate
LiFSI	lithium bis(fluorosulfonyl)imide
Li-ion	lithium-ion (as in the battery cell)
LiMO <sub>2</sub>	lithium transition metal oxide
LiNi <sub>1-x-y</sub> Mn <sub>x</sub> Co <sub>y</sub> O <sub>2</sub>	NMC
LiPF <sub>6</sub>	Lithium hexafluorophosphate
LiTFOP	Lithium tetrafluoro(oxalato) phosphate
LiTFSI	Lithium bis(trifluoromethane)sulfonimide
MA	methyl acetate
NB	normal boat
NMC532	LiNi <sub>0.5</sub> Mn <sub>0.3</sub> Co <sub>0.2</sub> O <sub>2</sub>
NMC811	LiNi <sub>0.8</sub> Mn <sub>0.1</sub> Co <sub>0.1</sub> O <sub>2</sub>
NMP	N-Methyl-2-pyrrolidone
NMR	nuclear magnetic resonance
PC	propylene carbonate
PNNL	Pacific Northwest National Laboratory
PVDF	polyvinylidene fluoride
RC	resistor-capacitor
R-CPE	resistor-constant phase element
SB	superboat
SEI	solid electrolyte interphase
SEM	scanning electron microscopy
Si	silicon
SOC	State of charge
TEM	transmission electron microscopy
TFEC	bis(2,2,2-trifluoroethyl) carbonate
TOC	top of charge
TTE	1,1,2,2-tetrafluoroethyl-2,2,3,3-tetrafluoropropyl ether
UCV	upper cut-off voltage
VC	vinylene carbonate
wt.%	weight percent
XRM	x-ray microscope
Zn	zinc

<i>Avg V</i>	average voltage
$\nabla C$	concentration gradient
<i>CC</i>	current collector
<i>I</i>	spin quantum number
<i>j</i>	imaginary number ( $\sqrt{-1}$ )
<i>m</i>	magnetic quantum number
<i>Neg</i>	negative
<i>Pos</i>	positive
<i>Q</i>	capacity
<i>Q<sub>A</sub></i>	areal capacity
<i>Q<sub>c</sub></i>	charge capacity
<i>Q<sub>d</sub></i>	discharge capacity
<i>R<sub>ct</sub></i>	charge transfer resistance
<i>Rel</i>	electronic resistance
<i>R<sub>s</sub></i>	solution resistance
<i>Sep</i>	separator
<i>V<sub>c</sub></i>	charge voltage
<i>V<sub>d</sub></i>	discharge voltage
<i>V<sub>ocv</sub></i>	open circuit voltage
<i>W</i>	Warburg
<i>Z</i>	impedance
$\Delta V$	delta V
$\sigma$	constant containing the diffusion coefficient
$\omega$	angular frequency (rad/s)
%	percent
<	less than
>	greater than
°C	degree Celsius
Ah	amp-hour (capacity)
Ah/L	Amp-hour per litre (volumetric capacity)
cm <sup>3</sup>	centimeter cubed
cm <sup>2</sup>	centimeter squared
hr	hour
Hz	hertz
in <sup>2</sup>	inch squared
kHz	kilohertz
km	kilometer
kPa	kilopascal
kWh	kilo-watt-hour (energy)
M	Molarity (concentration)
mA/cm <sup>2</sup>	milliamp per centimeter squared (current density)
mAh	milli-amp-hour (capacity)

mAh/cm <sup>2</sup>	milli-amp-hour per centimeter squared (areal capacity)
mAh/g	milli-amp-hour per gram (specific capacity)
mg/cm <sup>2</sup>	milligram per centimeter squared (loading)
MHz	mega hertz
mHz	millihertz
mm	millimeter
mol/kg	moles per kilogram (concentration)
mS/cm	milli-seimens per centimeter (conductivity)
nm	nanometer
T	tesla
um	micro-meter
V	volt (voltage)
Wh/kg	watt-hour per kilogram (specific energy density)
Wh/L	watt-hour per litre (volumetric energy density)

## Acknowledgements

I would like to thank the *Natural Sciences and Engineering Research Council* (NSERC CGS D), the Walter C. Sumner Fellowship, and the Nova Scotia Graduate Scholarship for their financial support, as well as Tesla Canada for partial funding of this work.

Thank you to Jeff Dahn, our fearless leader, for being an incredible mentor and supervisor—this work would not have been possible without your vision and enthusiasm, nor would I be the battery scientist I am today without your exceptional example. I am also thankful to the other members of my committee, Dr. Ted Monchesky and Dr. Jesse Maassen, as well as Tanya Timmins and the rest of the departmental staff for all their support and guidance.

I gratefully acknowledge everyone who has contributed to this work. Dr. Matt Genovese, Dr. Rochelle Weber, and Ahmed Eldesoky, the core anode-free team, as well as Sam Hames, Cameron Martin, Matt Coon, Jack deGooyer, and Annika Benson for their invaluable contributions to making this project as successful as it has been. I would also like to thank Michel Johnson, Simon Trussler, and Patricia Scallion for all their technical expertise. I am also grateful to have had such a great group of colleagues in the Dahn Lab who have always been so supportive.

I write this thesis in memory of my Baba who passed away during my graduate studies, and in honour of my Dido, Teta and Guedo, and all my other family whose shoulders I have stood on to get where I am today. Thank you to all my loved ones and of course to all my eclectic groups of friends (the dum dums, the North African Alliance, *etc*) who bring me joy—I am grateful for you all.



## Chapter 1: Introduction

### 1.1 Motivation

The development of efficient electrochemical energy storage has enabled revolutionary technological innovations. Portable electronics including power tools, cell phones, laptops are now all primarily powered by lithium-ion (Li-ion) batteries, and the electrification of transportation is well underway. This has been made possible by the high cell potential and low weight of lithium-based battery cells, making Li-ion cells the most energy dense rechargeable batteries on the market today.<sup>1,2</sup> Moderately priced electric vehicles (EVs) with driving ranges exceeding 300 km powered by Li-ion cells are now on the road, and prices are continuing to drop closer to parity with internal combustion cars—**Figure 1.1** compares the range and cost of EVs on the road today. Nevertheless, range anxiety and cost are still factors hindering the wide-spread adoption of electric vehicles. Increasing battery energy density is a solution to both problems. Cost can be reduced because fewer high energy dense cells are required to deliver the same total energy. Alternatively, packing an electric vehicle with more energy dense cells will extend its range by allowing it to drive further on a single charge. For example, a typical electric vehicle may have a 50 kWh battery pack with a driving range of 300 km. If the cells in this pack were replaced with cells with 60% greater energy density, then the pack would deliver 80 kWh and a range of 500 km. Such a significant increase in energy density would also enable new technologies. An emerging area of interest is electrified urban aviation—batteries with an energy density 60% greater than today's Li-ion cells could power these futuristic flying taxis.<sup>3,4</sup>



**Figure 1.1 | Electric vehicle range.** List of electric vehicle models and their range and price as of September 2020. The ranges are ranked and visualized depicting possible journeys over three different routes. This graphic was produced by Visual Capitalist: <https://www.visualcapitalist.com/range-evs-major-highway-routes/>

In 2016, the Uber Elevate whitepaper estimated that batteries with a specific energy density of 400 Wh/kg (compared to today's ~250 Wh/kg Li-ion cells) were required to enable

moderately ranged electric vertical take off and landing (eVTOL) vehicles capable of urban aviation.<sup>3</sup> In targeting a 2020 demo of their proposed eVTOLs,<sup>5</sup> Uber was perhaps overconfident in their ability to develop this technology in that timeframe. This demo never materialised; instead, Uber sold off its Elevate program in 2020.<sup>6</sup> Nevertheless, just over the last year there have been a number of newly announced eVTOLs apparently to emerge by 2024, with companies such as United Airlines and UPS even placing orders to these eVTOL start-ups.<sup>7-9</sup> There are already a few small cabin short-haul aircraft which have been electrified.<sup>10,11</sup> It should be noted that these vehicles employ conventional Li-ion batteries; but since the battery makes up about one third of the total weight of the aircraft, there is significant desire for increased energy density cells to improve flying range. Cuberg is one company working on lithium metal cells with liquid electrolytes to enable significantly increased battery energy density for electrified urban aviation.

Since their commercial introduction in 1991, the energy density of Li-ion cells has steadily increased over time.<sup>12</sup> This has mainly been a result of engineering optimizations via minimizing inactive material content (thinner current collectors, lessened electrode porosities, *etc.*) and incremental chemistry improvements via electrolyte design and some material developments.<sup>1,13</sup> The fundamental operating principles of Li-ion cells have not significantly changed in 30 years: lithium supplied by lithiated positive electrode is stored inside a graphitic carbon negative electrode host. This framework has been optimized over the last three decades and now most of the “low hanging fruit” for incremental improvements have been exhausted. Further significant improvements to energy density now require significant changes in cell chemistry. One such avenue is increasing the energy density of the electrode materials. Graphite has proven to be a reliable and robust negative electrode material for Li-ion cells. However, graphite only provides a fraction of the energy density of lithium metal. Evolving the lithium-ion cell to a lithium metal cell by replacing the graphite negative electrode with metallic lithium would provide a significant increase in energy density.

Ironically, lithium metal cells were devised 20 years prior to Li-ion cells. Lithium metal was experimented with as a negative electrode material as early as in the 1960s.<sup>14</sup> But, in

the years that followed preceding the advent of the graphite negative electrode, researchers encountered a number of then insurmountable challenges with lithium metal. Safety and longevity were the primary concerns. Cells with lithium metal could tolerate little abuse without experiencing catastrophic failure, often resulting thermal runaway and explosion.<sup>13</sup> Moreover, the lithium metal anode was found to quickly degrade. To compensate, large amounts of excess lithium was required to replenish lithium lost during cycling to deliver decent cell lifetime. However, this large lithium excess decreased the practical electrode energy density to be on par with graphite. So, when the graphite electrode was discovered to be safer and more robust, the lithium metal electrode was largely abandoned. Now that graphite can not provide the desired increase in energy density, significant research focus has reverted back to lithium metal.<sup>15</sup>

This thesis will detail my research effort on a particular kind of lithium metal cell design known as “anode-free” lithium metal cells. This cell design uses zero excess lithium. As such, safety should be improved by minimizing the content of reactive lithium in the cell. Furthermore, in eliminating excess lithium, this design maximizes energy density. The anode-free cells demonstrated in this work exhibit an energy density 60% greater than Li-ion cells—high enough to extend the range of electric vehicles by at least 200 km and even to enable flying taxis.<sup>3,4</sup>

## 1.2 Lithium-ion, Lithium Metal and Anode-Free Cells

All batteries consist of a positive electrode, a negative electrode, and an electrolyte. The electrodes in lithium-ion cells store charge in the form of lithium ions ( $\text{Li}^+$ ) and the electrolyte facilitates the transport of  $\text{Li}^+$  between electrodes during charge and discharge. Practically, these components need to be housed in some sort of package. **Figure 1.2** shows the different type of packages or cell formats: wound cylindrical, flat wound and stacked.\*

---

\* This graphic was retrieved from <https://honestenergy.substack.com/p/the-little-ion-that-could> which is a fantastic and easily accessible deep dive into the working components and principles of lithium-ion cells. This blog by Adrian Yao is a valuable resource for non-experts and even a useful (certainly entertaining) read for more veteran researchers.



Cylindrical cells are typically packaged in metallic cans, whereas flat wound and stacked cells are either packaged in compliant pouch or rigid prismatic casings.

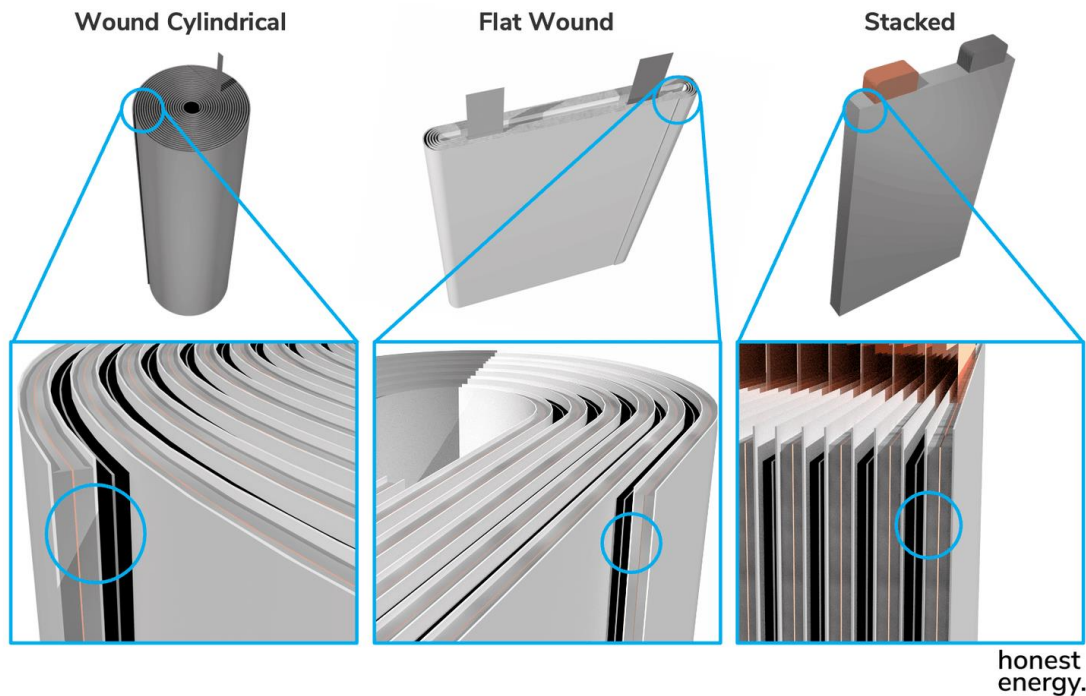


**Figure 1.2 | Li-ion cell formats.** Diagrams of wound cylindrical, flat wound, and stacked lithium-ion cells. The bottom panels are a zoomed in view which reveal the repeating electrode layers or “cell stack” that make up the entire cell. This graphic was produced by Adrian Yao: <https://honestenergy.substack.com/p/the-little-ion-that-could>

What is being wound or stacked in these cell formats? The bottom panels of **Figure 1.2** show a zoomed in view which reveals the electrochemical sandwich of the electrode materials which is repeated many times to form the entire cell. This is essentially an electrochemical unit cell which is referred to as the cell stack, shown in more detail in **Figure 1.3a**. The cell stack is comprised of, from bottom to top, a positive electrode (cathode) coating, an aluminum current collector, another positive electrode coating, a separator, a negative electrode (anode) coating, a copper current collector, another negative electrode coating, and a final separator. **Figure 1.3b** shows yet another zoomed in view, revealing that the electrodes are composed of micron-sized active material particles and that the separator is a porous film. Not shown are the additional inactive materials (binder

and conductive additive, typically ~4 wt.%) necessary bind and improve the electronic transport between active electrode particles. The entire electrode stack, affectionately referred to as the “jelly roll”, is immersed in liquid electrolyte which permeates the pores of the electrodes and separators to facilitate  $\text{Li}^+$  transport.

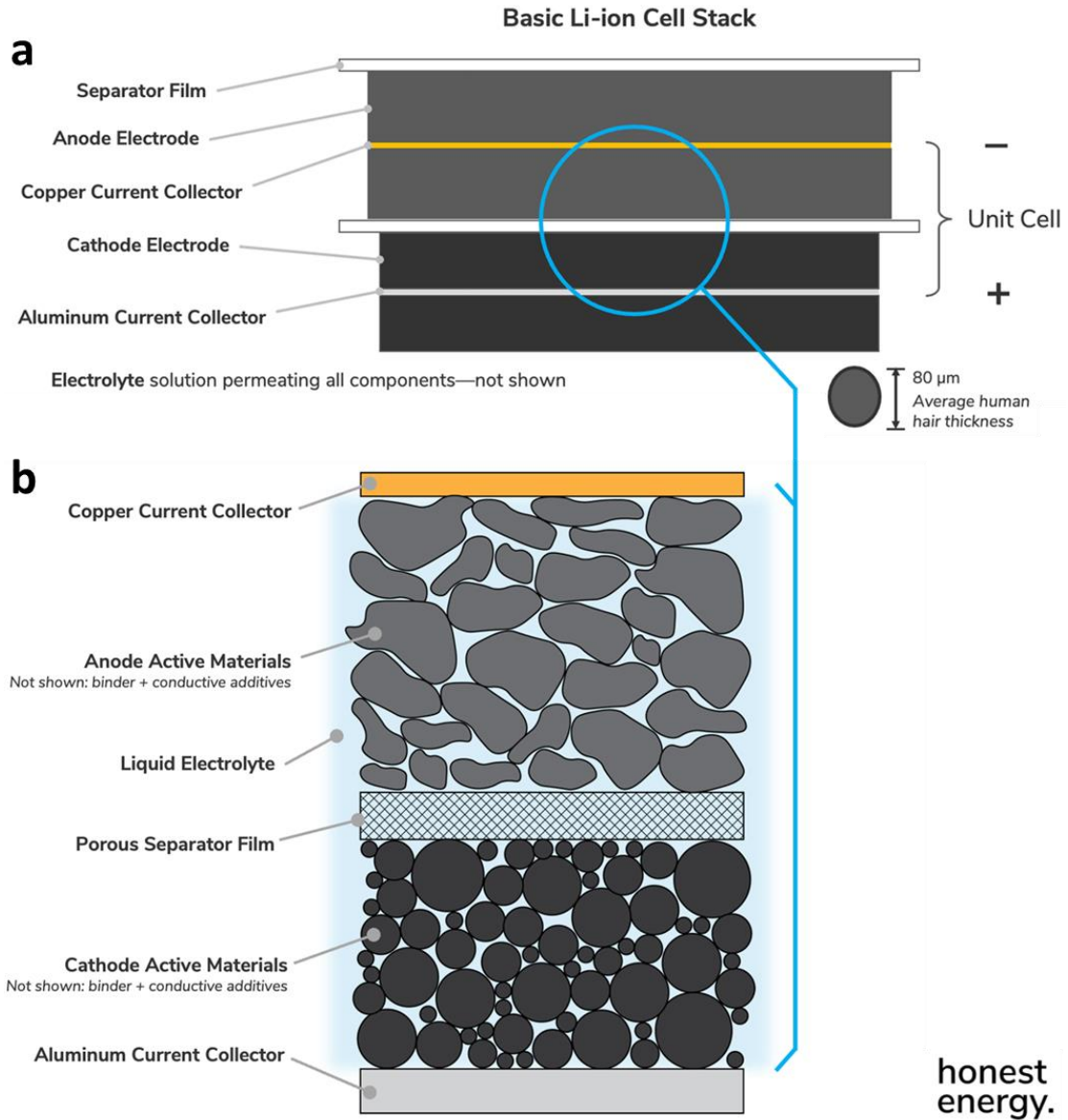


**Figure 1.3 | Li-ion cell stack. a,** The electrochemical unit cell called the “cell stack” which consists of a double sided positive electrode (cathode), a double sided negative electrode (anode), and two separators. **b,** A zoomed in view of the cell stack which reveals that the electrodes are composed of micrometer sized particles. This graphic was produced by Adrian Yao: <https://honestenergy.substack.com/p/the-little-ion-that-could>

The positive electrodes used in Li-ion cells are mainly lithium transition metal oxides ( $\text{LiMO}_2$ ) which exhibit an ordered rock-salt structure.<sup>16</sup> The transition metal (M) oxide form layered slabs between which lithium is stored. M can be a single or combination of transition metals.  $\text{LiCoO}_2$  (LCO) was the first commercialized positive electrode material used in Li-ion cells and is still in common use today as a result of the good cycle life and energy density it provides. LCO delivers a specific capacity of 160 mAh/g with an average voltage of 3.9 V. Most portable electronics are still powered by LCO positive electrodes.<sup>1,17</sup> However, LCO electrodes are not employed for larger capacity cells because of its relatively poor safety, with a thermal stability only up to  $\sim 200$  °C. The desire to improve safety and reduce cobalt content spawned the strategy of doping cobalt for nickel and manganese to form the class of  $\text{LiNi}_{1-x-y}\text{Mn}_x\text{Co}_y\text{O}_2$  (NMC) materials. NMC can deliver a higher specific capacity and a superior thermal stability. NMC materials are thus used for electric vehicle applications. For  $x = 0.3$  and  $y = 0.2$  ( $\text{LiNi}_{0.5}\text{Mn}_{0.3}\text{Co}_{0.2}\text{O}_2$ , NMC532), the specific capacity is 170 mAh/g and the thermal stability is increased to 290 °C.<sup>18</sup> Further increasing the nickel content and reducing the cobalt content had a two-fold benefit of reducing cost as well as increasing the specific capacity. However, this comes at a penalty of safety, as high nickel materials have thermal stabilities similar to LCO. NMC811 delivers a specific capacity of 200 mAh/g with a thermal stability of only 240 °C.<sup>18</sup> Non-layered positive electrode materials have also been developed. For example,  $\text{LiFePO}_4$  (LFP) hosts  $\text{Li}^+$  in a tunnel-like structure of octahedral channels. The iron based LFP is cheaper than LCO and NMC without cobalt or nickel; LFP also has a superior thermal stability. However, LFP has a specific capacity of only 165 mAh/g with an average voltage of 3.45 V resulting in a significantly lower energy density than LCO and NMC positive electrodes.<sup>16</sup>

Graphite is the predominant negative electrode used in lithium-ion cells. Like  $\text{LiMO}_2$  positive electrodes, graphite is an intercalation material which reversibly hosts lithium inside of its layered structure. Graphite is an excellent negative electrode material because it provides a low average voltage, good rate capability, and good thermal stability to name a few of its virtues.<sup>19</sup> Moreover, lithium insertion between graphene layers is a relatively benign process, only resulting in a 8-10% volume change of the graphite structure.<sup>20</sup> This

facilitates highly reversible lithiation, enabling lifetimes of thousands of cycles,<sup>21</sup> and has cemented graphite as the dominant negative electrode material for Li-ion cells for 25 years.<sup>21</sup> However, in the pursuit of ever higher cell energy density, the graphite negative electrode is a limiting factor. The fully lithiated graphite phase is  $\text{LiC}_6$ ; six carbon atoms are required to store a single lithium. Although this provides an accommodating lithium host, these carbon atoms are essentially dead weight insofar as they do not contribute to energy that is stored. As a result, graphite has a relatively low theoretical specific capacity (372 mAh/g) compared to other possible negative electrode materials. For example, one silicon atom can bond with almost 4 lithium atoms ( $\text{Li}_{15}\text{Si}_4$ ) resulting in a specific capacity of 3579 mAh/g. Unfortunately, this massive specific capacity is mostly out of reach since silicon negative electrode materials exhibit poor cyclability. This is largely a result of the large 300% volume expansion which occurs when lithium alloys with silicon.<sup>19</sup> Nevertheless, the high capacity of silicon has been harnessed to some extent by incorporating small fractions (~10%) in graphite electrodes which accommodates its large volume expansion while still providing a boost in energy density. Many advanced lithium-ion batteries in use today employ a graphite-silicon composite negative electrode.<sup>1</sup> Obviously, the most efficient way to store lithium would be by discarding the host or alloy materials all together and to use a pure lithium negative electrode. Storing capacity as plated metallic lithium would deliver a specific capacity of 3860 mAh/g. However, as we will discuss in further detail in Chapter 2, reversible lithium plating comes with its own set of significant challenges.

As per its namesake, the separator is used to physically separate the positive and negative electrode to prevent a short circuit. The separator must thus be an electronic insulator while also being an ionic conductor to facilitate the transport of  $\text{Li}^+$  between the electrodes. The separator is a microporous film usually composed of polyethylene and polypropylene.<sup>16</sup>

The liquid electrolyte used in Li-ion cells contains a lithium salt dissolved in solvent. The electrolyte must satisfy a pretty daunting set of requirements: stability with both electrodes (*i.e.* a large electrochemical stability window), high conductivity and transference number, low viscosity, high dielectric constant, low volatility, and a broad temperature range of



operation—all while maintaining an acceptable cost.<sup>22</sup> Although there is always room for improvement, a good mix of these qualities has been achieved with lithium hexafluorophosphate ( $\text{LiPF}_6$ ) salt dissolved in a combination of organic carbonates, such as ethylene carbonate (EC) and diethyl carbonate (DEC). A common electrolyte recipe using these ingredients is 1 M  $\text{LiPF}_6$  dissolved in a EC:DEC blend at a volume ratio of 1:2. Additional chemicals are often added as “electrolyte additives” at <10 wt.% generally to improve the stability of the graphite negative electrode.

**Figure 1.4** shows a schematic of the operating principles of a lithium-ion cell. The positive and negative electrodes are shown in the partially lithiated state. The transition metal oxide  $\text{MO}_2$  slabs can be seen on the positive electrode side with  $\text{Li}^+$  stored between these layers. Lithium ions intercalated in graphite are shown on the negative electrode side. During charge (red arrows in **Figure 1.4**), the positive electrode is oxidized by an external power supply and  $\text{Li}^+$  from the positive electrode are shuttled through the electrolyte and separator and intercalated into the graphite which is reduced by the electrons flowing through the external circuit. Conversely, during discharge (blue arrows in **Figure 1.4**), the graphite is spontaneously oxidized, and electrons do work through an external load and reduce the positive electrode while  $\text{Li}^+$  are removed from the graphite and re-intercalated into the transition metal oxide host.

**Figure 1.5** shows a schematic of a lithium metal cell. In principle, it works in the same way as a Li-ion cell, except that the graphite lithium host is replaced with a lithium metal negative electrode. Instead of intercalating into graphite,  $\text{Li}^+$  electroplate to form lithium metal. Since lithium metal is capable of storing more charge per weight and volume than graphite, lithium metal cells can deliver higher energy density than Li-ion cells.

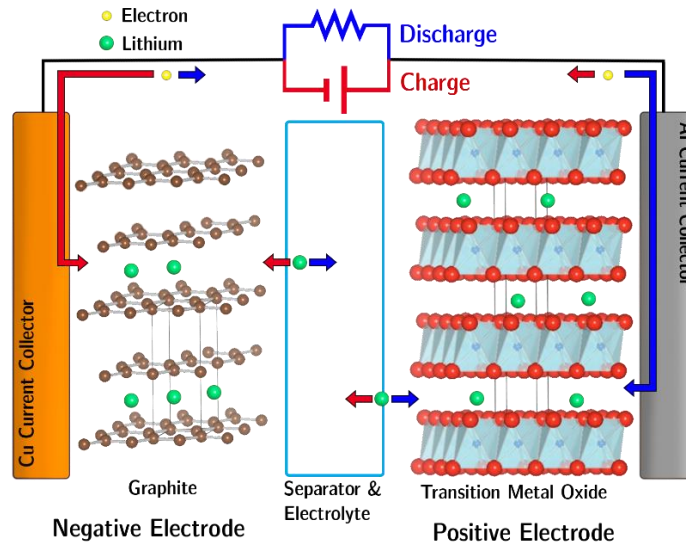


**Figure 1.4 | Lithium-ion cell schematic.** The operation of a Li-ion cell during charge (red arrows) and discharge (blue arrows). The positive electrode is a lithium transition metal oxide and the negative electrode is graphite. Lithium ions (the green spheres) are shuttled between electrodes via the electrolyte through the separator. The electrons (yellow spheres) flow through the external circuit.

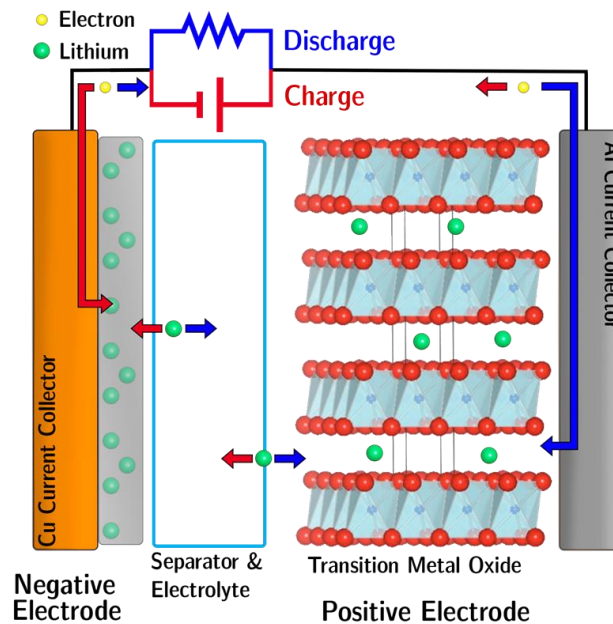


**Figure 1.5 | Lithium metal cell schematic.** The operation of a lithium metal cell during charge (red arrows) and discharge (blue arrows). Lithium is stored in metallic form as the negative electrode. Lithium metal stores  $\sim 10\times$  more capacity per gram and  $\sim 3\times$  more capacity per  $\text{cm}^3$  than graphite, enabling a significantly lighter and less voluminous cell.

**Figure 1.6a** shows another schematic of a Li-ion cell, this time in the fully discharged state (the positive electrode fully lithiated). **Figure 1.6d** is a picture of a lab-scale Li-ion pouch cell. This pouch cell, using the stack architecture shown in **Figure 1.6a**, has a stack specific energy density of 305 Wh/kg and a stack volumetric energy density of 720 Wh/L.

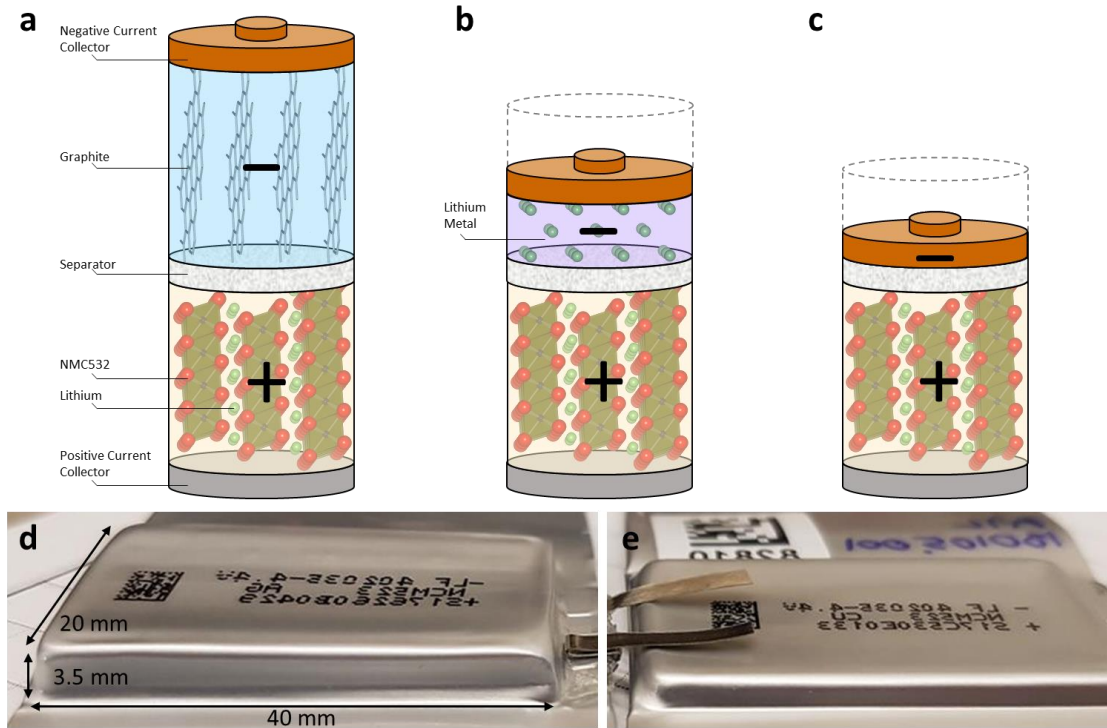


**Figure 1.6 | Li-ion, lithium metal and anode-free cells. a-c,** Cell schematics of a Li-ion (a), lithium metal (b), and anode-free (c) cell in the discharged state. **d-e,** Picture of a Li-ion (d) and an anode-free (e) pouch cell used in this work.

**Figure 1.6b** is a schematic of a lithium metal cell in the fully discharged state. Lithium metal cells are built with lithium metal foils, typically 50-400  $\mu\text{m}$  in thickness. Like Li-ion cells, lithium metal cells are built in the discharged state, meaning the positive electrode is fully lithiated. When the cell is charged,  $\text{Li}^+$  from the positive electrode travels to the negative electrode and deposits on top of the lithium foil. There are two important consequences to consider here. First, there will be a significant volume expansion of the

cell corresponding to the thickness of lithium which is plated.<sup>‡</sup> The expanded cell thickness in the fully charged state is denoted by the dotted volume overlaying the cell stack in **Figure 1.6b**. Second, the lithium foil originally coated on the copper current collector provides lithium *in excess* of the lithium provided by the positive electrode. Since discharge capacity is determined by how much lithium can be stored inside the positive electrode, this excess lithium does not contribute to the energy the cell can deliver. In fact, this excess lithium decreases the energy density of the cell by increasing its volume and mass without increasing delivered capacity. Therefore, the energy density will depend on the thickness of lithium foil built into the cell. When lithium foils thicker than 60  $\mu\text{m}$  are used, the cell energy density drops below the energy density of comparable Li-ion cells. Since improved energy density is the benefit of lithium metal, there is no virtue in making a lithium metal cell with less energy density than a Li-ion cell. Nevertheless, these impractical cell designs with thick lithium foils  $> 200 \mu\text{m}$  are often touted in the literature. Recently, there have been appeals to use limited, thin  $< 50 \mu\text{m}$  lithium foils to enable useful lithium metal cells.<sup>23,24</sup> However, thin lithium foils are not easy to manufacture and will not be cheap.<sup>25,26</sup> Moreover, handling reactive and delicate lithium foils during cell construction will introduce new difficulties to established cell production lines—not to mention the safety concerns associated with cells with excess lithium.<sup>13,27</sup> For all of these reasons, dispensing with excess lithium using an anode-free cell design is attractive.

**Figure 1.6c** shows a schematic of an anode-free cell. Per its namesake, these cells are built without a negative electrode (anode). Unlike Li-ion and lithium metal cells which are built with either a graphite or a lithium metal foil anode, anode-free cells are built with just a bare copper current collector on the negative side. During charge,  $\text{Li}^+$  from the positive electrode are electroplated onto the copper current collector to form a lithium metal anode *in-situ*.<sup>28,29</sup> Again, this lithium plating results in an increase in thickness of the cell, as

---

<sup>‡</sup> The areal capacity which should be cycled in a practical lithium metal cell is about 3  $\text{mAh}/\text{cm}^2$ , corresponding to a lithium thickness (assuming 100% densification) of  $\sim 15 \mu\text{m}$  when fully charged. For comparison, a 70  $\mu\text{m}$  thick graphite electrode which experiences an 8% volume expansion exhibits an increase in thickness of only 5.6  $\mu\text{m}$ .

shown with the dotted volume overlaid on the top of **Figure 1.6c**. All the cyclable lithium in an anode-free cell originates from the positive electrode. Without any excess lithium, the highest energy density cell is achieved. Moreover, dispensing with the lithium foil will make anode-free cells 50% cheaper than conventional lithium metal cells (anode-free cells should also be 20% cheaper than Li-ion cells due to costs saved from the removal of the graphite negative electrode).<sup>30</sup> Unfortunately, this does not come without a penalty, as without excess lithium the lifetime of anode-free cells is severely limited, as detailed further in Chapter 2. **Figure 1.6e** shows a picture of an anode-free pouch cell. Without the graphite negative electrode, the anode-free cell is significantly thinner (and less massive) than the Li-ion cell shown in **Figure 1.6d**. The anode-free cell delivers a stack specific energy density of 470 Wh/kg and a volumetric energy density of 1230 Wh/L. This corresponds to an energy density 60% higher than comparable Li-ion cells and is the motivation for this thesis work—to develop high energy density anode-free lithium metal cells with liquid electrolytes.

### 1.3 Thesis Outline

Chapter 2 provides a historical overview of the development of lithium metal and anode-free cells. A literature review of the major degradation modes associated with the lithium metal anode as well as strategies employed to stabilize lithium metal are presented.

Chapter 3 details our experimental methodology. The cell chemistries tested, the cycling experiments, and other tools used in this work are detailed here.

Chapter 4 presents our first results testing anode-free cells with NMC532 positive electrodes. This chapter details how we increased the lifetime of anode-free cells from 1 to 100 cycles using a combination of mechanical and electrolyte innovations. We describe a dual-salt electrolyte chemistry optimized for reversible lithium metal cycling.

Chapter 5 is an investigation of the impact of different cycling conditions. The effect of temperature, charge-discharge rates, and depth of discharge on the performance of anode-free cells are studied. The optimal cycling conditions for anode-free cells are presented.

Chapter 6 considers anode-free cells with different positive electrode materials: NMC532, NMC811, LCO and LFP. These different cell chemistries are tested head-to-head and their performance is characterized electrochemically, with electrolyte degradation analysis, and in terms of safety.

Chapter 7 introduces a novel cell design combining graphite and lithium metal to form hybrid lithium-ion/lithium metal cells. The performance of these cells which intentionally plate lithium on top of graphite to harness increased energy density is investigated.

Chapter 8 presents our conclusions and outlooks for the future anode-free lithium metal cells with liquid electrolytes. We also outline potential future work which may further our understanding and perhaps improve the performance of anode-free cells.

Some of the results presented in this thesis have been previously published in peer-reviewed journals. These publications are specified at the beginning of every chapter.

## Chapter 2: A Brief History of Lithium Metal

In 1965, a report commissioned by NASA titled “Research and Development of a High Capacity Nonaqueous Secondary Battery” was written.<sup>14</sup> By then, almost 60 years ago, already substantial work had begun studying the lithium metal anode for rechargeable batteries, motivated by the demand for a higher energy density than aqueous cells could deliver.<sup>31</sup> Lithium’s high capacity (3860 mAh/g, 2062 Ah/L) and low redox potential (-3.04 V vs standard hydrogen electrode) made it an attractive candidate as a negative electrode material. Although such a low redox potential makes lithium thermodynamically unstable with practically any electrolyte, it was later discovered that a passivating solid electrolyte interphase (SEI) formed at the lithium-electrolyte surface.<sup>32</sup> In theory, this could facilitate reversible lithium cycling. The NASA report identified key parameters that influenced reversible lithium plating which researchers still wrestle with today including current density, lithium utilization, plating substrate, and electrolyte formulation. Ultimately, that 1965 report concluded:

The relatively low efficiency and cycle life [...] and the poor physical form of the lithium of the lithium electrodeposit do not suggest that the lithium electrode at present is a likely candidate for incorporation in secondary cells.<sup>14</sup>

To compensate for this cycling inefficiency and resultant rapid capacity loss during aging, cells had to be built with a large excess of lithium—at least 3x the amount required for a single cycle. Consequently, the effective capacity of a lithium electrode with such a design was reduced to 965 mAh/g (515 Ah/L).<sup>13</sup>

The lithium metal anode needed to be paired with a suitable positive electrode to complete the lithium metal battery. This came in 1976 when Whittingham made the breakthrough discovery of intercalation materials for the reversible insertion of lithium.<sup>33</sup> In 1978, Exxon moved to commercialize this cell chemistry in 25 mAh and 100 mAh coin cell formats (**Figure 2.1a**).<sup>34†</sup> Lithium metal cells penetrated the market after Moli Energy Canada

---

† The negative electrode was a lithium-aluminum alloy—not strictly lithium metal.

commercialized another chemistry in a 600 mAh cylindrical format in 1988 (**Figure 2.1b**). By the end of 1988, 2 million MOLICELs were in the field powering laptops and cell phones. Unfortunately, this era of lithium metal cells was short lived, as catastrophic safety incidents prompted the recall of products powered by MOLICELs in 1989.<sup>12,13,31</sup> The tendency for lithium metal cells to vent with smoke and flame (read: explode) was obviously unacceptable. This was a result of an unavoidable challenge of lithium being prone to plate as high surface area deposits. The increased reactivity of high surface area lithium with liquid electrolyte and the inherently flammability of the organic liquid electrolyte made these cells highly vulnerable to thermal abuse, with temperatures as low as 100 °C initiating thermal runaway in some aged lithium metal cells.<sup>27</sup>

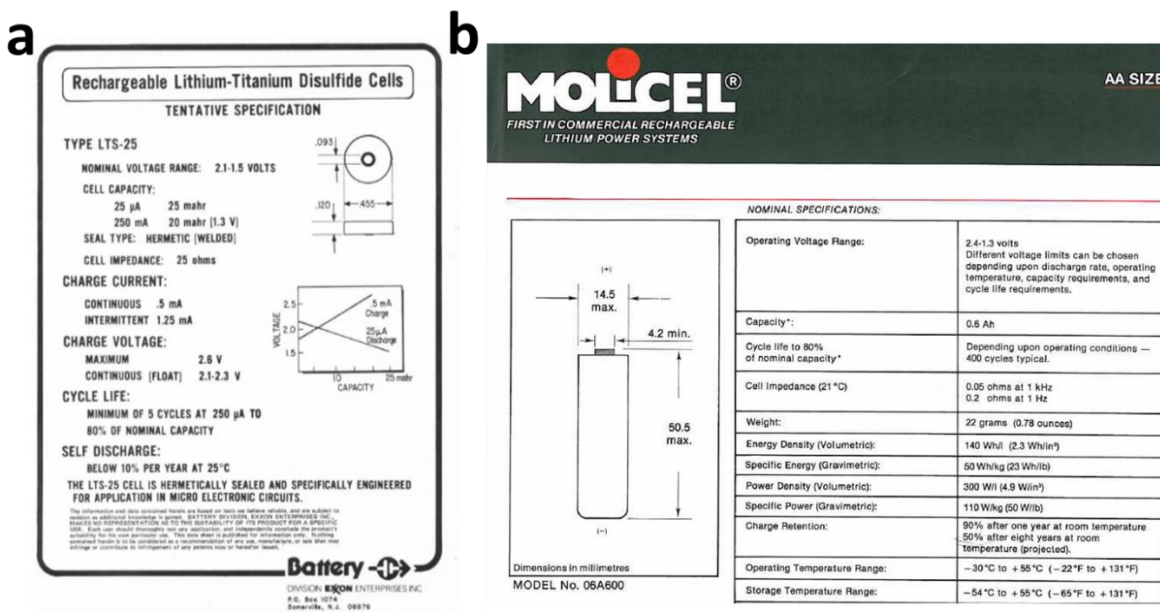


**Figure 2.1 | First commercial lithium metal cells. a**, Exxon 25 mAh Li-Al/TiS<sub>2</sub> cell spec sheet from 1978, reproduced from Ref.<sup>34</sup> **b**, Moli Energy Canada 600 mAh Li/MoS<sub>2</sub> cell spec sheet, reproduced from Dr. Jeff Dahn.

Amidst the rise and fall of lithium metal batteries, key discoveries paving the way towards lithium-ion cells were made. In the early 80s, lithium intercalation into graphite was demonstrated as a negative electrode host for lithium ions as opposed to plating lithium.<sup>35,36</sup> In 1980, Goodenough discovered LiCoO<sub>2</sub>, another layered material that accommodated



lithium intercalation at high voltage which would later become the modern day positive electrode.<sup>37</sup> In 1985, Yoshino built the first lithium-ion battery prototype, pairing the  $\text{LiCoO}_2$  positive electrode with a graphite negative electrode.<sup>38</sup> At that time, graphite was overlooked for commercialization because of its relatively low capacity (372 mAh/g, 837 Ah/L). However, this is not that low in comparison to the practical capacity of lithium metal electrodes with 3x excess. After the disastrous safety incidents which doomed lithium metal cells, the pivot to graphite-based lithium-ion cells was inevitable. In 1991, the first lithium-ion cell was commercialized by Sony Corporation.<sup>1,13</sup> Stanley Whittingham, John Goodenough, and Akira Yoshino went on to win the 2019 Nobel Prize in chemistry for the invention of the lithium-ion cell.<sup>‡</sup>

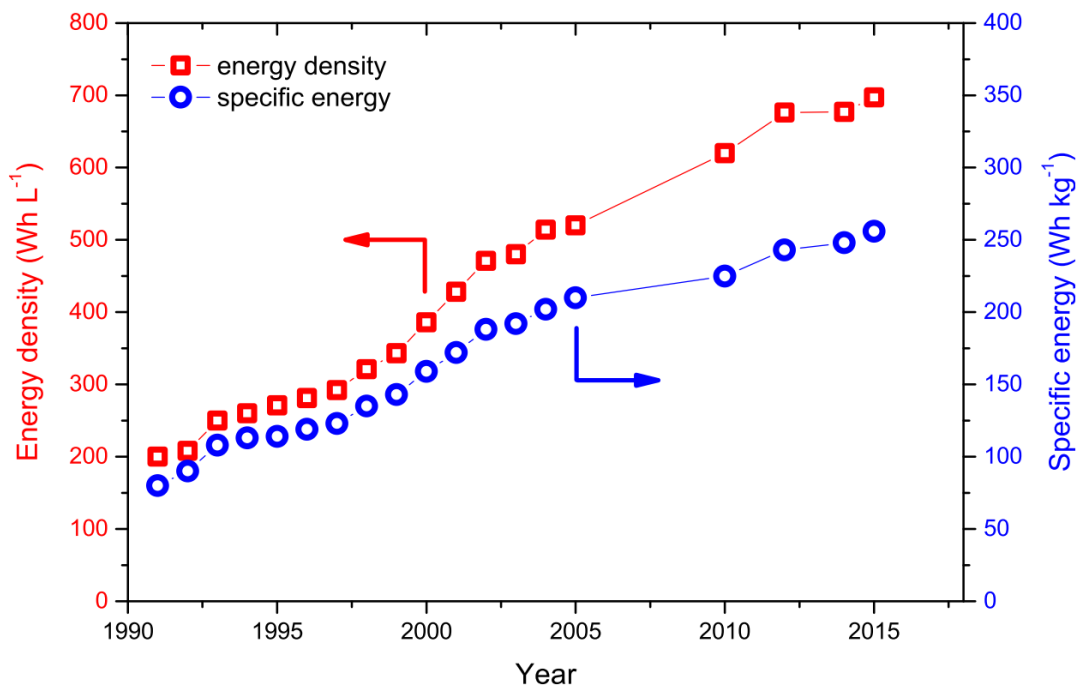


**Figure 2.2 | Improvement of Li-ion cell energy density.** Volumetric energy density (red, left axis) and specific energy density (blue, right axis) vs year of commercialized 18650-format lithium-ion cells as reproduced from Ref.<sup>12</sup> Note that most energy densities quoted in this thesis are at the stack level, whereas these numbers are for 18650 cells. Cell level energy densities are about 20% lower than at the stack level.

<sup>‡</sup> <https://www.nobelprize.org/prizes/chemistry/2019/press-release/>

The original Sony lithium-ion cell has been greatly improved over the last 30 years. However, today's lithium-ion cells still utilize the same fundamental components of the 1991 cell with a graphitic negative electrode paired with a layered transition metal oxide positive electrode. Therefore, the improvements to energy density (shown in **Figure 2.2**) have been largely accomplished by engineering cells with more active and less inactive materials.<sup>1,12</sup> As lithium-ion cells matured through the 2010s, it was clear that significant improvements to energy density would require more fundamental developments in cell chemistry. This desire for even more energy dense batteries re-focused the spotlight on the lithium metal anode, with a great effort from academia applied to improve lithium cycling efficiency.<sup>15,39</sup>

In 2000, the first "lithium-free" (a.k.a. anode-free) cell concept was published. This pioneer anode-free cell utilized a thin-film battery design and thus only cycled very low microamp areal capacities to overcome poor lithium cycling efficiency.<sup>28</sup> In 2016, the anode-free cell design was revived, now demonstrating cycling with more practical milliamp areal capacities. Although anode-free cells using conventional lithium-ion electrolytes could not even sustain a single cycle due to pitiful cycling efficiency, Qian *et al.* showed that electrolytes tailored to improving lithium plating efficiency could sustain longer cycle life, with this 2016 work exhibiting a lifetime of about 20 cycles.<sup>29</sup> A subsequent publication from Rodriguez *et al.* demonstrated the effect of a number of different electrolytes for anode-free cells.<sup>40</sup> The anode-free design is attractive because using zero excess lithium enables the entire 3860 mAh/g specific capacity promised by lithium metal to be harnessed. Moreover, with the least amount of reactive lithium present in the cell, anode-free cells should be the safest possible implementation of the lithium anode.

In 2018, anode-free lithium metal cells were commercialized by Pellion Technologies who reportedly produced cells capable of 50 cycles.<sup>41</sup> It was this effort from Pellion which inspired our work on anode-free cells. Although 50 cycles is still too short a cycle life for many applications, Pellion found a market in commercial drones. In this market, the trade-off of short cycle life for significantly increased energy density to enable longer flight times was acceptable. However, Pellion's efforts folded in 2019 after their primary investor had

grown impatient and wary about the prospects of such a niche market, ultimately pulling their funding.<sup>42</sup> Although Pellion reportedly got so far as to ship cells to manufacturers of commercial drones, it is unclear if these anode-free cells ever took flight in drones sold to customers. To date, the only company currently working on lithium metal cells with an anode-free design (as far as this author is aware) is QuantumScape; however, they are using a solid electrolyte as opposed to a liquid electrolyte which is the focus of this thesis.

Ultimately, the realization of anode-free cells with liquid electrolytes is hampered by poor lithium cycling efficiency impeding practical cell lifetime. Nevertheless, the exciting promise of this technology has attracted significant research. Reviews on the development of anode-free cells have been published by Nanda *et al.*<sup>26</sup> and Salvatierra *et al.*<sup>30</sup> In those reviews, the capacity retention and cycling efficiency were surveyed. This information has been compiled in **Table 2.1**. A quasi-coulombic efficiency shown in **Table 2.1** was calculated as

$$Efficiency = Fractional\ Capacity \frac{1}{Cycle}$$

This assumes that efficiency is constant throughout cycling and that capacity fade is only a result of cycling inefficiency. In other words, this is an approximation for coulombic efficiency calculated with simple capacity retention numbers. **Figure 2.3a** shows the capacity retention vs cycle and **Figure 2.3b** shows the efficiency vs cycle for the anode-free results listed in **Table 2.1**. **Figure 2.3c** is a plot from Ref.<sup>30</sup> which shows the theoretical cycle life for lithium metal cells with different cycling efficiencies and lithium excess. NP = 1 corresponds to zero excess (anode-free), NP = 1.5 means 0.5x excess, and NP = 2 means 1x excess. **Figure 2.3c** shows that efficiencies exceeding 99.5% are required for anode-free cells to have a cycle life greater than 60 cycles. It should be noted that in **Figure 2.3a** and **b**, numbers 2, 3, and 4 are references from our lab which will be discussed in this thesis; number 1 is an anode-free cell that uses a solid electrolyte. The longest lifetime anode-free cell with liquid electrolyte from **Table 2.1** is 200 cycles corresponding to an efficiency 99.89%. For comparison, optimized lithium-ion can have coulombic efficiencies of 99.985%.<sup>21</sup>

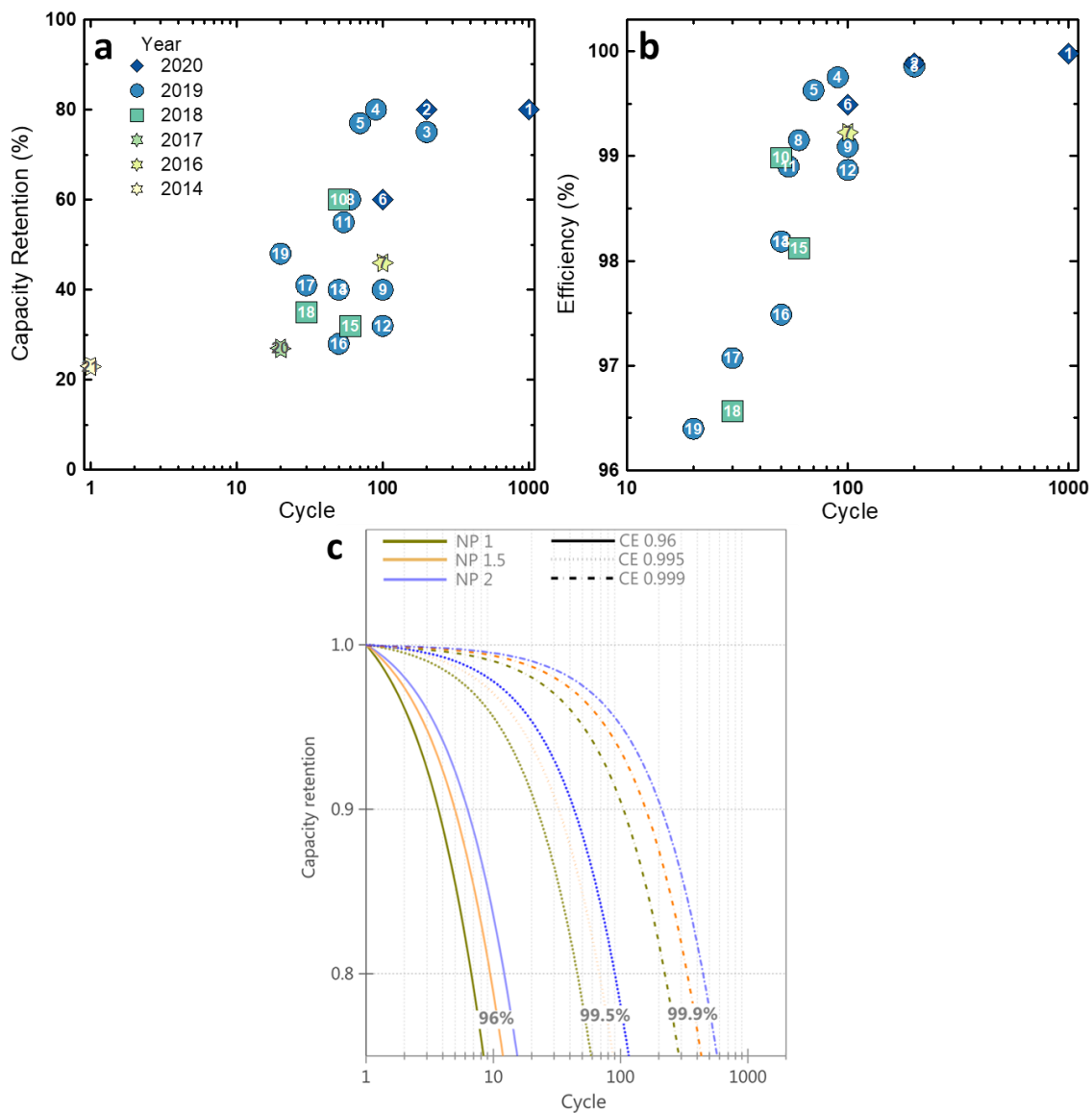


**Figure 2.3 | Anode-free cell development.** **a**, Capacity retention vs cycle and **b**, Efficiency vs cycle of anode-free lithium metal cells. The numbers on the data points correspond to the references listed in **Table 2.1**. **c**, Theoretical capacity retention for lithium metal cells with different coulombic efficiencies (CE) and lithium excess—NP = 1 corresponds to zero excess (anode-free design), NP = 1.5 is a 0.5x excess, NP = 2 is a 1x excess, as reproduced from Ref.<sup>30</sup>

**Table 2.1:** Summary of anode-free research reviewed by Nanda *et al.*<sup>26</sup> and Salvatierra *et al.*<sup>30</sup>

Ref. #	Reference	Year	Cycles	Capacity Retention (%)	Efficiency†
1	<sup>43</sup> *Y. Lee et al, <u>High-energy long-cycling all-solid-state lithium metal batteries enabled by silver–carbon composite anodes</u> , <i>Nat. Energy</i> . <b>5</b> (2020) 299–308.	2020	1000	80	99.98
2	<sup>44</sup> A.J. Louli et al, <u>Diagnosing and correcting anode-free cell failure via electrolyte and morphological analysis</u> , <i>Nat. Energy</i> . <b>5</b> (2020) 693–702.	2020	200	80	99.89
3	<sup>45</sup> M. Genovese et al, <u>Hot Formation for Improved Low Temperature Cycling of Anode-Free Lithium Metal Batteries</u> , <i>J. Electrochem. Soc.</i> <b>166</b> (2019) A3342–A3347.	2019	200	75	99.86
4	<sup>46</sup> R. Weber et al, <u>Long cycle life and dendrite-free lithium morphology in anode-free lithium pouch cells enabled by a dual-salt liquid electrolyte</u> , <i>Nat. Energy</i> . <b>4</b> (2019) 683–689.	2019	90	80	99.75
5	<sup>47</sup> X. Ren et al, <u>Enabling High-Voltage Lithium-Metal Batteries under Practical Conditions</u> , <i>Joule</i> . <b>3</b> (2019) 1662–1676.	2019	70	77	99.63
6	<sup>48</sup> Z. Yu et al, <u>Molecular design for electrolyte solvents enabling energy-dense and long-cycling lithium metal batteries</u> , <i>Nat. Energy</i> . <b>5</b> (2020) 526–533.	2020	100	60	99.49
7	<sup>29</sup> J. Qian et al, <u>Anode-Free Rechargeable Lithium Metal Batteries</u> , <i>Adv. Funct. Mater.</i> <b>26</b> (2016) 7094–7102.	2016	100	46	99.23
8	<sup>49</sup> A.J. Louli et al, <u>Exploring the Impact of Mechanical Pressure on the Performance of Anode-Free Lithium Metal Cells</u> , <i>J. Electrochem. Soc.</i> <b>166</b> (2019) A1291–A1299.	2019	60	60	99.15

9	<sup>50</sup>	T.T. Beyene et al, <u>Effects of Concentrated Salt and Resting Protocol on Solid Electrolyte Interface Formation for Improved Cycle Stability of Anode-Free Lithium Metal Batteries</u> , <i>ACS Appl. Mater. Interfaces</i> . <b>11</b> (2019) 31962–31971.	2019	100	40	99.09
10	<sup>40</sup>	R. Rodriguez et al, <u>Effect of the Electrolyte on the Cycling Efficiency of Lithium-Limited Cells and their Morphology Studied Through in Situ Optical Imaging</u> , <i>ACS Appl. Energy Mater.</i> <b>1</b> (2018) 5830–5835.	2018	50	60	98.98
11	<sup>51</sup>	J. Alvarado et al, <u>Bisalt ether electrolytes: a pathway towards lithium metal batteries with Ni-rich cathodes</u> , <i>Energy Environ. Sci.</i> <b>12</b> (2019) 780–794.	2019	54	55	98.90
12	<sup>52</sup>	T.T. Beyene et al, <u>Concentrated Dual-Salt Electrolyte to Stabilize Li Metal and Increase Cycle Life of Anode Free Li-Metal Batteries</u> , <i>J. Electrochem. Soc.</i> <b>166</b> (2019) A1501–A1509.	2019	100	32	98.87
13	<sup>53</sup>	T.T. Hagos et al, <u>Locally Concentrated LiPF<sub>6</sub> in a Carbonate-Based Electrolyte with Fluoroethylene Carbonate as a Diluent for Anode-Free Lithium Metal Batteries</u> , <i>ACS Appl. Mater. Interfaces</i> . (2019).	2019	50	40	98.18
14	<sup>54</sup>	N.A. Sahalie et al, <u>Effect of bifunctional additive potassium nitrate on performance of anode free lithium metal battery in carbonate electrolyte</u> , <i>J. Power Sources</i> . <b>437</b> (2019) 226912.	2019	50	40	98.18
15	<sup>55</sup>	M. Genovese et al, <u>Measuring the Coulombic Efficiency of Lithium Metal Cycling in Anode-Free Lithium Metal Batteries</u> , <i>J. Electrochem. Soc.</i> <b>165</b> (2018) A3321–A3325.	2018	60	32	98.12
16	<sup>56</sup>	Z.L. Brown et al, <u>Using Triethyl Phosphate to Increase the Solubility of LiNO<sub>3</sub> in Carbonate Electrolytes for Improving the Performance of the Lithium Metal Anode</u> , <i>J. Electrochem. Soc.</i> <b>166</b> (2019) A2523–A2527.	2019	50	28	97.49

17	<sup>57</sup>	V. Nilsson et al, <u>Highly Concentrated LiTFSI-EC Electrolytes for Lithium Metal Batteries</u> , <i>ACS Appl. Energy Mater.</i> <b>3</b> (2020) 200–207.	2019	30	41	97.07
18	<sup>58</sup>	X. Fan et al, <u>Non-flammable electrolyte enables Li-metal batteries with aggressive cathode chemistries</u> , <i>Nat. Nanotechnol.</i> <b>13</b> (2018) 1–8.	2018	30	35	96.56
19	<sup>59</sup>	T.M. Hagos et al, <u>Dual electrolyte additives of potassium hexafluorophosphate and tris (trimethylsilyl) phosphite for anode-free lithium metal batteries</u> , <i>Electrochim. Acta.</i> <b>316</b> (2019) 52–59.	2019	20	48	96.40
20	<sup>60</sup>	Z.L. Brown et al, <u>Investigation of the Lithium Solid Electrolyte Interphase in Vinylene Carbonate Electrolytes Using Cu  LiFePO<sub>4</sub> Cells</u> , <i>J. Electrochem. Soc.</i> <b>164</b> (2017) A2186–A2189.	2017	20	27	93.66
21	<sup>61</sup>	J.-J. Woo et al, <u>Symmetrical Impedance Study on Inactivation Induced Degradation of Lithium Electrodes for Batteries Beyond Lithium-Ion</u> , <i>J. Electrochem. Soc.</i> <b>161</b> (2014) A827–A830.	2014	1	23	23.00

\* This was an anode-free cell with a solid electrolyte, as opposed to all the other references here which use liquid electrolytes.

† Efficiency was calculated as  $\text{Fractional Capacity Retention}^{\frac{1}{\text{Cycles}}}$

Currently, efforts to commercialize lithium metal cells with liquid electrolytes in 2021 continue at Cuberg and SES (SolidEnergy Systems). To compensate for poor lithium cycling efficiency, both companies are using some amount of excess lithium. The latest reports from Cuberg revealed a lifetime of 370 cycles as validated by Idaho National Lab in June 2020.\* Cuberg's cells employ a 50  $\mu\text{m}$  lithium foil corresponding to a lithium excess of at least 2x. The lithium foil is "free standing" which means the copper current collector is removed to improve specific energy density. The validated 5 Ah cells had energy densities of 369 Wh/kg and 661 Wh/L. A pitch deck obtained from SES dated July 2020 claims that they have achieved 500 cycles with a specific energy density of 376 Wh/kg, although these numbers have not been validated by a third party. SES employs a 20  $\mu\text{m}$  thick lithium foil. Both companies are using a proprietary liquid electrolyte as well as increased mechanical pressure to improve cycling efficiency. SES may also be using an additional solid layer to improve lithium passivation.

## 2.1 Lithium Metal Cell Design

We have discussed how excess lithium has been used in lithium metal cells to compensate for poor cycling efficiency and overcome rapid capacity loss. Let's now consider how the amount of lithium excess and thickness of lithium foils used in lithium metal cells impacts their energy density. **Figure 2.4a** shows a series of lithium metal cell designs compared to a Li-ion cell. These schematics are of the cell stack, a to-scale rendition of the thickness of each cell component including the separators, double sided positive electrode, double sided negative electrode. The positive electrode coatings are 46.25  $\mu\text{m}$  thick NMC532 corresponding to an areal capacity of about 3 mAh/cm<sup>2</sup> (this cell design is described later in **Table 3.1**). The areal energy of these cell stacks is calculated by multiplying the areal capacity ( $2 \times 3 \text{ mAh/cm}^2$  since the electrodes are double-sided) by the average voltage (3.87 V for lithium metal and 3.7 V for lithium-ion cells). The stack volumetric energy density is then determined by dividing the areal energy by the cell stack thickness.

---

\* <https://cuberg.net/news/cuberg-battery-earns-us-doe-validation>



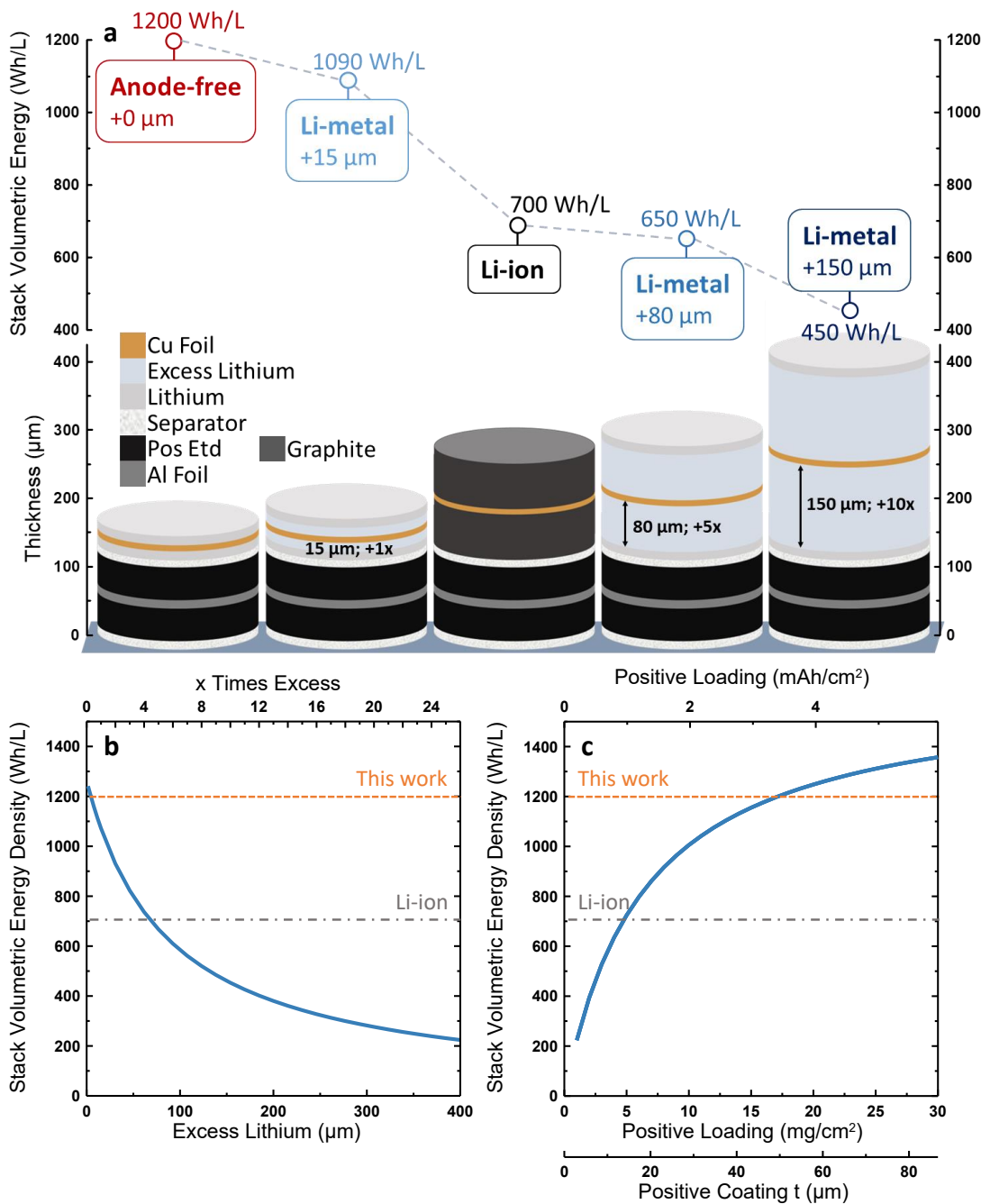


**Figure 2.4 | Energy density dependence on cell parameters.** **a**, Energy density for cell stacks with different amounts of excess lithium (top) and their respective stack diagrams (bottom). **b**, Stack energy density vs excess lithium in  $\mu\text{m}$  (bottom axis) and as  $x$  times excess (top axis). **c**, Stack energy density vs positive electrode coating thickness (bottom axis), positive electrode loading (middle axis) and positive electrode areal capacity (top axis).

**Figure 2.4a** shows that anode-free cells with zero excess lithium (0  $\mu\text{m}$  thick lithium foil) results in the highest energy density of 1200 Wh/L. The energy density of a lithium metal cell with a limited 1x excess (15  $\mu\text{m}$ ) is not heavily compromised, delivering 1090 Wh/L. However, lithium foils used in the literature often range from 100-400  $\mu\text{m}$ . With the use of 80  $\mu\text{m}$  thick lithium foils (5x excess), the energy density plummets below a comparable Li-ion cell at 700 Wh/L. With 150  $\mu\text{m}$  lithium foils (10x excess), the energy density is only 450 Wh/L. This is shown again in **Figure 2.4b**. Obviously, for lithium metal cells to be competitive and truly deliver increased energy density, very limited lithium excesses must be used. Limiting excess to 30  $\mu\text{m}$  as suggested by Albertus *et al.*,<sup>23</sup> corresponding to 2x excess, yields an energy density of 940 Wh/L. Naturally, anode-free cells with zero excess will always have the highest energy density.

**Figure 2.4c** shows the dependence of energy density on positive electrode loading and thickness. Adjusting the coating thickness would change the loading, areal capacity, and resulting energy density. To achieve Li-ion parity, the positive electrode loading must exceed 5  $\text{mg}/\text{cm}^2$  and an areal capacity of 1  $\text{mAh}/\text{cm}^2$ , at a minimum, must be cycled. It is sometimes claimed that high areal capacities of  $>4 \text{ mAh}/\text{cm}^2$  must be achieved. However, our analysis shows that increasing areal capacity beyond 3  $\text{mAh}/\text{cm}^2$  (as used in this work) to 4 and even 5  $\text{mAh}/\text{cm}^2$  increases the energy density by 50 and 100 Wh/L, only 4 and 8% higher.

Another metric which affects cell energy density is the amount of electrolyte or electrolyte loading, often measured as the mass or volume of electrolyte per capacity of the cell in  $\text{g}/\text{Ah}$  or  $\text{mL}/\text{Ah}$ . A higher electrolyte loading will decrease cell specific energy density; therefore, researchers have called for the use of “lean” electrolyte loadings of  $<3 \text{ g}/\text{Ah}$ .<sup>24</sup> It is this author’s understanding that electrolyte loadings as low as  $\sim 1.5 \text{ g}/\text{Ah}$  are used in industry. Cells in this work are filled with 2.2  $\text{mL}/\text{Ah}$  ( $\sim 2.7 \text{ g}/\text{Ah}$ ) of electrolyte.

## 2.2 Degradation of the Lithium Metal Anode

Unlike Li-ion cells that can exhibit long lifetimes of thousands of cycles,<sup>21</sup> anode-free lithium metal cells are plagued with rapid capacity loss and failure. A cycle life of only 20

cycles to 80% capacity retention is typical for anode-free cells.<sup>29,53</sup> The prescient 1965 NASA report identified “poor physical form” of the lithium anode and “concurrent reaction of lithium with electrolyte through continual exposure of fresh lithium” as the cause of short lifetime.<sup>14</sup> Indeed, a recurring topic in this thesis will be how the degradation of the lithium microstructure exacerbates cycling inefficiency.

**Figure 2.5a** shows a diagram reproduced from Ref<sup>15</sup> which summarizes the failure mechanisms associated with the lithium anode. The center of the diagram highlights the two issues at the heart of the problem: the high reactivity of lithium metal and its large volume change. The reactivity of lithium metal is both a blessing and a curse; its high redox potential facilitates large storable electrochemical energies but also exacerbates lithium-electrolyte parasitic reactions. Almost any chosen liquid electrolyte will react with lithium metal and decompose.<sup>62,63</sup> These reactions are called “parasitic” because like a parasite, they leech off the lithium metal, irreversibly consuming  $\text{Li}^+$ , depleting capacity from the cell’s lithium inventory.<sup>§</sup> Fortunately, these parasitic reactions can be self passivating, as shown by Peled in 1979.<sup>32</sup> Their reaction products are ionic conductors, facilitating transport of  $\text{Li}^+$  between the electrode and electrolyte, but electronic insulators, thereby inhibiting further electrochemical decomposition.<sup>64</sup> These passivating reaction products form what is known as the solid electrolyte interphase (SEI). An SEI is also formed on graphite negative electrodes in Li-ion cells. However, once an SEI is formed on graphite, it remains largely stable for the entire lifetime of the cell, thereby not constantly draining  $\text{Li}^+$  via continuous parasitic reactions. This is not the case on a lithium metal anode because of the second issue highlighted in the center of **Figure 2.5a**—the large volume change associated with plating a stripping lithium metal.<sup>†</sup> The SEI is not robust enough to withstand the tens-of-microns thickness change during plating and stripping. As a result,

---

<sup>§</sup> The “lithium inventory” refers to an accounting of all the active lithium and  $\text{Li}^+$  within a cell that can be cycled and delivered as capacity.<sup>147</sup> As the lithium inventory is depleted, cell capacity is lost.

<sup>†</sup> “Infinite” volume change described in this diagram refers to the fact that if you start with an anode-free design with zero lithium thickness, then technically any increase in thickness during plating is infinite.

the SEI is continually broken down and reformed as unpassivated lithium metal is re-exposed to the electrolyte. This continual SEI reformation acts as a constant drain of  $\text{Li}^+$ , depleting the lithium inventory. Moreover, depletion of the electrolyte as a result of these continual parasitic reactions is possible, thereby increasing the challenge of enabling lean electrolyte loadings for lithium metal cells.

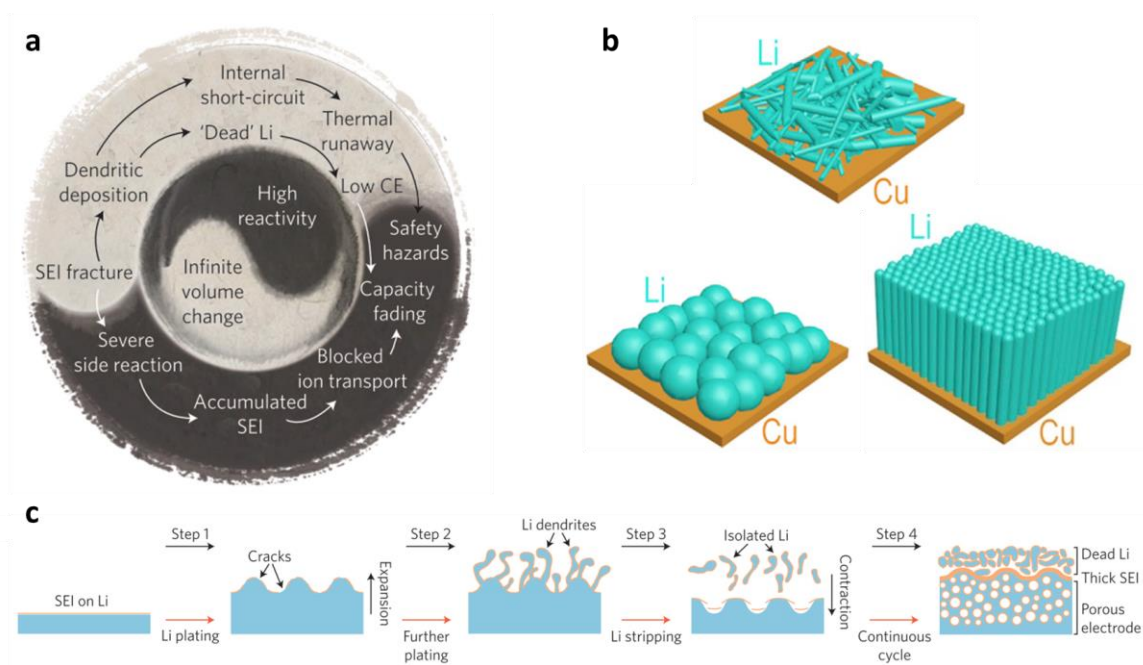


**Figure 2.5 | Lithium metal degradation mechanisms.** **a**, The “circle of death”—a diagram which lists the degradation mechanisms of a lithium metal anode, as retrieved from Ref.<sup>15</sup> **b**, Schematics of different plated lithium morphologies. Dendritic, mossy deposition (top), nodular deposition (bottom left) and columnar deposition (bottom right), as retrieved from Ref.<sup>65</sup> **c**, Mechanism for inhomogeneous and dendritic lithium deposition to form mechanically isolated lithium and a degraded lithium anode after continuous cycling, as retrieved from Ref.<sup>15</sup>

Another significant mechanism which accelerates the rapid degradation of the lithium anode is the dendritic deposition of lithium. Instead of forming flat metal sheets, lithium tends to deposit as a wild, mossy “dendritic” microstructure.<sup>66–68</sup> Heterogeneous lithium nucleation during lithium plating which spawns this mossy morphology (top panel of **Figure 2.5b**) has been attributed to the complicated surface chemistry that evolves on the lithium surface as the SEI-forming reactions result in a mosaic of insoluble surface species.

Typically, the chemical composition of SEI surface layer has been found to be highly non-uniform which in turn induces non-uniform current densities during lithium plating prompting the formation of lithium protrusions rather than a flat deposition.<sup>69</sup>

High surface area lithium accelerates capacity loss by facilitating more lithium-electrolyte parasitic reactions and SEI growth. Moreover, mossy lithium deposition also initiates loss of lithium inventory by forming mechanically isolated lithium.<sup>70,71</sup> **Figure 2.5c** shows the mechanism for the creation of dendritic lithium and how this can lead to mechanical isolation. When lithium plates on a substrate (**Figure 2.5c**, Step 1), non-uniform nucleation results from a variety of factors. Non-uniform passivation films (*i.e.* an SEI with areas of varied resistance),<sup>72,73</sup> concentration gradients in the electrolyte,<sup>74-76</sup> and electrolyte convection<sup>77</sup> all initiate inhomogeneous current densities at the deposition surface resulting in the formation of lithium protrusions. Non-uniform lithium plating then becomes self-accelerating, with increased local current densities generated at the tips of the lithium protrusion attracting further deposition (**Figure 2.5c**, Step 2).<sup>78</sup> Upon lithium stripping (**Figure 2.5c**, Step 3), if the base of a lithium protrusion is stripped before the tip, mechanically isolated lithium is formed.<sup>70,71</sup> This mechanically isolated lithium is no longer electrically connected to the rest of the cell. Therefore, the lithium capacity that remains in this severed chunk is no longer available during discharge. After many repeating cycles of this process (**Figure 2.5c**, Step 4), there is a significant accumulation of “dead lithium”—lithium inventory which has been lost to mechanically isolated lithium and the formation of SEI. This significant loss of lithium inventory coupled with the rapid increase in cell resistance due to the tortuous matrix of dead lithium is the cause of the rapid failure of lithium metal cells. Although it had be conventionally thought that SEI growth was the dominant form of capacity loss in lithium metal cells, more recently quantification of inactive lithium has demonstrated that mechanical isolation of lithium is the more significant degradation mode.<sup>79</sup>

As previously described, lithium metal cells are built with an excess of lithium. This excess acts a lithium reservoir—any lithium inventory lost to the degradation mechanisms discussed above can be replaced from this reservoir. Therefore, capacity fade resulting

from lithium inventory loss should only occur once the lithium reservoir has been depleted. This artificially extends cycle life (artificial insofar as lithium plating efficiency is not actually improved), but it does so at the cost of energy density. In contrast, anode-free cells have no lithium reservoir to prop up their cycle life, and as a result, generally exhibit immediate and rapid capacity fade.<sup>28,29</sup>

The formation of a mossy lithium microstructure and the consequences of a high surface area morphology are the primary cause of lithium metal cell death.<sup>15,63,69</sup> Moreover, high surface area lithium results in significantly worse safety.<sup>27</sup> Therefore, the formation of a dense, compact lithium microstructure is essential to overcoming cell failure. The bottom panels of **Figure 2.5b** show ideal lithium morphologies: lithium nodules (left) and lithium columns (right). Both exhibit low surface area and low porosity. If these compact microstructures can be formed and maintained, the cycle life of lithium metal cells can be increased. This is the goal of all researchers working on lithium metal anodes.

## 2.3 Strategies to Stabilize Lithium Metal

### 2.2.1 Mechanical Pressure

During the early days developing lithium metal cells, researchers at Moli Energy discovered that mechanical pressure had a significant influence on lithium plating morphology and thus its cyclability.<sup>80</sup> Unconstrained lithium metal cells performed worse than those tested with a uniaxial pressure applied in the direction of lithium plating. A significant improvement in cyclability was achieved through the application of pressures in the range of 400-600 kPa, with less substantial improvements up to 1400 kPa.<sup>81</sup> They found that at higher pressures, a much denser lithium deposition was enabled. They attributed this behavior to lithium creep which occurs in this pressure range.<sup>82</sup> In other words, lithium was being mechanically deformed at higher pressure, physically thwarting the formation of lithium protrusions and densifying the morphology. It was also shown that increased mechanical pressure decreased the irreversible thickening of lithium metal cells concomitant with the accumulation of dead lithium.<sup>81,83</sup> This positive influence of

mechanical pressure was also demonstrated for lithium metal cells with a number of different electrolyte chemistries.<sup>84</sup>

The Moli researchers acknowledged that applying significant mechanical pressures to ensure optimal lithium performance could be tricky for practical cell designs. Therefore, their strategy was to use a fixed volume cell format in which the necessary pressures could form *in-situ*. When lithium electrodes are constrained in a fixed volume enclosure, the stack expansion of lithium plating during charge will push against the enclosure and increase the pressure. Moreover, irreversible thickening of the lithium electrode will also contribute to increased pressure in the cell. A cylindrical cell format was used at Moli. During cell construction, the wound electrode stack “jelly roll” was inserted snugly in to the metallic can. It was demonstrated that the pressure generated *in-situ* could reach 500 kPa after a couple of cycles.<sup>81</sup>

Continued modern efforts to understand the role of mechanical pressure have been undertaken by Fang *et al.*<sup>85</sup> A focused ion beam at cryogenic temperatures was used to produce pristine cross sections of cycled lithium which facilitated imaging of the internal structure and lithium porosity not possible with conventional top-down imaging techniques. They showed that the internal lithium microstructure was increasingly densified with the application of pressures up to 350 kPa with the porosity decreasing by about a factor of ten. Through molecular dynamics simulations, Fang *et al.* showed that while at low pressure lithium was free to grow in the vertical direction, higher pressure acted to promote the lateral deposition of lithium. The authors concluded that this was a result of the resistance introduced at the lithium surface by the compressive strength which exceeds the surface energy of lateral lithium deposition.<sup>85</sup> So, whereas mossy lithium deposition is intrinsically the lowest energy and thus most favorable lithium morphology, increasing the energy cost of mossy deposition with mechanical pressure promotes densified deposition.

### 2.2.2 Electrolyte Chemistry

The major components of the liquid electrolyte for lithium-ion cells—the lithium salt and solvents—have not evolved dramatically over the last 30 years. The 1991 Sony cell contained electrolyte composed of  $\text{LiPF}_6$  salt dissolved in carbonate solvents, a recipe which is still the basis of modern lithium-ion electrolytes.<sup>1</sup> Nowadays, development of electrolyte additives, additional chemicals added at  $< 10$  wt.% drive the major innovations of lithium-ion electrolyte chemistry. Simply put, this is because  $\text{LiPF}_6$  in carbonate blends (ethylene carbonate, diethyl carbonate, dimethyl carbonate, *etc.*) work well, with electrolyte additives generally employed to further optimize graphite passivation. In contrast, the picture is a lot less clear for optimal electrolytes to enable reversible lithium metal cycling. Many different lithium salt and solvent combinations are continually being tested in lithium metal cells to improve cycling efficiency.

Some of the earliest electrolyte formulations for lithium metal cells were  $\text{LiClO}_4$  salt in propylene carbonate (PC) and  $\text{LiAlCl}_4$  in PC, although these electrolytes had dismal cycling efficiencies below 70%.<sup>13,14</sup> Later,  $\text{LiAsF}_6$  salt and PC:ethylene carbonate (EC) solvent blends were found to improve cycling efficiency. The commercialized Moli cell in the late 80s utilized 1 M  $\text{LiAsF}_6$  PC:EC. This electrolyte, cycled in a cylindrical cell with pressure and 3x excess lithium, enabled a cycling efficiency of about 99% translating to a cycle life of 300 cycles.<sup>86</sup>

There is now a massive body of research exploring the impact of different electrolyte solvents,<sup>58,66,87,88</sup> salts,<sup>66,87,89–91</sup> and even additives<sup>78,89,92,93</sup> on lithium metal. An extensive characterization of 8 different carbonate solvents and 9 different lithium salts in lithium-copper half cells was performed by Ding *et al.*<sup>66</sup> The solvents were tested with  $\text{LiPF}_6$  salt and the salts were tested in PC solvent. The morphology and cycling efficiency of these 17 electrolyte formulations were reported. The use of  $\text{LiDFOB}$  and  $\text{LiBF}_4$  salts in this paper were the inspiration for our investigations with these salts reported later in this thesis. Although  $\text{LiDFOB}$  and  $\text{LiBF}_4$  were not amongst the best salts reported by Ding *et al.*, our later success with them is an important lesson not to take anything from the literature for



granted—everything should be tested since some reports from literature will turn out better and some will turn out worse when reproduced. This can be for a number of reasons; in the paper by Ding *et al*, the lithium-copper half cell format and PC solvent did not synergize with LiDFOB and LiBF<sub>4</sub> as our testing conditions ultimately did. Ding *et al*. also studied the SEI formed in each electrolyte formulation with x-ray photoelectron spectroscopy and identified different concentrations of organic and inorganic (LiF, Li<sub>2</sub>CO<sub>3</sub>) species, although correlations between the chemical composition of the SEI and cycling efficiency were not manifestly obvious.

Fluorinated electrolyte chemistries have proven successful in improving the plating morphology of lithium metal. Particularly, the use of fluoroethylene carbonate (FEC)<sup>94–96</sup> and other fluorinated carbonates and ethers.<sup>58</sup> This has been attributed to a higher LiF content in the SEI as a result of the increased presence of fluorinated species during electrolyte decomposition. LiF is beneficial by discouraging high surface area mossy lithium formation due to its high interfacial energy.<sup>58</sup> Moreover, LiF is proposed to improve lithium passivation by mechanically strengthening the robustness of the SEI. The benefit of an FEC-derived SEI is not surprising as FEC has also proven valuable for stabilizing silicon negative electrode materials which exhibit similar mechanisms of lithium inventory loss as lithium metal electrodes.<sup>97</sup>

Early efforts developing electrolytes for lithium metal cells focused on carbonate solvents (*e.g.* PC, FEC) due to their high oxidative stability for compatibility with > 4.0 positive electrodes. However, ether solvents have demonstrated less reactivity with lithium metal.<sup>58</sup> If their poor oxidative stability could be overcome, ether solvents would be attractive electrolyte candidates. Moreover, LiFSI is a promising lithium salt due to its higher chemical and thermal stability compared to LiPF<sub>6</sub>, but unfortunately results in aluminum corrosion at high voltage.<sup>98</sup> A recent trend of high concentration electrolytes (HCE, > 3 M) have been proposed to overcome both of these concerns, facilitating the compatibility of ether solvents and LiFSI salt with high voltage lithium metal cells.<sup>99</sup> In dilute (~1 M) electrolytes, the Li<sup>+</sup> is typically coordinated by 3-4 solvent molecules. At higher concentrations, the coordination number is reduced to 1-2 due to the scarcity of solvent

molecules, and salt anions enter the solvation sheath to form contact ion pairs and cation-anion aggregates. As a result, salt anions participate more readily in SEI formation, significantly affecting the SEI composition.<sup>98</sup> HCE have thus enabled the use LiFSI salt, with 10 M LiFSI DMC electrolyte exhibiting a CE of 99.2%,<sup>90</sup> as well as ether solvents, with 4 M LiFSI 1,2-dimethoxyethane (DME) exhibiting a CE of 99.1% in lithium metal cells.<sup>100</sup> This has been attributed to improved stability of the anion-derived SEI.<sup>101</sup>

Since 2018, a flurry of impressive work out of Pacific Northwest National Laboratory (PNNL) developing electrolytes for lithium metal cells has emerged. Their efforts have focused on overcoming the disadvantages that come with high concentration electrolytes such as high cost, high viscosity, and poor wettability.<sup>102</sup> To this end, they introduced a localized high concentration (LHC) electrolyte which consists of a high concentration electrolyte diluted with an “inert” solvent. The diluent does not dissolve the salt but is miscible with the other solvent components. As a result, the diluent does not affect the Li<sup>+</sup> coordination while still lowering the overall salt concentration. Therefore, the beneficial anion-derived SEI facilitated by high concentration electrolytes is still realized while simultaneously decreasing the viscosity and increasing the wettability. Researchers at PNNL demonstrated that 5.5 M LiFSI DME diluted with bis(2,2,2-trifluoroethyl) ether (BTFE) forming a localized high concentration 2.5 M LiFSI DME:BTFE electrolyte enabled a CE of 99.3%.<sup>103</sup> 1,1,2,2-tetrafluoroethyl-2,2,3,3-tetrafluoropropyl ether (TTE) was also demonstrated as a successful diluent in 1.73 M LiFSI DME:TTE 1:4 electrolyte. This LHC electrolyte enabled a CE of 99.5% and was demonstrated in an anode-free configuration to deliver a capacity retention of 77% after 70 cycles.<sup>47</sup>

In 2020, researchers at Stanford developed an electrolyte based on a fluorinated 1,4-dimethoxybutane (FDMB) solvent.<sup>48</sup> Yu *et al.* showed that 1 M LiFSI FDMB electrolyte enabled a relatively compact nodular lithium morphology, enabling a CE of 99.5% and an anode-free cell capacity retention of 60% to 100 cycles. Cryo transmission electron microscopy (TEM) measurements were used to probe the SEI which was found to be very compact—40% thinner than the SEI in control electrolyte. Yu *et al.* thus attributed the success of this electrolyte, in part, to superior lithium passivation. Cryo TEM

measurements also revealed that the passivation layer was rich in fluorine and sulfur indicating an anion-derived SEI. However, some ion-insulating species were also observed which resulted in a high resistance SEI.<sup>48</sup>

Despite these highly promising electrolytes chemistries, there are still challenges to overcome. For example, both the FDMB and LHC electrolytes exhibit kinetic limitations which increase cell resistivity and lower reversible capacity. These issues will be explored later in this thesis.

### 2.2.3 Plating Substrate

We have discussed how plating morphology is intrinsically tied to lithium metal cell performance. In an anode-free cell design, the lithium metal anode is formed *in-situ* upon the first charge. The resultant lithium morphology is ultimately spawned from the initial lithium nucleation. For example, heterogenous nucleation will drive non-uniform current densities to form lithium protrusions and mossy lithium rather than a compact morphology. Therefore, lithium nucleation is key in determining the bulk lithium microstructure. Pei *et al.* showed that lower plating overpotentials resulted in larger lithium grains.<sup>73</sup> This is preferred over many smaller lithium nuclei as larger lithium grains will facilitate a lower surface area morphology. It was also shown that lithium plating on lithium resulted in a more homogenous deposition, presumably because of a lower overpotential than plating lithium on copper. Therefore, Pei *et al.* suggested that plating on top of a seed layer of lithium could facilitate improve lithium reversibility as later demonstrated by Fang *et al.*<sup>73,85</sup>

This strategy to improve lithium deposition by tweaking the nucleation behavior can be harnessed with different substrates as well. This has been demonstrated with faceted Cu<sup>104</sup> and partial alloying Li-Sn<sup>105,106</sup> and Li-Zn<sup>107,108</sup> substrates. Pande *et al.* showed theoretically that each of these substrates should decrease the lithium plating overpotential.<sup>109</sup> Therefore, improved lithium metal cycling is achieved through decreasing the energy barrier for lithium nucleation to improve lithium deposition.

#### 2.2.4 Solid Electrolytes

Many of the woes of the lithium metal anode are a result of unwanted reactions with the liquid electrolyte. Not to mention that organic liquid electrolytes are flammable and act as fuel to facilitate the burning of lithium metal cells during thermal runaway. Solid electrolytes inert to lithium metal could potentially overcome cycling inefficiency and the poor safety of lithium metal cells. Moreover, solid electrolytes could act to mechanically constrain the growth of lithium metal to maintain more ideal compact lithium morphologies. However, as with all things—especially battery related—it is not that simple. Although lithium metal cells with liquid electrolytes are the focus of this thesis, it is worth stopping to briefly describe some competitive solid-state technologies, especially considering the significant commercial efforts presently focused on solid electrolytes.

There are three broad categories of solid electrolytes currently in development for lithium metal cells: polymers, oxides, and sulfides. **Figure 2.6** is a spider plot comparing the important characteristics that should be satisfied for a successful solid electrolyte.<sup>110</sup> Processing cost, mechanical properties, air stability, thermal stability, and chemical stability are all important for practical manufacturing and operation of solid electrolytes. The transference number and ionic conductivity relate to electrolyte kinetics and ultimately how fast a solid electrolyte cell can be charged and discharged. Electronic conductivity should be low so as to prevent short circuits. Oxidation stability refers to the electrolyte compatibility with positive electrode materials—poor oxidative stability will result in electrolyte oxidation and decomposition at high voltage. Finally, reduction stability refers to the electrolyte compatibility with lithium metal—poor reductive stability will result in electrolyte reduction and decomposition at low voltage.

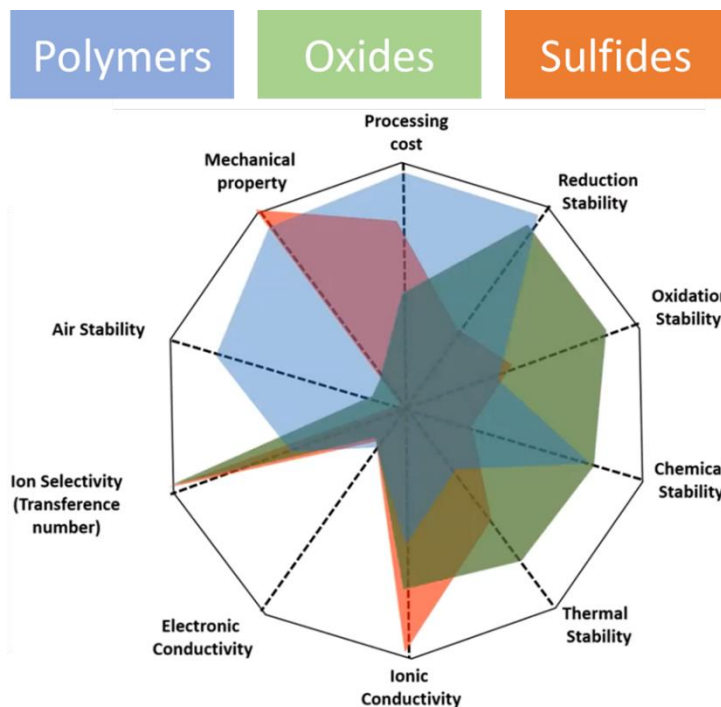


**Figure 2.6 | Solid electrolyte comparison.** Spider plot comparing the important characteristics of solid electrolytes for polymer (blue), oxide (green), and sulfide (orange) chemistries. Values with a larger radius are optimal except for electronic conductivity which should be minimized. This figure is reproduced with permission from Dr. Shirley Meng.<sup>110</sup>

Polymer electrolytes were first proposed by Armand in 1978 as researchers struggled to find liquid electrolytes that could efficiently cycle lithium metal.<sup>111</sup> Polymers can be cheap and they exhibit good compatibility with lithium metal. However, they provide poor ionic conductivity and oxidative stability. As a result, compatibility with typical  $>4$  V positive electrode materials is challenging. The technology developed by Armand was commercialized by Hydro Quebec and now Blue Solutions, a subsidiary of Bolloré.<sup>31</sup> These polymer electrolyte cells are the only commercialized solid-state batteries utilized in electric vehicles at an industrial scale to date, powering Daimler electric busses for over 4000 cycles.<sup>112</sup> However, these cells have not achieved widespread market penetration due to their relatively low energy density of 250 Wh/kg, on par with lithium-ion cells, as a result of the low voltage LFP electrode used to circumvent electrolyte oxidation. Moreover, due to the poor ionic conductivity of polymer electrolytes, these cells must be heated to

temperatures between 50-80 °C for operation.<sup>112</sup> A new effort to commercialize polymer electrolytes has emerged in 2021 from Factorial Energy who have reportedly developed high voltage NMC811 polymer solid-state cells that last 460 cycles with an energy density of 350 Wh/kg (770 Wh/L).<sup>113</sup> This relatively low volumetric energy density is likely a result of the unspecified lithium excess used in these cells. Furthermore, to overcome the poor ionic conductivity of the polymer electrolyte, some liquid electrolyte is also being used in Factorial's cells.

Oxides have a good electrochemical stability but they will be more costly to process. Oxides have been shown to successfully constrain lithium metal; however, grain boundaries in the electrolyte are vulnerable to penetration of lithium protrusions which result in short circuits.<sup>114,115</sup> Large scale synthesis of defect-free oxide electrolytes will be challenging. Nevertheless, perhaps currently the most well-known effort to commercialize solid-state lithium metal cells by QuantumScape utilizes a ceramic oxide solid electrolyte. QuantumScape boasts an impressive lifetime of 1000 cycles under some of the most aggressive testing conditions reported for lithium metal cells, including an anode-free cell design.<sup>116</sup> However, they have not yet disclosed the energy density of their cells. We can only speculate as to why this may be—perhaps the thickness of their electrolyte is currently too thick to provide the high energy densities promised by lithium metal cells. To overcome poor ionic conductivity, particularly at the ceramic-positive electrode interface, some amount of liquid or “gel” electrolyte is included. Overall, QuantumScape has shared promising results, but there are still challenges to overcome. Primarily, their small prototype cells must be scaled up to larger multi-stack cells required for commercial use. Although liquid lithium metal cells with conventional polyolefin separators have some compliance which can accommodate some of the large volume expansion of plating lithium, one can imagine that this would be difficult for rigid solid-state cells, particularly for many layers stacked on top of each other.

Recently, a highly conductive class of  $\text{Li}_6\text{PS}_5\text{X}$  sulfide solid electrolytes have emerged ( $\sim 5$  mS/cm compared to  $\sim 1$  mS/cm for oxides and  $\sim 10$  mS/cm for liquid electrolytes).<sup>117,118</sup> With sufficient ionic conductivity and good mechanical stability, many believe sulfides to

be the most promising solid electrolyte chemistry. Unfortunately, sulfides have a low electrochemical stability and are marred by interfacial challenges.<sup>114,119</sup> Solutions to passivate both the positive electrode and lithium metal must be implemented to overcome electrolyte degradation. In 2020, a publication from Samsung demonstrated a long-lasting sulfide-based anode-free cell.<sup>43</sup> They utilized an oxide coating to protect the positive electrode and a Ag-C layer to passivate the lithium metal to achieve a lifetime of 1000 cycles. However, a massive 4000 kPa isostatic pressure had to be applied during operation to keep conformal contact between the electrolyte and the positive electrode particles through repeated volume expansion of the electrode materials, obviously presenting a practical problem. Solid Power is a company working to commercialize sulfide solid electrolytes. In contrast to QuantumScape who has demonstrated good performance but challenges scaling up, the latest results shared by Solid Power only demonstrated a cycle life of about 250 cycles but they have produced and shipped 2 Ah 10-layer and 20 Ah 22-layer automotive sized cells. The large Solid Power cells deliver an energy density of 330 Wh/kg.<sup>120</sup> In 2021, Solid Power announced that they have been working on solid-state cells with silicon negative electrodes instead of lithium metal.<sup>121</sup> This may indicate that they have begun to pivot away from challenges associated with enabling long-lasting practical sulfide-based lithium metal cells.

#### 2.2.5 Current Commercial Efforts

Throughout this chapter we have highlighted some of the current efforts to commercialize lithium metal cells. **Figure 2.7** shows a comprehensive view of the landscape in 2021 compiled by Kieran O'Regan. Clearly, there is a flurry of activity working on solid-state electrolytes, while efforts with liquid electrolytes are currently limited to SES and Cuberg.

When considering the commercial efforts, one must remember that the promise of lithium metal cells is increased energy density and the promise of solid-state cells is improved safety. Energy density will be negatively affected by use of significant lithium excess and thick solid electrolytes. It remains to be seen whether the hybrid approach of using some liquid electrolyte in solid-state cells will result in improved safety in comparison to

traditional liquid electrolyte cells. Solid-state cells will also undoubtedly face production challenges and increased cost, at least initially, since current lithium-ion cell manufacturing capabilities are not setup to handle solid electrolytes. In contrast, anode-free lithium metal cells with liquid electrolytes would be a drop-in solution compatible with today's manufacturing capabilities since they are constructed in the exact same way as conventional lithium-ion cells minus the graphite electrode coating. As a result, anode-free cells with liquid electrolytes would immediately deliver a ~20% reduction in production cost compared to lithium-ion cells.<sup>30</sup> Anode-free cells with liquid electrolytes will also almost certainly deliver higher energy density than solid-state cells as they do not employ a heavy solid electrolyte. Of course, safety and longevity remain the key challenges to overcome. However, if a long-lasting anode-free cell with liquid electrolyte can be demonstrated, companies working on solid-state cells would be in trouble.

### Lithium-metal anode developments for EVs



**Figure 2.7 | Landscape of commercial Li metal efforts.** List of companies working to commercialize lithium metal cells based on solid-state and liquid electrolyte chemistries. This graphic was reproduced from Kieran O'Regan: [https://twitter.com/Kieran\\_Faraday/status/1392100083538276354](https://twitter.com/Kieran_Faraday/status/1392100083538276354)



## Chapter 3: Experimental Methods

### 3.1 Cell Chemistry

#### 3.1.1 Pouch Cells

The pouch cells used in this work were manufactured by Li-FUN Technology (Xinma Industry Zone, Golden Dragon Road, Tianyuan District, Zhuzhou City, Hunan Province, China). These cells were built with a wound electrode design in which the cell “stack”—the sandwich of double-sided positive electrode | separator | double-sided negative electrode | separator—are wound to form the prismatic 20 × 40 mm “jelly roll” depicted in **Figure 3.1a**. These small lab-scale pouch cells deliver a capacity of ~0.25 Ah. **Figure 3.1b** shows examples of unwound positive and negative electrodes retrieved from disassembling a charged anode-free cell. A tri-layer laminate material composed of aluminum sandwiched between two plastic layers houses the jelly roll as well as the “gas bag”, an empty volume of the laminate casing above the jelly roll to accommodate any gases generated during cycling.

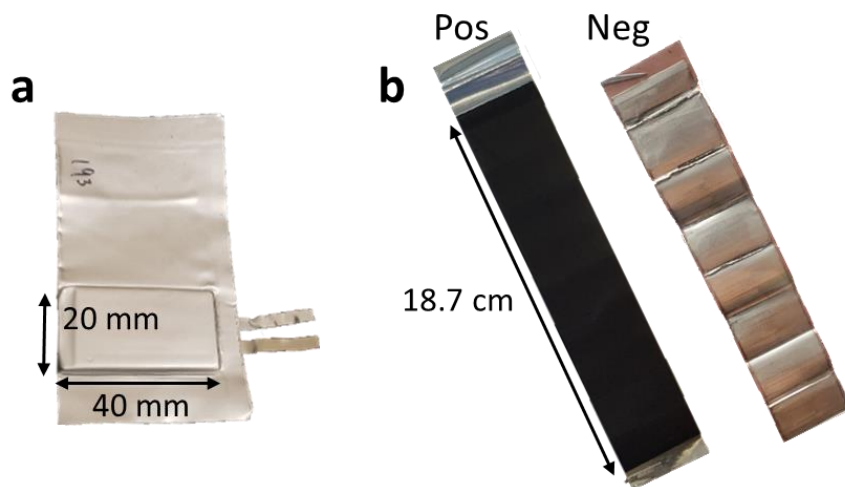


**Figure 3.1 | Pouch cell.** **a**, Picture of the small format ~0.25 Ah wound prismatic pouch cell used in this work. **b**, Unwound constituent positive and negative electrodes. The negative electrode shown here has been removed from an anode-free cell after the first charge with lithium plated on the copper current collector.

**Table 3.1** lists the various pouch cells tested in this work. Three types of cell chemistries were tested: conventional Li-ion cells with graphite negative electrodes, anode-free cells with lithium metal negative electrodes, and hybrid Li-ion/lithium metal cells with hybrid graphite/lithium metal negative electrodes. Four different positive electrode materials were used—LiNi<sub>0.5</sub>Mn<sub>0.3</sub>Co<sub>0.2</sub>O<sub>2</sub> (NMC532), LiNi<sub>0.8</sub>Mn<sub>0.1</sub>Co<sub>0.1</sub>O<sub>2</sub> (NMC811), LiCoO<sub>2</sub> (LCO), and LiFePO<sub>4</sub> (LFP). For each cell type, the positive (*Pos*) and negative (*Neg*) electrode material, as well as the electrode thickness, loading, and stack area are listed in **Table 3.1**. The thickness and loading of the inactive components of the pouch cells, the electrode current collectors (*CC*) and separator (*Sep*), are listed in **Table 3.2**. **Figure 2.4** showed that a single stack is composed of a double-sided positive electrode (two positive electrode layers coated on a current collector), a double-sided negative electrode (two negative electrode layers coated on a current collector), and two separator layers. Therefore, the stack thickness and mass for each cell is calculated as:

$$2Pos + Pos_{CC} + 2Neg + Neg_{CC} + 2Sep$$

The reversible capacity ( $Q$ ), areal capacity ( $Q_A = Q / \text{stack area}$ ), and average voltage (*Avg V*) for each cell are also listed in **Table 3.1**. The above can then be used to calculate energy density. Ideally, the energy density at the cell level—the energy delivered divided by the entire cell mass or volume—would be reported. However, most research is not performed using optimized cell formats. For example, our small lab-scale pouch cells have an excess of inactive material including the large gas bag, extra laminate casing, excess separator and current collectors which all result in a worse active:inactive material ratio and thus a lower cell-level energy density than optimized cell formats. Therefore, to make fair comparisons between cell formats, the energy density at the stack-level can be reported.<sup>‡</sup> The stack-level volumetric and specific energy densities are calculated as:

---

<sup>‡</sup> The cell-level energy density of a commercial 18650-format cylindrical cell is approximated 20% less than the stack-level energy density.<sup>180</sup>

$$\frac{2Q_A * Avg V}{Stack},$$

where *Stack* is either the stack thickness or stack loading. The factor of 2 accounts for the fact that each stack contains two positive electrode layers and therefore has double the areal capacity. With the correct unit conversions, this calculation yields the volumetric energy density in Wh/L and the specific energy density in Wh/kg. These values, along with the normalized energy densities (normalized to NMC532 Li-ion cells), are listed in **Table 3.1**. The hybrid cell delivers a volumetric and specific energy density approximately 20% greater than the Li-ion cell. The anode-free cell with an LFP positive electrode is almost equivalent to Li-ion cells in terms of energy density. The anode-free cells with NMC532, LCO, and NMC811 deliver the highest energy densities, achieving specific energy densities 60, 65, and 87% greater than Li-ion cells and volumetric energy densities 72, 94, and 96% greater than Li-ion cells.<sup>§</sup>

---

<sup>§</sup> Note that these comparisons are to a lithium-ion cell with an NMC532 positive electrode. An NMC811 Li-ion cell would have a higher energy density and thus the relative benefit would be somewhat lower.

**Table 3.1:** Specifications of pouch cells used in this work.

	Lithium-ion	Anode-Free				Hybrid
Colloquial Name	NMC532	AF-NMC532	AF-NMC811	AF-LCO	AF-LFP	Semi-AF
	$\text{LiNi}_{0.5}\text{Mn}_{0.3}\text{Co}_{0.2}$	$\text{LiNi}_{0.5}\text{Mn}_{0.3}\text{Co}_{0.2}$	$\text{LiNi}_{0.8}\text{Mn}_{0.1}\text{Co}_{0.1}$			$\text{LiNi}_{0.5}\text{Mn}_{0.3}\text{Co}_{0.2}$
Positive electrode	$\text{O}_2$	$\text{O}_2$	$\text{O}_2$	$\text{LiCoO}_2$	$\text{LiFePO}_4$	$\text{O}_2$
Negative electrode	Graphite	Lithium	Lithium	Lithium	Lithium	Graphite/Li
Pos thickness ( $\mu\text{m}$ )	46.25	46.25	47.5	53.75	56.5	46.25
Pos loading ( $\text{mg}/\text{cm}^2$ )	15.70	15.70	15.72	19.91	12.32	15.70
Neg thickness ( $\mu\text{m}$ ) <sup>*</sup>	65.50	15.03	17.31	16.51	9.41	41.50
Neg loading ( $\text{mg}/\text{cm}^2$ )	9.93					5.07
Stack thickness ( $\mu\text{m}$ )	272.50	171.56	178.62	189.52	180.82	224.50
Stack loading ( $\text{mg}/\text{cm}^2$ )	63.75	43.89	43.93	52.31	37.13	54.03
Stack area ( $\text{cm}^2$ )	86.58	86.58	86.58	73.58	131.56	86.58
Capacity <sup>†</sup> (mAh)	229	238	285	245	243	229
Areal Capacity <sup>*</sup> ( $\text{mAh}/\text{cm}^2$ )	2.65	2.75	3.29	3.329	1.8497	2.65
Average Voltage (V)	3.70	3.87	3.84	3.98	3.37	3.76
Volumetric Energy Density <sup>‡</sup> (Wh/L)	719	1241	1414	1398	690	887
Normalized Vol. Energy Density	1	1.724	1.96	1.942	0.96	1.23
Specific Energy Density <sup>†</sup> (Wh/kg)	308	485	575	506	336	369
Normalized Spec. Energy Density	1	1.58	1.87	1.65	1.09	1.20

\* Anode-free cells are built with zero-thickness negative electrodes; the values here are the theoretical thickness of lithium that is plated at the top of charge.

† Reversible first discharge capacity and areal capacity.

‡ Energy density calculated at the stack level.

**Table 3.2:** Inactive pouch cell component specifications.

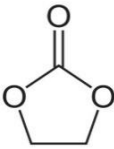
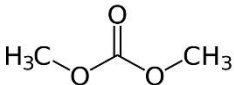
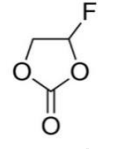
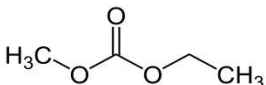
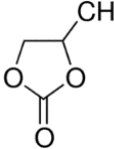
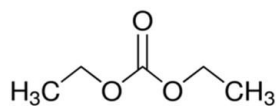
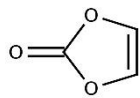
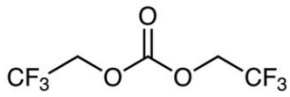
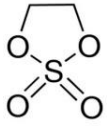
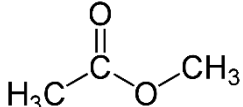
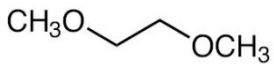
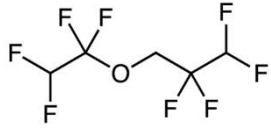
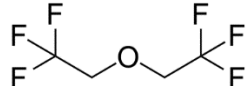
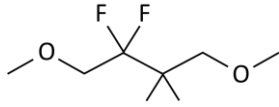
	Material	Thickness ( $\mu\text{m}$ )	Loading ( $\text{mg}/\text{cm}^2$ )
Positive Current Collector	Aluminum	13	3.23
Negative Current Collector	Copper	8	7.24
Separator	Polyethylene/ Polypropylene	14	1.01

### 3.1.2 Electrolyte

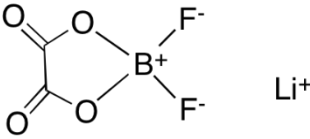
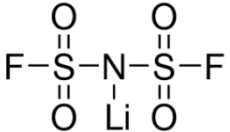
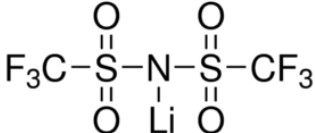
Pouch cells were received from the manufacturer with no electrolyte. Therefore, we mixed and filled the electrolytes in-house in an argon-filled glovebox. A number of different solvents (**Table 3.3**) and lithium salts (**Table 3.4**) were used in the many electrolyte formulations tested in this work. Solvents were mixed to volume ratios (v:v) and salt was added to achieve a specific molarity. For example, one electrolyte developed in this work is the dual-salt 0.6 M LiDFOB 0.6 M LiBF<sub>4</sub> FEC:DEC (1:2) formulation. In certain cases where the salt did not easily dissolve in the solvents, stirring and heating was used to encourage salt dissolution. The specific electrolyte formulations used for each experiment will be clearly detailed in figure legends and captions.

Before electrolyte filling, pouch cells were vacuum dried at 120 °C for 14 hours to remove any excess moisture. Cells were predominantly filled with 0.5 mL (2.2 mL/Ah  $\approx$  3 g/Ah) of electrolyte. Experiments with electrolyte volumes different than 0.5 mL will be clearly indicated in figure captions and legends. After filling, cells were held at 1.5 V for 24 hours to allow the electrolyte to fully wet the positive electrode and separator before testing.

**Table 3.3:** List of solvents used in electrolytes in this work.

	Chemical Name	Chemical Structure		Chemical Name	Chemical Structure
EC	ethylene carbonate		DMC	dimethyl carbonate	
FEC	fluoroethylene carbonate		EMC	ethylmethyl carbonate	
PC	propylene carbonate		DEC	diethyl carbonate	
VC	vinylene carbonate		TFEC	bis(2,2,2-trifluoroethyl) carbonate	
DTD	1,3,2-Dioxathiolane-2,2-dioxide		MA	methyl acetate	
			DME	1,2-dimethoxyethane	
			TTE	1,1,2,2-tetrafluoroethyl-2,2,3,3-tetrafluoropropyl ether	
			BTFE	bis(2,2,2-trifluoroethyl) ether	
			FDMB	fluorinated 1,4-dimethoxybutane	

**Table 3.4:** List of lithium salts used in electrolytes in this work.

	Chemical Name	Chemical Structure
LiPF <sub>6</sub>	Lithium hexafluorophosphate	$\text{Li}^+ \left[ \begin{array}{c} \text{F} \\   \\ \text{F} \text{---} \text{P} \text{---} \text{F} \\ / \quad \backslash \\ \text{F} \quad \text{F} \\   \\ \text{F} \end{array} \right]^-$
LiDFOB	Lithium difluoro(oxalato)borate	
LiBF <sub>4</sub>	Lithium tetrafluoroborate	$\text{Li}^+ \left[ \begin{array}{c} \text{F} \\   \\ \text{F} \text{---} \text{B} \text{---} \text{F} \\ / \quad \backslash \\ \text{F} \quad \text{F} \end{array} \right]^-$
LiFSI	Lithium bis(fluorosulfonyl)imide	
LiTFSI	Lithium bis(trifluoromethane)sulfonimide	
LiTFOP	Lithium tetrafluoro(oxalato)phosphate	
LiDFDOP	Lithium difluoro(dioxalato)phosphate	
LFO	Lithium difluorophosphate	

### 3.1.3 Coin Cells and Symmetric Cells

Coin cells were built for this work using the architecture shown in **Figure 3.2a**. The electrodes used in coin cells were harvested from fresh or cycled pouch cells. Typical coin cells contain a layer of positive and negative electrodes (or bare copper foil for anode-free coin cells). Coin cells were used to test materials not available in the pouch cell format.\*

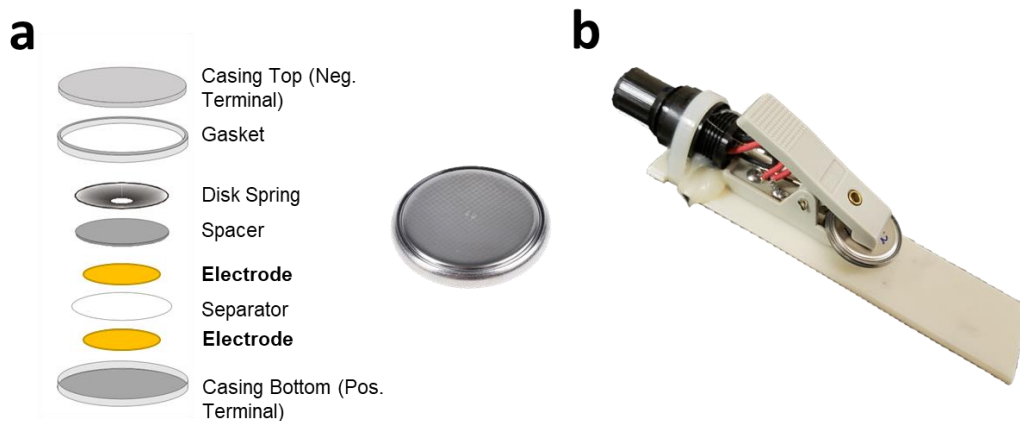


**Figure 3.2 | Coin cell hardware. a,** The hardware for constructing coin cells including a bottom casing, the electrode stack, a spacer and spring on top of the stack, and the top casing and gasket. A picture of a built coin cell is included on the right. **b,** Coin cell testing fixture.

Symmetric cells, which employ a positive-positive or negative-negative electrode pairing, were also used in this work. These cells are a testing vehicle to deconvolute processes which occur at the positive and negative electrode. By testing a positive-positive symmetric cell (measuring its impedance, for example), one can identify properties which belong to just the positive electrode which would otherwise be convoluted with the properties of the negative electrode in a full cell. The same can be said for negative-negative symmetric

---

\* Since pouch cells are delivered in batches by the hundreds, coin cells are necessary for small scale testing when a full pouch build is not practical.



cells. Symmetric cells were constructed with electrodes at 50% state of charge (SOC) harvested from pouch cells that were charged once and then brought to 50% SOC.

Previously, coin cells in our lab were connected to chargers via aluminum tabs that had to be spot welded to the coin cell surface. This process was a bit of a hassle. Therefore, inspired by the cell testing fixtures used by other institutions, we developed simpler clip testing fixtures pictured in **Figure 3.2b**.

## 3.2 Cycling Experiments

### 3.2.1 Electrochemical Testing

Charge-discharge cycle testing was performed using MACCOR Series 4000, NEWARE, E-One Moli Energy Canada, and Novonix battery charger systems. Cells were cycled with constant current between specified upper and lower cut-off voltages. Throughout this work, we will specify the charge-discharge rates by C-rates  $C/x$  and  $D/x$ , where  $x$  is the number of hours to complete one full charge or discharge. The control charge-discharge conditions used in this work were to charge in five hours ( $C/5$ ) and to discharge in two hours ( $D/2$ ). This asymmetrical protocol was chosen since it has long been established that charging slower is beneficial for reversible lithium plating.<sup>69,122,123</sup> The current density can be determined via the C-rates and areal capacity of cells given in **Table 3.1**. For example, the NMC532 anode-free cells used in this work have an areal capacity of  $2.75 \text{ mAh/cm}^2$ . Therefore, the current density required to charge in one hour ( $C/1$  or  $1C$ ) is  $2.75 \text{ mA/cm}^2$ . Our typical  $C/5$  and  $D/2$  charge and discharge rates thus correspond to current densities of  $0.55 \text{ mA/cm}^2$  and  $1.37 \text{ mA/cm}^2$ , respectively. The effect of charge-discharge rates on cell performance will be explored in Chapter 5. The charge and discharge C-rates used throughout this work will be specified in the figure captions.

The voltage limits used during cycling varied for different experiments and for different cell chemistries. Typically, the upper cut-off voltage was chosen such that most of the lithium stored in the positive electrode was de-lithiated during charge (*e.g.* 4.5 V). The lower cut-off voltage determines the depth of discharge—the fraction of lithium from the

positive electrode that is reversibly cycled. Typically, we cycled cells to ~80% depth of discharge. For the NMC532 anode-free cells used in this work, this corresponded to a 3.6 V lower cut-off voltage. Therefore, NMC532 anode-free cells were typically cycled between 3.6-4.5 V. The effect of depth of discharge on cell performance will be explored in Chapter 5. The voltage ranges cycled throughout this work will be specified in the figure captions.

### 3.2.2 Temperature

Cycling was performed in temperature boxes with a temperature control of  $\pm 0.1^\circ\text{C}$ . Testing predominantly occurred at  $40^\circ\text{C}$  due to the increased availability of  $40^\circ\text{C}$  temperature boxes in our lab. However, more limited testing at  $20^\circ\text{C}$ ,  $30^\circ\text{C}$ , and  $55^\circ\text{C}$  was also explored. To enable superior  $20^\circ\text{C}$  cycling performance, a “hot formation” protocol was devised. The role of hot formation will be discussed in Chapter 5. This formation protocol consisted of two charge-discharge cycles at  $40^\circ\text{C}$  and C/10 D/2. After these initial cycles at elevated temperature, cells were transferred to  $20^\circ\text{C}$  temperature boxes for room temperature cycling. The cycling temperature will be specified in the figure captions.

### 3.2.3 Pressure

During cycling, pouch cells were constrained under uniaxial pressure. **Figure 3.3** shows the different cell testing fixtures used to apply pressures ranging from 100-2000 kPa. For low pressures up to 200 kPa, a plastic testing fixture—referred to as a testing “boat” or “normal boat” (NB)—was used to constrain cells with rubber blocks and aluminum shims, shown in **Figure 3.3a**. To achieve higher pressures, an aluminum boat or “superboat” (SB, **Figure 3.3b**) was used. The applied pressure was controlled via screws which tightened an adjustable wall against the cell. A load cell (model LCKD, Omega Engineering) was used to measure the pressure applied to the cell. Two force distributing plates and a disc spring were inserted between the pouch cell and load cell, shown in **Figure 3.4**. This setup, first described in Refs,<sup>49,124</sup> also facilitated operando pressure measurements during cycling. Pouch cells were fastened in this enclosure such that any change of volume of the cell stack caused a change of force within the enclosure measured by the load cell. The pressure on

the pouch cell was thus calculated as the force recorded by the load cell divided by the area of the pouch cell electrode stack,  $6.0 \text{ cm}^2$  ( $0.93 \text{ in}^2$ ). Any gas evolved during cycling is pushed into the gas bag of the pouch cell and does not result in a change in pressure measured by the load cell; only uniaxial expansion of the cell stack is probed with this method.

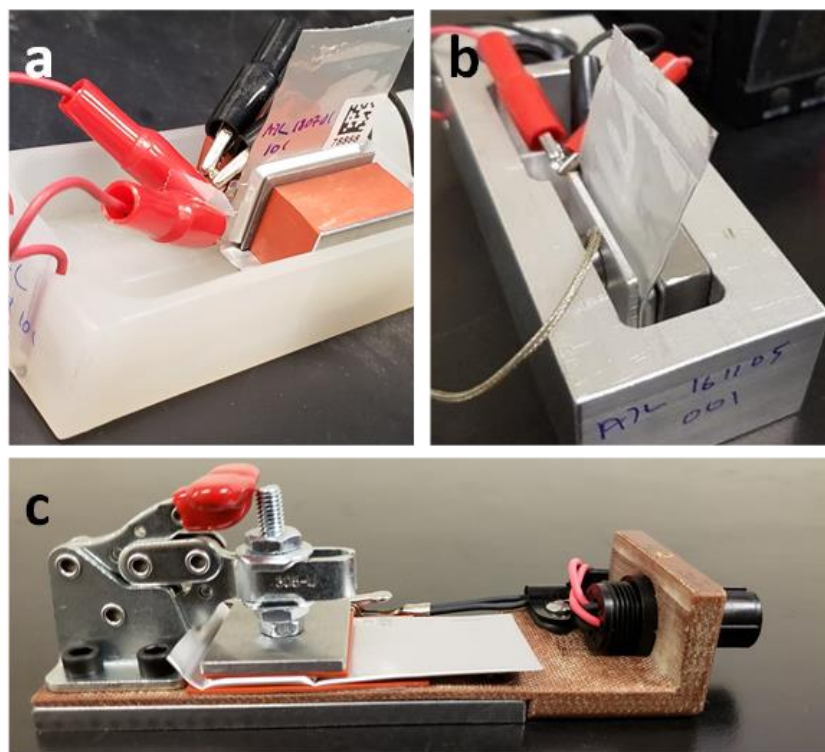


**Figure 3.3 | Pouch cell testing fixtures. a,** A plastic fixture which constrains cells under low pressure ( $< 200 \text{ kPa}$ ) using rubber blocks, referred to as a normal boat (NB). **b,** An aluminum fixture with an adjustable wall allowing for the applied pressure to be controlled, referred to as a superboat (SB). **c,** A fixture which applies high uniaxial stack pressure ( $1200 \text{ kPa}$ ) via clamping with a DESTACO clamp, referred to as an airboat (AB).

The load cells were connected to DP25B-S-A panel meters (Omega Engineering). Operando measurements were performed using an E-One Moli Energy Canada battery testing system. Pouch cells were cycled on Moli channels and the analog 0-10 V output of the panel meter was connected to an adjacent Moli “slave” channel, allowing for simultaneous electrochemical and pressure measurements.



**Figure 3.4 | Superboat pressure measurement.** Picture (left) and schematic representation (right) of the superboat cell testing setup. Pouch cells are fastened by an adjustable wall which can be tightened to change the pressure and a load cell used to measure the pressure, separated by force distributing plates and a disc spring.

When it was determined that a moderately high pressure ( $\sim 1200$  kPa) was sufficient to improve the performance of anode-free cells and that operando pressure measurements were not always necessary, a simpler testing fixture was devised to apply uniaxial pressure to cells during typical cycling experiments. This fixture, referred to as an airboat (AB), is shown in **Figure 3.3c**. A DESTACO clamp with a screw plunger is clamped over a force distributing plate on top of a pouch cell. The screw plunger was adjusted to yield a uniaxial pressure of  $\sim 1200$  kPa during cycling. This pressure was confirmed using pressure paper inserted between the pouch cell and clamp during cycling. In practice, pouch cells are clamped into the airboats by “feel”; the user should experience some resistance to ensure the initial clamping force is sufficient. This force will not initially correspond to 1200 kPa exerted on the cell—the rest of this pressure is built up *in-situ* as lithium plates during charge. The resulting volume expansion of the cell expands against the airboat clamp increasing the uniaxial pressure. There is some concern that this method may result in fatigue of the DESTACO clamps. Therefore, adjustments of the screw plunger between airboat uses may be required to maintain a good clamping force. To try to maintain a more uniform pressure over the surface of pouch cells, thin silicone sheets were inserted above and below the pouch cell in the airboat fixture to help distribute the pressure.

The effect of pressure on cell performance will be explored in Chapter 4. The pressure exerted on cells during cycling will be specified in figure captions and legends.

### 3.3 Data Management

As the number of cells built and tested increased, it became more and more difficult to manage and keep track of the accumulated data. There are many experimental conditions to keep track of (chemistry, cycling rates, temperature, *etc.*). By default, this information is not paired to the cycling data files generated by the cyclers. Therefore, keeping track of past experiments relied largely on the fallible memories of students and their hand-written notes in lab books—an unreliable system. Moreover, the formats of cycling data generated by different cyclers are not consistent, adding further difficulty for comparing data collected on various systems. To overcome these challenges, we devised a system for categorizing data in a universal format. This system was designed and built by Jack deGooyer and myself, with the major coding work performed by Jack. This system involves (1) maintaining a database containing metadata of all cells tested, (2) converting the raw data files generated by the cyclers into a universal output file that is paired with the cell metadata, and (3) a platform for sorting and viewing the data by the various metadata parameters.

#### 3.3.1 Cell Database

Google Sheets was used to build the cell database. Cell information is stored in two spreadsheets—one that contains all dry-cell chemistry information (cell dimensions, constituent electrode materials, *etc.*, as detailed in **Table 3.1** and **Table 3.2**) and another that contains a list of all cells built including their experimental parameters (electrolyte, testing conditions, *etc.*). **Figure 3.5** shows screenshots of these spreadsheets. Google Sheets was a convenient platform to use because it made sharing and editing these sheets amongst several lab members very simple. Moreover, the Google Sheets mobile app made it possible to view the database on-the-fly while roaming around the lab searching for cells (**Figure 3.6**). As of May 10<sup>th</sup> 2021, there are approximately 1700 entries in the cell database corresponding to 1700 anode-free cells built (and counting). It is important to note

that this body of work is not attributed to any single individual, but a result of the combined effort of current and past lab members who contributed to this project: Matthew Genovese, Rochelle Weber, Sam Hames, Cameron Martin, Matthew Coon, Jack deGooyer, Ahmed Eldesoky, Annika Benson, and myself.

**a**

Dahn Lab Cell Types

File Edit View Insert Format Data Tools Add-ons Help Last edit was on July 8, 2020

1	Box code	Colloquial	Formal Name	Anode-free?	Punch Area	Jelly roll m (g)	Jelly roll V (cm <sup>3</sup> /Positive Etd)	Pos L (cm)	Pos S (cm)	Pos w (cm)	Active Area (cm <sup>2</sup> )
7	54891	811 afree	54891 - 811 (AF)	Yes	1.276763	2.30823	NMC811	18.7	14.6	2.6	86.58
8	54902	LCO afree	54902 - LCO (AF)	Yes	1.276763	2.32066	LCO	16.1	12.2	2.6	73.58
9	54903	LFP afree	54903 - LFP (AF)	Yes	1.276763	2.91476	LFP	27.3	23.3	2.6	131.56
10	54795	NMCS32/Ag	54795 - NMCS32 / AC No	No	1.276763	3.18769	NMCS32	14.9	11.3	2.6	68.12
11	54884	SC811	54884 - SC811	No	1.276763		SC811	19.1	15.1	2.6	88.92
12	54844	EA622	54844 - EA622	No	0.985203		EA622	15.3	11.4	2.6	69.42

**b**

Anode-Free Tracking Sheet

File Edit View Insert Format Data Tools Add-ons Help Last edit was seconds ago

1	Book	Barcode	Box	Salt	Solvent	Additive	Volume	Boat	Crate	V range	Temp	Channel	T Box	status	notes	To do after
1402	1401	AJL200710.Book3.pg127	183001 532 54919	0.6M LIDFOB + 0.6M LBF4	FEC-DEC 1:2		0.5mL	NB	C/8 D/3	3.6-4.5V	40C	308M 24	3M11	off	rate test	discharge
1403	1402	AJL200710.Book3.pg127	183002 532 54919	0.6M LIDFOB + 0.6M LBF4	FEC-DEC 1:2		0.5mL	NB	C/8 D/3	3.6-4.5V	40C	308M 25	3M12	off	rate test	discharge
1404	1403	AJL200710.Book3.pg127	183003 532 54919	0.6M LIDFOB + 0.6M LBF4	FEC-DEC 1:2		0.5mL	NB	C/5 D/2	3.6-4.5V	40C	312M 47		off	20c nail param	nail test
1405	1404	AJL200710.Book3.pg127	183004 532 54919	0.6M LIDFOB + 0.6M LBF4	FEC-DEC 1:2		0.5mL	NB	C/5 D/2	3.6-4.5V	40C	312M 48		off	20c nail param	nail test

**Figure 3.5 | Cell database.** **a**, Subset of the spreadsheet used to store the dry-cell information for the different pouch cell types used in this work. **b**, Subset of the spreadsheet used to store the experimental parameters of every cell tested.

1	Boat	Crate	V range	Temp	Channel	T Box	status	notes	To do after
823	AB	C/5 D/2	3.6-4.5V	40C	312M 84		off	1c boom test	boom test
824	NB	C/5 D/2	3.6-4.5V	40C	312M 87		off	20c boom test	boom test
825	AB	C/5 D/2	3.6-4.5V	40C	312M 88		off	20c boom test	boom test
826	NB	C/5 D/2	3.6-4.5V	40C	312M 89		off	50c boom test	boom test
827	AB	C/5 D/2	3.6-4.5V	40C	312M 90		off	50c boom test	boom test
828	NB	C/10 D/10	1.25-4.5V	40C	312M 81		off	2c slow full DoD	PT, discharge
829	NB	C/5 D/2	3.6-4.5V	40C	312M 91		off	80c boom test	boom test
830	AB	C/5 D/2	3.6-4.5V	40C	312M 92		off	80c boom test	boom test
831	AB	C/5 D/2	3.75-4.5V; ; 40C		312M 94		off	spec DoD 40C	
832	AB	C/5 D/2	3.75-4.5V; ; 40C		312M 100		off	spec DoD 40C	
833	AB	C/5 D/2	3.75-4.5V; ; 20C		308M 6	1B3	off	spec DoD 20C hot form	
834	AB	C/5 D/2	3.75-4.5V; ; 20C		308M 7	1B4	off	spec DoD 20C hot form	
835									

**Figure 3.6 | Mobile app interface.** Screenshot of the cell tracking sheet as viewed from the mobile app. Beyond storing experimental parameters, this sheet also includes the location (channel and temperature box) of cells as well as notes for what to do with cells after testing.

### 3.3.2 Universal Exporter

The Universal Exporter was built to reformat cycling data from the different charger systems into a universal output file paired with the metadata from the cell database. This program was coded by Jack deGooyer using MATLAB and the MATLAB App Designer. The graphical user interface (GUI) of the Universal Exporter is shown in **Figure 3.7**. As input, it requires the original cycling data files generated by the Maccor, Moli, Novonix, or Neware chargers. Using the charge and discharge capacity and average voltage values pulled from the original data files, as well as dry-cell parameters pulled from the cell database, the Universal Exporter generates all the other calculated quantities shown in **Figure 3.8**.

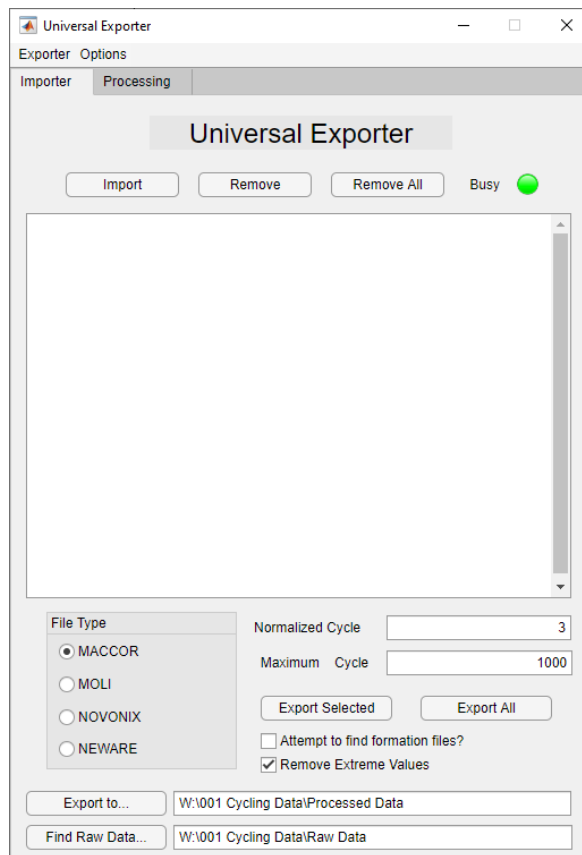


**Figure 3.7 | Universal Exporter.** Interface for the Universal Exporter, used to generate universal cycling data files paired with cell metadata stored in the cell database.



2	k	Boo Colloquial Name	Barcode	Box	Box Colloquial Name	Positive Electrode	Negative Electrode	Salt	Solvent	Additive	Volume	Boat	C rate	V range	Temp	notes	Cycle Normalized	100% DoD cap (mAh)	Electrode Area (cm <sup>2</sup> )	Stack Thickness (cm)	Stack mass (g/cm <sup>2</sup> )
3	AIL-CAM190326-C		124044	54880	Box	low loading	NMC532	Cu	0.6M LiDFOB + 0.6M LiBF4	FEC-DEC 1:2	0.5mL	NB	C/5 D/2	3.6-4.5V	40C	50c electrolyte refill	3 Cycles	273.6544677	86.58	0.017215331	0.04382959
4	e	Cycl Time (hr)	Charge Capacity (mAh)	Discharge Capacity (mAh)	Normalized Charge Capacity	Normalized Discharge Capacity	True Normalized	Areal Loading (mAh/cm <sup>2</sup> )	CE	Avg Charge Volt (V)	Avg Discharge Volt (V)	DeltaV (V)	Normalized Charge Energy (mWh)	Normalized Discharge Energy (mWh)	Energy Hysteresis (mWh)	Volumetric Energy Density (Wh/L)	Energy Density (Wh/kg)	metric Energy Density (Wh/kg)	CEndPt		
5	1	5.949288889	273.6045	221.052641	1.218889824	0.985296594	0.807927746	2.553160556	0.807927746	3.94438926	3.906271931	0.038117329	0.641720446	1079.202524	863.491267	215.7107973	1158.657894	455.0961767	372.7634955		
6	2	12.71559722	222.8310	223.0681	0.992697499	0.994280275	0.815294224	2.576439618	1.001064105	3.975085181	3.907983057	0.067102124	1.129691032	885.7723	871.7465	14.0258	1169.734411	459.4467971	376.8270334		
7	3	19.33506389	224.4702	224.5124	1	1	0.819984209	2.591309118	0.99947053	3.970172488	3.907129098	0.00080319	1.061693972	891.1855	876.5653	14.0202	1176.20422	461.9605205	378.4072787		
8	4	26.38937778	225.5600	225.0513	1.004854706	1.003119674	0.822542392	2.599344807	0.997744795	3.967444406	3.90648943	0.060954976	1.026201339	894.8966	879.1604	15.7362	1179.642596	463.3542323	379.5275639		
9	5	33.26241111	226.1411	225.3426	1.0074436	1.004418263	0.823607215	2.60270979	0.996469136	3.965914158	3.905927534	0.059986624	1.009898761	896.8561	880.1719	16.6842	1181.039853	463.8873341	379.9642208		
10	6	40.14215833	226.3334	225.3337	1.008300319	1.004378355	0.823574491	2.602606379	0.995582912	3.965040691	3.905614016	0.059426675	1.000471796	897.4211	880.0663	17.3548	1180.898133	463.8316095	379.9186267		
11	7	47.02131667	226.3099	225.1647	1.008195634	1.003625187	0.823956905	2.600654725	0.994939637	3.964755215	3.905459387	0.059295828	0.998268926	897.2633	879.3715	17.8918	1179.965877	463.4654993	379.6187013		

**Figure 3.8 | Universal Exporter output file.** Example output from the Universal Exporter. The file name (shown on the top bar) includes cell metadata information. The cell metadata is also displayed in the third row of the file output. The cycling data parameters in the fourth row are calculated from the input cycling data as well as the dry-cell parameters input from the cell database.

**Figure 3.8** shows an example output file. The cell metadata pulled from the database is used in the output file name (shown in the top bar) as well as displayed in the third row of the spreadsheet. The cycling data parameters in the fourth row are calculated from the charge capacity ( $Q_c$ ), discharge capacity ( $Q_d$ ), average charge voltage ( $V_{avg,c}$ ), and average discharge voltage ( $V_{avg,d}$ ) pulled from the original data files as follows:

$$\text{Normalized Capacity} = Q_x / Q_x(n)$$

Where  $x = c$  or  $d$ , referring to charge or discharge, and  $n$  is the  $n$ th value of  $Q_x$  as input into the Universal Exporter in the “normalized cycle” box ( $n = 3$  for the example shown in **Figure 3.8**).

$$\text{True Normalized} = Q_d / 100\% \text{ DoD cap}$$

Where  $100\% \text{ DoD cap}$  is the capacity of the very first charge, displayed in cell R3 in **Figure 3.8**.

$$\text{Areal Loading} = Q_d / \text{Electrode Area}$$

Where  $\text{Electrode Area}$  is pulled from the cell database, displayed in cell S3 in **Figure 3.8**.

$$CE = Q_d / Q_c$$



Where  $CE$  is the coulombic efficiency.

$$\Delta V = V_{avg,c} - V_{avg,d}$$

$$\text{Normalized } \Delta V = \Delta V / \Delta V(m)$$

Where  $m$  is the  $m$ th value of  $\Delta V$  as input into the Universal Exporter in the options toolbar ( $m = 10$  for the example shown in **Figure 3.8**).

$$\text{Energy} = Q_x * V_{avg,x}$$

Where  $x = c$  or  $d$ , referring to charge or discharge.

$$\text{Energy Hysteresis} = \text{Charge Energy} - \text{Discharge Energy}$$

*Stack Volumetric Energy Density* and *Stack Specific Energy Density* (columns Q and R) are calculated using  $Q_d$ ,  $V_{avg,d}$ , *Electrode Area* (cell S3), *Stack Thickness* (cell T3), and *Stack Mass* (cell U3) as previously described in Section 3.1.1.

### 3.3.3 Universal Viewer

The Universal Viewer was built to organize and view cycling data via the array of different experimental parameters tested. This program was coded by Jack deGooyer using MATLAB and the MATLAB App Designer. The “data selection” pane of the Universal Viewer GUI is shown in **Figure 3.9**. The top part of this interface shows the list of cells built along with their metadata as pulled from the cell database. Each experimental parameter is then collated into individual lists which contain each unique entry, shown in the boxes on the bottom half of the interface.

Name	ID	Box	Solvent	Salt	Additive	Temp	Pressure/Box	Negativity/Dir	C Rate	V Range	Volume	Boat	Notes	HL	Run	Status	Channel
102368		BLANK Box	BLANK Sol	BLANK Salt	BLANK Add	BLANK Temp	BLANK Pos	BLANK Neg	BLANK CR	BLANK VR	BLANK Vol	BLANK Boat	Na	102368	0	BLANK STATUS	BLANK CH
102371	54884 - SCR11	EC EMC DMC 25.5.70	1.5M LFPF6	1%LFO 2%FEC	40C	SCR11	Kajin AM400	C3 D3	3-4.2V	BLANK VR	Na	Na	102371	0	BLANK STATUS	BLANK CH	
102374	54884 - SCR11	EC EMC DMC 3A 20.4.50.20	1.5M LFPF6	1%LFO 2%FEC	40C	SCR11	Kajin AM400	C3 D3	3-4.2V	BLANK VR	Na	Na	102374	0	BLANK STATUS	BLANK CH	
102382	532	FEC DEC 1.2	0.8M LDFOB + 0.8M LBF4	BLANK Add	40C	BLANK Pos	BLANK Neg	C5 D2	3-4.4V	0.5mL	Na	Na	102382	0	off	312M 103	
103000	BLANK Box	BLANK Sol	BLANK Salt	BLANK Add	BLANK Temp	BLANK Pos	BLANK Neg	BLANK CR	BLANK VR	BLANK Vol	BLANK Boat	Na	BLANK ID	0	BLANK STATUS	BLANK CH	
103001	BLANK Box	BLANK Sol	BLANK Salt	BLANK Add	BLANK Temp	BLANK Pos	BLANK Neg	BLANK CR	BLANK VR	BLANK Vol	BLANK Boat	Na	BLANK ID	0	BLANK STATUS	BLANK CH	
103740	54907 - LFun811	EC EMC DMC 25.5.70	1.5M LFPF6	2%VC 1%DTD	40C	811	BLANK Neg	C3 C3	3-4.2V	BLANK VR	Na	Na	103740	0	BLANK STATUS	BLANK CH	
103741	54907 - LFun811	EC EMC DMC 25.5.70	1.5M LFPF6	2%VC 1%DTD	40C	811	BLANK Neg	C3 C3	3-4.2V	BLANK VR	Na	Na	103741	0	BLANK STATUS	BLANK CH	
103742	54907 - LFun811	EC EMC DMC 25.5.70	1.5M LFPF6	2%FEC 1%LFO	40C	811	BLANK Neg	C3 C3	3-4.2V	BLANK VR	Na	Na	103742	0	BLANK STATUS	BLANK CH	
103743	54907 - LFun811	EC EMC DMC 25.5.70	1.5M LFPF6	2%FEC 1%LFO	40C	811	BLANK Neg	C3 C3	3-4.2V	BLANK VR	Na	Na	103743	0	BLANK STATUS	BLANK CH	
123121	54857 - Orig. L.	FEC DEC 1.2	1M old LDFOB	BLANK Add	40C	NMC532	Cu	C5 D2	3.6-4.5V	0.5mL	SB 100s	Na	123121	0	BLANK STATUS	BLANK CH	
123122	54857 - Orig. L.	FEC DEC 1.2	1M old LDFOB	BLANK Add	40C	NMC532	Cu	C5 D2	3.6-4.5V	0.5mL	SB 100s	Na	123122	0	BLANK STATUS	BLANK CH	
123123	54857 - Orig. L.	FEC DEC 1.2	1M old LDFOB	BLANK Add	40C	NMC532	Cu	C5 D2	3.6-4.5V	0.5mL	SB 100s	Na	123123	0	BLANK STATUS	BLANK CH	
123154	54857 - Orig. L.	EC DEC 1.2	1M LFPF6	CO2	40C	NMC532	Cu	C5 D2	3.6-4.5V	0.5mL	in situ gas	-CO2	123154	0	BLANK STATUS	BLANK CH	
123155	54857 - Orig. L.	EC DEC 1.2	1M LFPF6	CO2	40C	NMC532	Cu	C5 D2	3.6-4.5V	0.5mL	in situ gas	-CO2	123155	0	BLANK STATUS	BLANK CH	
123189	54857 - Orig. L.	EC DEC 1.2	1M LFPF6	BLANK Add	40C	NMC532	Cu	C5 D2	3.6-4.5V	0.5mL	in situ gas	Na	123189	0	BLANK STATUS	BLANK CH	
123190	54857 - Orig. L.	EC DEC 1.2	1M LFPF6	BLANK Add	40C	NMC532	Cu	C5 D2	3.6-4.5V	0.5mL	in situ gas	Na	123190	0	BLANK STATUS	BLANK CH	
123191	54857 - Orig. L.	FEC DEC 1.2	1M LFPF6	CO2	40C	NMC532	Cu	C5 D2	3.6-4.5V	0.5mL	in situ gas	-CO2	123191	0	BLANK STATUS	BLANK CH	
123192	54857 - Orig. L.	FEC DEC 1.2	1M LFPF6	CO2	40C	NMC532	Cu	C5 D2	3.6-4.5V	0.5mL	in situ gas	-CO2	123192	0	BLANK STATUS	BLANK CH	
123193	54857 - Orig. L.	FEC DEC 1.2	1M LFPF6	BLANK Add	40C	NMC532	Cu	C5 D2	3.6-4.5V	0.5mL	in situ gas	Na	123193	0	BLANK STATUS	BLANK CH	
123194	54857 - Orig. L.	FEC DEC 1.2	1M LFPF6	BLANK Add	40C	NMC532	Cu	C5 D2	3.6-4.5V	0.5mL	in situ gas	Na	123194	0	BLANK STATUS	BLANK CH	

**Figure 3.9 | Universal Viewer data selection window.** Interface window of the Universal Viewer for data selection. A list of all constructed cells with their experimental parameters appear on the top half of the window. A box for each parameter appears at the bottom half of the window listing every unique entry for these parameters from the cell database.

**Figure 3.10** shows the graph pane of the Universal Viewer. In this window, the data selected from the aptly named data selection pane is visualized. No specific subset of data was selected in **Figure 3.9**, therefore, the resulting graph produced in **Figure 3.10** shows the data for every cell loaded into the database. Obviously, it is impossible to discern anything meaningful from this graph beyond showing off how many cells have been tested. To generate more useful graphs, subsets of data must be selected in the data selection pane. This is demonstrated in **Figure 3.11** and **Figure 3.12**.

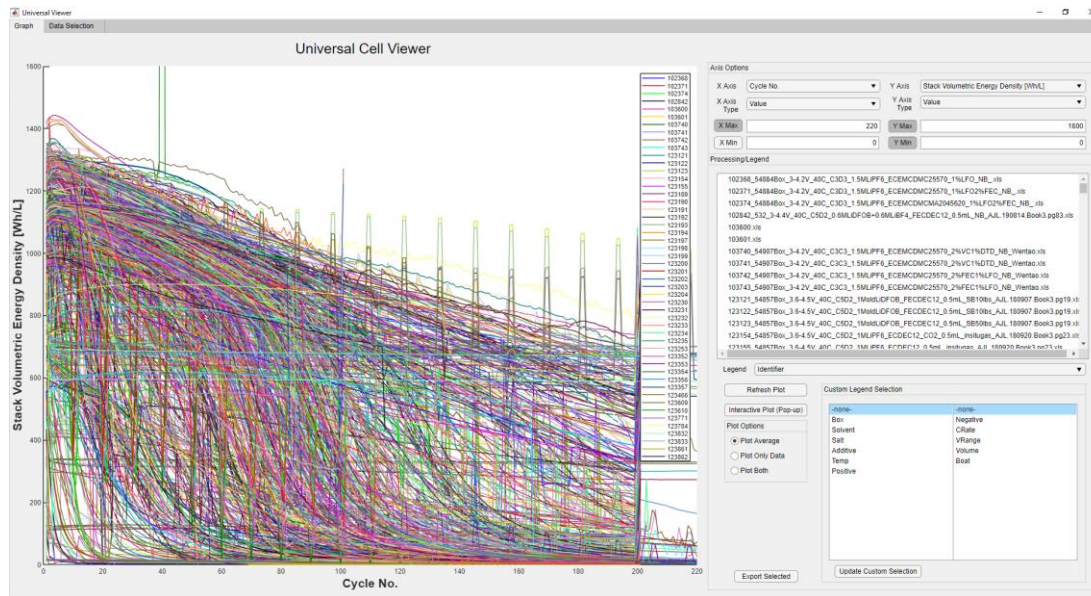


**Figure 3.10 | Universal Viewer graph window.** Interface window of the Universal Viewer for data visualization. This shows the resulting graph when no data subset is selected from the data selection pane—all cycling data is plotted at once. The data belonging to over 1100 cycled cells are shown here.

**Figure 3.11** shows the data selection pane of the Universal Viewer with specific experimental parameters selected (shown highlighted in blue). The top panel lists all cells that correspond to this parameter selection. In this example, the selection is for cells with no additive, with an NMC532 positive electrode, tested at a C/5 D/2 C-rate, with 0.5, 0.8 or 1.0 mL of FEC:DEC 1:2 0.6 M LiDFOB 0.6 M LiBF<sub>4</sub> electrolyte tested between 3.6-4.5 V at 40 °C in a normal boat.

**Figure 3.12** shows the resulting graph generated from the data selection of **Figure 3.11** with additional NMC811 data included. This graph compares NMC532 and NMC811 cells tested with different volumes of electrolyte. The legend displayed in this graph is controlled by the selection of parameters in the bottom right of the window.

ID	Box	Solvent	Salt	Additive	Temp	Pos/Elec	Neg/Elec	C Rate	V Range	Volume	Boat	Notes	HL	Num	Status	Channel
123960	54880 - Low Loading (AF)	FEC:DEC 1:2	0.6M LiDFOB + 0.6M LiBF4	BLANK Add	40C	NMC532	Cu	CR D2	3.6-4.5V	0.5mL	NB	1c SEM 1.25V	123960	0	BLANK STATUS	BLANK CH
123961	54880 - Low Loading (AF)	FEC:DEC 1:2	0.6M LiDFOB + 0.6M LiBF4	BLANK Add	40C	NMC532	Cu	CR D2	3.6-4.5V	0.5mL	NB	1c SEM 3.6V	123961	0	BLANK STATUS	BLANK CH
123962	54880 - Low Loading (AF)	FEC:DEC 1:2	0.6M LiDFOB + 0.6M LiBF4	BLANK Add	40C	NMC532	Cu	CR D2	3.6-4.5V	0.5mL	NB	20c SEM 1.25V	123962	0	BLANK STATUS	BLANK CH
123963	54880 - Low Loading (AF)	FEC:DEC 1:2	0.6M LiDFOB + 0.6M LiBF4	BLANK Add	40C	NMC532	Cu	CR D2	3.6-4.5V	0.5mL	NB	20c SEM 3.6V	123963	0	BLANK STATUS	BLANK CH
123964	54880 - Low Loading (AF)	FEC:DEC 1:2	0.6M LiDFOB + 0.6M LiBF4	BLANK Add	40C	NMC532	Cu	CR D2	3.6-4.5V	0.5mL	NB	50c SEM 1.25V	123964	0	BLANK STATUS	BLANK CH
124024	54880 - Low Loading (AF)	FEC:DEC 1:2	0.6M LiDFOB + 0.6M LiBF4	BLANK Add	40C	NMC532	Cu	CR D2	3.6-4.5V	0.5mL	NB	50c SEM 3.6V	124024	0	BLANK STATUS	BLANK CH
124025	54880 - Low Loading (AF)	FEC:DEC 1:2	0.6M LiDFOB + 0.6M LiBF4	BLANK Add	40C	NMC532	Cu	CR D2	3.6-4.5V	0.5mL	NB	80c SEM 1.25V	124025	0	BLANK STATUS	BLANK CH
124026	54880 - Low Loading (AF)	FEC:DEC 1:2	0.6M LiDFOB + 0.6M LiBF4	BLANK Add	40C	NMC532	Cu	CR D2	3.6-4.5V	0.5mL	NB	80c SEM 3.6V	124026	0	BLANK STATUS	BLANK CH
124027	54880 - Low Loading (AF)	FEC:DEC 1:2	0.6M LiDFOB + 0.6M LiBF4	BLANK Add	40C	NMC532	Cu	CR D2	3.6-4.5V	0.5mL	NB	100c SEM 1.25V	124027	0	BLANK STATUS	BLANK CH
124028	54880 - Low Loading (AF)	FEC:DEC 1:2	0.6M LiDFOB + 0.6M LiBF4	BLANK Add	40C	NMC532	Cu	CR D2	3.6-4.5V	0.5mL	NB	100c SEM 3.6V	124028	0	BLANK STATUS	BLANK CH
124079	54881 - Thick Sep&CC (L)	FEC:DEC 1:2	0.6M LiDFOB + 0.6M LiBF4	BLANK Add	40C	NMC532	Cu	CR D2	3.6-4.5V	0.5mL	NB	Na	124079	0	BLANK STATUS	BLANK CH
124080	54881 - Thick Sep&CC (L)	FEC:DEC 1:2	0.6M LiDFOB + 0.6M LiBF4	BLANK Add	40C	NMC532	Cu	CR D2	3.6-4.5V	0.5mL	NB	Na	124080	0	BLANK STATUS	BLANK CH
124081	54881 - Thick Sep&CC (L)	FEC:DEC 1:2	0.6M LiDFOB + 0.6M LiBF4	BLANK Add	40C	NMC532	Cu	CR D2	3.6-4.5V	0.5mL	NB	20c 4V CCCC	124081	0	BLANK STATUS	BLANK CH
124082	54881 - Thick Sep&CC (L)	FEC:DEC 1:2	0.6M LiDFOB + 0.6M LiBF4	BLANK Add	40C	NMC532	Cu	CR D2	3.6-4.5V	0.5mL	NB	80c 4V CCCC	124082	0	BLANK STATUS	BLANK CH
124087	54881 - Thick Sep&CC (L)	FEC:DEC 1:2	0.6M LiDFOB + 0.6M LiBF4	BLANK Add	40C	NMC532	Cu	CR D2	3.6-4.5V	0.5mL	NB	100c 4V CCCC	124087	0	BLANK STATUS	BLANK CH
124088	54881 - Thick Sep&CC (L)	FEC:DEC 1:2	0.6M LiDFOB + 0.6M LiBF4	BLANK Add	40C	NMC532	Cu	CR D2	3.6-4.5V	0.5mL	NB	80c 4V CCCC	124088	0	BLANK STATUS	BLANK CH
124115	54880 - Low Loading (AF)	FEC:DEC 1:2	0.6M LiDFOB + 0.6M LiBF4	BLANK Add	40C	NMC532	Cu	CR D2	3.6-4.5V	0.5mL	NB	low v alarm 090	124115	0	BLANK STATUS	BLANK CH
124116	54880 - Low Loading (AF)	FEC:DEC 1:2	0.6M LiDFOB + 0.6M LiBF4	BLANK Add	40C	NMC532	Cu	CR D2	3.6-4.5V	0.5mL	NB	Na	124116	0	BLANK STATUS	BLANK CH
124135	54880 - Low Loading (AF)	FEC:DEC 1:2	0.6M LiDFOB + 0.6M LiBF4	BLANK Add	40C	NMC532	Cu	CR D2	3.6-4.5V	0.5mL	NB	Na	124135	0	BLANK STATUS	BLANK CH
124136	54880 - Low Loading (AF)	FEC:DEC 1:2	0.6M LiDFOB + 0.6M LiBF4	BLANK Add	40C	NMC532	Cu	CR D2	3.6-4.5V	0.5mL	NB	Na	124136	0	BLANK STATUS	BLANK CH
124149	54880 - Low Loading (AF)	FEC:DEC 1:2	0.6M LiDFOB + 0.6M LiBF4	BLANK Add	40C	NMC532	Cu	CR D2	3.6-4.5V	0.5mL	NB	Na	124149	0	BLANK STATUS	BLANK CH

**Figure 3.11 | Universal Viewer data selection.** A subset of data from selecting the desired experimental parameters (highlighted in blue). The top panel lists all data that shares the selected parameters.

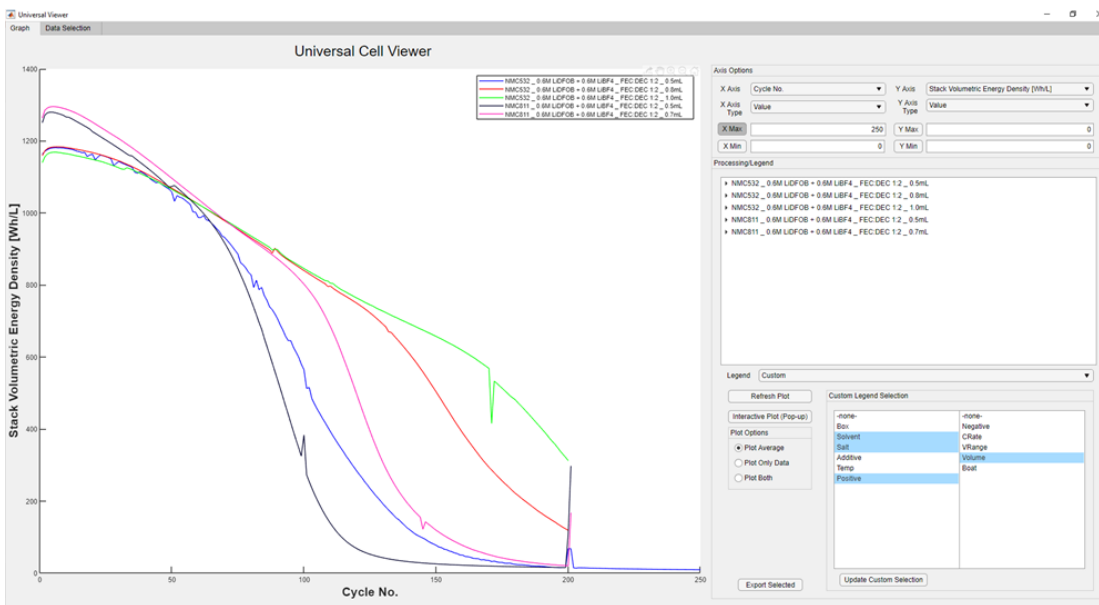


**Figure 3.12 | Universal Viewer graph example.** The output graph resulting from selecting a subset of data. NMC532 and NMC811 cells with different volumes of 0.6 M LiDFOB 0.6 M LiBF4 FEC:DEC (1:2) electrolyte, as indicated in the legend, are plotted. The plotted lines are the average of all duplicate cells built and tested with the same parameters.

### 3.4 Nuclear Magnetic Resonance Spectroscopy

Liquid nuclear magnetic resonance (NMR) spectroscopy was performed on electrolyte extracted from cycled cells to semi-quantitatively determine changes in electrolyte composition during cell aging. NMR experiments make use of interactions between nuclear magnetic moments and externally applied magnetic fields to determine the chemical composition of a sample. Nuclear magnetic moments originate from the intrinsic angular momentum (or spin) of nuclei. In the case of proton and fluorine NMR used in this work, we are probing  $^1\text{H}$  and  $^{19}\text{F}$  nuclei which have spin quantum numbers of  $I = \frac{1}{2}$ . The magnetic quantum numbers,  $m$ , which quantize the possible spin states in an external magnetic field are given as  $+I$  to  $-I$  in integer steps. Therefore, for  $^1\text{H}$  and  $^{19}\text{F}$ ,  $m = +\frac{1}{2}$  and  $-\frac{1}{2}$ . Upon application of an external magnetic field, the spins must thus align ( $+\frac{1}{2}$ ) or anti-align ( $-\frac{1}{2}$ ) to the field. The aligned spins occupy a lower energy state; therefore, there is a larger population of aligned spins. During an NMR experiment, these ordered spins are perturbed by electromagnetic (EM) radiation to induce transitions between spin states—the lower energy aligned spins are promoted to the higher energy anti-aligned states via the absorption of EM radiation. Since the spin states are quantized, an exact quanta of energy corresponding to the difference in energy between the states is required to induce a spin flip. This energy, and thus the frequency of the electromagnetic radiation, is characteristic of the nuclei in question as well as its chemical environment. The frequency of the absorbed EM radiation in the NMR spectrum, known as the resonant frequency, thus facilitates chemical identification of the sample.

**Figure 3.13** shows example  $^{19}\text{F}$  NMR spectra collected from various electrolyte samples analyzed in this work. Since resonance frequency depends on the chemical environment surrounding the nuclei, NMR spectra are conventionally plotted vs a parameter called “chemical shift” which is defined as the frequency normalized to the frequency of NMR spectrometer magnet (500 MHz) in reference to the resonant frequency of the NMR solvent used in the experiment. In this work, we utilized a Bruker AV500 spectrometer with a magnetic field strength of 11.74 T.

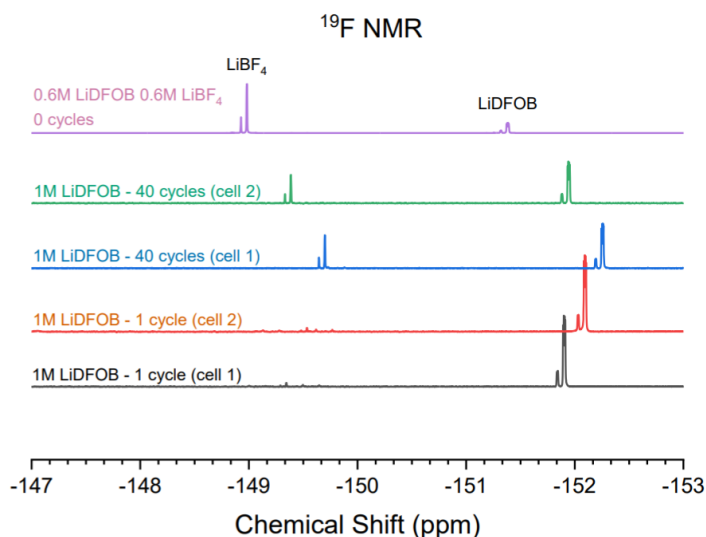


**Figure 3.13 | Fluorine NMR spectra.**  $^{19}\text{F}$  absorption vs chemical shift NMR spectra for various electrolyte samples tested in this work measured with a Bruker AV500 spectrometer.

NMR electrolyte analysis was performed primarily on dual-salt LiDFOB/LiBF<sub>4</sub> FEC:DEC 1:2 electrolyte formulations. Electrolyte extraction from cycled cells was performed in a glovebox. Dimethyl sulfoxide (DMSO) was used as the extraction liquid as it dissolves the electrolyte salts, is miscible with the electrolyte solvents, and does not react with either. 1 mL of DMSO was inserted into opened pouch cells and massaged into the jelly roll for 5 minutes. For coin cells, the extracted electrodes were placed in 1 mL of DMSO and shaken for 5 minutes. Afterwards, the DMSO-electrolyte mixture was transferred into NMR tubes and subsequently into the spectrometer. No internal standard was used because presently we have not identified an internal standard that is inert to all electrolyte components (LiDFOB in particular). Therefore, the following analysis is semi-quantitative in nature.

The solvent components of the electrolyte are quantified via proton NMR. Resonance peaks for both FEC and DEC can be identified in the  $^1\text{H}$  spectra. Both peaks are integrated; the FEC peak is assigned the value of 1 and the DEC peak is weighted relative to FEC. The area under an NMR peak is proportional to the number of spins involved, therefore, the area of the FEC and DEC peaks are divided by the number of involved protons (3 and 6,



respectively). This results in the relative number of moles of FEC and DEC. Multiplying by their molar mass then yields the relative mass of each solvent component.

The salt components are quantified via fluorine NMR. The fluorine-containing molecules, FEC, LiDFOB, and LiBF<sub>4</sub> show up in the <sup>19</sup>F spectra. These peaks are integrated, weighted relative to FEC, and then divided by the number of fluorine nuclei involved (1, 2, and 4, respectively) to determine the relative number of moles of each species. The relative number of moles for each salt component is then divided by the total relative mass of the solvents (determined from the <sup>1</sup>H analysis) to yield the salt concentration molality (mol/kg).

### 3.5 Scanning Electron Microscopy Imaging

Top-down scanning electron microscopy (SEM) images were taken of plated lithium metal for morphological characterization. After cycling, pouch cells were opened in an argon-filled glovebox. The lithium electrodes were unwound, punched into ~0.5 cm<sup>2</sup> samples and washed with dimethyl carbonate (DMC). Samples were transported from the glove box to a Hitachi S-4700 Field Emission Scanning Electron Microscope in a crude airtight container (originally designed to store food). Samples were briefly (< 10 s) exposed to air while they were loaded in the SEM. Images were taken in secondary electron imaging mode with an accelerating voltage of 3.0 kV and a working distance of 12 mm.

### 3.6 X-ray Computed Tomography

Cycled anode-free cells were sent to Carl Zeiss Microscopy (Pleasanton, USA) for x-ray computed tomography measurements. X-ray tomographic imaging was performed using Zeiss Xradia Versa 520 X-ray Microscope (XRM). The XRM allows for high resolution imaging and high contrast sensitivity to non-destructively visualize the internal morphology of anode-free pouch cells. All imaging was performed without opening or otherwise disturbing the cells. The XRM employs a tungsten target anode with an accelerating voltage of 80 kV. During the tomography, 1601 projection images were acquired over an angle range of -183 to 3 degrees utilizing the 4x optical magnification

objective. Reconstruction was performed using commercial software package XMReconstructor (Carl Zeiss X-ray Microscopy Inc., Pleasanton, CA) utilizing a cone-beam filtered back-projection algorithm.

### 3.7 Ultrasonic Transmission Mapping

Ultrasonic transmission mapping was used to examine how well “wet” anode-free cells were with electrolyte. For efficient  $\text{Li}^+$  transport, the entire cell jelly roll should be filled with electrolyte. This means electrolyte should fill all the pores of the electrode materials and separator. Electrolyte wetting was probed by measuring the attenuation of an ultrasonic signal through anode-free cells. This technique was demonstrated on Li-ion cells in Ref.<sup>125</sup> The bottom right panel of **Figure 3.14a** shows an example ultrasonic transmission map overlaid on top of the corresponding cell the measurement was collected on. The other panels in **Figure 3.14a** show transmission maps collected on cells filled with different volumes of electrolyte. Cells filled with a sufficient volume of electrolyte exhibit high degrees of transmission. As the electrolyte volume is decreased, the transmission is attenuated. When there is insufficient electrolyte to wet the entire jelly roll, cell “dry-out” is said to have occurred (top left panel of **Figure 3.14a**).<sup>125</sup>

Ultrasonic transmission mapping was performed with an ultrasonic battery scanner (UBSC-LD50, Jiangsu Jitri-Hust Intelligent Equipment Technology Co., Ltd).<sup>125</sup> A pair of ultrasonic focus transducers (2 MHz frequency, 30 mm focal distance, customized from Shantou Institute of Ultrasonic Instruments Co., Ltd.) were positioned on either side of the cell. Transducers and cells were immersed in low viscosity silicone oil which serves as an ultrasonic coupling agent. The transducers were installed on a 2-dimensional motion system with a precision of 0.2 mm to perform mechanical progressive scanning. The ultrasonic signal was emitted by a transducer on one side of the cell and received by the transducer on the other side, as illustrated in **Figure 3.14b**. The peak-to-peak values of received transmission waves were converted into colour heat maps to make the pseudo colour image. Cells were degassed before ultrasonic measurements performed at 20 °C.



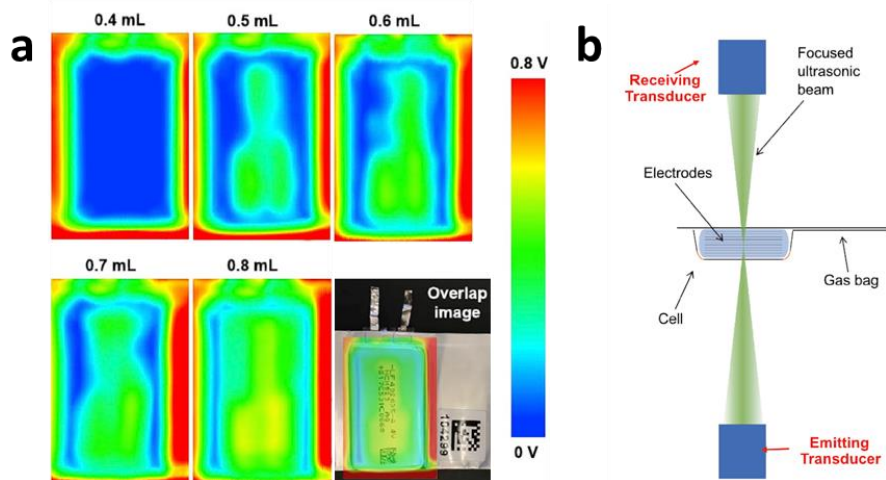


**Figure 3.14 | Ultrasonic transmission mapping.** **a**, Ultrasonic transmission maps of Li-ion cells filled with different volumes of electrolyte. Higher transmission (redder colours) indicates superior electrolyte wetting. The bottom right panel shows an example transmission map overlaid on a Li-ion pouch cell. **b**, Schematic of how the ultrasonic transmission mapping system works. These images were adapted from Ref.<sup>125</sup>

### 3.8 Electrochemical Impedance Spectroscopy

Electrochemical impedance spectroscopy (EIS) is a technique used to investigate the resistance to charge movement (impedance,  $Z$ ) through an electrochemical system. EIS is a useful tool for studying the contributions to impedance growth in lithium-ion and lithium metal cells, including ohmic resistance of  $\text{Li}^+$  travelling through the electrolyte (solution resistance,  $R_s$ ), impedance through interfaces (charge transfer resistance,  $R_{ct}$ ), and impedance due to solid state diffusion.<sup>126</sup> For an EIS experiment, a sinusoidal voltage is applied to a cell and the current response is recorded. The impedance is determined as the ratio between the applied voltage and the measured current. This is done for a range of frequencies of interest, typically 100 kHz to 10 mHz.

The impedance through an interface can be modelled by an RC circuit comprised of a resistor in parallel with a capacitor (**Figure 3.15a**). The impedance of a resistor with resistance  $R$  is simply given by  $Z = R$ , and the impedance of a capacitor with capacitance  $C$  is given by

$$Z = \frac{1}{j\omega C},$$

where  $j$  is an imaginary number and  $\omega$  is the angular frequency. The resistor models charge transfer through the interface and the capacitor models charging of the interfacial double layer. The interfaces in question include the electrolyte-electrode interface through the SEI as well as electrode-current collector interfaces. The results of EIS experiments are often reported as Nyquist curves which plot the negative imaginary impedance vs the real impedance for the range of frequencies measured. In a Nyquist plot, the impedance of an RC circuit appears as perfect semi-circle (**Figure 3.15c**, orange x's). However, the impedance spectra of real lithium metal cells often feature a depressed semi circle. This is attributed to surface roughness and frequency dispersions in real systems.<sup>127,128</sup> To incorporate this into the model, a constant phase element (CPE) is used in place of an ideal capacitor to form a R-CPE circuit (**Figure 3.15b**). The CPE models an imperfect capacitor with an effective capacitance resulting from a distribution of time constants.<sup>129</sup> The parameter  $\varphi$  determines the degree to which the semi-circle is depressed, where  $0 < \varphi < 1$  and lower values result in a more depressed semi-circle and  $\varphi = 1$  results in the typical RC behaviour, as demonstrated in **Figure 3.15c**. The impedance of a CPE is given by

$$Z = \frac{1}{T(j\omega)^\varphi},$$

where  $T$  is the CPE constant analogous to  $C$ . The diameter of the Nyquist semi-circle is determined by the value of the resistor in the RC or R-CPE circuit, often referred to as the charge transfer resistance ( $R_{ct}$ ).

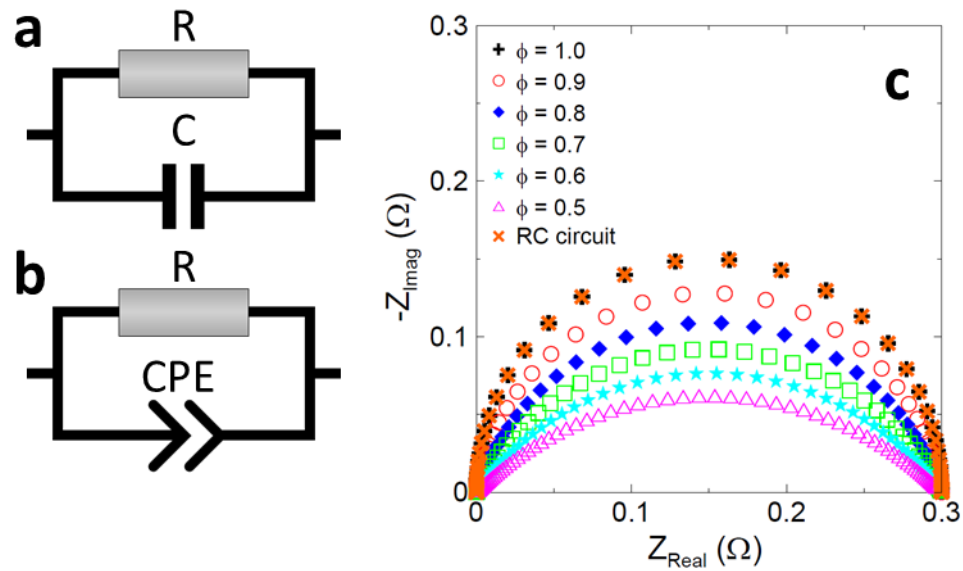


**Figure 3.15 | Impedance through an interface a-b**, Circuit models for impedance through an interface. A RC circuit comprised of a resistor in parallel with a capacitor (a), and a R-CPE circuit comprised of a resistor in parallel with a constant phase element (CPE, b). **c**, Nyquist plot of the impedance of a RC circuit and R-CPE circuits with different values of  $\phi$ , as adapted from Ref.<sup>129</sup>

The ohmic resistance of a cell can be modelled by a resistor in series with a RC or R-CPE circuit (**Figure 3.16a**). The contributing elements to ohmic resistance are  $\text{Li}^+$  diffusion in the electrolyte, referred to as solution resistance ( $R_s$ ), and electronic resistance ( $R_{el}$ ) of electrons through the electrodes, current collectors, and external circuit. These two contributions are difficult to deconvolute and therefore are generally incorporated into the circuit model using a single resistor. The solution resistance is expected to be the dominant contribution of the ohmic resistance which evolves during cycling, therefore the ohmic resistance is often just referred to as the solution resistance. In a Nyquist plot, the solution resistance shifts the semi-circle on the real axis by the value of  $R_s$ . An example of a real Nyquist curve is shown in **Figure 3.16d**, as modelled by the equivalent circuit in **Figure 3.16a**.

Warburg (W) impedance elements are used to model  $\text{Li}^+$  solid state diffusion through the electrode materials.<sup>127</sup> The impedance of a Warburg element is given by

$$Z = \frac{\sigma}{\omega^{1/2}} - j \frac{\sigma}{\omega^{1/2}},$$

Where  $\sigma$  is a constant containing the diffusion coefficient.<sup>130</sup> **Figure 3.16b** shows that the Warburg element is placed in series with  $R_s$  and the R-CPE circuit. In a Nyquist plot, the Warburg impedance appears as a 45° tail at low frequencies as shown in the right-most portion of **Figure 3.16d**.

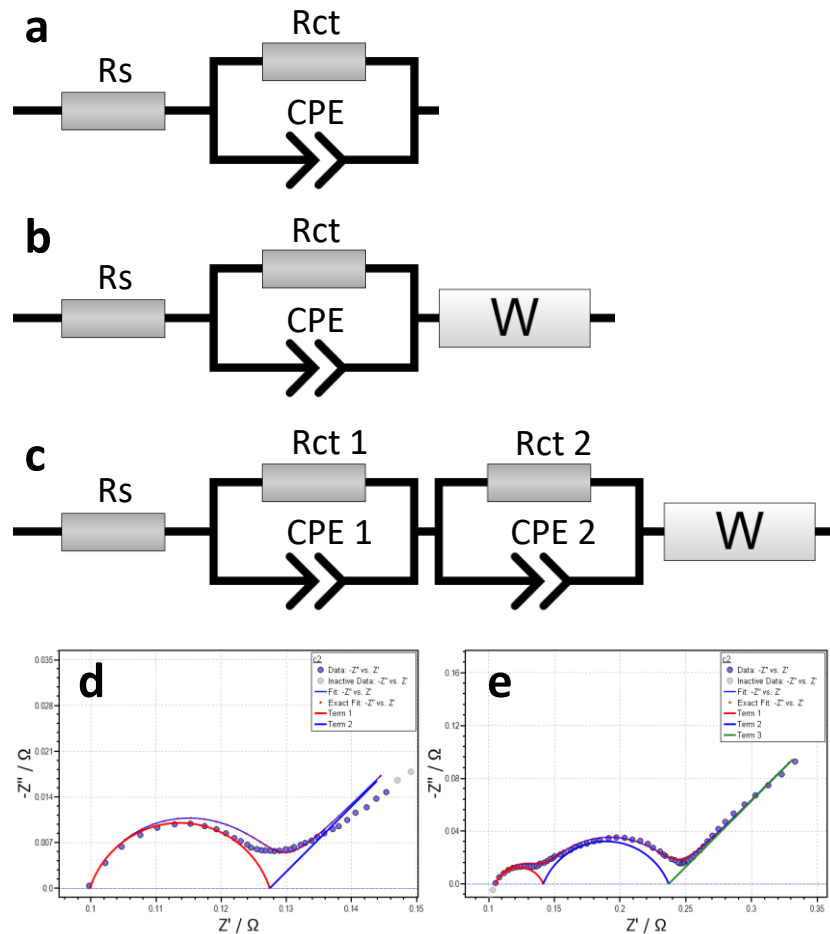


**Figure 3.16 | Circuit models.** **a**, A resistor used to model solution resistance ( $R_s$ ), in series with a R-CPE circuit used to model charge transfer and charge transfer resistance ( $R_{ct}$ ). **b**, A resistor in series with a R-CPE circuit and a Warburg element ( $W$ ) used to model solid state diffusion. **c**, A resistor in series with a Warburg element and two R-CPE circuits used to model a system with charge transfer occurring through two interfaces with distinct characteristic frequencies. **d-e**, Real Nyquist curves fit with the equivalent circuits shown in **b** and **c**, respectively.

In practice, the Nyquist impedance spectra of lithium metal cells may have more than one semi-circle. This can be rationalized as charge transfer through interfaces with distinct characteristic frequencies. For example, the electrode-current collector interface vs the electrolyte-positive electrode interface vs the electrolyte-negative electrode interface.<sup>130</sup> For this work, in cases where two distinct semi-circles are observed, we use a circuit model with two R-CPE circuits in series as shown in **Figure 3.16c**, with an example Nyquist curve exhibiting this behaviour shown in **Figure 3.16e**. There have been many other proposed equivalent circuit models in the literature with increasing degrees of complexity.<sup>130</sup> However, introducing many extra parameters can result in over-fitting and obfuscate any rational physical interpretations of the parameters. Our strategy was to use a model we could simply rationalize with as few parameters as possible.

In this work, we use two methods for interpreting EIS results. First, in Chapter 4—in the spirit of extracting as much information from as simple an interpretation possible—we simply analyze the solution resistance and charge transfer resistance by attributing the Nyquist curve real-axis shift from zero to  $R_s$  and the entire “semi-circle” diameter to  $R_{ct}$ . In Chapter 6, we use a less primitive approach in which we fit the impedance spectra using the equivalent circuit models shown in **Figure 3.16b** and **c** and extract the relevant parameters ( $R_s$ ,  $R_{ct}$ , etc) from these fits. The fitting was performed using the RelaxIS 3 software suite (rhd instruments GmbH & Co. KG, Germany <https://www.rhd-instruments.de/en/products/software/relaxis>).

EIS measurements can be performed quickly without altering the cell. Therefore, EIS measurements during cycle testing is possible. These types of *in-situ* experiments where EIS was measured as a function of cycle number were performed along with additional *ex-situ* measurements in which impedance spectra were collected before and after cycle testing. For the *ex-situ* measurements, a BioLogic VMP3 system was used. These measurements were performed at 10 °C. The *in-situ* measurements were performed using a frequency response analyzer (FRA). Computer controlled relays automatically switched cell connections between Neware cyclers during charge-discharge cycling and Gamry FRA cards during EIS measurements.<sup>129</sup> EIS spectra were measured every 10 cycles. These

measurements were performed at 40 °C—the typical temperature for charge-discharge testing used in this work. For both *in-situ* and *ex-situ* measurements, EIS spectra were collected with ten points per frequency decade using an input voltage amplitude of 10 mV. *In-situ* FRA measurements were collected between frequencies of 50 kHz to 10 mHz; *ex-situ* measurements were typically collected between frequencies of 100 kHz to 10 mHz.

### 3.9 Smart Nail Safety Testing

To characterize the safety of anode-free cells with different electrolytes and positive electrodes, we performed nail penetration tests to simulate an internal short. Cells were aged to various cycle numbers and brought to their fully charged state before penetration. At the top of charge cells should be most vulnerable to safety hazards since all their capacity is available for discharge, the maximum amount of reactive lithium is plated, and the positive electrode material is most volatile. “Smart nails” were used to perform the penetration. The shaft of these nails were hollow such that a thermocouple can be threaded through and attached to the copper tip as described previously.<sup>131</sup> This is shown in **Figure 3.17a**. The thermocouple allowed for temperature measurements at the nail tip and point of penetration.

Two setups for driving the nail into pouch cells were used. The first setup, pictured in **Figure 3.17b**, consisted of a Enerpac A258 hydraulic press connected to an Enerpac PER1301B hydraulic pump. An analog knob on the pump controlled the speed of the press and an attached controller allowed the user to start, stop, and reverse the driving action of the press and attached nail. Therefore, the speed and depth of the penetrations were controlled by touch. The estimated depth and speed of the penetrations using this method are 2.5 mm at 5 mm/s. This setup was used for the nail penetrations performed in Section 4.3. A second more advanced setup to precisely control the penetrations via a computer-controlled step motor was devised by Connor Aiken. This allowed for controlled penetrations with to a depth of 2.5 mm at a speed of 0.5 mm/s and was used for the penetrations performed in Section 6.1.4.

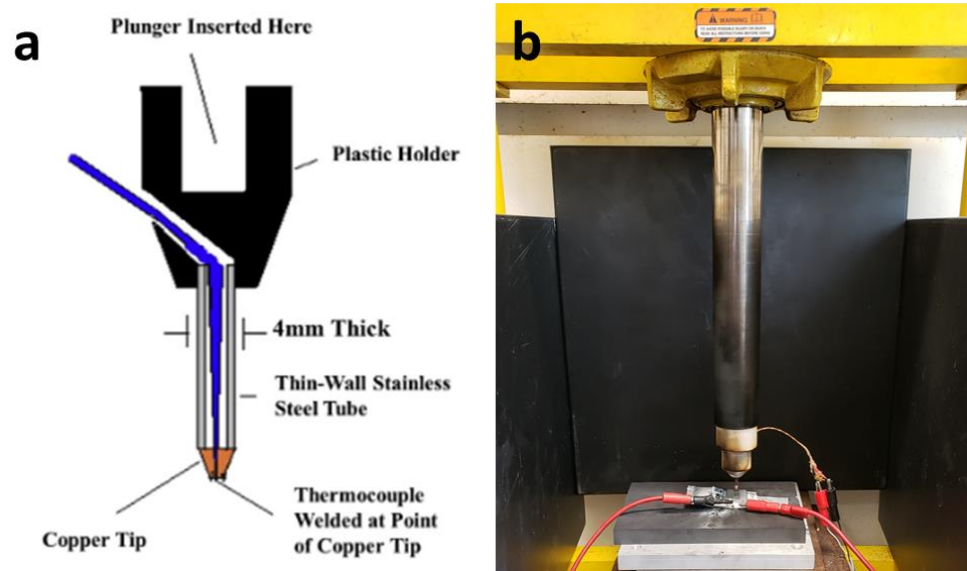


**Figure 3.17 | Smart nail setup.** **a**, Schematic of the smart nail used for nail penetration tests adapted from Ref.<sup>131</sup> This nail consists of a hollow shaft with a thermocouple attached to the copper tip. **b**, The smart nail connected to an Enerpac PER1301B hydraulic pump used to control the penetrations. The pouch cells tested are fastened beneath the nail while attached to a voltmeter to monitor cell voltage.

## Chapter 4: Anode-Free Cells with NMC532 Positive Electrodes

There have been many efforts to mitigate and overcome the failure modes of the lithium metal anode outlined in **Figure 2.5**. Some examples of this work include developing an artificial SEI,<sup>132–134</sup> implementing current collector modifications,<sup>104,135,136</sup> improving electrolyte design,<sup>47,66,87,91,103</sup> and applying mechanical pressure.<sup>81,137,138</sup> In this section, we describe our work improving the performance of anode-free cells with NMC532 positive electrodes using the latter two strategies—electrolyte optimization and the application of mechanical pressure. The pouch cells tested here exhibit an areal capacity of about 2.5 mAh/cm<sup>2</sup>; the rest of the specifications for these cells are listed in **Table 3.1**. The other experimental conditions, temperature (40 °C), electrolyte volume/loading (0.5 mL/2.2 mL/Ah), voltage range (3.6–4.5 V), and cycling rates (C/5 D/2) are fixed to the values in parentheses unless otherwise stated. This work is a culmination of efforts that were initiated in the Dahn lab by the original anode-free team: Matthew Genovese, Rochelle Weber, and myself. Matthew Genovese was the first lab member to try LiDFOB salt; Rochelle Weber spearheaded the electrolyte analysis; the x-ray CT and ultrasonic measurements were performed by Robin White and Zhe Deng—the rest of the work is primarily my contributions. Some of this work has been previously published in Refs.<sup>44,46,49†</sup>

### 4.1 Increasing Lifetime from 1 to 100 Cycles

A summary of our progress increasing lifetime of anode-free cells from 1 to 100 cycles is shown in **Figure 4.1a**. This figure plots the volumetric stack energy density vs cycle for a

---

† A.J. Louli, M. Genovese, R. Weber, S.G. Hames, E.R. Logan, J.R. Dahn, Exploring the Impact of Mechanical Pressure on the Performance of Anode-Free Lithium Metal Cells, *J. Electrochem. Soc.* **166** (2019).

R. Weber, M. Genovese, A.J. Louli, S. Hames, C. Martin, I.G. Hill, J.R. Dahn, Long cycle life and dendrite-free lithium morphology in anode-free lithium pouch cells enabled by a dual-salt liquid electrolyte, *Nat. Energy*. **4** (2019).

A.J. Louli, A. Eldesoky, R. Weber, M. Genovese, M. Coon, J. deGooyer, Z. Deng, R.T. White, J. Lee, T. Rodgers, R. Petibon, S. Hy, S.J.H. Cheng, J.R. Dahn, Diagnosing and correcting anode-free cell failure via electrolyte and morphological analysis, *Nat. Energy*. **5** (2020) 693–702.



variety of different anode-free cells compared with an optimized lithium-ion cell (gray squares). Most often, researchers report cycling performance by plotting capacity or normalized capacity vs cycle. However, in our case where the goal is to develop cells with increased energy density, plotting stack energy density gives us an easily visualized benchmark. We want to deliver a higher energy density than lithium-ion cells for as long as possible. Moreover, plotting energy density incorporates effects of voltage fade and irreversible capacity which can otherwise be obfuscated by only plotting capacity or normalized capacity.

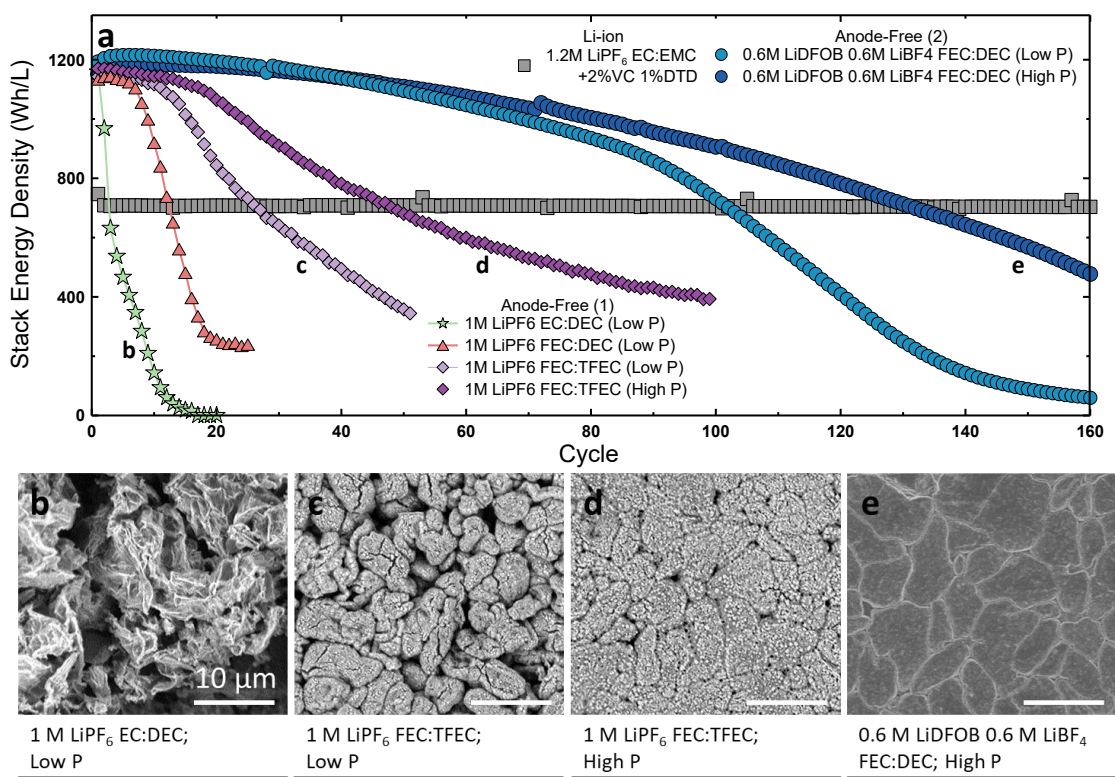


**Figure 4.1 | Increasing lifetime of anode-free cells.** **a**, Stack volumetric energy density vs cycle of anode-free cells compared to an optimized Li-ion cell. Cells were tested using different electrolytes as listed in the legends; the data labeled b-e correspond to the respective SEM images in the panels below. **b-e**, SEM images of the initial lithium morphology after a single charge extracted from cells with different electrolytes and cycled under different pressure. Anode-free cells were tested under low pressure (Low P, 200 kPa) and high pressure (High P, 1200 kPa) and cycled between 3.6-4.5 V at C/5 D/2 and 40 °C. The Li-ion cell was cycled between 3.0-4.3 V at C/3 D/3 and 40 °C and contained the same NMC532 positive electrode as the anode-free cell. Lithium samples retrieved from anode-free cells charged to 4.5 V at 40 °C. The scale bars are 10 μm.

**Figure 4.1a** shows that the lithium-ion benchmark to beat is  $\sim 700$  Wh/L. NMC532 anode-free cells initially deliver an energy density of  $\sim 1200$  Wh/L. However, as discussed in Chapter 2, the cycle life of anode-free cells is typically very short due to the rapid degradation of the lithium anode. Using a conventional Li-ion electrolyte formulation, 1 M LiPF<sub>6</sub> EC:DEC, anode-free cells can only deliver an energy density greater than Li-ion for a couple of cycles before plummeting below 700 Wh/L (**Figure 4.1a**, green stars). This rapid failure can be attributed to the mossy and highly porous lithium morphology formed in this primitive electrolyte system, shown in **Figure 4.1b**. The lithium morphology and resulting cell lifetime can be significantly impacted by the formulation of the electrolyte.<sup>66</sup> Fluoroethylene carbonate (FEC), the fluorinated analog of ethylene carbonate (EC), has proven valuable in stabilizing silicon negative electrodes which suffer from similar failure mechanisms as lithium metal cells.<sup>19</sup> When EC is replaced with FEC in the electrolyte, anode-free lifetime is extended from 2 cycles to 15 cycles (**Figure 4.1a**, red triangles). It has been suggested that fluorinated decomposition products (such as LiF) are useful in a more robust SEI.<sup>94,96</sup> To this end, further fluorinating the electrolyte solvent by replacing diethyl carbonate (DEC) with its fluorinated analog bis(2,2,2-trifluoroethyl) carbonate (TFEC) extends lifetime to 25 cycles (**Figure 4.1a**, light purple diamonds). This is attributed to the superior nodular lithium morphology enabled by this electrolyte, shown in **Figure 4.1c**.

Increased mechanical pressure can improve lithium morphology by mechanically constraining lithium growth and promoting lateral densification over the creation of lithium protrusions.<sup>85</sup> The use of mechanical pressure to physically thwart the formation of dendrites has been known for 30 years.<sup>81</sup> In this work, we applied various mechanical pressures to our pouch cells via the mechanical enclosures depicted in **Figure 3.3**. Here, we distinguish between “low” and “high” pressure; cells cycled in normal boats (**Figure 3.3a**) under  $\sim 200$  kPa are labeled “low pressure”, and cells cycled in superboats (**Figure 3.3b**) and airboats (**Figure 3.3c**) under  $\sim 1200$  kPa are labelled “high pressure”. Anode-free cells with the same electrolyte (1 M LiPF<sub>6</sub> FEC:TFEC) cycled under a higher mechanical pressure exhibit a 20 cycle increased lifetime, going from 25 to 45 cycles (**Figure 4.1a**,

light vs dark purple diamonds). Again, this is attributed to the superior lithium morphology shown in **Figure 4.1d** to be more compact lithium nodules.

Improvements to the electrolyte can also be made by changing the lithium salt.<sup>66</sup> Our most significant improvement to the longevity of anode-free cells to date was achieved by replacing the  $\text{LiPF}_6$  salt with a dual-salt combination of  $\text{LiDFOB/LiBF}_4$ . Under low pressure, this dual-salt electrolyte extends lifetime to 100 cycles (**Figure 4.1a**, light blue circles). Under higher pressure, the lifetime is further extended to 130 cycles (**Figure 4.1a**, dark blue circles). Again, the cycle life can be correlated to the lithium morphology. **Figure 4.1e** shows that anode-free cells with this dual-salt electrolyte constrained under high pressure form the most ideal lithium microstructure yet: a flat surface of highly compact lithium nodules. At the time of this discovery and resulting publication of Ref,<sup>46</sup> the lithium morphology and anode-free cycle life enabled by this  $\text{LiDFOB/LiBF}_4$  dual-salt electrolyte was—as far as this author is aware—the best that had been achieved in the literature to date. A comparison of different lithium morphologies previously reported in the literature is shown in **Figure A.1**.

**Figure 4.1** is an overview of the developmental highlights showcasing the significant steps we made along the way increasing the lifetime of anode-free cells with liquid electrolytes beyond 100 cycles. The following sections will detail more of the intermediary steps optimizing the applied pressure and electrolyte formulations.

#### 4.1.1 Mechanical Pressure

**Figure 4.1** showed a simplified picture of using either low (200 kPa) or high (1200 kPa) pressure to cycle cells. However, several pressures were tested before determining that 1200 kPa was a sufficiently “high” pressure to cycle at. The lowest pressures were achieved with the normal boat (NB) testing fixture shown in **Figure 3.3a**. The pressure applied in this fixture depends on how many aluminum shims are inserted along with the cell and rubber blocks. A soft clamping may result in a pressure of 75 kPa whereas forcing as many shims in as possible can increase the pressure to around 200 kPa. Since it was known that higher pressure improves lithium cyclability, we endeavoured to clamp cells in normal

boats to as high pressure as possible, aiming for the high end of 200 kPa. These pressures were measured via a load cell as described in the experimental section. Unlike operando pressure measurements performed in superboats, these were one-time measurements to validate the initial pressure in a normal boat. Operando measurements were not performed in normal boats since the pressure during cycling was not expected to significantly change due to the compliant nature of the testing fixtures. Therefore, the average pressure during cycling in a normal boat is the same as the initial clamping pressure.

In contrast, the pressure applied to cells constrained in the rigid superboat fixtures (**Figure 3.3b**) does not remain constant. Cells were initially constrained before cycling in their least voluminous state—with all lithium originally stored in the positive electrode. The pressure at this point is referred to as the pressure at the bottom of discharge (BOD). As lithium is plated during cell charging, the cell stack expands in thickness, pushing against the superboat wall thereby increasing the uniaxial pressure to some maximum, referred to as the pressure at the top of charge (TOC). Then on discharge, the plated lithium is stripped and returned to the cathode, decreasing the stack thickness and pressure. Therefore, an average pressure during charge and discharge can be determined. Unless otherwise stated, quoted values for the pressure during cycling refers to the initial average pressure. The pressure conditions tested are listed in **Table 4.1**.

**Table 4.1:** Force and pressure loading experiments. Cells were constrained in normal boats (NB) for low pressure tests and in superboats (SB) for high pressure tests. The force at the bottom of the discharge (BOD), top of the initial charge (TOC) and the initial average pressures are listed.

Enclosure	Force at BOD		Pressure at BOD (kPa)	Pressure at TOC (kPa)	Average Pressure (kPa)
	(N)	(lbs)			
NB	120	28	200	200	<b>200</b>
SB	45	10	75	890	<b>485</b>
SB	220	50	370	1170	<b>795</b>
SB	440	100	740	1590	<b>1205</b>
SB	760	170	1260	2080	<b>1725</b>

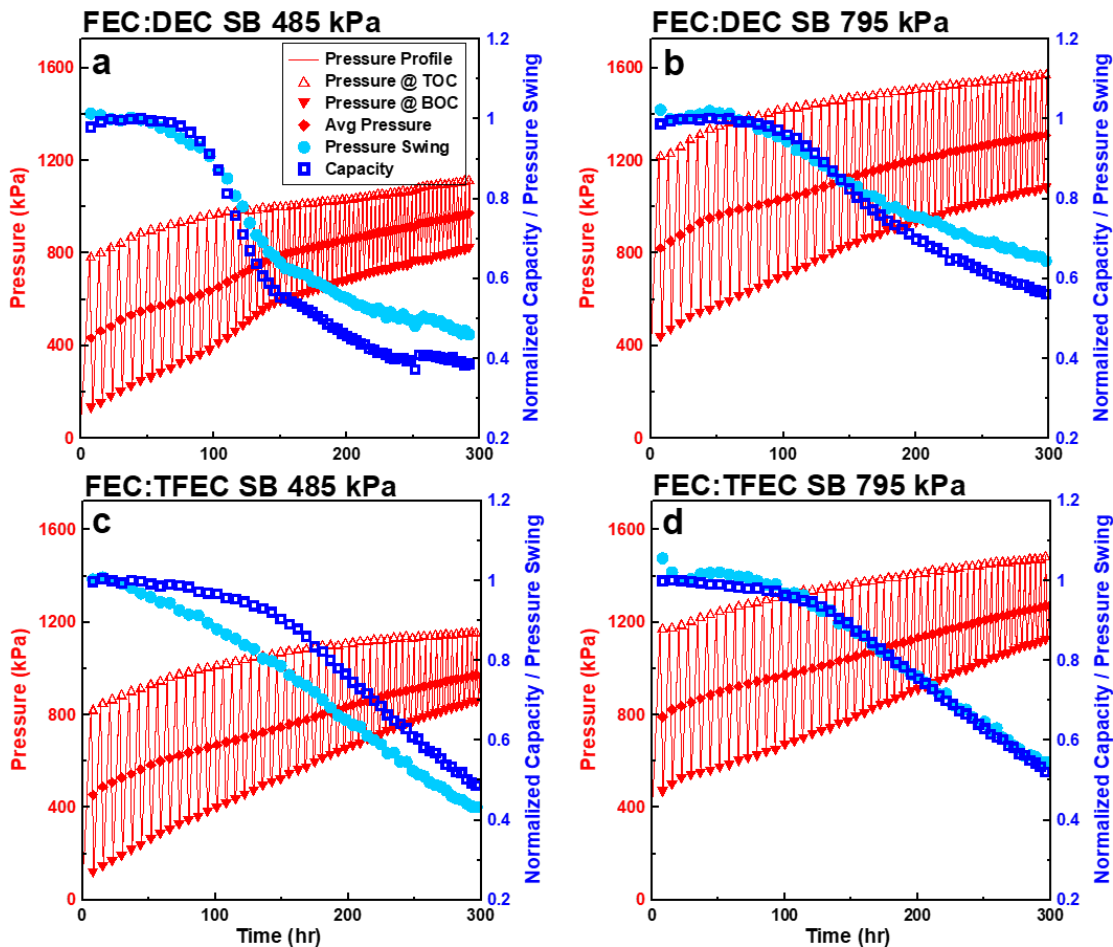


**Figure 4.2 | Operando pressure data.** a-d, Pressure data for cells containing FEC:DEC (a,b) and FEC:TFEC (c,d) electrolyte constrained at initial average pressures of 485 kPa (a,c) and 795 kPa (b,d). The pressure profile, pressure at top of charge, pressure at bottom of charge and average pressure are shown in red (left axes), and the normalized capacity and normalized pressure swing are shown in dark and light blue, respectively (right axes). Cells contained 1 M LiPF<sub>6</sub> and were cycled between 3.6-4.5 V at C/5 D/2 and 40 °C. Anode-free NMC532 cells were used.

The electrolyte used for our first pressure experiments contained 1 M LiPF<sub>6</sub> salt. Two solvent systems were tested, FEC:DEC 1:2 and FEC:TFEC 1:2 (v:v). **Figure 4.2** shows the pressure evolution and capacity retention of FEC:DEC (a,b) and FEC:TFEC cells (c,d) constrained with initial average pressures of 485 kPa (a,c) and 795 kPa (b,d). The operando pressure vs time data (red, left axes) over 100 cycles is shown for each testing condition. The pressure at the top of charge (TOC) is shown with open triangles, the pressure at the bottom of discharge (BOD) is shown with upside-down triangles, and the average pressure

is shown with diamonds. The capacity and pressure swing (the difference between the pressure at the top of charge and the pressure at the bottom of discharge) normalized to the third cycle are shown in dark and light blue, respectively (right axes).

**Figure 4.2** shows that along with the reversible volume expansion due to lithium plating and stripping, there is also an irreversible cell expansion that evolves over extended cycling. Previous works which have measured irreversible expansion in Li-metal cells<sup>81,139</sup> and Li-ion cells<sup>124,140</sup> have attributed this to SEI growth, and in the case of Li-metal cells, porous lithium morphology evolution and the formation mechanically isolated lithium. Therefore, increased irreversible expansion is an indicator of worsened cell health. The reversible volume expansion caused by lithium plating and stripping is quantified by the pressure swing. As lithium inventory is lost, less lithium will be plated and thus the pressure swing will decrease concomitant to capacity loss. **Figure 4.2** shows a good correlation between the normalized pressure swing and normalized capacity. Worse performance and cell health, indicated by pressure growth, capacity loss and decreasing pressure swing, is shown to occur at lower pressure (left panels).

**Figure 4.3** shows cycling data for cells containing FEC:DEC electrolyte (a,c) and FEC:TFEC electrolyte (b,d). Normalized capacity vs cycle is shown in the top panels (a,b) and  $\Delta V$  ( $\Delta V$ ) is shown in the bottom panels (c,d). Tests at different pressures are denoted by the symbols as indicated by the legend; repeat tests are plotted with open symbols. **Figure 4.3a,b** demonstrate the impact of applied pressure between 200-2205 kPa on capacity retention. The most significant improvement to lifetime is achieved in the transition from cycling under low pressure in the compliant normal boat fixture at 200 kPa to cycling in the superboat fixture at 485 kPa. Further increasing the initial average pressure > 485 kPa benefits FEC:DEC cells more significantly than cells containing FEC:TFEC electrolyte. Capacity retention over 100 cycles is improved for FEC:DEC cells by increasing the initial average pressure up to 1725 kPa, whereas the benefit for FEC:TFEC cells saturates at a lower pressure of 795 kPa. As shown in **Figure 4.1**, the benefit of increased mechanical pressure can be attributed to the benefit to the lithium morphology, as constrained lithium will more readily compact laterally than expand in mossy vertical

deposits. This behaviour is also demonstrated in Appendix **Figure A.2** which shows SEM images of plated lithium after 1 charge and 50 cycles for cells cycled at 200 and 485 kPa in FEC:DEC and FEC:TfEC electrolyte.

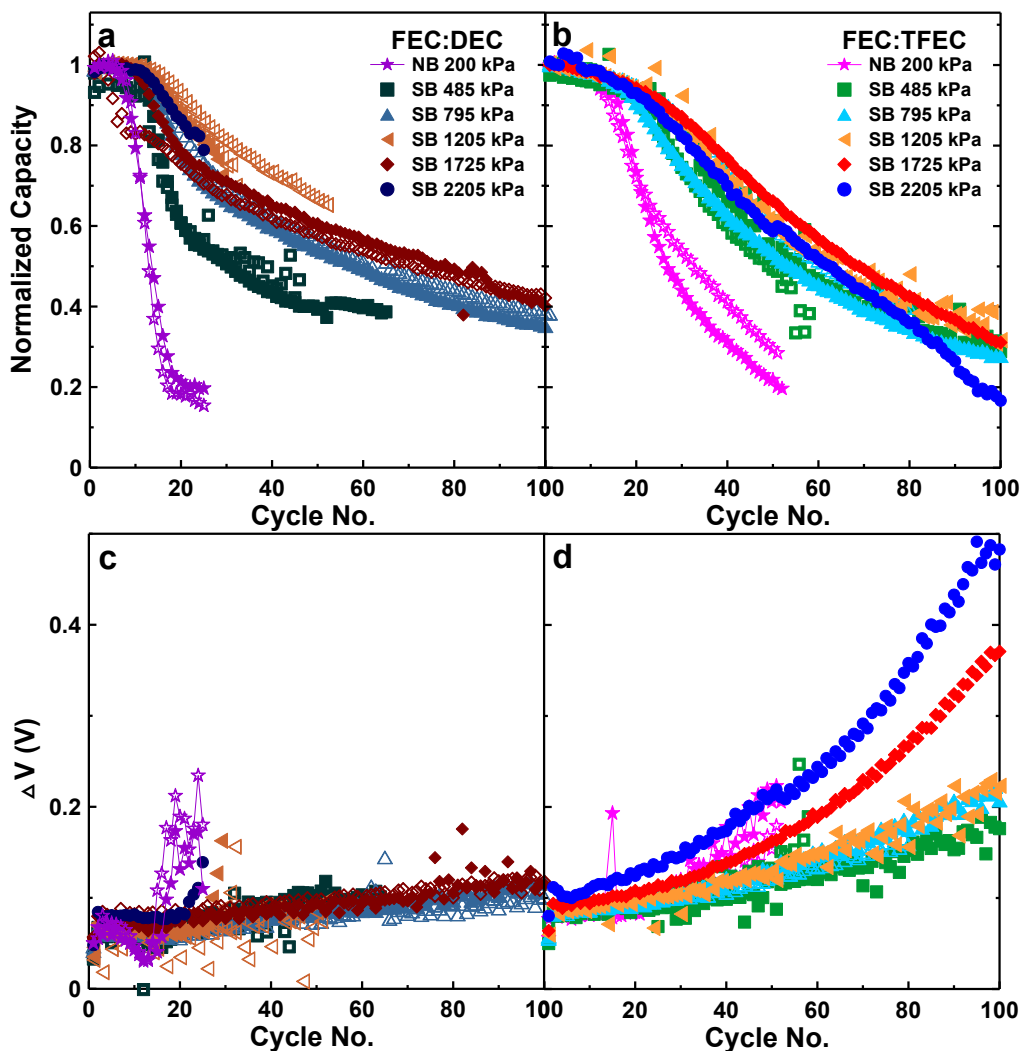


**Figure 4.3 | Pressure test. a-d,** Cycling data for cells containing FEC:DEC (a,c) and FEC:TfEC electrolyte (b,d) constrained under different pressures between 200-2205 kPa. Normalized capacity vs cycle is shown in the top panels (a,b) and delta V ( $\Delta V$ ) vs cycle is shown in the bottom panels (c,d). Cells contained 1 M LiPF<sub>6</sub> salt and were cycled between 3.6-4.5 V at C/5 D/2 and 40°C. Anode-free NMC532 cells were used.

**Figure 4.3c,d** show the effect of pressure on  $\Delta V$  growth. Increasing the average pressure has negligible effect on cells containing FEC:DEC electrolyte; for each pressure, the  $\Delta V$

growth was only about 50 mV over 100 cycles, except in the low pressure normal boat test which experienced rapid failure over just 20 cycles. In contrast, applied pressure had a significant impact on  $\Delta V$  for FEC:TFEC cells. The initial  $\Delta V$  of FEC:TFEC cells was about 30 mV higher than FEC:DEC cells. Moreover,  $\Delta V$  growth appears non-linear for FEC:TFEC cells. For cells constrained up to an initial average pressure of 1205 kPa, the polarization growth was about 110 mV over 100 cycles.  $\Delta V$  was more significantly affected at higher pressures, with a 270 mV and 380 mV growth for cells constrained at 1725 kPa and 2205 kPa, respectively. It is also observed that the initial  $\Delta V$  for FEC:TFEC cells increases as a function of pressure. This contrast of polarization response to applied pressure suggests both an electrochemical and a physical difference exists between these two solvent systems. This was investigated by measuring the ionic conductivity of each electrolyte as a function of temperature, shown in **Figure A.3**. At 40 °C, the temperature at which cells were cycled for these experiments, 1 M LiPF<sub>6</sub> FEC:TFEC electrolyte has a conductivity of 3.9 mS/cm compared to 9.2 mS/cm for 1 M LiPF<sub>6</sub> FEC:DEC electrolyte. The particularly low conductivity of FEC:TFEC coupled with high applied pressure is likely the cause of large  $\Delta V$  growth observed here. This may be due to impeded ionic transport through the separator at high pressure; however, this hypothesis requires further investigation.

**Figure 4.3** reaffirms the well-established benefit of increased mechanical pressure to lithium cyclability. The pouch cells tested in this work show that the benefit of increasing mechanical pressure saturates somewhere between 500-1200 kPa, and that further increasing the pressure beyond 1700 kPa can begin to have negative repercussions, possibly due to impeding ionic transport through the separator. It is somewhat lucky that this saturation pressure is relatively low since higher applied pressures would be more difficult to achieve under practical conditions.

Pressure tests were also performed on cells with the successful 0.6 M LiDFOB 0.6 M LiBF<sub>4</sub> electrolyte, shown in **Figure 4.4**. **Figure 4.4a** shows the capacity retention of cells constrained to different initial average pressures in superboats with load cells for operando pressure measurements (green squares) along with data for cells cycled at low pressure in



normal boats (200 kPa, blue circles) and cells constrained at high pressure in airboats (red diamonds). The average pressure vs cycle of the operando pressure measurements is shown in **Figure 4.4b**, and the pressure vs time signal recorded for a cell constrained to 1172 kPa is shown in **Figure 4.4d**. At an even lower pressure than cycling in normal boats, the cells constrained to just 7 kPa perform the worse, as one would expect. We again see the saturation of the benefit of increased pressure as cells constrained to 241 and 793 kPa exhibit a significantly improved performance compared to 7 kPa, but negligible difference between each other. The 241 and 793 kPa tests exhibit slightly better performance than “low pressure cells” constrained in normal boats. At 1171 kPa, the cell performance tracked the best performance observed from cells constrained in airboats.

To determine the stack pressure applied in the airboat fixture, a cell was cycled in this fixture with pieces of pressure paper placed between the jelly roll and the clamp face. The activated pressure paper after cycling is pictured in **Figure 4.4c**. Pressure paper that activates at 600 kPa (top) and another that saturates at 1500 kPa (bottom) were used. The 600 kPa capacity pressure paper was completely saturated, while the 1500 kPa pressure paper was only partially activated after the test. We therefore conclude that the average pressure should be between 600-1500 kPa. This, along with the fact that the cycling data for cells constrained to 1171 kPa in **Figure 4.4a** track the cells cycled in airboats, indicates that the average pressure exerted by airboats is around 1200 kPa. Although this is more of an estimation than a direct measurement, we see that the absolute value of pressure is not critical, just so long that “enough” pressure is applied above the saturation limit that benefits performance. This is clearly achieved in for cells cycled in airboats. Therefore, for the rest of this thesis, we will go back to the simplified nomenclature of cycling either at “low pressure”, corresponding to ~200 kPa in a normal boat, or cycling at “high pressure”, corresponding to ~1200 kPa in an airboat.

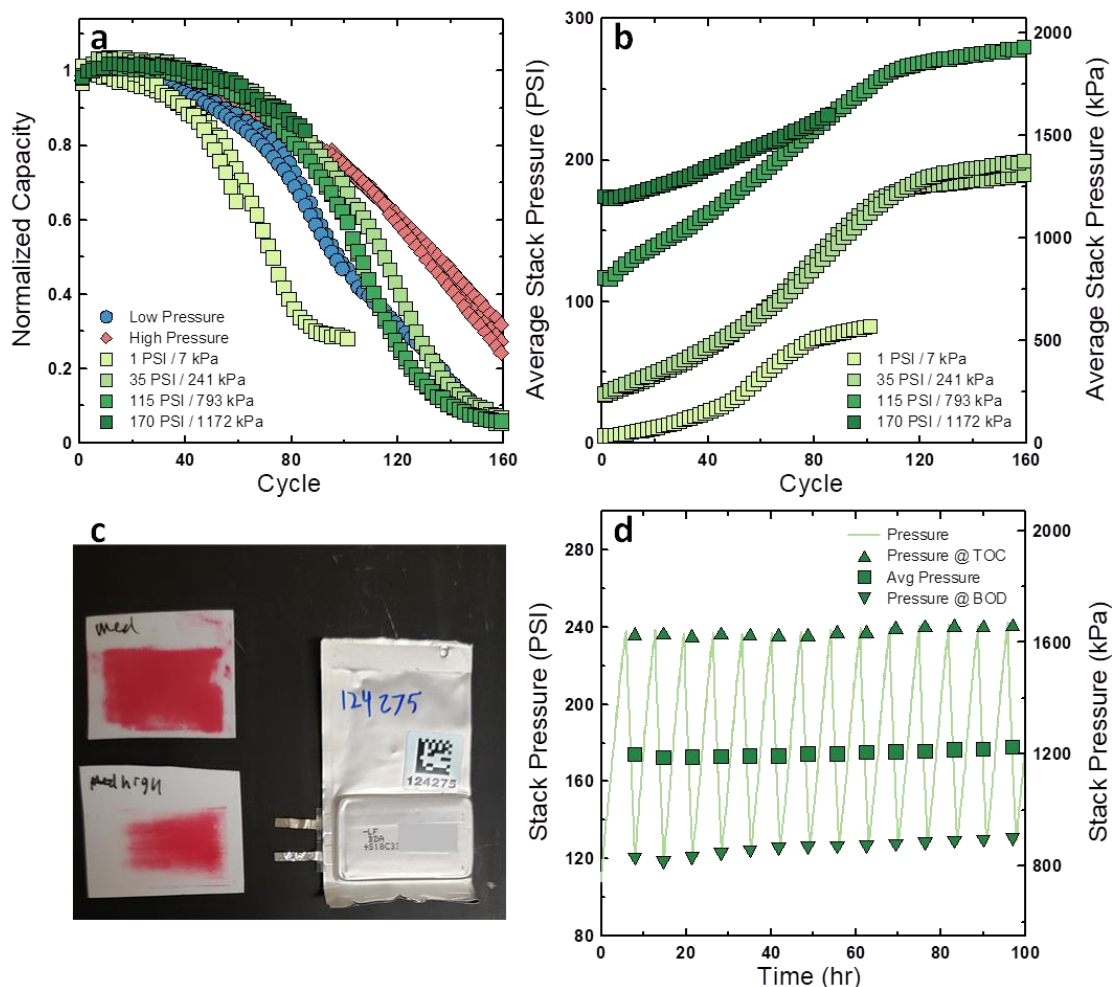


**Figure 4.4 | Dual-salt pressure test.** **a**, Capacity retention of cells constrained under different pressures and testing fixtures (low pressure = 200 kPa in a NB, high pressure ~1200 kPa in an AB). **b**, Average stack pressure of cells cycled superboats for operando pressure measurements. **c**, Picture of activated 600 kPa (top) and 1500 kPa (bottom) pressure paper that had been constrained with the adjacent pouch cell in an airboat. **d**, Stack pressure vs time of a cell cycled in a superboat with a load cell. Cells contained 0.6 M LiDFOB 0.6 M LiBF<sub>4</sub> FEC:DEC 1:2 electrolyte and were cycled between 3.6-4.5 V at C/5 D/2 and 40°C. Anode-free NMC532 cells were used.

#### 4.1.2 Electrolyte Formulation

**Figure 4.1** showed that fluorinating the electrolyte solvent—swapping the ethylene carbonate (EC) for its fluorinated analog fluoroethylene carbonate (FEC)—improved performance. This has previously been attributed to the introduction of fluorinated decomposition products to the SEI, such as LiF, which have been suggested to improve

lithium cyclability.<sup>94,96</sup> Another proposed mechanism explaining the positive role of FEC is the formation of CO<sub>2</sub>. FEC can decompose to form CO<sub>2</sub>,<sup>97,141</sup> and CO<sub>2</sub> has been shown to improve negative electrode passivation.<sup>142–144</sup> Therefore, the introduction of CO<sub>2</sub> via solvent decomposition likely also contributes to the benefit of FEC. To investigate the benefit of CO<sub>2</sub> to cells with and without FEC-based electrolytes, we used dry ice pellets to introduce CO<sub>2</sub> to pouch cells. **Figure 4.5a** pictures a collection of dry ice pellets; pellets around the size of the pellet circled in red (a few mm in diameter) were inserted into the gas bag of a pouch cell before sealing. This resulted in approximately 2.8 mL of CO<sub>2</sub> gas introduced to a pouch cell, shown on the left of **Figure 4.5b**, as measured by Archimedes principle.

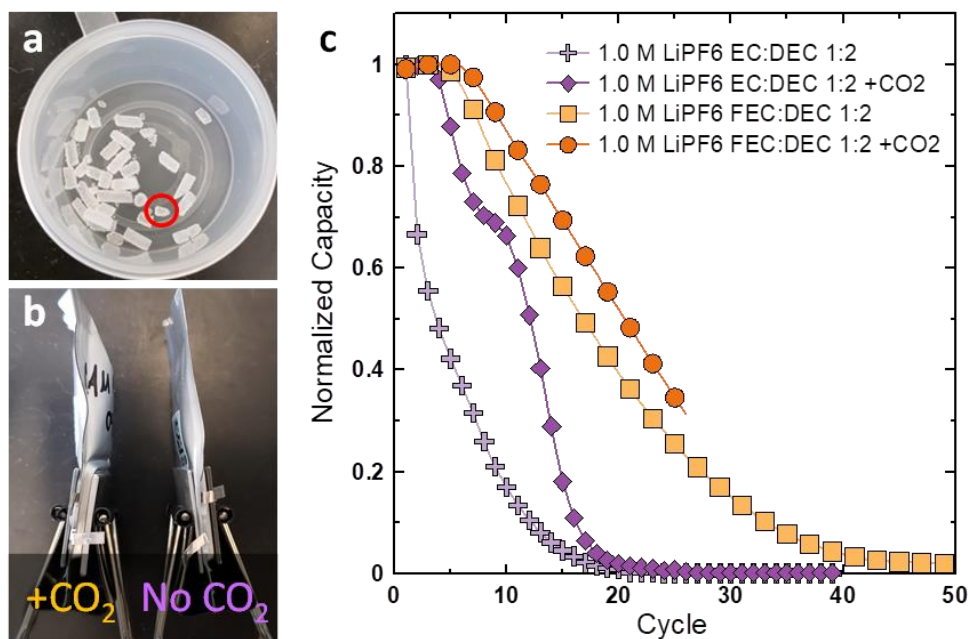


**Figure 4.5 | Effect of CO<sub>2</sub>.** **a**, Dry ice pellets used to introduce CO<sub>2</sub> to pouch cells. **b**, Pouch cell with added CO<sub>2</sub> (left) and without added CO<sub>2</sub> (right). CO<sub>2</sub> was added by dropping a dry ice pellet into the gas bag before sealing the pouch cells. Approximately 2.8 mL of CO<sub>2</sub> was introduced with this method. **c**, Normalized capacity vs cycle for cells with and without added CO<sub>2</sub>. Data for cells with EC:DEC and FEC:DEC electrolyte are shown in purple and orange, respectively. Cells contained 1.0 M LiPF<sub>6</sub> salt and were cycled under low pressure between 3.6–4.5 V at C/5 D/2 and 40°C. Anode-free NMC532 cells were used.

**Figure 4.5c** shows the effect of the addition of CO<sub>2</sub> to cycled anode-free pouch cells. First, EC:DEC electrolyte with no FEC, and therefore no source of CO<sub>2</sub>, was tested (purple data points). Cells with EC:DEC electrolyte without added CO<sub>2</sub> rapidly failed, losing over 30% capacity during the first cycle. The addition of CO<sub>2</sub> to cells with this primitive EC:DEC solvent system improved performance as expected, demonstrating the benefit of CO<sub>2</sub>. This is compared to cells tested with FEC:DEC electrolyte (orange data points). As previously discussed, cells with FEC produce CO<sub>2</sub> *in-situ*. FEC:DEC cells without added CO<sub>2</sub> performed similarly to EC:DEC + CO<sub>2</sub> cells over the first 15 cycles. After 15 cycles, the FEC:DEC cells pull away, maintaining a superior capacity retention compared to the EC:DEC + CO<sub>2</sub> cells. This indicates that the benefit of including FEC in the electrolyte cannot solely be attributed to the introduction of CO<sub>2</sub>—further benefit to the SEI is achieved through the introduction of fluorinated decomposition products. Finally, FEC:DEC cells with added CO<sub>2</sub> were tested. The addition of CO<sub>2</sub> to FEC:DEC cells has a small impact on performance compared to FEC:DEC cells without added CO<sub>2</sub>. This is likely because cells with FEC:DEC electrolyte produce their own CO<sub>2</sub>, and increasing the CO<sub>2</sub> content does not provide further benefit. **Figure 4.5c** shows that CO<sub>2</sub> certainly benefits the performance of anode-free cells, and that the beneficial introduction of CO<sub>2</sub> can be achieved by selecting the right solvent system. Therefore, moving forward, FEC-containing solvents systems were used for most experiments.

**Figure 4.6** explores the effect of increasing the concentration of LiPF<sub>6</sub> lithium salt as well as increasing the volume of electrolyte used in pouch cells. The solvent system used for these experiments was FEC:DEC 1:2 (v:v). **Figure 4.6a** shows the impact of increasing the concentration of LiPF<sub>6</sub> from 1.0-3.0 M. A slight improvement from increasing the LiPF<sub>6</sub> concentration is observed, increasing lifetime from 20 cycles to 80% capacity retention using 1.0 M LiPF<sub>6</sub> to 30 cycles to 80% capacity retention using 3.0 M LiPF<sub>6</sub>.

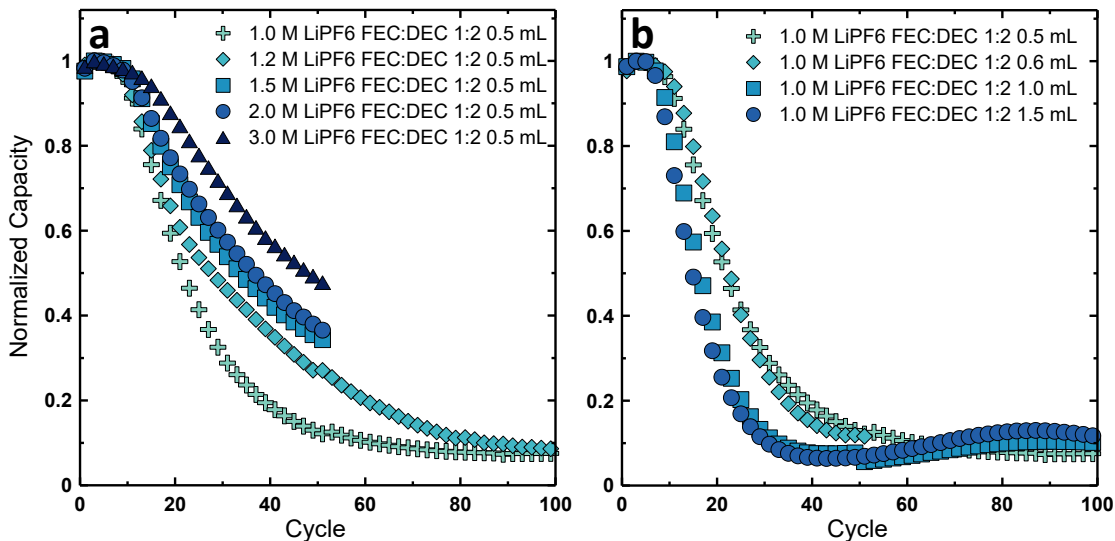


**Figure 4.6 | LiPF<sub>6</sub> concentration and volume. a-b,** Normalized capacity vs cycle of anode-free cells tested with different concentrations (a) and different volumes (b) of LiPF<sub>6</sub> FEC:DEC 1:2 electrolyte. Cells were cycled under low pressure between 3.6-4.5 V at C/5 D/2 and 40°C. Anode-free NMC532 cells were used.

**Figure 4.6b** shows results for different volumes of 1.0 M LiPF<sub>6</sub> FEC:DEC 1:2 electrolyte that were tested. The typical volume of electrolyte used in pouch cells in this work is 0.5 mL (2.2 mL/Ah). We tested increased volumes of 0.6, 1.0, and 1.5 mL and observed no significant benefit from this increased electrolyte volume. This behaviour gives some insight to the failure mode of this electrolyte system. Some electrolyte systems paired with a lithium metal anode have exhibited electrolyte consumption during cycling.<sup>69</sup> In those cases, increased electrolyte volume improves performance since there is more electrolyte that can be consumed before depletion. The behaviour shown in **Figure 4.6b** indicates that electrolyte consumption is not a mode of failure of this electrolyte system. Another potential benefit of increased electrolyte volume is improved electrolyte wetting throughout a mossy lithium morphology. As lithium is cycled and its porosity is increased, more lithium surface area that must be wet with electrolyte is generated. Even if there is no electrolyte depletion, as the lithium porosity increases, the original volume of electrolyte used in the cell may become insufficient to wet the increased lithium surface area, resulting in electrolyte dry-out and poor lithium transport. The lithium morphology formed in this electrolyte system certainly becomes more porous during cycling, shown in **Figure A.2**.

Therefore, one would expect increased electrolyte volume to improve lithium transport as the lithium microstructure deteriorates. However, **Figure 4.6b** shows this is not the case. This indicates that the porous lithium morphology which forms in this electrolyte system has likely become mechanically disconnected, and that the extra electrolyte volume does not improve lithium transport since the lithium is no longer electrochemically active. In other words, the capacity loss observed in **Figure 4.6b** is likely a result of lithium inventory loss due to the mechanical isolation of lithium, and increased electrolyte volume does not mitigate this mode of failure. Moving forward, the electrolyte volume used in experiments will always be 0.5 mL unless explicitly states otherwise.

So far, most of the electrolyte formulations discussed here have used a conventional  $\text{LiPF}_6$  salt. However, there are many different lithium salts to choose from. Many of these salts have been previously tested in the literature to varying degrees of success.<sup>66,145</sup> Therefore, we set out to test these different lithium salts in our anode-free pouch cells. In particular, we looked at  $\text{LiDFOB}$  and  $\text{LiBF}_4$  salts, as well as dual- and tri- salt combinations with  $\text{LiPF}_6$ . This was the basis of our publication Ref.<sup>46</sup> and the highly successful dual-salt  $\text{LiDFOB}/\text{LiBF}_4$  electrolyte formulation shown in **Figure 4.1**. In Ref.<sup>46</sup>, we showed cells with  $\text{LiDFOB}$  salt (80 cycles to 80%) performed significantly better than cells using  $\text{LiBF}_4$  (10 cycles to 80%) and  $\text{LiPF}_6$  (20 cycles to 80%) in a FEC:DEC 1:2 solvent blend. However,  $\text{LiDFOB}$  electrolyte performed worse when tested at lower voltage ( $< 4.5$  V). The dual-salt combination of 0.6 M  $\text{LiDFOB}$  0.6 M  $\text{LiBF}_4$  overcame this voltage-dependence, facilitating the same cycle life when tested to 4.5, 4.3, or 4.2 V. Dual-salt combinations of  $\text{LiDFOB}/\text{LiPF}_6$  and tri-salt combinations containing  $\text{LiDFOB}/\text{LiBF}_4/\text{LiPF}_6$  all performed worse than the  $\text{LiDFOB}/\text{LiBF}_4$  dual-salt formulation.

For optimizing the  $\text{LiDFOB}/\text{LiBF}_4$  dual-salt electrolyte, we tested different solvent blends. We tried different blends of cyclic carbonates (EC, FEC, PC) as well as blends of linear carbonates (DEC, EMC, TFEC) shown in **Figure 4.7**. Swapping out or diluting the FEC component with EC and PC decreased cycle life, with the FEC-free formulation of EC:DEC performing the worst. Swapping out or diluting the DEC component with EMC or TFEC did not significantly impact performance compared to the standard FEC:DEC

formulation. Additional solvent experiments testing the performance of different ethers combined with 0.6 M LiDFOB 0.6 M LiBF<sub>4</sub> were performed to no success—these results are shown in **Figure A.4**.

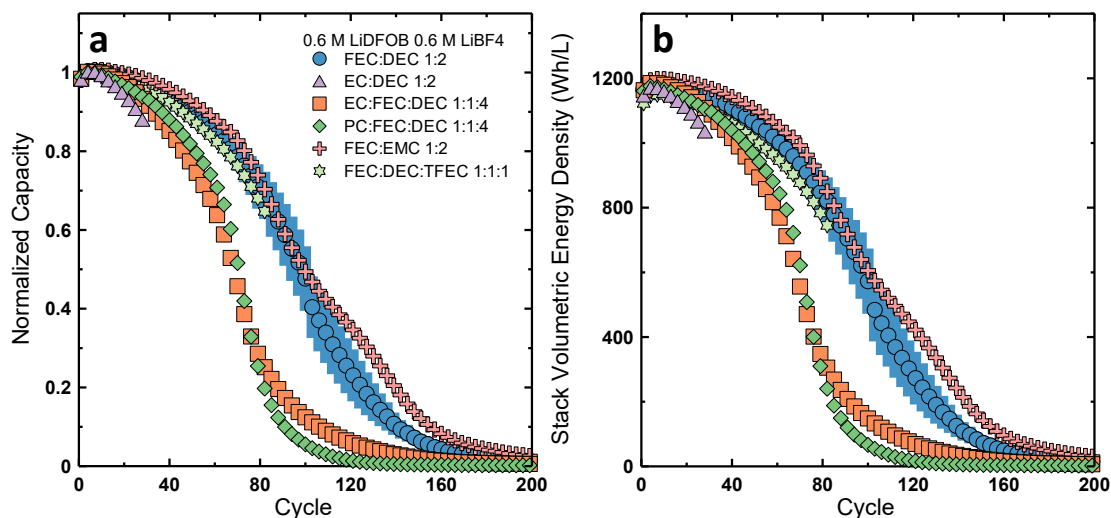


**Figure 4.7 | Dual-salt solvent test. a-b,** Normalized capacity (a) and stack volumetric energy density (b) vs cycle of anode-free cells with 0.6 M LiDFOB 0.6 M LiBF<sub>4</sub> tested with different solvent blends. Cells were cycled under low pressure between 3.6-4.5 V at C/5 D/2 and 40 °C. Anode-free NMC532 cells were used. The average of at least two cells are shown here; the error bars are calculated as the standard deviation.

We have also evaluated other promising electrolytes promoted in the literature in our anode-free pouch cells. **Figure 4.8** shows several different electrolyte systems compared against our control 0.6 M LiDFOB 0.6 M LiBF<sub>4</sub> dual-salt electrolyte. The electrolytes we have tested so far have been primarily carbonate-based (fluoroethylene carbonate, dimethyl carbonate, *etc.*). Ether-based solvents (1,2-dimethoxyethane, DME) using LiFSI and LiTFSI salts have demonstrated good compatibility with lithium metal.<sup>99,100</sup> Researchers at Pacific Northwest National Laboratory have developed a class of electrolyte systems they refer to as localized high concentration (LHC) electrolytes which employ a solvent blend that only partially solvates the salt, thereby effectively increasing the concentration. These electrolytes use a conventional solvent (DME) to solvate the lithium salt mixed with a diluent (TTE, BTFE).<sup>47,103</sup> Another research group at Stanford has developed an electrolyte based on a solvent they synthesized which they call FDMB.<sup>48</sup>

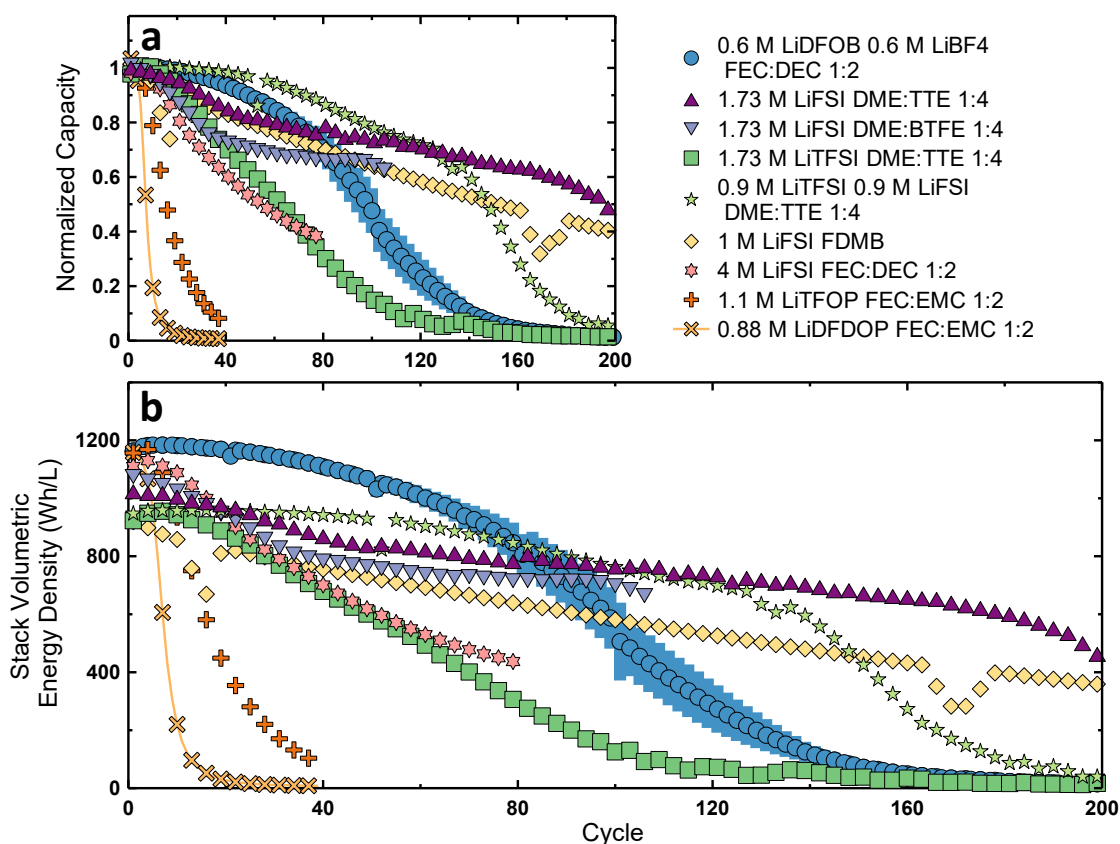


**Figure 4.8 | Electrolyte evaluation. a-b**, Normalized capacity (a) and stack volumetric energy density (b) vs cycle of anode-free cells with various electrolyte formulations from the literature. Cells were cycled under low pressure between 3.6-4.5 V at C/5 D/2 and 40 °C. Anode-free NMC532 cells were used. The average of at least two cells are shown here; the error bars are calculated as the standard deviation.

**Figure 4.8** shows that most of these ether-based electrolytes, including the LHC electrolytes (1.73 M LiFSI in DME:TTE 1:4 and DME:BTFE; 0.9 M LiTFSI 0.9 M LiFSI DME:TTE 1:4) and the FDMB electrolyte (1 M LiFSI FDMB) cycle quite well. These systems exhibit a superior normalized capacity retention compared with our LiDFOB/LiBF<sub>4</sub> electrolyte. However, these systems deliver a lower stack volumetric energy density than LiDFOB/LiBF<sub>4</sub> cells (1000 vs 1200 Wh/L). This is because the reversible capacity is lowered due to worse electrolyte transport properties. This behaviour would have been otherwise obfuscated if only the normalized capacity data was considered. This demonstrates the value of plotting energy density. Regardless, even with a lower



energy density, the LHC electrolytes demonstrate stable cycling performance. However, there are safety concerns for these electrolytes which will be addressed in Section 4.3. Other less successful electrolyte systems were also tested in **Figure 4.8**. These include a LiTFSI LHC electrolyte (1.73 M LiTFSI DME:TTE 1:4), LiFSI in a carbonate solvent (4 M LiFSI FEC:DEC 1:2), and two LiDFOB-adjacent salts tested in a carbonate system (1.1 M LiTFOP FEC:EMC 1:2, 0.88 M LiDFDOP FEC:EMC 1:2). More tests evaluating less successful LHC electrolyte compositions including different solvents and diluents are shown in **Figure A.5**.

A repeated notion throughout this thesis is that anode-free lifetime is improved when denser lithium morphologies are achieved. **Figure 4.1** showed how electrolyte formulation can significantly improve lithium morphology. The role the electrolyte plays in determining the morphology of plated lithium has largely been attributed to the SEI that is formed. Since the SEI is made from the reaction products of decomposed electrolyte, the chemical composition of the SEI is directly coupled to that of the electrolyte it is formed in. Moreover, recent studies have indicated that beyond its chemical makeup, the nanostructure of the SEI plays an important role.<sup>58,94,96,146</sup> A favorable SEI should help govern uniform lithium deposition. For example, an SEI with homogeneous transport properties should discourage local non-uniform current densities and preferential lithium deposition. An SEI with a high surface energy would also discourage high surface area lithium deposition.

Although it may be easy to imagine how the SEI affects the lithium microstructure, in practice, translating this into real life deliverables is a significant challenge. Beyond identifying the compositional and structural makeup of an SEI that forms in successful cell chemistries, fundamental insight into the engineering of an SEI that facilitates optimal lithium plating has yet to be demonstrated. For example, it is hard to imagine that anyone would have predicted that the combination of LiDFOB and LiBF<sub>4</sub> salts would synergize to facilitate dense lithium plating. We are fortunate to have the facilities to be able to test many different electrolyte formulations through a combinatorial approach instead of relying on trying to predict successful chemistries. Regardless, some luck was still required

with our approach. Unbeknownst to us, the original LiDFOB salt we tested was contaminated with an equal part LiBF<sub>4</sub>, leading to the serendipitous discovery of the dual-salt synergy. The intimate connection between electrolyte, SEI, and lithium morphology will continue to drive research on electrolyte development to improve the cycle life of lithium metal cells.

## 4.2 LiDFOB/LiBF<sub>4</sub> Dual-Salt Electrolyte

The success of the dual-salt LiDFOB/LiBF<sub>4</sub> electrolyte we developed in Ref.<sup>46</sup> is very promising for anode-free cells. However, as shown in **Figure 4.1**, these cells still die. The 130 cycle lifetime enabled by dual-salt electrolyte is just not enough for practical applications. Therefore, we have made a significant effort to understand the degradation modes for anode-free cells with dual-salt electrolyte with the goal of improving this system further to achieve an even longer lifetime.

### 4.2.1 Electrochemical Analysis

A lot can be learned from even the simple electrochemical cycling data that is collected by any charger system such as capacity retention and delta V (**Figure 4.9a,b**) and even more insight is gained from high precision coulometry measurements (*CE* and charge endpoint slippage, **Figure 4.9c,d**). **Figure 4.9a** and **b** show that the normalized capacity loss closely mirrors the increase in delta V. Delta V ( $\Delta V$ ) is defined as the difference between average charge ( $V_c$ ) and discharge ( $V_d$ ) voltage,

$$\begin{aligned}V_c &= V_{ocv} + IR \\V_d &= V_{ocv} - IR \\ \Delta V &= V_c - V_d = 2IR\end{aligned}$$

where  $V_{ocv}$  is the equilibrium open circuit voltage,  $I$  is the current, and  $R$  is the internal cell resistance.

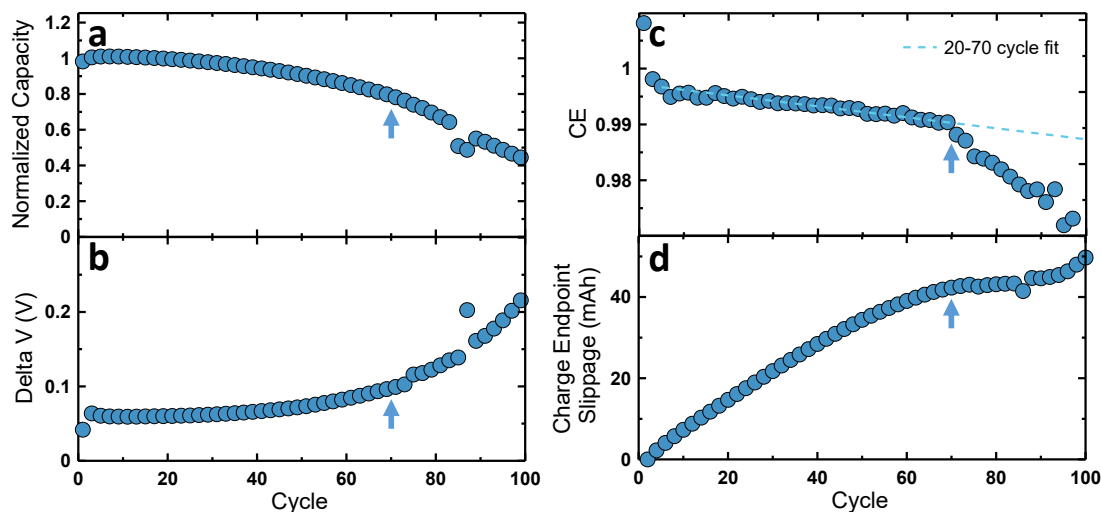


**Figure 4.9 | Dual-salt electrochemical analysis.** **a-d**, Normalized capacity (a), delta V (b), coulombic efficiency (CE, c), and charge endpoint slippage (d) vs cycle of anode-free cells with 0.6 M LiDFOB 0.6 M LiBF<sub>4</sub> FEC:DEC 1:2 electrolyte. Arrows pointing at cycle 70 of the data have been included to guide the eye. A linear fit of the CE between cycle 20-70 is plotted on top of the CE data. Cells were cycled under low pressure between 3.6-4.5 V at C/5 D/2 and 40 °C. Anode-free NMC532 cells were used.

Since  $\Delta V$  is proportional to the internal resistance,  $R$ ,  $\Delta V$  is a measure of cell resistance. Therefore, **Figure 4.9b** indicates that increasing cell resistance plays a significant role in cell degradation. **Figure 4.9c** shows the coulombic efficiency ( $CE$ ).  $CE$  is defined as the ratio between discharge ( $Q_D$ ) and charge ( $Q_C$ ) capacity ( $CE = Q_D/Q_C$ ). If no capacity is lost, then  $Q_D = Q_C$  and  $CE = 1$ . Practically, capacity is always lost, so  $Q_D < Q_C$  and  $CE < 1$ . Obviously, the highest  $CE$  is always desired. **Figure 4.9c** shows a high but steadily decreasing  $CE$  over the first 70 cycles. After cycle 70, a sharp decline in the  $CE$  is observed. **Figure 4.9d** shows the charge endpoint capacity slippage—a measure of electrolyte oxidation. When electrolyte is oxidized,  $Li^+$  from the electrolyte is inserted into the positive electrode, resulting in a transfer of lithium inventory from the electrolyte to the cyclable lithium inventory of the positive electrode.<sup>147</sup> Oxidized  $Li^+$  can also be involved in shuttle mechanisms in which the oxidized species is then reduced at the negative electrode.<sup>148</sup> This facilitates repetitive electrolyte oxidation that contributes to the charge endpoint capacity slippage shown in **Figure 4.9d**. About 50 mAh of capacity is oxidized from the electrolyte

over 100 cycles,<sup>†</sup> but this oxidation significantly slows around cycle 70. The correlation between *CE* and charge endpoint capacity slippage indicates that when electrolyte oxidation slows down, the *CE* is not sustained, and cell performance suffers. This correlation is also present for cell cycled to only 4.3 V, but it is slightly delayed to 80 cycles (**Figure A.6**). The electrochemical data in **Figure 4.9** reveal that increased cell resistance and changes to the electrolyte are culprits in degradation of anode-free cells with LiDFOB/LiBF<sub>4</sub> electrolyte.

With cell resistance growth being a concern, electrochemical impedance (EIS) measurements were performed during cycling to quantify the contributions of impedance growth. Cells were cycled on a FRA system which performed impedance measurements every 10 cycles. **Figure 4.10a** shows the recorded Nyquist curves from every 20 cycles. Both the solution resistance (the shift from zero on the real axis, *R<sub>s</sub>*) and the charge transfer resistance (the diameter of the Nyquist curves, *R<sub>ct</sub>*) exhibit significant growth during cycling. Both parameters are plotted vs cycle in **Figure 4.10b**. The portion of the impedance spectra below zero on the imaginary *Z* axis can be attributed to an inductive component of the impedance which we do not consider here. Although both *R<sub>s</sub>* and *R<sub>ct</sub>* increase during cycling, the magnified inset in **Figure 4.10b** show that the charge transfer resistance is initially stable over the first 50 cycles, whereas the solution resistance growth is initiated from the beginning of cycling. The charge transfer resistance corresponds to the intrinsic impedance of both electrodes, whereas the solution resistance corresponds to the resistance of ionic transport through the electrolyte. The fact that the solution resistance is increasing from the beginning of cycling indicates that there is something going on with the electrolyte, in accordance with the charge endpoint slippage measurements indicating electrolyte oxidation in **Figure 4.9d**. This led us to investigate electrolyte degradation.

---

<sup>†</sup> For context, this is 50 mAh of charge endpoint capacity slippage occurs amidst 17000 mAh of lithium which is reversibly cycled over 100 cycles.

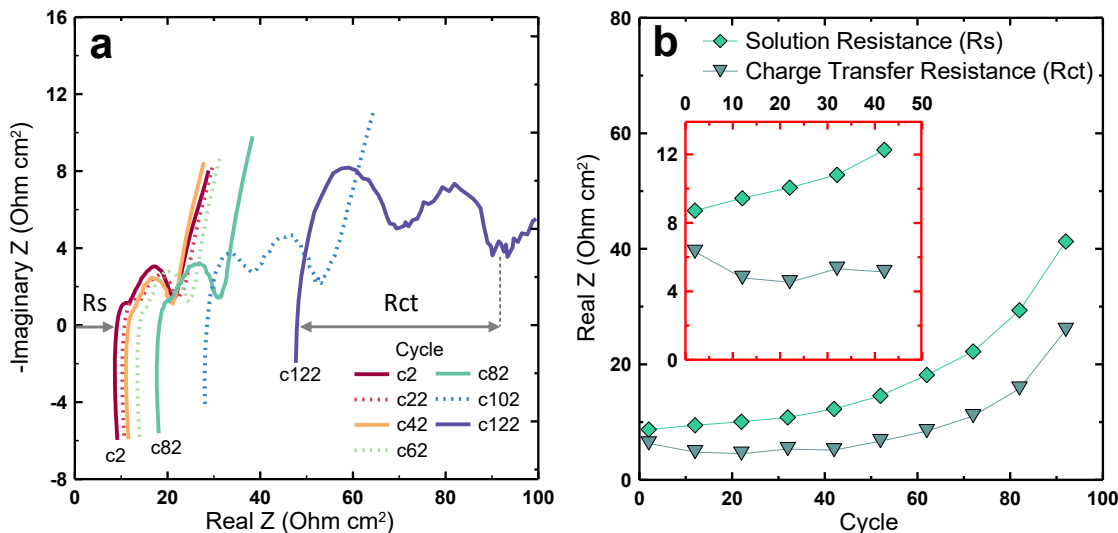


**Figure 4.10 | Dual-salt electrochemical impedance spectroscopy.** **a**, -Imaginary vs real impedance Nyquist plots measured for dual-salt cells during cycling. The shift on the real axis from zero (solution resistance,  $R_s$ ) and the diameter of the Nyquist curves (charge transfer resistance,  $R_{ct}$ ) are denoted. **b**, Solution resistance and charge transfer resistance vs cycle extracted from the Nyquist curves. The inset shows a magnified view of the first 50 cycles. Impedance values were multiplied by cell area. Cells contained 0.6 M LiDFOB 0.6 M LiBF<sub>4</sub> FEC:DEC 1:2 electrolyte and were cycled under low pressure between 3.6-4.5 V at C/5 D/2 and 40 °C. Anode-free NMC532 cells were used.

#### 4.2.2 Electrolyte Degradation

Previous studies have reported changes to the electrolyte in cycled lithium metal cells.<sup>69</sup> Constant parasitic reactions concomitant with cycling lithium metal provides a scenario ripe for electrolyte degradation—if the electrolyte is continually reacting at the lithium surface, significant changes in its chemical composition are likely to result. **Figure 4.9** and **Figure 4.10** showed strong electrochemical evidence of electrolyte degradation. To directly measure changes to the electrolyte, cells aged to various cycle numbers were disassembled and their electrolyte extracted for <sup>1</sup>H and <sup>19</sup>F liquid NMR analysis, allowing us to quantify the concentration of salt components in our dual-salt electrolyte. **Figure 4.11a** shows the change in concentration vs cycle of LiDFOB and LiBF<sub>4</sub> salts in pouch cells with dual-salt electrolyte. The concentrations of both salts decrease during cycling. The consumption of LiBF<sub>4</sub> occurs at a lower rate, and analogous experiments with cells cycled only to 4.3 V show that this behaviour is seemingly independent of voltage (**Figure**

A.7). In contrast, comparing **Figure 4.11a** with **Figure A.7** shows that LiDFOB is consumed at a higher rate for cells cycled at 4.5 V than at 4.3 V. Sometime between 50 and 80 cycles, the rate of LiDFOB consumption slows down. The evidence of electrolyte oxidation in **Figure 4.9** is consistent with the salt consumption observed here. The correlation between *CE* and charge endpoint slippage at 70 cycles appears consistent with a slowing rate of LiDFOB consumption. This suggests that the reactions involving the consumption of LiDFOB are beneficial to lithium plating efficiency; when these reactions stop, the benefit is no longer maintained, thus precipitating large charge transfer impedance, lithium inventory loss, and a lowered *CE*.

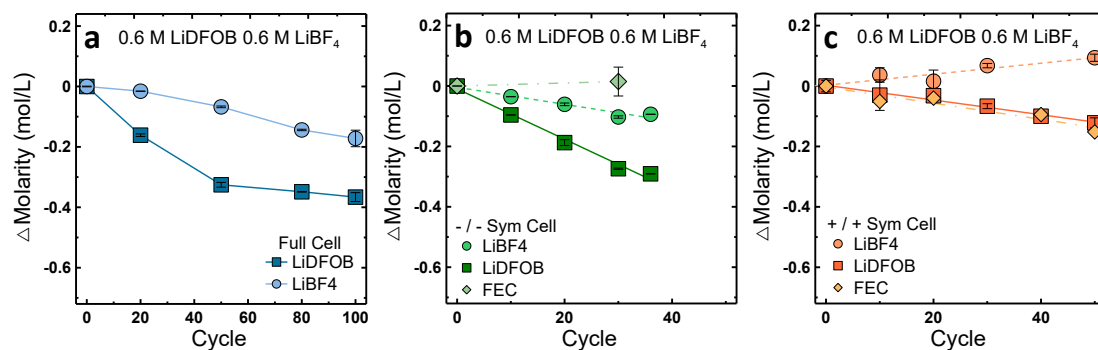


**Figure 4.11 | Electrolyte degradation.** a-c, Change in salt concentration vs cycle for anode-free NMC532 full cells (a), negative Li-Li symmetric cells (b), and positive NMC532-NMC532 symmetric cells with 0.6 M LiDFOB 0.6 M LiBF<sub>4</sub> FEC:DEC 1:2 electrolyte. The LiDFOB and LiBF<sub>4</sub> salt components are shown in each panel, as well as the FEC concentration for the symmetric cells (b,c). Cells were cycled under low pressure between 3.6-4.5 V at C/5 D/2 and 40 °C. Anode-free NMC532 cells were used. Error bars represent the range between pair cell measurements.

Both the lithium negative and NMC532 positive electrodes may participate in reactions with the electrolyte. To deconvolute the negative and positive electrode contributions to electrolyte degradation, NMR analysis was performed on electrolyte extracted from cycled symmetric cells (**Figure 4.11b-c**). The electrochemical cycling data for these symmetric cells are shown in **Figure A.8**. **Figure 4.11b** shows that both LiBF<sub>4</sub> and LiDFOB are consumed in negative symmetric cells, supporting the hypothesis that this consumption effects lithium plating. **Figure 4.11c** shows that in positive symmetric cells, LiDFOB is consumed while an approximately equal amount of LiBF<sub>4</sub> is produced. The positive

symmetric cells here were cycled to be representative of 4.5 V full cell cycling. **Figure A.9** shows data for positive symmetric cells cycled to be representative of 4.3 V cycling, and the rates of consumption and production of LiDFOB and LiBF<sub>4</sub> are less than the consumption at 4.5 V, analogous to the full cell data shown in **Figure 4.11a** and **Figure A.7**.

To further investigate the mechanisms of electrolyte degradation, cells with a single-salt 1.2 M LiDFOB cells electrolyte were also tested (**Figure A.10**). In this system with initially no LiBF<sub>4</sub> in the electrolyte, it is observed that LiBF<sub>4</sub> is produced during cycling, and this occurs at a higher rate at 4.5 V than at 4.3 V. In negative symmetric cells, LiDFOB is shown to be consumed at approximately the same rate as in the dual-salt negative symmetric cells, while the concentration of LiBF<sub>4</sub> remains at zero. In positive symmetric cells, LiDFOB is consumed and LiBF<sub>4</sub> is produced at nearly twice the rate compared to the dual-salt electrolyte cells, suggesting a first-order reaction pathway. The electrochemical data for these symmetric cells are shown in **Figure A.11**.

This analysis confirms the oxidative decomposition of LiDFOB in dual-salt electrolyte. Electrolyte oxidation at the positive electrode results in the decomposition of LiDFOB to form LiBF<sub>4</sub>. On the negative electrode, both LiDFOB and LiBF<sub>4</sub> decompose in reactions with lithium metal contributing to SEI formation. As previously discussed, these salts clearly benefit the lithium plating morphology, likely because of the resulting SEI composition that is formed from LiDFOB and LiBF<sub>4</sub> decomposition. These reaction mechanisms are discussed further in Ref.<sup>44</sup> Crosstalk, a phenomenon where reactions occurring on one electrode impact reactions and the performance of the other electrode, clearly plays an important role in the efficacy of LiDFOB/LiBF<sub>4</sub> dual-salt electrolyte. LiBF<sub>4</sub> generated at the positive electrode benefits the negative electrode. However, LiDFOB is also beneficial to the lithium electrode, therefore its depletion via oxidative decomposition on the positive as well as consumption on the negative accelerates its depletion.

The consumption of LiDFOB and LiBF<sub>4</sub> thus contributes to both the success and the failure of cells with this electrolyte chemistry. As the salts are depleted, cell performance is negatively impacted in a couple of ways. First, the ionic conductivity of the electrolyte depends on the salt concentration.<sup>149</sup> Decreasing LiDFOB/LiBF<sub>4</sub> concentrations will lower the ionic conductivity in the electrolyte, contributing to the increase of solution resistance ( $R_s$ ) observed in **Figure 4.10**. Practically, this manifests as an increase in internal cell resistance, decreasing the average discharge voltage and thus the deliverable energy. Second, the depletion of these salts will terminate the beneficial SEI composition that is formed from LiDFOB and LiBF<sub>4</sub> decomposition.<sup>46,150</sup> **Figure 4.11** shows that this success of dual-salt electrolyte comes at the cost of consuming these salts. Therefore, this synergistic decomposition and beneficial SEI cannot be indefinitely maintained, and this will initiate failure by precipitating the degradation of the lithium anode.

#### 4.2.3 Morphology Degradation

To investigate the deterioration of the lithium microstructure, lithium negative electrodes were retrieved from aged cells for SEM analysis. **Figure 4.12** shows the evolution of lithium morphology as a function of cycle number for cells cycled under high pressure. The same analysis was performed with cells under low pressure shown in **Figure A.12**. To probe the morphology as a function of plating depth, SEM images were taken at 3 stages of lithium plating: 100% plating at the top of charge (4.5 V, **Figure 4.12a-d**); after most of the lithium has been stripped away at the bottom of discharge (3.6 V, **Figure 4.12e-h**); and after all active lithium has been stripped away (1.2 V, **Figure 4.12i-l**). A section of the lithium electrode retrieved from disassembled cells is optically pictured in the insets of **Figure 4.12**. The main panels show SEM images taken from sections of the samples in the inset.



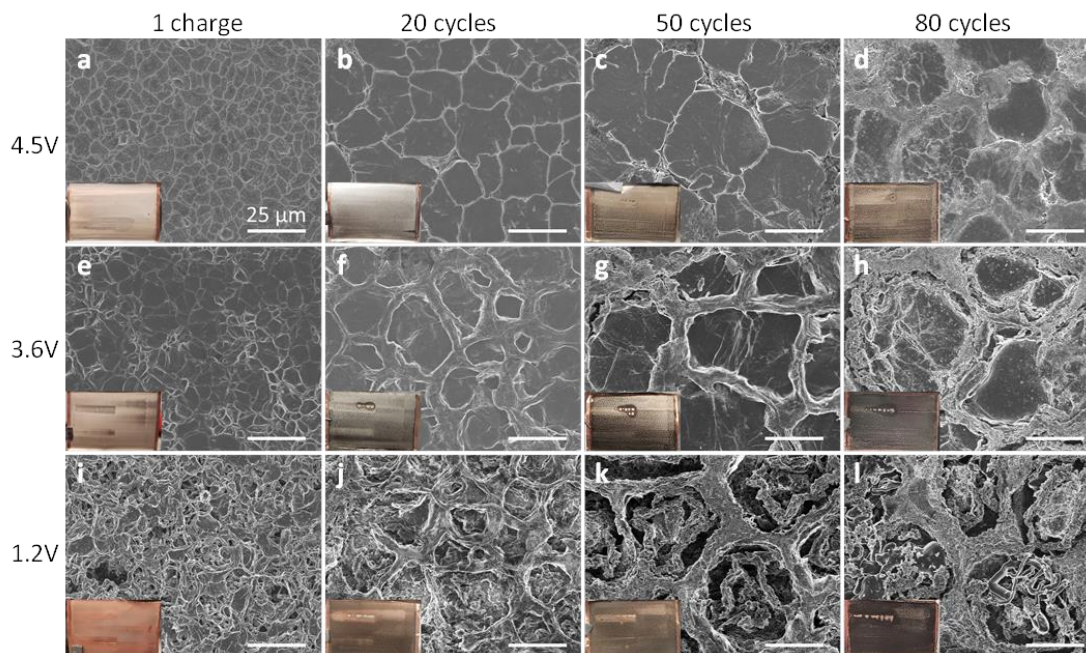


**Figure 4.12 | Morphology degradation.** a-d, SEM and optical images (insets) of fully plated lithium (4.5 V). e-f, Images after most lithium is stripped away (3.6 V). i-l, Images after all active lithium is stripped away (1.2 V). Lithium samples were retrieved after 1 charge (a,e,i), 20 (b,f,j), 50 (c,g,k), and 80 (d,h,l) cycles. The insets are optical images of lithium plated on single electrode layer harvested from the pouch cell. Samples were retrieved from cells cycled under high pressure (1200 kPa) between 3.6-4.5 V at C/5 D/2 and 40 °C. The electrolyte in the cells was 0.6 M LiDFOB 0.6 M LiBF<sub>4</sub> FEC:DEC 1:2. The scale bars are 25 μm, and the width of the electrodes shown in the insets are 2.6 cm.

The SEM images reveal the ideal lithium morphology formed in dual-salt electrolyte, appearing as a smooth mosaic composed of tightly packed lithium grains. Such low surface area morphology is ideal for avoiding lithium loss.<sup>15,63,71</sup> Interestingly, the lithium grains become larger through 50 cycles. This is likely a result of the differences to lithium nucleation on a bare copper current collector which occurs on the first charge versus lithium-on-lithium nucleation which occurs for all subsequent cycles. After a single charge, the grain size is about 5-10 μm (**Figure 4.12a**). After 20 cycles, the lithium grains are still tightly packed, now about 10-25 μm in size (**Figure 4.12b**). By 50 cycles, some of the lithium grains have expanded to about 50 μm in diameter (**Figure 4.12c**). It should be stressed that the size of these lithium grains are unprecedented in the literature (see **Figure**

**A.1).** However, after 50 cycles, high surface area mossy lithium deposits begin to appear between the large lithium grains. At 80 cycles (**Figure 4.12d**), the mossy deposits have further expanded and the grains have begun to fracture. **Figure A.13** shows EDS measurements demonstrating the compositional differences between the smooth Li grains and the mossy surroundings. These SEM images clearly demonstrate a deterioration of the lithium microstructure as cells age. Interestingly, this degradation can also be identified from the optical images of the plated lithium in the insets of **Figure 4.12**; lithium with a pristine microstructure appears more silver-coloured, and a deteriorated lithium microstructure with an accumulation of dead lithium appears blackened.

**Figure 4.12e-h** show that after most of the lithium is stripped (3.6 V), the base of the smooth lithium grains are observed. This indicates that the lithium grains are in fact tightly packed lithium columns. Obviously, it would be ideal to confirm columnar microstructure via lithium cross sections. However, we do not have access to cryo-FIB facilities required to achieved pristine lithium cross sections. Nevertheless, we were able to generate a crude cross section from a lithium sample aged to 50 cycles shown in **Figure 4.13**. This cross section was generated by simply cutting a lithium sample with a knife. This mechanical cut likely damaged the native internal lithium structure. However, lithium columns are implied by the grain boundaries which can be identified by the glancing view of this SEM image.

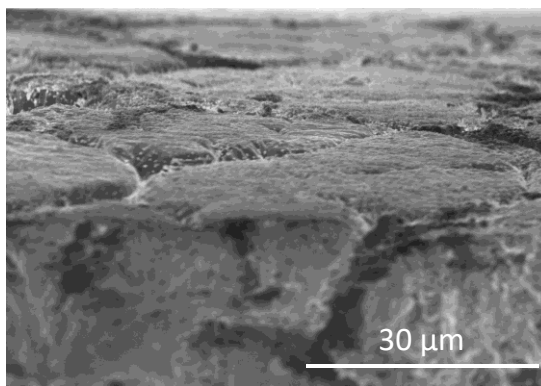


**Figure 4.13 | Crude lithium cross-section.** SEM image of a lithium cross section with a glancing view. This cross section was generated by cutting the lithium sample with a knife at room temperature. The sample was retrieved from a cell cycled 50 times under high pressure (1200 kPa) between 3.6-4.5 V and C/5 D/2 at 40°C with 0.6 M LiDFOB 0.6 M LiBF<sub>4</sub> FEC:DEC 1:2 electrolyte.

During a deep discharge down to 1.2 V, all active lithium which can be stripped will be reinserted to the positive electrode. Any lithium that remains must therefore be “dead”; inactive lithium which has been mechanically isolated or reacted to form the SEI. **Figure 4.12i-l** shows this dead lithium after a deep discharge (1.2 V). **Figure 4.12i** shows the dead lithium that is generated after a single cycle. The corresponding optical image in the inset shows an almost translucent lithium layer on the copper current collector. After 20 cycles (**Figure 4.12j**), the dead lithium appears patterned;  $\sim 20\ \mu\text{m}$  cavities are surrounded by walls of dead lithium. The lithium columns must be depositing in these cavities, pushing aside newly accumulated dead lithium to form these mossy walls observed between smooth Li grains. This is further observed after 50 and 80 cycles (**Figure 4.12k-l**). Incredibly, the columnar lithium enabled by dual-salt electrolyte forms a matrix of dead lithium which facilitates reversible lithium deposition. As the electrolyte degrades with cell aging, this matrix begins to fill with dead lithium, disallowing smooth grains to form as shown in the SEM images after 80 cycles (**Figure 4.12d**).

A consequence of this degrading microstructure will be an increase in porosity and thickness of the lithium electrodes. This was confirmed via x-ray computed tomography shown in **Figure 4.14**. These x-ray CT images show a portion of the electrode stack, about 3 layers, from the entire cell jelly roll. The double-sided lithium electrodes, highlighted with red arrows, thicken through 80 cycles. After one cycle (**Figure 4.14a**), the double-sided lithium electrode is  $36\ \mu\text{m}$ . After 50 cycles (**Figure 4.14b**), the electrode is  $41\ \mu\text{m}$ , and after 80 cycles (**Figure 4.14c**) the electrode is  $54\ \mu\text{m}$  thick. This thickening is not surprising and has been reported before in other electrolyte systems.<sup>138</sup> However, the implied increase in lithium porosity raises an important question about electrolyte wetting. Since these cells were filled with a fixed and limited (0.5 mL) volume of electrolyte, a significant increase in electrode porosity may initiate electrolyte dry-out.<sup>‡</sup> For  $\text{Li}^+$  transport

---

<sup>‡</sup> It should be noted that there is a distinction between this scenario, which describes dry-out as a result of increasing electrode porosity, as opposed to the previously described scenario of dry-out due to electrolyte consumption and decreased electrolyte volume. Unpublished total-electrolyte-extraction NMR results show no evidence of solvent consumption in the dual-salt electrolyte system.

not to be impeded, there must be sufficient electrolyte to completely wet all the components of the cell. As the lithium porosity increases, there may become insufficient electrolyte to wet all the new lithium surfaces that are generated. To investigate this potential issue, aged cells were probed via ultrasonic transmission imaging.

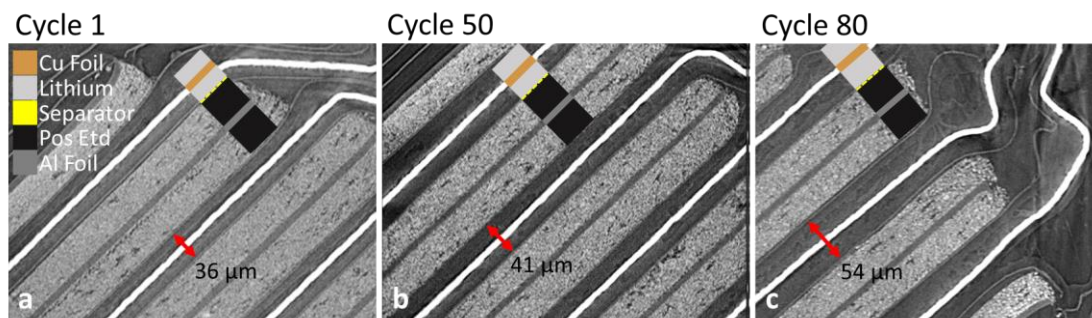


**Figure 4.14 | Thickening of the lithium electrode.** a-c, X-ray computed tomography images of cycled anode-free cells with dual-salt electrolyte after one (a), 50 (b), and 80 (c) cycles. The electrode stacks are overlaid with coloured blocks to distinguish each component of the stack from the legend, and the thickness of the lithium electrodes are noted. Cells were cycled under high pressure (1200 kPa) between 3.6-4.5 V at C/5 D/2 and 40 °C with 0.6 M LiDFOB 0.6 M LiBF<sub>4</sub> FEC:DEC 1:2 electrolyte. Images were taken near the bottom of charge (3.6 V).

**Figure 4.15** shows ultrasonic transmission mapping of cycled anode-free cells along with the corresponding lithium morphologies at each cycle number. Cells with sufficient electrolyte wetting should exhibit a high degree of ultrasonic transmission, shown here in a red-to-blue colour map scale, as described in previous work.<sup>125</sup> **Figure 4.15a-d** shows transmission maps for cells cycled under low pressure. Through 20 cycles, most of the jelly roll exhibits a moderate-to-high degree of acoustic transmission and thus electrolyte wetting. After 50 cycles, there is no transmission through the jelly roll, indicating at least one complete layer of electrolyte dry-out.<sup>125</sup> The situation is not as dire for cells cycled under high pressure (**Figure 4.15i-l**). More significant transmission is recorded after just one charge, correlating a superior degree of electrolyte wetting to the denser lithium morphology generated under higher pressure. After further cell aging, the transmission becomes significantly attenuated. By 80 cycles, a significant portion of the cell exhibits insufficient electrolyte wetting.

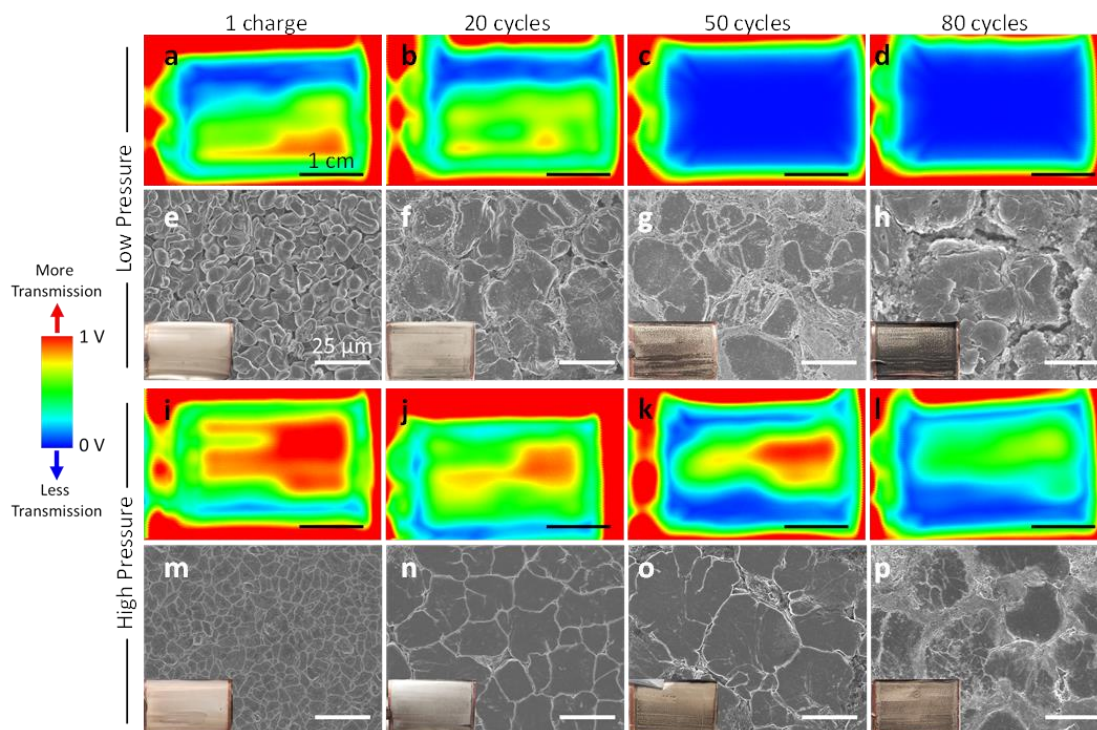


**Figure 4.15 | Electrolyte dry-out.** **a-d**, Ultrasonic transmission mapping of anode-free pouch cells with dual-salt electrolyte cycled under low pressure (200 kPa). **e-h**, Corresponding lithium morphology for cells cycled under low pressure. **i-j**, Ultrasonic transmission mapping of cells cycled under high pressure (1200 kPa). **m-p**, Corresponding lithium morphology for cells cycled under high pressure. Red indicates more transmission and electrolyte wetting and blue indicates less transmission and wetting. Cells were cycled between 3.6-4.5 V at C/5 D/2 and 40 °C with 0.6 M LiDFOB 0.6 M LiBF<sub>4</sub> FEC:DEC 1:2 electrolyte. Images were taken at the top of charge (4.5 V).

**Figure 4.15** demonstrates a compelling correlation between lithium microstructure degradation and electrolyte dry-out. Beyond facilitating lithium inventory loss, a worsening lithium morphology contributes to cell failure by impeding Li<sup>+</sup> transport, another factor resulting in the increased solution resistance observed in **Figure 4.10** and thus contributing to decreased deliverable energy.

There is a chicken-and-the-egg scenario for explaining the role of lithium degradation in failure of anode-free cells with dual-salt electrolyte. We observe that the presence of LiDFOB and LiBF<sub>4</sub> salts in the electrolyte facilitates dense lithium plating. We also observe that these salts are consumed during cycling. Therefore, it stands to reason that the



depletion of LiDFOB and LiBF<sub>4</sub> initiate morphology degradation, lithium inventory loss, and resistance growth. However, resistance growth will also initiate morphology degradation, as impeded Li<sup>+</sup> transport intensifies concentration gradients in the electrolyte known to result in mossy lithium growth.<sup>§77</sup> In other words, there is positive feedback loop between worsening lithium morphology and increasing cell resistance. More targeted experiments are required to deconvolute the contributing factors of salt loss and electrolyte wetting.

#### 4.2.4 Diagnosing & Treating Failure

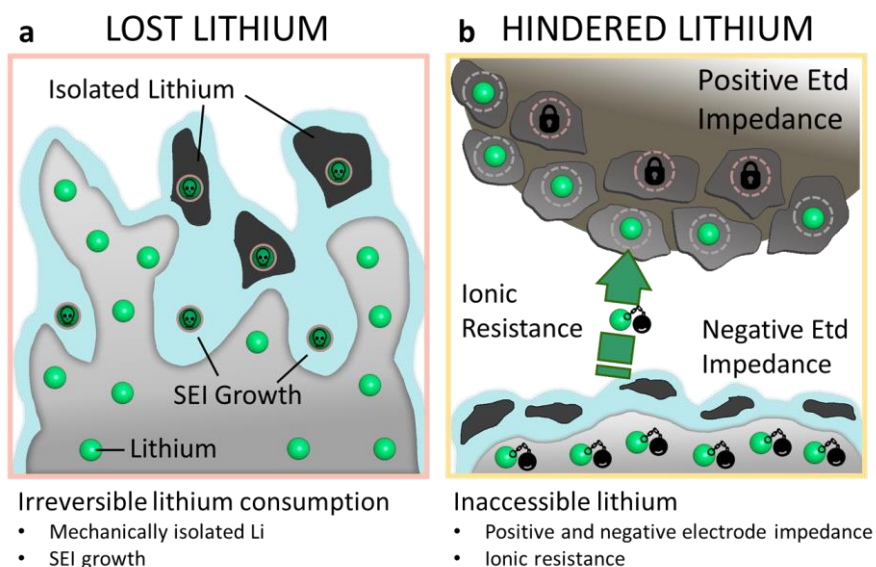


**Figure 4.16 | Diagnosing Failure.** Schematic representations of anode-free failure modes. **a**, Failure due to lost lithium. Lithium inventory irreversibly lost (represented as Li with skulls) due to the degradation of the lithium anode via SEI growth and mechanical isolation. **b**, Failure due to hindered lithium. This lithium is not irreversibly lost, but inaccessible due to increased impedance. This arises from impedance growth at both the positive electrode (represented as lithium sites with locks on the positive side) and the negative electrode (represented at Li tethered to a ball-and-chain), as well as increased ionic resistance due to decreased electrolyte salt concentration and electrolyte dry-out.

<sup>§</sup> This concept will be explored more deeply in Chapter 5.2.

In this section, we have explored failure mechanisms of anode-free cells with dual-salt 0.6 M LiDFOB 0.6 M LiBF<sub>4</sub> FEC:DEC 1:2 electrolyte. These failure modes can be separated into two categories: lost lithium and hindered lithium. This is schematically illustrated in **Figure 4.16**. Lost lithium refers to lithium inventory that is irreversibly consumed, *i.e.* “dead lithium” formed via SEI growth and mechanical isolation. As previously described, the formation of dead lithium is exacerbated by a mossy lithium morphology. Therefore, the depletion of LiDFOB and LiBF<sub>4</sub> salts and increased cell resistance which precipitate the degradation of the lithium microstructure are the primary causes of failure due to lithium loss.

Hindered lithium refers to lithium inventory that is not irreversibly lost but has become inaccessible because of impedance growth. Useful lithium inventory must be accessible during a discharge—lithium must be stripped from the negative electrode and inserted into the positive electrode to deliver capacity. In dual-salt electrolyte, lithium transport is hindered as the ionic conductivity of the electrolyte decreases due to the depletion of LiDFOB and LiBF<sub>4</sub> salts. The dry-out of electrolyte concomitant with the degradation of the lithium microstructure also contributes to lithium inaccessibility. Both these factors increase the solution ( $R_s$ ) and internal cell resistance, thereby diminishing deliverable capacity. Moreover, the intrinsic impedance of both the positive and negative electrode (charge transfer impedance,  $R_{ct}$ ) can further contribute to lithium accessibility. It has previously demonstrated that the positive electrode impedance increases during prolonged cycling to high voltage.<sup>151</sup> For the negative electrode, as the lithium anode becomes more tortuous, the transport of Li<sup>+</sup> will be impeded.<sup>75</sup> Beyond resulting in inaccessible lithium, impedance growth will also result in a decreased average cell voltage which also contributes to the loss of energy delivered by anode-free cells.

Most of the failure modes illustrated in **Figure 4.16** are a general picture applicable to all cells cycling lithium metal, whereas the consumption of LiDFOB and LiBF<sub>4</sub> is unique to this system and the depletion of lithium salts more broadly will depend on the electrolyte

chemistry. \*\* From this diagnosis of the failure of anode-free cells with dual-salt electrolyte, some relatively simple-minded treatments can be administered to improve lifetime.

Dry-out due to insufficient electrolyte may be overcome by simply increasing the volume of electrolyte. **Figure 4.17** shows results for cells tested with different volumes of dual-salt electrolyte. The loading in grams of electrolyte per amp-hour of capacity stored by the cell is another way of quantifying the amount of electrolyte. It is desired to minimize this loading to minimize cost as well as to maximize specific energy density. The academic target to achieve industrially relevant electrolyte loadings is to be under 3 g/Ah.<sup>24</sup> Our typical 0.5 mL volume of electrolyte is under this target at 2.70 g/Ah, whereas increasing the electrolyte volumes to 0.8 mL (4.38 g/Ah) and 1.0 mL (5.49 g/Ah) exceed the target. Nevertheless, increasing the electrolyte volume does improve lifetime. The metrics for gauging cycling performance, normalized capacity and stack volumetric energy density vs cycle, are shown in **Figure 4.17a-b**. The performance is similar through 80 cycles; cells with more electrolyte volume only begin to show improvement during the later half of testing. As a result, the number of cycles to 80% capacity retention—the conventional metric for cycle life—is the same for each electrolyte loading (80 cycles). The number of cycles to 50% capacity retention, approximately the cross over point at which anode-free cells deliver less stack volumetric energy density than comparable lithium-ion cells at 700 Wh/L, is 100 cycles for 0.5 mL, 140 cycles for 0.8 mL, and 160 cycles for 1.0 mL of electrolyte. **Figure 4.17c** shows  $\Delta V$  vs cycle, useful for elucidating performance. The  $\Delta V$  is very similar through 80 cycles. After 80 cycles, the 0.5 mL electrolyte volume cells begin to exhibit rapid  $\Delta V$  growth indicating increased cell resistance. **Figure 4.17c** indicates that increased electrolyte volume improves performance by mitigating resistance growth, as we would expect for a solution targeted to improve electrolyte wetting and stop dry-out. These results validate our earlier conclusion that electrolyte dry-out is an issue for anode-free cells. However, increased electrolyte volume is not necessarily a

---

\*\* For example, no significant salt loss is observed for cells with 1 M LiPF<sub>6</sub> FEC:DEC 1:2 electrolyte.<sup>46</sup>



practical solution since it does not improve lifetime to 80% capacity retention, will increase cost, and decrease specific energy density.

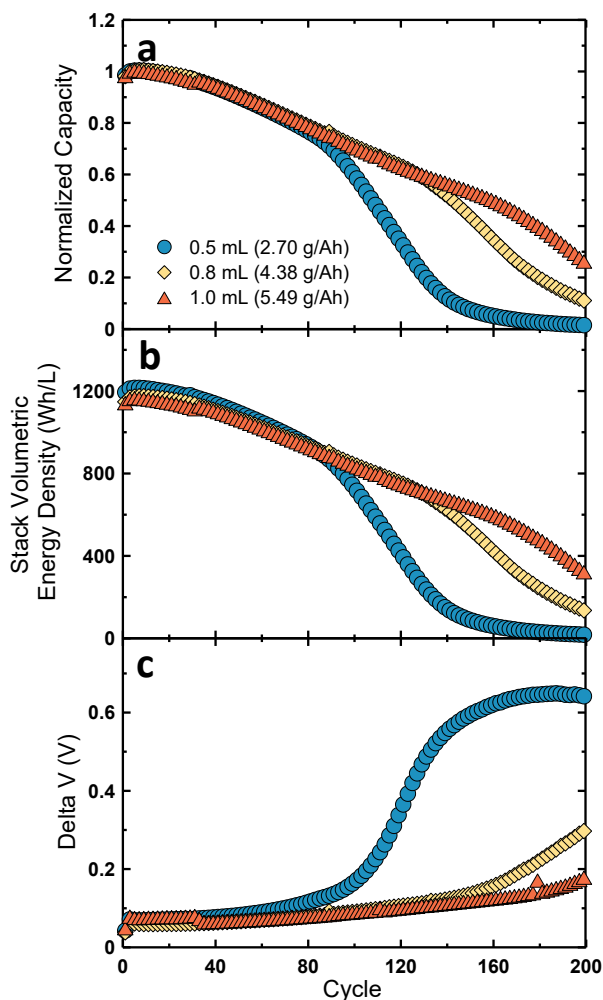


**Figure 4.17 | Dual-salt electrolyte volume.** a-c, Cycling data for anode-free cells with different volumes of 0.6 M LiDFOB 0.6 M LiBF<sub>4</sub> FEC:DEC 1:2 electrolyte. Normalized capacity (a), stack volumetric energy density (b), and delta V (c) vs cycle. Anode-free NMC532 cells were cycled between 3.6-4.5 V at C/5 D/2 and 40 °C.

Salt depletion is another major failure mode for cells with dual-salt electrolyte. Therefore, a simple way to increase longevity should be to increase the concentrations of LiDFOB and LiBF<sub>4</sub>. Cycling results testing different salt concentrations are shown in **Figure 4.18**. In an attempt to make all this data easier to parse, results were split up in three groups: medium-concentration dual-salt formulations (first column), high-concentration dual-salt

formulations (second column), and high-concentration dual-salt formulations that were cycled under high pressure (third column). “Control” results for cells with the classic 0.6 M LiDFOB 0.6 M LiBF<sub>4</sub> dual-salt formulation tested under low pressure are shown in all panels as a baseline (medium blue circles). Normalized capacity, stack volumetric energy density, and delta V vs cycle are shown in the three rows.

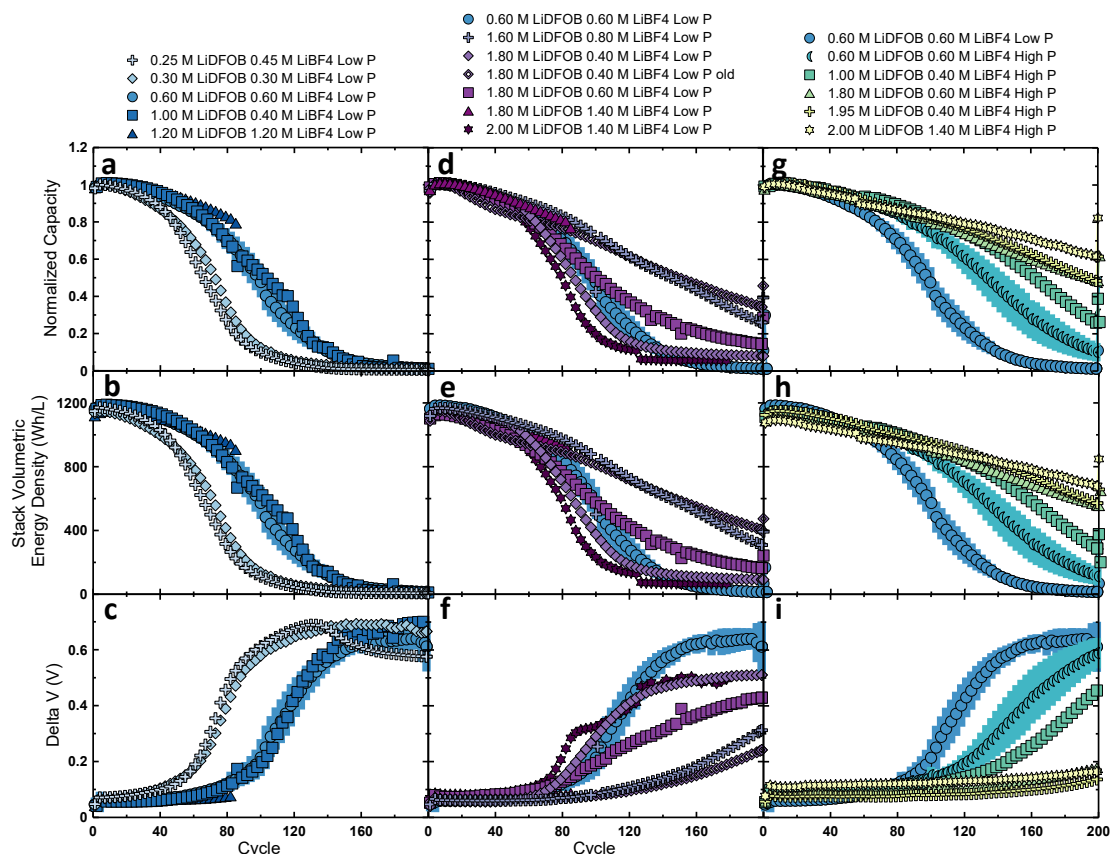


**Figure 4.18 | High concentration dual-salt. a-i,** Cycling data for anode-free cells with different dual-salt concentrations. Medium-concentration (a-c), high-concentration (d-f), and high-concentration formulations tested under high pressure (g-h). Normalized capacity is shown in the top row (a,d,g), stack volumetric energy density in the middle row (b,e,h) and delta V vs cycle in the bottom row (c,f,i). The LiDFOB and LiBF<sub>4</sub> concentrations are denoted in the legend; all electrolytes used FEC:DEC 1:2. Cells were cycled between 3.6-4.5 V at C/5 D/2 and 40 °C at low pressure (Low P, 200 kPa, a-f) and high pressure (High P, 1200 kPa, g-i) as indicated in the legend. The average of at least two cells are shown and the error bars are calculated as the standard deviation.

Generally, increased dual-salt concentration electrolyte formulations performed better. The low concentration tests (0.25 M/0.45 M and 0.30 M/0.30 M LiDFOB/LiBF<sub>4</sub>, **Figure 4.18a-c**) exhibit a cycle life about 40 cycles less than control. However, improved performance was not observed for every instance of increased salt concentration. This is demonstrated in **Figure 4.18d-f**. The 1.60 M/0.80 M formulation performed better than control, but the other formulations with even higher salt concentrations did not. This is with one peculiar exception for the 1.80 M/0.40 M formulation that was tested twice; this electrolyte was used to fill cells immediately after electrolyte mixing, and then the exact same electrolyte was used to fill different cells again about one week later (these results distinguished in the legend with “old” referring to cells filled on the second week). The “old” electrolyte (open diamonds) performed better than control, while the fresh electrolyte (solid diamonds) did not. This significant difference in cycle life is puzzling. We had trouble dissolving salts in electrolyte formulations with LiDFOB concentrations >1.80 M—heat and stirring were used to promote dissolution for these electrolytes. Perhaps the fresh 1.80 M/0.40 M electrolyte was not well mixed, and by the time this electrolyte was used again the salts were completely dissolved. Overall, a more inconsistent trend is observed as the LiDFOB and LiBF<sub>4</sub> concentrations get high.

**Figure 4.18g-i** show that cells cycled under high pressure exhibit a more consistent benefit from high concentration dual-salt formulations. The classic electrolyte mixture (0.60 M/0.60 M) tested under high pressure (crescents) enables a longer cycle life than control as demonstrated previously. All higher concentration formulations tested under high pressure improve performance even further, with the 2.0 M/1.4 M formulation resulting in a capacity retention of 60% after 200 cycles. Increasing the salt concentrations will also increase the electrolyte loading, but not as significantly as increasing the volume of electrolyte—0.5 mL of 2.0 M LiDFOB 1.4 M LiBF<sub>4</sub> electrolyte has a loading of 3.34 g/Ah compared to 1.0 mL of control 0.6 M LiDFOB 0.6 M LiBF<sub>4</sub> electrolyte which has a loading of 5.49 g/Ah. Cells with the 2.0 M/1.4 M formulation exhibit a slightly decreased volumetric stack energy density and higher initial delta V compared to control electrolyte, indicating that this high concentration formulation is beginning to impair Li<sup>+</sup> transport, likely a result of increased viscosity. This is not ideal; therefore, we do not believe this is

the optimal dual-salt formulation. Further optimization can be achieved by slightly tuning the salt concentrations to maximize cycle life without introducing transport limitations.

The benefit of high concentration dual-salt electrolyte comes from mitigating cell resistance growth as the lithium salts are depleted, demonstrated by lowered  $\Delta V$  growth (**Figure 4.18i**), as well as decreasing lithium inventory loss by enabling a superior lithium morphology. **Figure 4.19** compares the lithium morphology after 100 cycles generated in 0.6 M LiDFOB 0.6 M LiBF<sub>4</sub> (a-c) and in 2.0 M LiDFOB 1.4 M LiBF<sub>4</sub> (d-f) electrolyte. In general, SEM is a useful tool for qualitatively assessing lithium morphology. However, as shown in the optical pictures of the electrodes (**Figure 4.19a,d**), there is a heterogeneity that spans centimeters which can be obfuscated by SEM images only spanning hundreds of micrometers. In other words, it is generally possible to find both good and bad regions of lithium microstructure from any single electrode sample. Up until now, we have been comparing the best microstructures observed from samples to be as fair as possible. In **Figure 4.19**, we include two SEM images picturing different areas of the lithium samples generated in each electrolyte. The optical images show that on average, the lithium generated in the high concentration dual-salt electrolyte is less blackened, indicating superior lithium morphology. This is confirmed with the SEM images that show the best areas of lithium morphology (**Figure 4.19b,e**) and the worst areas of lithium morphology (**Figure 4.19e,f**) are superior for the samples generated in 2.0 M LiDFOB 1.4 M LiBF<sub>4</sub> electrolyte.

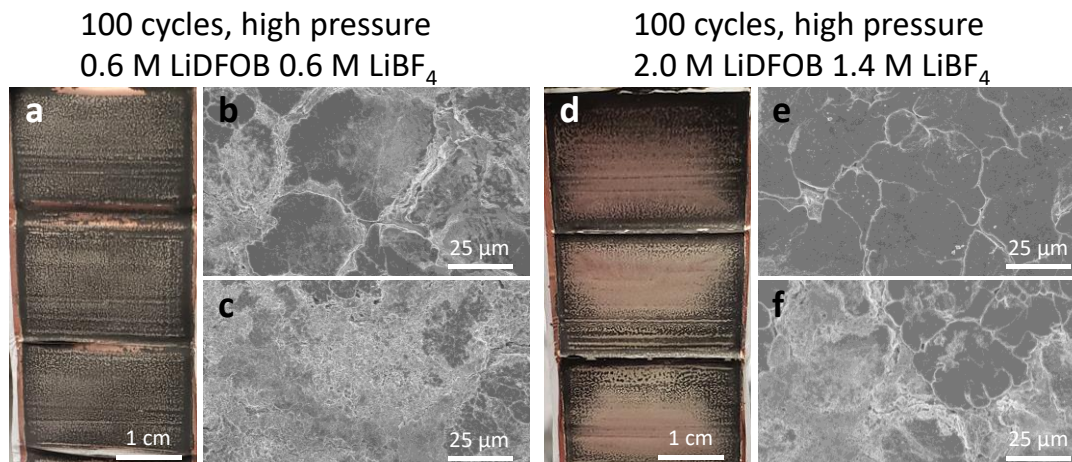


**Figure 4.19 | High concentration lithium morphology.** **a-c**, Optical (a) and SEM (b,c) images of lithium plated in 0.6 M LiDFOB 0.6 M LiBF<sub>4</sub> FEC:DEC 1:2 electrolyte after 100 cycles. **d-f**, Optical (d) and SEM (e,f) images of lithium plated in 2.0 M LiDFOB 1.4 M LiBF<sub>4</sub> FEC:DEC 1:2 electrolyte after 100 cycles. The SEM images were taken from two different areas of the lithium samples. Samples were retrieved from cells cycled under high pressure (1200 kPa) between 3.6-4.5 V at C/5 D/2 and 40 °C.

Our progress increasing the lifetime of NMC532 anode-free lithium metal cells with liquid electrolytes is summarized in **Figure 4.20**. **Figure 4.20a** replots the data shown originally **Figure 4.1** to be compared to our best effort results in **Figure 4.20b**. The normalized capacity and delta V vs cycle for these best effort results are shown in **Figure A.14**. Lifetime, as defined as number of cycles with higher stack energy density than the lithium-ion comparator, is improved using a high volume of our classic 0.6 M LiDFOB 0.6 M LiBF<sub>4</sub> formulation just as much as cycling under high pressure with a typical 0.5 mL electrolyte volume (**Figure 4.20b**). By increasing the salt concentrations to 2.0 M LiDFOB 1.4 M LiBF<sub>4</sub>, lifetime is further extended to 200 cycles. However, this comes with the consequence of a slightly decreased initial energy density. A 200 cycle lifetime can also be achieved with a 1.0 mL high volume high concentration 1.0 M LiDFOB 0.40 M LiBF<sub>4</sub> electrolyte. One of the best performing electrolytes from the literature tested in this work, the localized high concentration 1.73 M LiFSI DME:TTE 1:4 electrolyte, is also included for comparison.

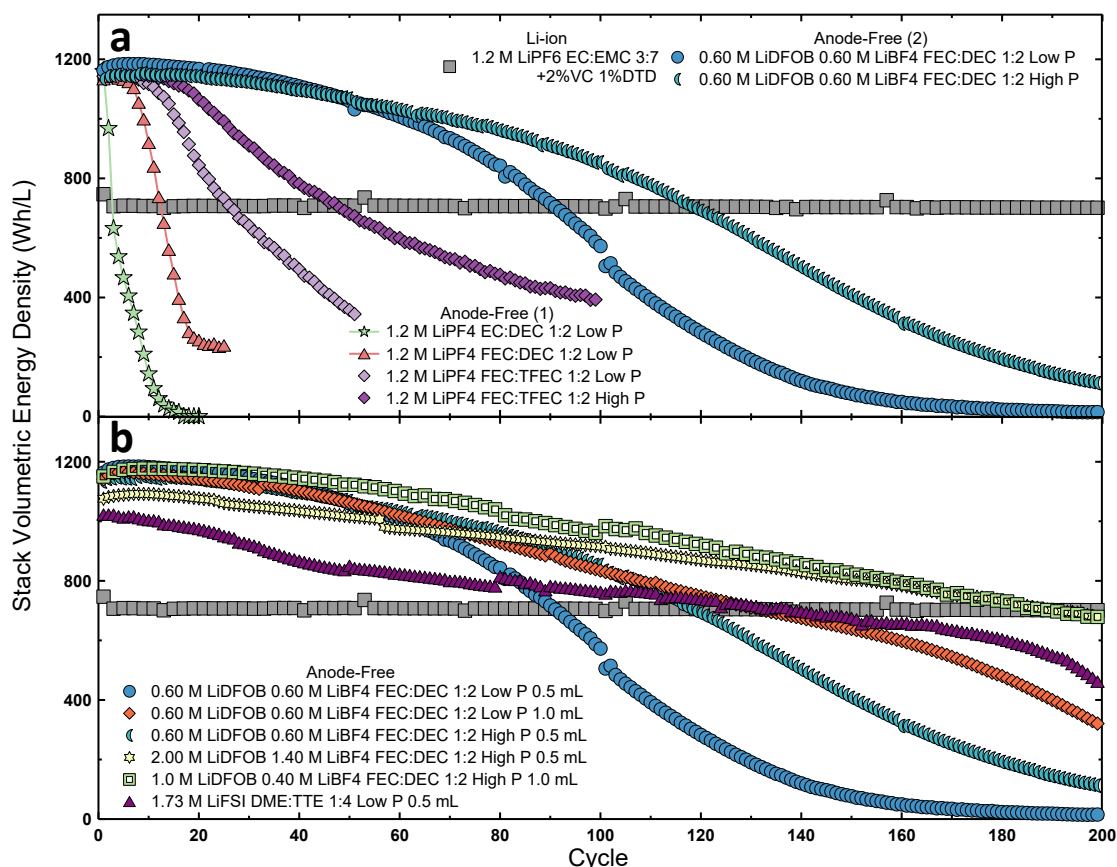


**Figure 4.20 | Best effort electrolyte. a-b**, Stack volumetric energy density vs cycle of various anode-free cells with lifetimes below 100 cycles (a) and above 100 cycles (b) compared to a Li-ion cell. Anode-free cells were cycled between 3.6-4.5 V at C/5 D/2 and 40 °C at low pressure (Low P, 200 kPa) and high pressure (High P, 1200 kPa) as indicated in the legend. The Li-ion cell was cycled between 3.0-4.3 V at C/3 D/3 and 40 °C and contained the same NMC532 positive electrode as the anode-free cells. The average of at least two cells are shown.

We have made excellent progress increasing the cycle life of anode-free cells, now achieving 200 cycles with our best electrolyte formulations. This is a significant advancement for lithium metal cells with no excess lithium. However, this is still not enough for practical applications such as electric vehicles which require a cycle life of at least 800 cycles. Moreover, there are other performance metrics beyond cycle life which will be considered throughout the rest of this thesis. As we have shown in this section, we have pushed the synergies of dual-salt LiDFOB/LiBF<sub>4</sub> electrolyte about as far as it can go.

Future significant improvements to cycle life will require new electrolyte breakthroughs which will come as a result of a lot of work and probably quite a bit of luck.

### 4.3 Safety

Throughout this chapter we have only discussed performance in terms of cycle life. Although a long-lived cell is necessary, it is not sufficient for a practical battery. Safety is another essential performance metric that needs to be satisfied. Safety issues with lithium metal cells have been well documented since the 1980s.<sup>13</sup> Safety is often discussed but rarely tested under realistic conditions in the literature. Some reports claim to use “non-flammable” electrolytes by virtue of electrolyte-soaked separators not catching fire under flame.<sup>152,153</sup> However, this clearly is not a practical test under realistic conditions, and does not incorporate potential effects of the other cell components such as the positive and negative electrodes. Therefore, more realistic characterization and cell abuse tests are required.<sup>27,154</sup>

To qualitatively examine the safety prospects of lithium negative electrodes that were generated in different electrolyte chemistries, we submerged plated lithium samples in water and observed their reactions (colloquially referred to as the goblet of fire test, **Figure 4.21**). As a reference, we also performed this experiment for lithiated (charged) graphite samples from a lithium-ion cell. The graphite sample (**Figure 4.21a**) produced gas and formed in water. **Figure 4.21b** and **c** show the results for samples produced with 0.6 M LiDFOB 0.6 M LiBF<sub>4</sub> FEC:DEC 1:2 electrolyte after 20 and 80 cycles, respectively. The ideal lithium morphology after 20 cycles merely gassed and foamed like the graphite sample, while the 80 cycle sample produced a small flame. **Figure 4.21d** and **e** show lithium samples produced with 1.2 M LiPF<sub>6</sub> in FEC:DEC 1:2 and EC:DEC 1:2 electrolytes, respectively. These highly mossy lithium morphologies formed in primitive electrolytes result in violent explosions when submerged in water. **Figure 4.21b-e** show that lithium morphology is coupled to the safety prospects of lithium metal and that lithium with a dense microstructure can exhibit relatively mild reactivity analogous to charged graphite.



The worsened safety of aged lithium metal cells has previously been demonstrated with accelerating rate calorimetry experiments.<sup>27</sup>

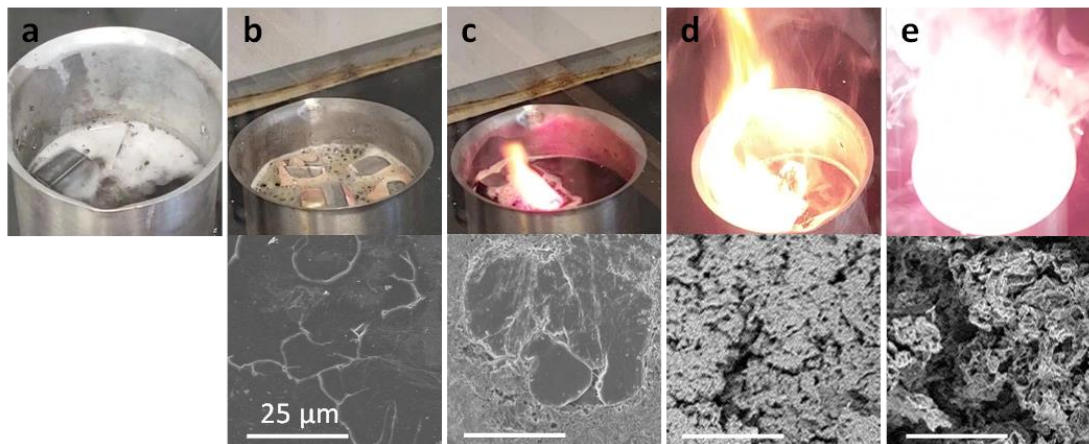


**Figure 4.21 | Goblet of fire.** **a**, Charged graphite submerged in water. **b-e**, Plated lithium submerged in water (top) and respective morphology of lithium sample submerged (bottom). The lithium samples submerged were retrieved from cells cycled with 0.6 M LiDFOB 0.6 M LiBF<sub>4</sub> FEC:DEC 1:2 electrolyte after 20 cycles (**b**) and 80 cycles (**c**); 1.2 M LiPF<sub>6</sub> FEC:DEC 1:2 electrolyte after 50 cycles (**d**); 1.2 M LiPF<sub>6</sub> EC:DEC 1:2 electrolyte after 50 cycles (**e**). All samples were retrieved from fully charged cells. Anode-free cells were cycled between 3.6-4.5 V at C/5 D/2 and 40 °C.

More rigorous safety characterization studies were motivated after two safety incidents occurred in the lab. The first involved an aged cell containing 4 M LiFSI FEC:DEC 1:2 electrolyte. When the cell was being moved after testing, it exploded after being accidentally shorted. The external short initiated an uncontrolled discharge, and the resulting joule heating must have initiated thermal runaway.

The second incident involved an aged cell containing 1.73 M LiFSI DME:TTE 1:4, the localized high concentration (LHC) electrolyte from literature<sup>47</sup> that enabled good cycle life shown in **Figure 4.8**. After testing for 200 cycles, one cell with this electrolyte was found exploded, as pictured in **Figure 4.22a**, which shows the cell in its testing fixture inside a temperature box. The jelly roll of the pouch cell has been ejected from the explosion. **Figure 4.22b** shows another view. The explosion of this cell is especially troubling since it was seemingly spontaneous—it occurred sometime after the cell



completed charge-discharge testing while it was sitting idle. The electrochemical data was examined to determine if there were any signs warning of a safety hazard. **Figure 4.22c** shows the charge capacity vs cycle for cells with dual-salt electrolyte compared to the LHC electrolyte that resulted in the explosion. An anomalous behaviour of increasing charge capacity is observed after 160 cycles for the cells with LHC electrolyte. This is an indication of shunting—a “soft” internal short. When a lithium dendrite snakes its way through the separator to the positive electrode causing a short circuit it will initiate cell discharge. A soft short occurs when this discharge terminates the offending dendrite via joule heating, essentially burning it away. After the soft short self-corrects in this way, the cell can continue charging normally. However, the voltage drop from the brief discharge must be recovered, resulting in re-charging over capacity that had already been charged before. Many continuous soft shorts result in the shunting behaviour shown in **Figure 4.22d** in which a significantly increased charge capacity will be measured by the charger. Therefore, **Figure 4.22c-d** indicate that cells with LHC electrolyte were shunting. Sometime after the cell pictured in **Figure 4.22a-b** completed testing, a fatal shunt must have generated enough heat to initiate thermal runaway.

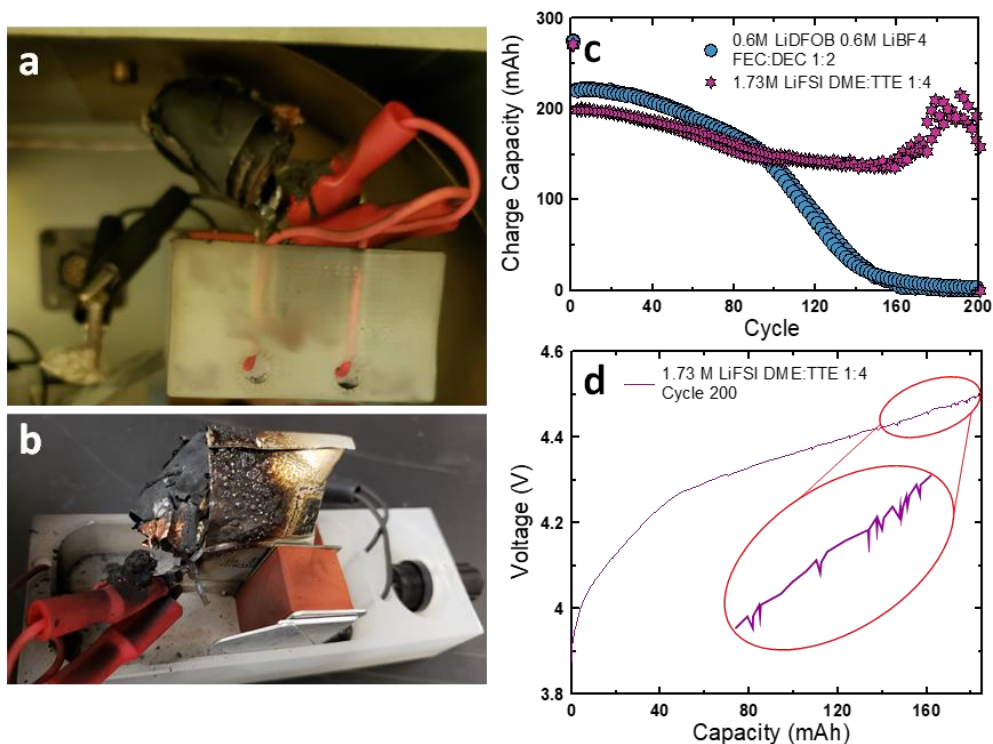


**Figure 4.22 | Localized high concentration safety issues.** **a-b**, Pictured anode-free cell with 1.73 M LiFSI DME:TTE 1:4 electrolyte which had spontaneously exploded after 200 cycle testing. The cell is pictured in its testing fixture inside the temperature box where it was found (a) and outside the temperature box for a better view (b). **c**, Charge capacity vs cycle for cells containing 1.73 M LiFSI DME:TTE 1:4 electrolyte compared to 0.6 M LiDFOB 0.6 M LiBF4 FEC:DEC 1:2 electrolyte. **d**, Voltage vs capacity of the 200<sup>th</sup> cycle for the cell pictured in a and b. Cells were cycled between 3.6-4.5 V at C/5 D/2 and 40 °C.

A safety test performed in industry to investigate the tolerance of cells to an internal short is a nail penetration test. **Figure 4.23** show results of smart nail tests performed on aged anode-free pouch cells. By measuring the temperature at the nail tip during penetration (**Figure 4.23d-f**), this test enabled a more quantifiable analysis beyond a binary pass-fail judgement based off if the cell was forced into thermal runaway and exploded or not (**Figure 4.23a-c**). The cells were penetrated at the top of charge (4.5 V) after 1 charge, 20 and 50 cycles. Cells with dual-salt electrolyte promoted in this work as well as cells with the electrolytes involved in the safety incidents previously described—LHC 1.73 M LiFSI DME:TTE 1:4 and 4 M LiFSI FEC:DEC 1:2 electrolytes were tested. The peak temperature of cells with dual-salt electrolyte increased through 50 cycles but never exceeded 100 °C

and did not explode. The peak temperature of cells with 1.73 M LiFSI DME:TTE 1:4 and 4 M LiFSI FEC:DEC 1:2 electrolyte increased through 20 cycles. After 50 cycles, both of these chemistries resulted in thermal runaway and violent explosions, reaching max temperatures of 500 °C and 370 °C, respectively.

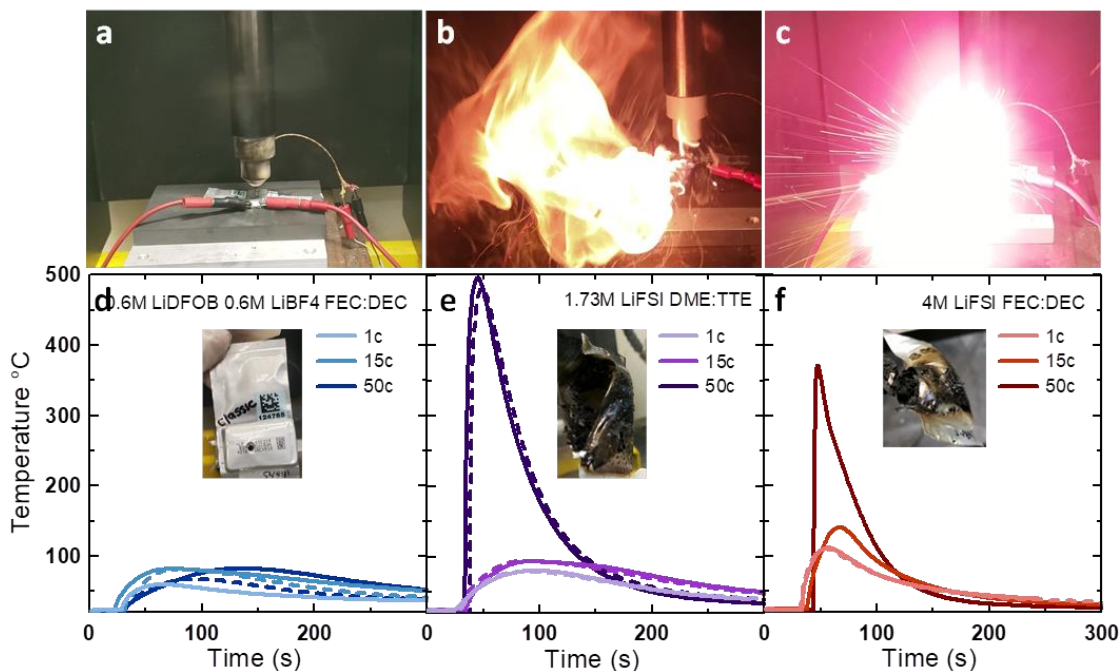


**Figure 4.23 | Smart-nail testing.** a-c, Anode-free cells aged to 50 cycles pictured during nail penetration. d-f, Temperature of nail tip vs time during nail tests and images of cells post 50 cycle penetration (inset). The electrolyte chemistries tested were 0.6 M LiDFOB 0.6 M LiBF<sub>4</sub> FEC:DEC 1:2 (a,d), 1.73 M LiFSI DME:TTE 1:4 (b,e), and 4 M LiFSI FEC:DEC 1:2 (c,f). Nail tests were performed on cells in their fully charged state after 1 charge, 15, and 50 cycles to an estimated depth of 2.5 mm at an estimated speed of 5 mm/s. Cells were cycled between 3.6-4.5 V at C/5 D/2 and 40 °C.

**Figure 4.24** shows results of more smart nail tests for additional electrolyte systems, 1.2 M LiDFOB FEC:DEC 1:2 (**Figure 4.24c**) and 1.2 M LiPF<sub>6</sub> FEC:DEC 1:2 (**Figure 4.24d**). Also included are a series of tests performed on dual-salt cells that cycled under high pressure which do not exhibit a significant difference to their low pressure counterparts (**Figure 4.24b** vs **Figure 4.24a**). Data for nail tests performed after 80 cycles are also included. **Figure 4.24a-c** show that LiDFOB-based electrolytes all show similar temperature evolution during the nail tests, although the single-salt 1.2 M LiDFOB resulted

in a higher maximum temperature during the nail penetration after 1 charge. After slight increases in the maximum temperature through 50 cycles, the maximum temperature significantly decreases by 80 cycles. This is likely a result of the diminished capacity by 80 cycles and therefore less heat to evolve during short circuit discharge. The other electrolytes systems (**Figure 4.24d-f**) exhibit even higher max temperatures. Again, cells with LHC (**Figure 4.24e**) and 4 M LiFSI electrolyte (**Figure 4.24f**) go into thermal runaway during 50 and 80 cycle tests.

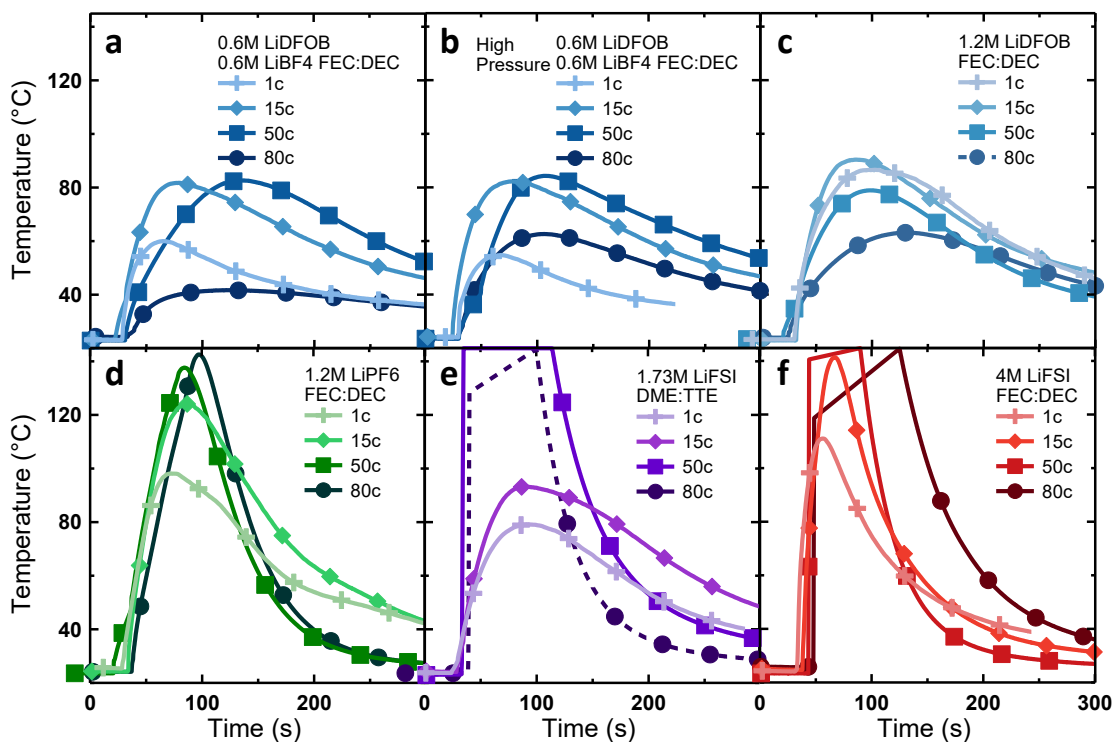


**Figure 4.24 | Smart-nail electrolyte tests.** a-f, Temperature vs time during nail tests of cells with different electrolytes. The electrolyte chemistries tested are listed in the legends. Nail tests were performed on cells in their fully charged state after 1 charge, 15, 50, and 80 cycles to an estimated depth of 2.5 mm at an estimated speed of 5 mm/s. Cells were cycled under low pressure (except for the results shown in panel b) between 3.6-4.5 V at C/5 D/2 and 40 °C.

It is important to note that we are not claiming that anode-free cells with dual-salt electrolyte will necessarily be safe. Larger format cells would likely perform worse in nail tests, generating more heat thereby increasing the likelihood of initiating thermal runaway.

Nevertheless, it is clear that not all electrolyte systems are equally safe; some electrolyte systems will be safer than others, as demonstrated here. This is promising, but the safety of cells cycling lithium metal with liquid electrolytes will be an ongoing cause for concern. Perhaps if we can control the lithium morphology to remain compact throughout the entirety of a cell's lifetime, the safety of anode-free cells may be suitable. Obviously, overcoming the issue of morphology degradation is not trivial, but it would solve a lot of problems. If a dense lithium morphology can be maintained, the intrinsic safety of the electrolyte must be optimized. For example, high concentration dual-salt electrolyte prolonged a superior lithium morphology, but the safety of this electrolyte has not yet been characterized. Safety will certainly be crucial for any attempt at commercialization of anode-free lithium metal cells with liquid electrolytes.

## Chapter 5: Effects of Different Cycling Conditions

In Chapter 4, we tested anode-free cells under our “control” conditions: 40 °C, cycled at a charge rate of C/5 (0.55 mA/cm<sup>2</sup>) and a discharge rate of D/2 (1.37 mA/cm<sup>2</sup>), to a depth of discharge of 80% (2.5 mAh/cm<sup>2</sup>). However, each of these conditions—temperature, charge-discharge rate, and depth of discharge—will also impact cell lifetime. Ideally, the performance of a battery should be robust throughout a range of different operating conditions. Therefore, in this chapter, we explore how these testing conditions affect the performance (mostly cycle life) of NMC532 anode-free cells. These tests were performed using our dual-salt LiDFOB/LiBF<sub>4</sub> electrolyte developed in Chapter 4. This work has previously been published in Refs.<sup>45,155††</sup>

### 5.1 Temperature

#### 5.1.1 Room Temperature Operation

Our “control” temperature for testing anode-free cells has been 40 °C. This was simply because we had more temperature boxes in our lab set to 40 °C for accelerated testing of lithium-ion cells.<sup>‡‡</sup> For practical purposes, we must demonstrate that anode-free cells can be successfully operated at ambient temperature. To this end, we tested cells at 20 °C and 30 °C, shown in **Figure 5.1**. Unfortunately, we find that lifetime is significantly reduced; at 20 and 30 °C, 20% capacity is lost after just 20 and 35 cycles, respectively, compared to 40 °C operation which results in just 10% capacity loss through 50 cycles. This is a

---

†† M. Genovese, A.J. Louli, R. Weber, C. Martin, T. Taskovic, J.R. Dahn, Hot Formation for Improved Low Temperature Cycling of Anode-Free Lithium Metal Batteries, *J. Electrochem. Soc.* **166** (2019).

A.J. Louli, M. Coon, M. Genovese, J. deGooyer, A. Eldesoky, J.R. Dahn, Optimizing Cycling Conditions for Anode-Free Lithium Metal Cells, *J. Electrochem. Soc.* **168** (2021).

‡‡ Lithium-ion cells are known to have a shorter lifetime when cycled at elevated temperatures.<sup>21,156</sup> Since the Li-ion cells tested in our lab can last for thousands of cycles, these tests take a long time. Therefore, 40 °C testing is performed to accelerate the degradation of Li-ion cells to generate results more rapidly.

troubling development for anode-free cells. Unlike lithium-ion cells which exhibit increased longevity at 20 °C due to a reduced rate of parasitic reactions,<sup>21,156</sup> anode-free cells seem to die faster at lower temperatures. This may be attributed to the mechanical properties of lithium metal which have been shown to vary over this temperature range. At room temperature, lithium has a lower creep stress than at 40 °C.<sup>82,157</sup> In other words, lithium is softer and more easily deformed at elevated temperature. This may be beneficial for facilitating a superior lithium morphology. When lithium is less compliant at 20 °C, the growth of mossy lithium deposits will be more difficult to constrain than softer lithium at 40 °C—particularly when cycling under low pressure. Perhaps, then, lithium at 20 °C may be more successfully constrained with the application of higher mechanical pressure.

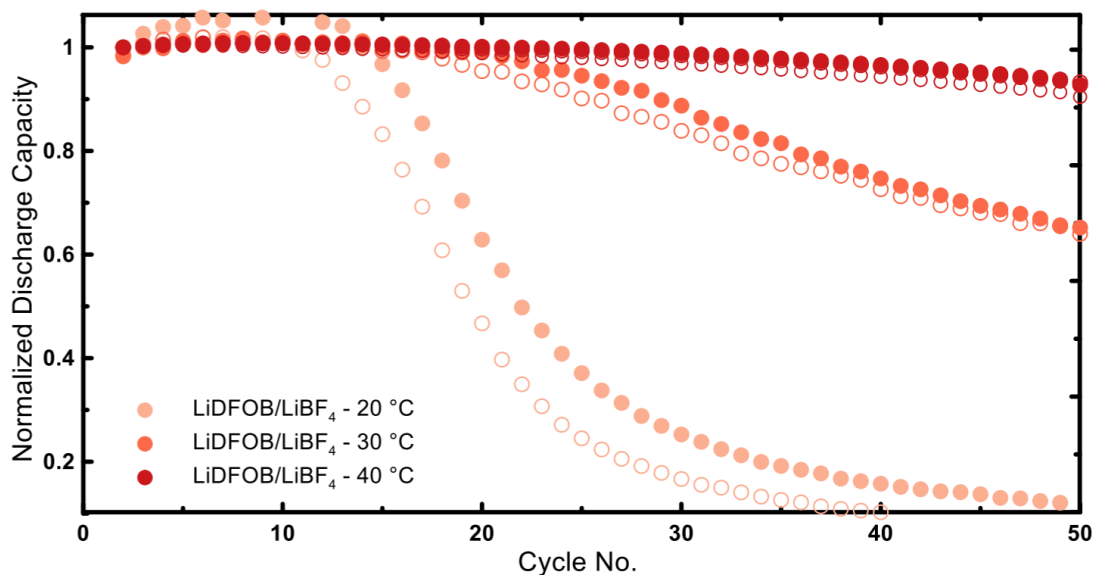


**Figure 5.1 | Effect of temperature.** Normalized capacity vs cycle for anode-free cells tested at different temperatures. Cells were cycled between 3.6-4.5 V at C/5 D/2 and low pressure with 0.6 M LiDFOB 0.6 M LiBF<sub>4</sub> FEC:DEC 1:2 electrolyte. Anode-free NMC532 were used. Pair cells are shown with open and closed symbols in the same colour.

The coupled behaviour of cycling at different temperatures and pressures is shown in **Figure 5.2**. We have previously demonstrated that cycling under higher mechanical pressure is beneficial to the performance of anode-free cells at 40 °C. This effect is even stronger at 20 °C. At low pressure (75 kPa), cells tested at 20 °C make it to only 20 cycles

to 80% capacity, and this is extended to 70 cycles with the application of high pressure (1200 kPa). The magnified impact of pressure between 40 and 20 °C is consistent with the hypothesis that the mechanical deformation of lithium plays an important role in cell performance. At 40 °C, the creep stress of lithium is ~500 kPa, compared to ~600 kPa at 20 °C.<sup>82</sup> Therefore, the pressures and temperatures applied here will impact the deformation of lithium and ultimately the lithium morphology that forms under these different cycling conditions, as confirmed in **Figure 5.3**. The SEM image of lithium plated at 20 °C (**Figure 5.3a**) exhibits a higher surface morphology than the lithium plated at 40 °C (**Figure 5.3b**). **Figure 5.3** also shows that the lithium grains formed at 40 °C are significantly larger than those at 20 °C, indicating that lithium nucleation is also improved. Higher temperatures will improve the transport properties and mitigate concentration gradients in the electrolyte which should facilitate the nucleation of larger lithium grains.

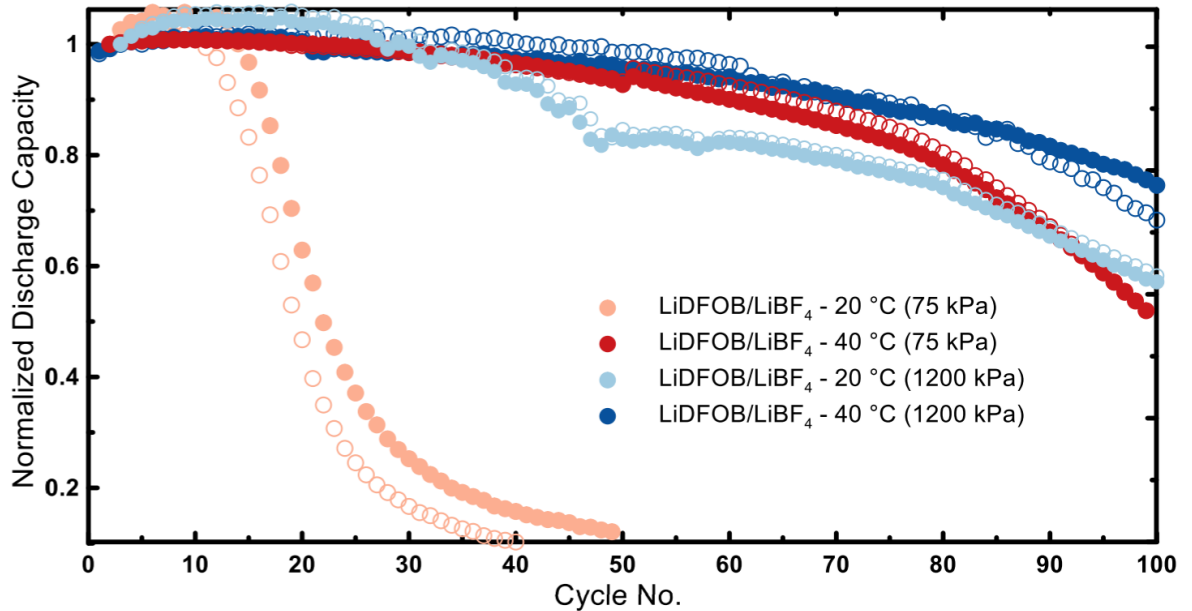


**Figure 5.2 | Temperature & pressure.** Normalized capacity vs cycle for anode-free cells tested at different temperatures and pressures. Cells were cycled between 3.6-4.5 V at C/5 D/2 with 0.6 M LiDFOB 0.6 M LiBF<sub>4</sub> FEC:DEC 1:2 electrolyte. Anode-free NMC532 cells were used. Pair cells are shown with open and closed symbols in the same colour.



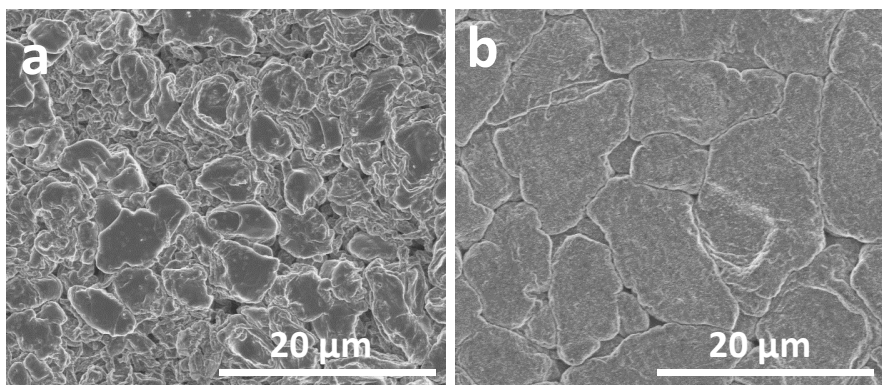


**Figure 5.3 | Temperature impact on lithium morphology. a-b,** SEM images of lithium plated after two cycles at 20 °C (a) and 40 °C (b). Samples were retrieved from cells at the top of charge (4.5 V) after cycling under low pressure between 3.6-4.5 V at C/5 D/2 with 0.6 M LiDFOB 0.6 M LiBF<sub>4</sub> FEC:DEC 1:2 electrolyte. The scale bars are 20 μm.

#### 5.1.2 Hot Formation

**Figure 5.2** showed that the significantly worsened 20 °C performance can be overcome by cycling under high pressure. However, ideally, ambient temperature operation would be possible at low pressures as well. The concept of formation cycles, wherein a cell is initially cycled under specialized conditions before nominal cycling, has been used to optimize the performance of lithium-ion cells. The idea is to use this formation procedure to set up beneficial conditions that will have ongoing positive effects. For lithium-ion cells, this means forming a robust SEI via a slow first charge-discharge cycle. Since we have observed that anode-free cells perform better at 40 °C, we were inspired to see if we could translate this formation idea to temperature. That is, to use a hot formation protocol where cells perform two cycles at 40 °C before 20 °C cycling. The results of this hot formation protocol are shown in **Figure 5.4**.

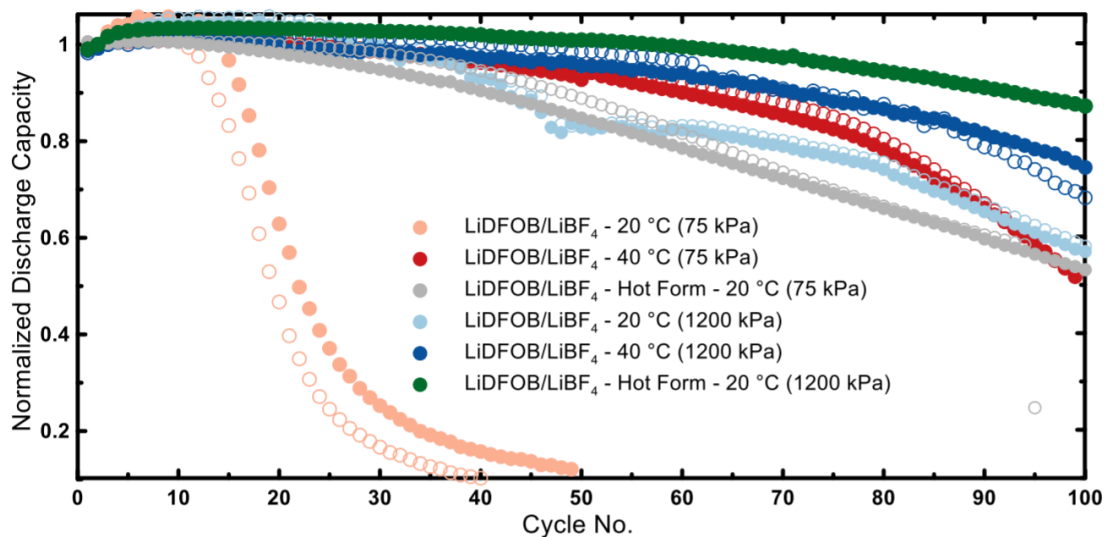


**Figure 5.4 | Hot formation.** Normalized capacity vs cycle for anode-free cells tested at different temperatures, pressures, and with hot formation. Hot formation (hot form) consists of two C/10 D/2 cycles at 40 °C before C/5 D/2 20 °C cycling. Cells were cycled between 3.6-4.5 V at C/5 D/2 with 0.6 M LiDFOB 0.6 M LiBF<sub>4</sub> FEC:DEC 1:2 electrolyte. Anode-free NMC532 cells were used. Pair cells are shown with open and closed symbols in the same colour.

After hot formation, cells cycled at low temperature and pressure (gray circles in **Figure 5.4**) exhibit a dramatically improved lifetime compared to cells cycled at 20 °C without hot formation (60 vs 20 cycles to 80% capacity). With hot formation, cells cycled at low temperature and pressure exhibit similar performance to cells cycled at 20 °C under high pressure as well as cells that cycled at 40 °C under low pressure. Therefore, decent 20 °C cycling of anode-free cells is enabled via the use of hot formation. Better yet, cells cycling under high pressure that underwent hot formation before 20 °C testing (green circles) perform even better than cells cycled under high pressure exclusively at 40 °C (blue circles).

The effect of hot formation on the cycle life of anode-free cells is quite remarkable. The long-lasting impact of just the first two cycles highlights the importance of lithium nucleation and the very first lithium plating and stripping steps. This enduring benefit is further demonstrated in **Figure 5.5** which shows SEM images comparing the lithium morphology after 20 cycles at 20 °C (**Figure 5.5a**) and after 20 cycles at 20 °C with hot

formation (**Figure 5.5b**). The superior lithium nucleation and growth enabled by hot formation can still be observed after 20 cycles at 20 °C, consistent with the superior cycling performance. However, improved lithium nucleation cannot explain the entirety of the behaviour observed here. In particular, at high pressure, cells cycled with hot formation that perform better than cells cycling exclusively at 40 °C—both should have the benefit of improved nucleation at elevated temperature. The difference in performance in this case is attributed to the decreased magnitude of parasitic reactions at 20 °C after hot formation. The effect of less electrolyte-electrode parasitic reactions was observed in Ref.<sup>45</sup> where we measured less gas formation in cells cycled at 20 °C after hot formation compared to those which cycled exclusively at 40 °C. In other words, the benefit of elevated temperature can be harnessed by hot formation, and then subsequent 20 °C operation is beneficial by minimizing parasitic reactions, similar to the behaviour of lithium-ion cells. The effect of higher temperature formation at 55 °C was also investigated but it did not yield any addition improvement to cycle life.<sup>45</sup>

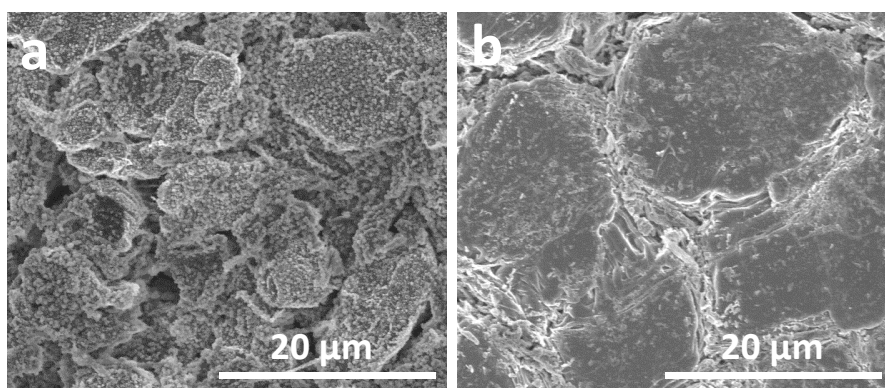


**Figure 5.5 | Hot formation impact on lithium morphology. a-b**, SEM images of lithium plated after 20 cycles at 20 °C (a) and 20 °C after hot formation (b). Samples were retrieved from cells at the top of charge (4.5 V) after cycling under low pressure between 3.6-4.5 V at C/5 D/2 with 0.6 M LiDFOB 0.6 M LiBF<sub>4</sub> FEC:DEC 1:2 electrolyte. The scale bars are 20 μm.

Since salt depletion is a major failure mode for cells with LiDFOB/LiBF<sub>4</sub> electrolyte, fewer parasitic reactions enabled by prolonged cycling at 20 °C after formation contribute to increased cycle life by extending the longevity of both salts. Another strategy to further

increase lifetime is to pair hot formation with high-concentration dual-salt electrolyte formulations. **Figure 5.6** shows the results of anode-free cells tested with high-concentration LiDFOB/LiBF<sub>4</sub> electrolyte formulations cycled under high and low pressure at 40 °C and at 20 °C after hot formation. Lithium-ion cells with the same NMC532 positive electrodes tested at 40 °C and at 20 °C are also included for comparison. Anode-free cells tested with hot formation exhibit similar or improved cycle life compared to their 40 °C counterparts. However, one thing to consider about 20 °C operation is that, due to impeded solid-state diffusion, the positive electrode will deliver less capacity, thereby reducing the energy density. **Figure 5.6b** shows that anode-free cells with high concentration dual-salt electrolyte cycled at 20 °C after hot formation exhibit a reduced energy density of ~1000 Wh/L compared to ~1150 Wh/L at 40 °C. This behaviour is also observed for the lithium-ion cells, which are reduced in energy density from ~700 Wh/L at 40 °C to ~600 Wh/L at 20 °C.

**Figure 5.6** shows two different tests using 2.0 M LiDFOB 1.4 M LiBF<sub>4</sub> electrolyte cycled under high pressure at 20 °C with hot formation. The first test was clamped at a higher pressure than the second test.<sup>§§</sup> As a result, the first test exhibits a superior normalized capacity retention. However, the initial energy density is even lower. The compounding effects to lithium diffusion of high concentration electrolyte, low temperature operation, and high pressure all contribute to this lower energy density. All three of these conditions improve lifetime, but at the cost of precious energy density. The cliché “there is no free lunch” is often true for lithium-ion and lithium metal cells where improving one performance metric comes at the cost of another.

---

<sup>§§</sup> These high pressure tests were performed rigid testing fixtures without pressure sensors, as described in Section 3.2.3 and 4.1.1. The average pressure during cycling is estimated to be around 1200 kPa. However, the clamping pressure is achieved by “feel” and therefore can result in some variation. In this case, it is clear that the first test was clamped to a higher pressure due to the decreased reversible capacity.

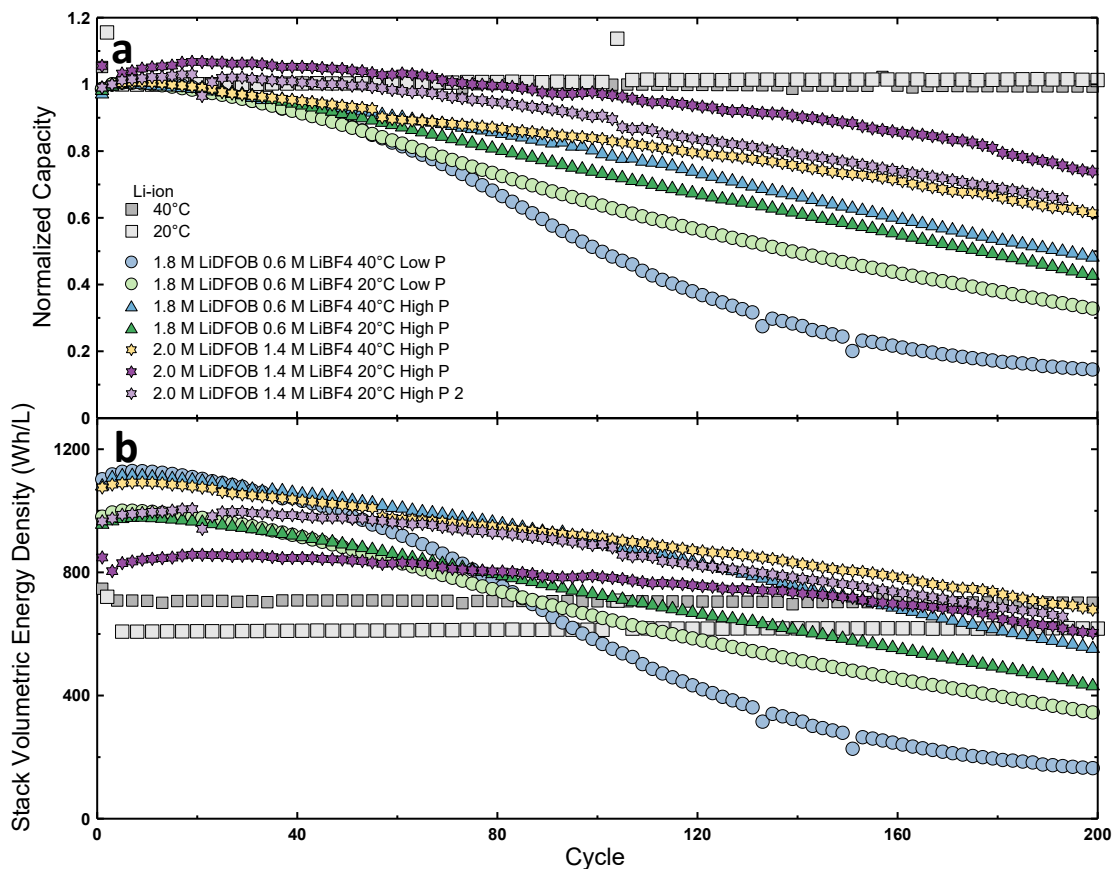


**Figure 5.6 | Best effort hot formation. a-b,** Normalized capacity (a) and stack volumetric energy density (b) vs cycle for anode-free cells tested with high-concentration dual-salt electrolyte and hot formation compared to Li-ion cells. Anode-free cells were cycled between 3.6-4.5 V at  $C/5$   $D/2$  at low pressure (Low P, 200 kPa) and high pressure (High P, ~1200 kPa) and at 40 °C or at 20 °C after hot formation. Li-ion cells were cycled between 3.0-4.3 V at  $C/3$   $D/3$  at 40 °C or 20 °C with 1.2 M  $\text{LiPF}_6$  EC:EMC 3:7 + 2% VC 2% DTD electrolyte. The average value of pair cells is shown.

## 5.2 Charge-Discharge Rates

So far, we have cycled anode-free cells with a 5 hour charge ( $C/5$ ) and a 2 hour discharge ( $C/2$ ). This is because it has long been established that plating lithium (charging) slowly benefits lifetime by forming more compact lithium morphologies.<sup>69,122,123</sup> However, these studies have been performed for lithium metal cells with excess lithium. Moreover, investigation as to the effect of discharge rate are limited.<sup>158</sup> Therefore, here we explore how the cycling rates impact the performance of anode-free cells with dual-salt electrolyte.

Three types of cycling protocols were tested. First, a symmetric protocol in which the charge and discharge rates were equal was used since lithium-ion cells are often tested in this way. An example voltage-time profile for this symmetric protocol is shown in the top panel of **Figure 5.7a**. We then tested two asymmetric charge-discharge protocols: one where the charge was faster than the discharge, and another with the charge being slower than the discharge. These two asymmetric protocols, asymmetric faster charge (AFC) and asymmetric slower charge (ASC) are shown in the middle and bottom panels of **Figure 5.7a**, respectively. For the asymmetric protocols, the charge was set to be 2.5 times faster or 2.5 times slower than the discharge. We tested a wide range of C-rates over an order of magnitude spanning from 1 hour to 20 hours. All C-rates tested are listed in **Table 5.1**.

**Table 5.1:** List of charge-discharge rates tested. C = charge, D = discharge.  $1C = 1D = 230 \text{ mA} \rightarrow 2.66 \text{ mA/cm}^2$ .

Symmetric		Asymmetric			
C/x	D/x	Faster Charge		Slower Charge	
C/x	D/x	C/x	D/2.5*x	C/2.5*x	D/x
C/2.5	D/2.5	C/2	D/5	C/2.5	D/1
C/5	D/5	C/4	D/10	C/5	D/2
C/10	D/10			C/10	D/4
C/20	D/20			C/20	D/8

### 5.2.1 Cycling Behaviour

The cycling performance of cells tested with the different charge-discharge protocols is shown in **Figure 5.7b-d**. The symmetric protocol resulted in cells lasting about 50 cycles to 80% capacity retention (**Figure 5.7b**). There is good agreement between the performance of all the symmetric C-rate tests except the fastest C/2.5 D/2.5 test which showed more severe capacity loss. The cells tested with the asymmetric faster charge (AFC) protocol exhibited a worse cycle life of about 40 cycles to 80% capacity retention (**Figure 5.7c**). It is unsurprising that this protocol with a faster charge results in worse cycle life since lithium plating is known to be less efficient at higher charge rates.<sup>69</sup> Finally, **Figure 5.7d** shows the results of cells tested with the asymmetric slower charge (ASC)

protocol. Here, when lithium is plated slower than when it is stripped, the cycle life was extended to about 80 cycles to 80% capacity retention, with the exception of the C/2.5 D/1 test which experienced worse capacity retention.

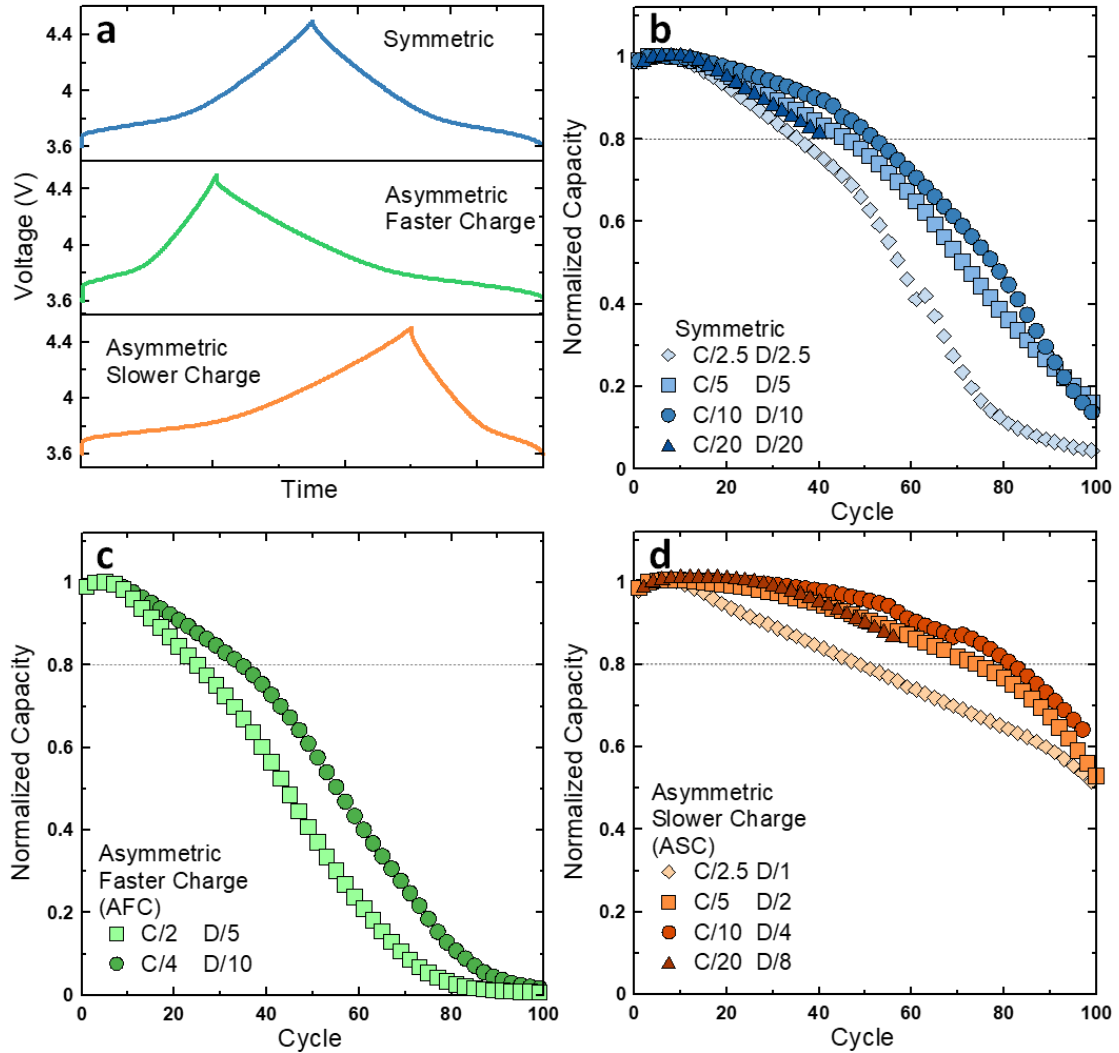


**Figure 5.7 | Charge-discharge rate test.** **a**, Voltage vs time profiles for the three types of charge-discharge protocols tested: symmetric charge-discharge, asymmetric faster charge (AFC), and asymmetric slower charge (ASC). **b-d**, Normalized capacity vs cycle for cells tested with a symmetric charge-discharge protocol (**b**), an asymmetric protocol with faster charge (**c**), and an asymmetric protocol with a slower charge (**d**). NMC532 anode-free cells were cycled between 3.6-4.5 V at 40 °C under low pressure with 0.6 M LiDFOB 0.6 M LiBF<sub>4</sub> FEC:DEC 1:2 electrolyte. The average of pairs cells is shown.

Again, it is unsurprising that plating at a slower rate would be beneficial, as this has been previously demonstrated in the literature.<sup>158</sup> However, here we show that it is not just the absolute charge and discharge rates that are important, but that the relative rates of charge and discharge impact performance. For example, the cycle life is not compromised by charging faster when doubling the charge rate from C/10 to C/5 provided the discharge rate is scaled accordingly to maintain the same ratio between the charge-discharge rates as shown in **Figure 5.7b** and **d**. Furthermore, tests with similar charge rates such as C/5 D/5 (symmetric), C/4 D/10 (AFC) and C/5 D/2 (ASC) demonstrate the benefit of having a comparatively slower charge than discharge, since the cycle life exhibited in **Figure 5.7b-d** is C/5 D/2 (ASC) > C/5 D/5 (symmetric) > C/4 D/10 (AFC).

**Figure 5.8a** shows the data displayed in **Figure 5.7b-d** on a single panel to emphasize the benefit to cycle life of the ASC protocol. Even the worst performing test of this protocol (C/2.5 D/1) retains 50% capacity after 100 cycles compared to the symmetric C/2.5 D/2.5 test which exhibits almost 0% capacity after 100 cycles—demonstrating that faster charging can be enabled by leveraging this asymmetric protocol. Although plotting normalized discharge capacity is useful for direct comparison of cycle life, one must realize that the C-rates tested here will also impact the deliverable capacity in mAh due to kinetic effects and lithium diffusion. Therefore, we have also included this data plotted as discharge capacity vs cycle as well as normalized capacity vs equivalent full cycle in **Figure A.15a** and **b**. This is important to consider because the deliverable capacity is directly related to the energy density, which of course is most important for practical applications. The stack volumetric energy density vs cycle is shown in **Figure A.16**.



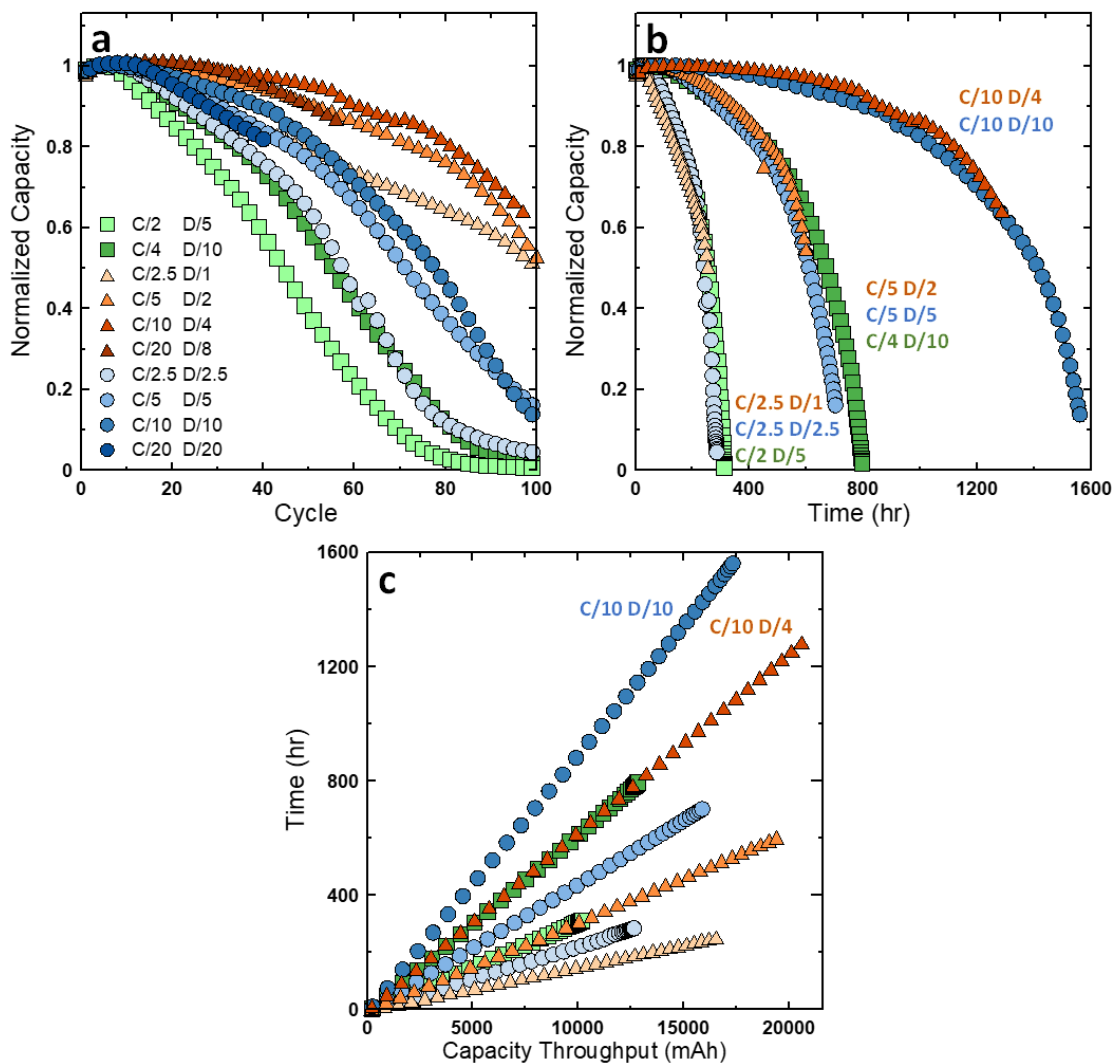


**Figure 5.8 | Rate test comparisons.** **a**, Normalized capacity vs cycle number for all charge-discharge rate tests; cells tested with a symmetric charge-discharge protocol (blue), an asymmetric protocol with faster charge (AFC, green), and an asymmetric protocol with a slower charge (ASC, orange). **b**, Normalized capacity vs time for all charge-discharge rate tests. **c**, Time cycled vs total capacity throughput. Anode-free cells were cycled between 3.6-4.5 V at 40 °C under low pressure with 0.6 M LiDFOB 0.6 M LiBF<sub>4</sub> FEC:DEC 1:2 electrolyte. The average of pairs cells are shown.

**Figure 5.8b** shows the rate test data plotted vs time. Surprisingly, unlike the cycle life which is benefited by tuning the relative rate of charge vs discharge with an asymmetric slower charge protocol, the calendar life only depends on the absolute charge rate. Regardless of the discharge rates, cells run with similar charging rates have virtually

identical calendar lives. Cells run with a charge rate of  $C/2.5$  last about 400 hours;  $C/5$  cells last about 800 hours and  $C/10$  cells last about 1600 hours. Calendar life is therefore simply scaled by the charge rate. **Figure 5.8a** and **b** reveal a surprising disparity between cycle life and calendar life: the discharge rate appears to have little impact on calendar life while significantly affecting cycle life. This is somewhat confusing in trying to determine what the optimal cycling protocol really is. For further insight, it is instructive to look at the total time vs total capacity cycled (capacity throughput) in **Figure 5.8c**. Obviously, the highest capacity throughput possible is desired. **Figure 5.8c** shows that cells run with the asymmetric slower charge protocol (orange triangles) generally deliver the highest capacity throughput. The two highest throughputs are given by the ASC  $C/10$   $D/4$  and the symmetric  $C/10$   $D/10$  tests. The main difference between these tests is that the symmetric protocol delivers the same throughput stretched over a longer time. Ultimately, the answer to which of these protocols is optimal will depend on whether the desired application necessitates capacity delivered over a longer or shorter period of time.

Increasing impedance during cycling plays a role in the capacity fade observed in **Figure 5.7** and **Figure 5.8**. We track resistance growth during cycling by monitoring the growth of delta  $V$  ( $\Delta V$ ) which is plotted in **Figure 5.9a-c** for each of the charge-discharge protocols tested here. Protocols with higher C-rates have a higher  $\Delta V$  since  $\Delta V$  is proportional to the applied current. **Figure 5.9a-c** shows that there is severe impedance growth in most cells except for those cycled with the asymmetric slower charge protocol where impedance is relatively stable. This impedance growth can be largely ascribed to electrolyte salt consumption as well as insufficient electrolyte wetting of the electrodes as the lithium morphology degrades, as discussed in Section 4.2. However, it is important to note that the capacity fade cannot be entirely attributed to impedance growth and that these different cycling protocols are affecting the rate of lithium inventory loss.

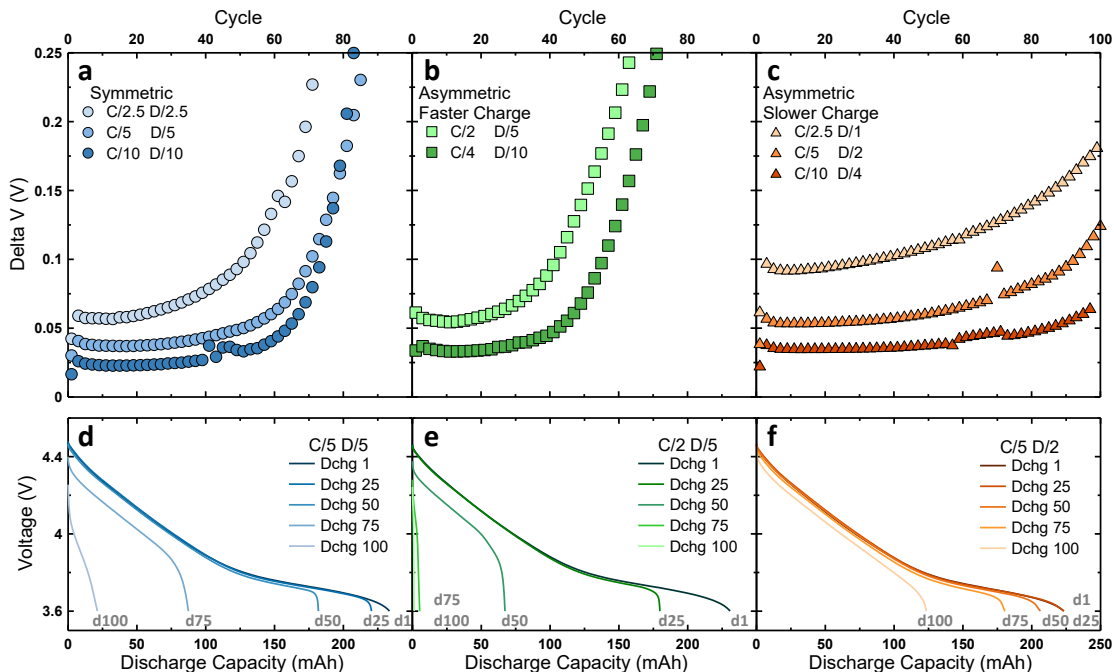


**Figure 5.9 | Impedance growth and inventory loss. a-c,** Delta V vs cycle for cells tested with a symmetric charge-discharge protocol (a), an asymmetric protocol with faster charge (b), and an asymmetric protocol with a slower charge (c). **d-f,** Discharge voltage curves for cells tested with a symmetric charge-discharge C/5 D/5 rate (d), an asymmetric protocol with a C/2 D/5 rate (e), and an asymmetric protocol with a C/5 D/2 rate (f). NMC532 anode-free cells were cycled between 3.6-4.5 V at 40 °C under low pressure with 0.6 M LiDFOB 0.6 M LiBF<sub>4</sub> FEC:DEC 1:2 electrolyte.

Capacity loss due to impedance growth vs lithium inventory loss can be deconvoluted by careful study of the discharge voltage curves. The voltage vs capacity curves for cycles 1, 25, 50, 75 and 100 for an example cell of each protocol are shown in **Figure 5.9d-f**. The voltage curves for the symmetric C/5 D/5 protocol are shown in **Figure 5.9d**. For cycles 1, 25 and 50, the voltage curves are virtually on top of each other indicating no evidence of significant impedance growth (which would appear as a downward shift of the voltage curves). Regardless, the voltage curves get cut off at lower discharge capacities. With no significant impedance growth, this must result from a depleted lithium inventory no longer able to fully lithiate the positive electrode. Therefore, the ~50 mAh capacity loss through 50 cycles exhibited in **Figure 5.9d** is a result of lithium inventory loss. For the asymmetric faster charge C/2 D/5 test shown in **Figure 5.9e**, the same behaviour is observed but it is accelerated, with ~50 mAh of lithium inventory loss occurring through only 25 cycles.

Finally, for the asymmetric slower charge C/5 D/2 test (**Figure 5.9f**), the voltage curves exhibit minimal vertical shift due to impedance growth through 75 cycles. Therefore, the capacity loss up to cycle 75 can be attributed mainly to lithium inventory loss. Since only ~50 mAh is lost through 75 cycles compared to the same capacity lost after only 50 and 25 cycles with the other protocols, the asymmetric slower charge protocol clearly results in less lithium inventory loss per cycle.

### 5.2.2 Lithium Morphology

To explore why these different charge-discharge protocols affect lithium inventory loss, the lithium morphologies generated in cells after 20 cycles with these protocols were studied, shown in **Figure 5.10**. The morphology is comprised of varying degrees of compact lithium nodules with some high surface area porous lithium deposits between the grains. Using the symmetric C/5 D/5 protocol (**Figure 5.10a**), medium sized 10-15  $\mu\text{m}$  lithium nodules are formed. There is some space between the nodules, and areas of porous lithium deposits can be identified. Since the ideal lithium morphology should have minimal surface area, these medium sized nodules result in a moderate cycle life of ~50 cycles. The lithium morphologies generated in cells cycled with an asymmetric faster charge protocol are shown in **Figure 5.10b-c**. Smaller 5-10  $\mu\text{m}$  lithium grains are formed with this protocol. The faster C/2 D/5 protocol (**Figure 5.10b**) exhibits loose grains with interspersed porous lithium deposits, whereas the slower C/4 D/10 protocol (**Figure 5.10c**) exhibits a more compact morphology. Smaller lithium grains, concomitant with increased surface area, are known to result in lower lifetime,<sup>69</sup> consistent with the worse ~40 cycle lifetime for cells cycled with this asymmetric faster charge protocol. The lithium morphologies generated with the superior performing asymmetric slower charge protocol are shown in **Figure 5.10d-f**. With this protocol, large 15-25  $\mu\text{m}$  lithium grains are formed. Porous lithium deposits are observed between these large grains at C/2.5 D/1 (**Figure 5.10d**) and less so at C/5 D/2 (**Figure 5.10e**). At C/10 D/4 (**Figure 5.10f**), the large lithium grains are tightly packed resulting in a flat lithium mosaic. This ideal lithium morphology should result in the lowest lithium inventory loss, and this is consistent with a cycle life of about 80 cycles obtained using this protocol. It is interesting to observe that although there is a stark

difference of morphology between the C/5 D/2 (**Figure 5.10e**) and C/10 D/4 (**Figure 5.10f**) tests, the capacity retention of these two tests are very similar (**Figure 5.7d**).

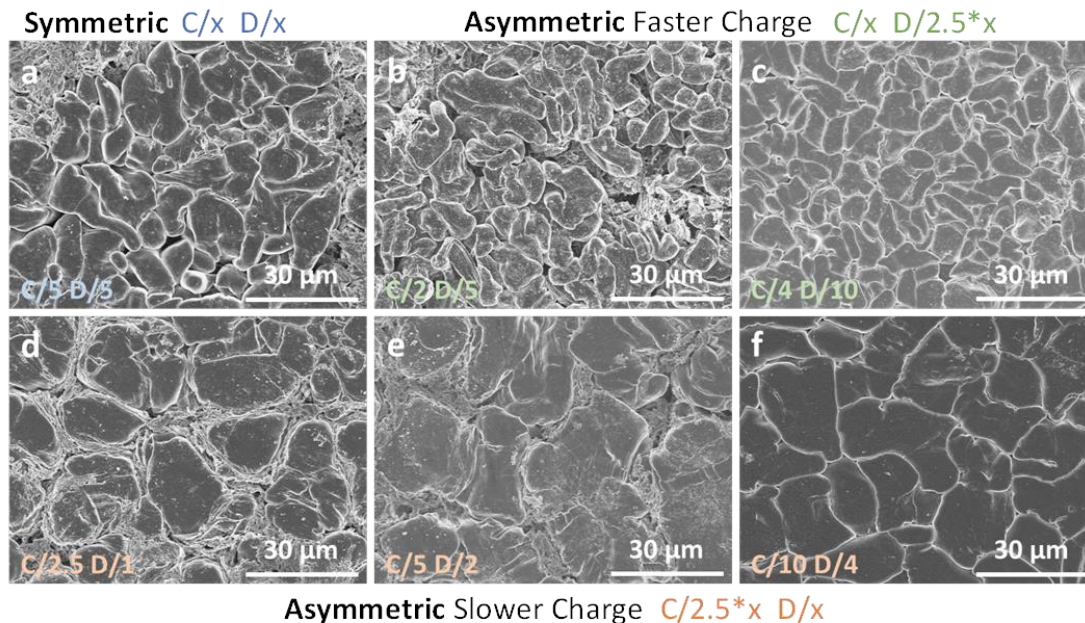


**Figure 5.10 | Lithium morphology from different charge-discharge rates.** **a**, Lithium morphology generated in a cell cycled with a symmetric charge-discharge protocol of C/5 D/5. **b-c**, Morphology from an asymmetric faster charge protocol of C/2 D/5 (**b**) and C/4 D/10 (**c**). **d-f**, Morphology from an asymmetric slower charge protocol of C/2.5 D/1 (**d**), C/5 D/2 (**e**) and C/10 D/4 (**f**). Lithium samples were retrieved from cells cycled 20 times between 3.6-4.5 V at 40 °C under low pressure with 0.6 M LiDFOB 0.6 M LiBF<sub>4</sub> FEC:DEC 1:2 electrolyte.

**Figure 5.7-Figure 5.9** show that beyond simply charging slower, the relative rates of charge and discharge are important. **Figure 5.10** showed that it is optimal to use an asymmetric protocol where the charge is slower than the discharge because this facilitates a superior lithium morphology. However, the question of why charging slow and discharging fast enables superior lithium morphology remains. **Figure 5.11** tries to answer this question with a cartoon model illustrating the proposed mechanisms which drive this behaviour. The blue spheres represent lithium cations in the electrolyte and the grey spheres represent lithium atoms plated in metallic form. This model is based on how lithium cations

are distributed in the electrolyte solution during different charge-discharge conditions, and how this contributes to uniform vs preferential lithium stripping and plating.

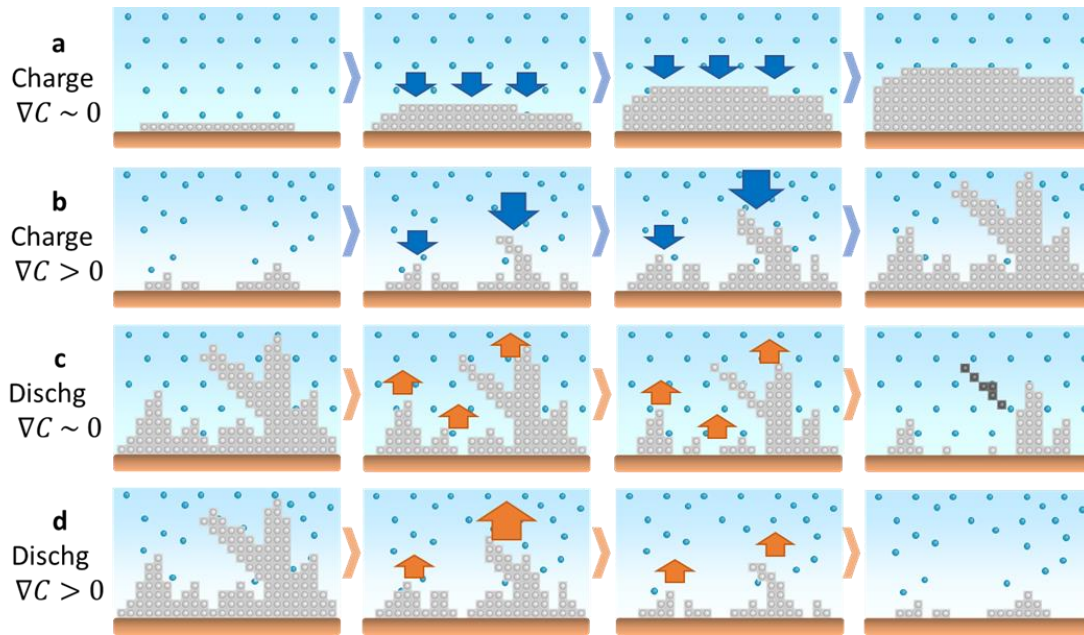


**Figure 5.11 | Proposed plating and stripping mechanisms. a,** Lithium plating during slow charge in an environment with a minimal concentration gradient ( $\nabla C \sim 0$ ) resulting in a dense morphology. **b,** Lithium plating during fast charge in an environment with a significant concentration gradient ( $\nabla C > 0$ ) resulting in porous morphology. **c,** Lithium being stripped from a porous morphology during slow discharge in an environment with a minimal concentration gradient resulting in a non-uniform stripped surface and generating dead lithium. **d,** Lithium being stripped from a porous morphology during fast discharge in an environment with a significant concentration gradient resulting in a fairly uniformly stripped surface. The blue spheres represent lithium cations in the electrolyte and the gray spheres represent lithium plated in metallic form. The dark grey spheres represent mechanically isolated lithium.

**Figure 5.11a** depicts lithium plating during slow charging conditions. The concentration gradient that develops in the electrolyte is proportional to the applied current.<sup>159,160</sup> Therefore, during slow charge, the concentration gradient will be less than during a fast charge. Although some concentration gradient will always exist for any finite applied current, for the sake of this model we say that the concentration gradient is minimized ( $\nabla C \sim 0$ ) during a slow charge. Therefore, the lithium cations are uniformly distributed in the electrolyte in **Figure 5.11a**. As a result, no preferential plating will occur, facilitating



homogenous lithium nucleation and growth during plating.<sup>74</sup> This enables large lithium grains or even highly favorable lithium columns to form, which is the benefit of a slow charge.

**Figure 5.11b** depicts lithium plating under fast charging conditions. In this scenario, a significant concentration gradient ( $\nabla C > 0$ ) forms in the electrolyte. Although theoretically this concentration gradient is strictly parallel to the applied current (z direction), **Figure 5.11b** also shows a heterogenous lithium cation distribution along the xy-plane (parallel to the current collector). In reality, the xy distribution of lithium cations will never be perfectly uniform, and any non-uniformities will be exacerbated when the concentration of  $\text{Li}^+$  is depleted at the plating surface due to significant concentration gradients. Electrolyte convection will also interfere in the xy distribution of cations, also exacerbated by concentration gradients.<sup>77</sup> Therefore, significant concentration gradients will initiate non-uniform localized current densities,<sup>74</sup> as depicted with the non-uniform xy distribution of lithium cations. Moreover, the transport properties of the SEI will influence lithium nucleation. Areas of the passivation film with lower resistance will drive a higher localized current density and promote lithium deposition resulting in non-uniform lithium nucleation.<sup>72,73</sup> Heterogenous lithium plating then becomes self-accelerating, with increased localized current densities generated at the tips of the lithium protrusions attracting further deposition.<sup>77,78</sup> This initiates a high surface area, porous morphology. Such a tortuous microstructure severely inhibits mass transport of lithium cations and enhances the concentration gradient within the porous lithium surface referred to as the electrolyte confinement region.<sup>75,76</sup> Therefore, inhomogeneous local current densities facilitated by concentration gradients during fast charge initiate non-uniform lithium plating and thus increased lithium inventory loss. This is, in part, why the asymmetric faster charge protocol performs the worst.

**Figure 5.11c-d** illustrate the proposed mechanism of lithium stripping during slow and fast discharge. During a slower discharge, lithium will be stripped evenly from the surface because the minimal concentration gradient ( $\nabla C \sim 0$ , **Figure 5.11c**) facilitated by the slow discharge disallows inhomogeneous local current densities to develop. The issue with

uniformly stripping an initially non-uniform surface is that this will perpetuate the non-uniform surface throughout discharge. Without preferentially stripping the tips, the lithium morphology will remain mossy. As a result, the base of the lithium protrusions may be stripped before the tips, resulting in the formation of isolated dead lithium,<sup>70</sup> depicted in the fourth panel of **Figure 5.11c**. This is second reason why the asymmetric faster charge protocol performs the worst: slower discharge perpetuates high surface area morphology and precipitates increased lithium inventory loss.

In contrast, during a faster discharge, a significant concentration gradient will develop at the lithium surface ( $\nabla C > 0$ , **Figure 5.11d**) due to the higher current and electrolyte confinement in the porous lithium morphology.<sup>75</sup> This enables non-uniform local current densities to form, resulting in increased current densities at the most accessible lithium surfaces thereby resulting in preferential stripping of the tips of the lithium protrusions. This facilitates the removal of non-uniform lithium deposits and results in a fairly uniform surface at the end of discharge, shown in the fourth panel of **Figure 5.11d**. To summarize, we like discharging fast for the opposite reason we like charging slow: during charge, we do not want any preferential plating, whereas during discharge, we want preferential stripping. This acts to correct any mossy lithium morphology that has been previously generated. The asymmetric slower charge protocol facilitates this optimal plating and stripping behaviour, which is why it is the optimal charge-discharge protocol demonstrated here.

### 5.3 Depth of Discharge & Lithium Utilization

The next cycling condition we consider is depth of discharge (DoD). The depth of discharge is determined by the lower cut-off voltage cells are discharged to and is measured as the percent capacity discharged of the total deliverable capacity. For example, the first charge of our NMC532 anode-free cells to 4.5 V delivers an areal capacity of 3.16



mAh/cm<sup>2</sup>. Upon discharge to 3.6 V, only 2.56 mAh/cm<sup>2</sup> is delivered. Assuming all the capacity from the first charge could theoretically be discharged,<sup>\*\*\*</sup> then

$$\frac{2.56 \text{ mAh/cm}^2}{3.16 \text{ mAh/cm}^2} * 100\% = 81\%,$$

*i.e.*, cycling from 3.6-4.5 V results in a depth of discharge of about 80%. In an anode-free cell, limiting the depth of discharge means that not all the lithium plated during the first charge is stripped during discharge, thereby creating a lithium reservoir. The capacity of the reservoir divided by the capacity cycled is conventionally termed the “lithium excess”. Therefore, in the above example, the lithium excess is about 0.2. Increased lithium excess via limited depth of discharge has previously been shown to be beneficial to the lifetime of lithium metal cells.<sup>161</sup> Changing the depth of discharge also affects the areal capacity of lithium plated and stripped with every cycle. Therefore, in this section, we investigate how depth of discharge and lithium utilization impact the lifetime of anode-free NMC532 cells with dual-salt electrolyte.

### 5.3.1 Depth of Discharge

**Figure 5.12** demonstrates how the chosen lower cut-off voltage and depth of discharge creates a lithium reservoir. **Figure 5.12a** shows the very first charge-discharge cycle of an NMC532 anode-free cell. Discharging to 3.6 V reveals that not all the capacity from the first charge is delivered. This irretrievable capacity is generally referred to as the cathode irreversible capacity (IRC), and the ~20% IRC exhibited here is typical of a single crystal NMC532 cathode if it is only discharged to 3.6 V.<sup>162</sup> However, **Figure 5.12a** shows that most of this capacity can be recovered through a deep discharge to 1.25 V via a capacity plateau appearing at 1.5 V. Mueller-Neuhaus *et al.* demonstrated this phenomenon and

---

<sup>\*\*\*</sup> Some lithium inventory is lost to the formation of dead lithium, so not all the capacity from the first charge is truly available to be discharged. However, calculating DoD by dividing the discharge capacity by the first charge capacity is the most straightforward method. Therefore, it should be noted that this method systematically underestimates DoD by a few percent.

identified that “irreversible” capacity is a misnomer—the capacity is not irreversibly lost, but merely impeded due to sluggish kinetics in  $\text{Li}_x\text{MO}_2$  materials as  $x \rightarrow 1$ .<sup>163</sup> This was further confirmed by Kang *et al.* for a variety of  $\text{Li}_x\text{MO}_2$  materials.<sup>164</sup>

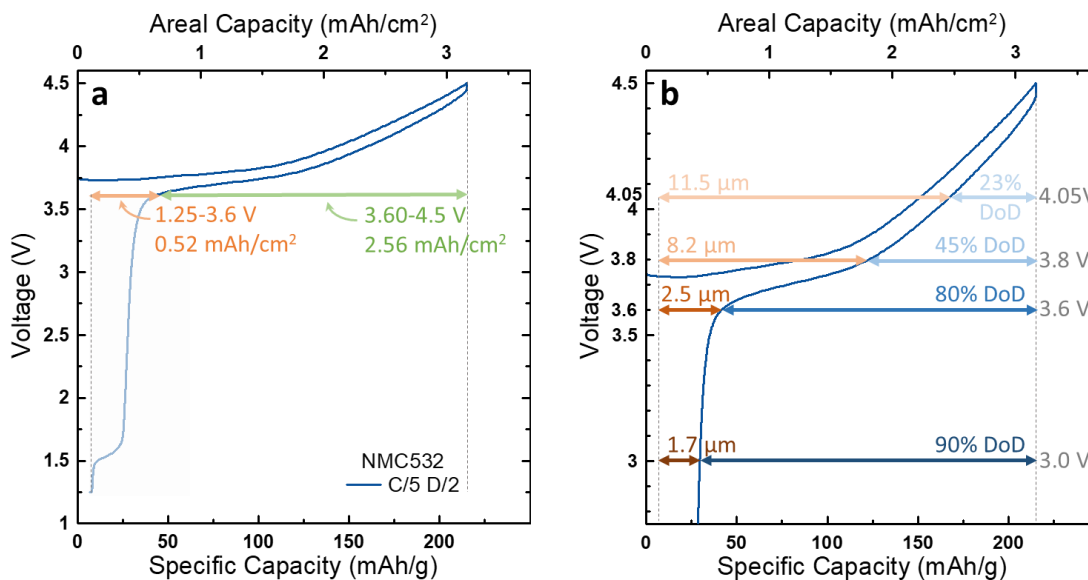


**Figure 5.12 | Creating a lithium reservoir with a limited depth of discharge.** a-b, Voltage vs specific capacity (bottom axis) and areal capacity (top axis) of the first charge-discharge of a NMC532 anode-free cell. The capacity delivered during a typical 4.5-3.6 V discharge is highlighted with a green arrow, and the capacity delivered during a deep 3.6-1.25 V discharge is highlighted with an orange arrow (a). The depths of discharge and thickness of lithium reservoirs are highlighted with blue and orange arrows, respectively, for cells cycled with lower cut-off voltages of 3.0, 3.6, 3.8 and 4.05 V (b). Cells were charged to an upper cut-off voltage of 4.5 V at 40 °C with 0.6 M LiDFOB 0.6 M LiBF<sub>4</sub> FEC:DEC 1:2 electrolyte.

The areal capacity delivered during charge in **Figure 5.12a** is 3.16 mAh/cm<sup>2</sup>. The capacity available for discharge can be separated into three regions. Between 3.6-4.5 V, there is 2.56 mAh/cm<sup>2</sup> of reversible capacity. Between 1.25-3.6 V, there is 0.52 mAh/cm<sup>2</sup> of capacity that is not reinserted into the cathode during typical 3.6-4.5 V cycling. This does not account for all the capacity delivered during the first charge; 2.56 + 0.52 = 3.08 mAh/cm<sup>2</sup>. The remaining 0.08 mAh/cm<sup>2</sup> is truly irreversible capacity—lithium inventory that has been consumed to form the SEI and lost to mechanically isolated lithium. Technically, since this capacity is not available, it should not be considered in the DoD

calculation. However, a deep discharge to 1.25 V is not always performed and this capacity is not always known. Therefore, for simplicity, the DoD is calculated as a percentage of the first charge capacity. During standard voltage range cycling between 3.6-4.5 V, the extra 0.52 mAh/cm<sup>2</sup> which is not reinserted into the cathode remains plated on the current collector. This acts as a small (~2.5 μm) lithium reservoir formed *in-situ*. Like any lithium excess, normally achieved in lithium metal cells with lithium foils thicker than 100 μm (20 mAh/cm<sup>2</sup>), this small lithium reservoir can compensate for lithium inventory loss during cycling until it is depleted.

**Figure 5.12** demonstrates that even in an anode-free cell built with zero excess lithium, a lithium reservoir is formed *in-situ*. The capacity of the lithium reservoir can be controlled via the lower cut-off voltage, demonstrated in **Figure 5.12b**. A higher lower cut-off voltage results in a thicker lithium reservoir and a lower the depth of discharge. In this work, we test four different depths of discharge, illustrated in **Figure 5.12b**. **Table 5.2** lists the four voltage ranges highlighted in **Figure 5.12b** and their corresponding depth of discharge, Li excess, reservoir capacity and thickness. The lithium excess is calculated for any DoD as  $Li\ excess = (100 - DoD)/DoD$ . Forming a lithium reservoir by limiting the depth of discharge allows for extremely thin (1-10 μm) and very small values of Li excess to be created. A lithium reservoir will extend the lifetime of a lithium metal cell by facilitating the replacement of lost lithium inventory during cycling. In conventional lithium metal cells, these reservoirs are implemented as thick lithium foils which significantly reduce cell energy density. By creating ultra thin lithium reservoirs via tuning the lower cut-off voltage, lifetime should be extended without significantly impacting energy density.

**Table 5.2:** Parameters of the depth of discharge experiment.

Voltage Range (V)	Depth of Discharge (%)	Li Excess	Areal Capacity (mAh/cm <sup>2</sup> )	Reservoir (mAh/cm <sup>2</sup> )	Reservoir (mAh)	Reservoir (μm)
3.00-4.5	90	0.11	2.75	0.35	30	1.7
3.60-4.5	80	0.25	2.57	0.52	45	2.5
3.80-4.5	45	1.2	1.39	1.70	146	8.2
4.05-4.5	23	3.3	0.71	2.38	204	11.5

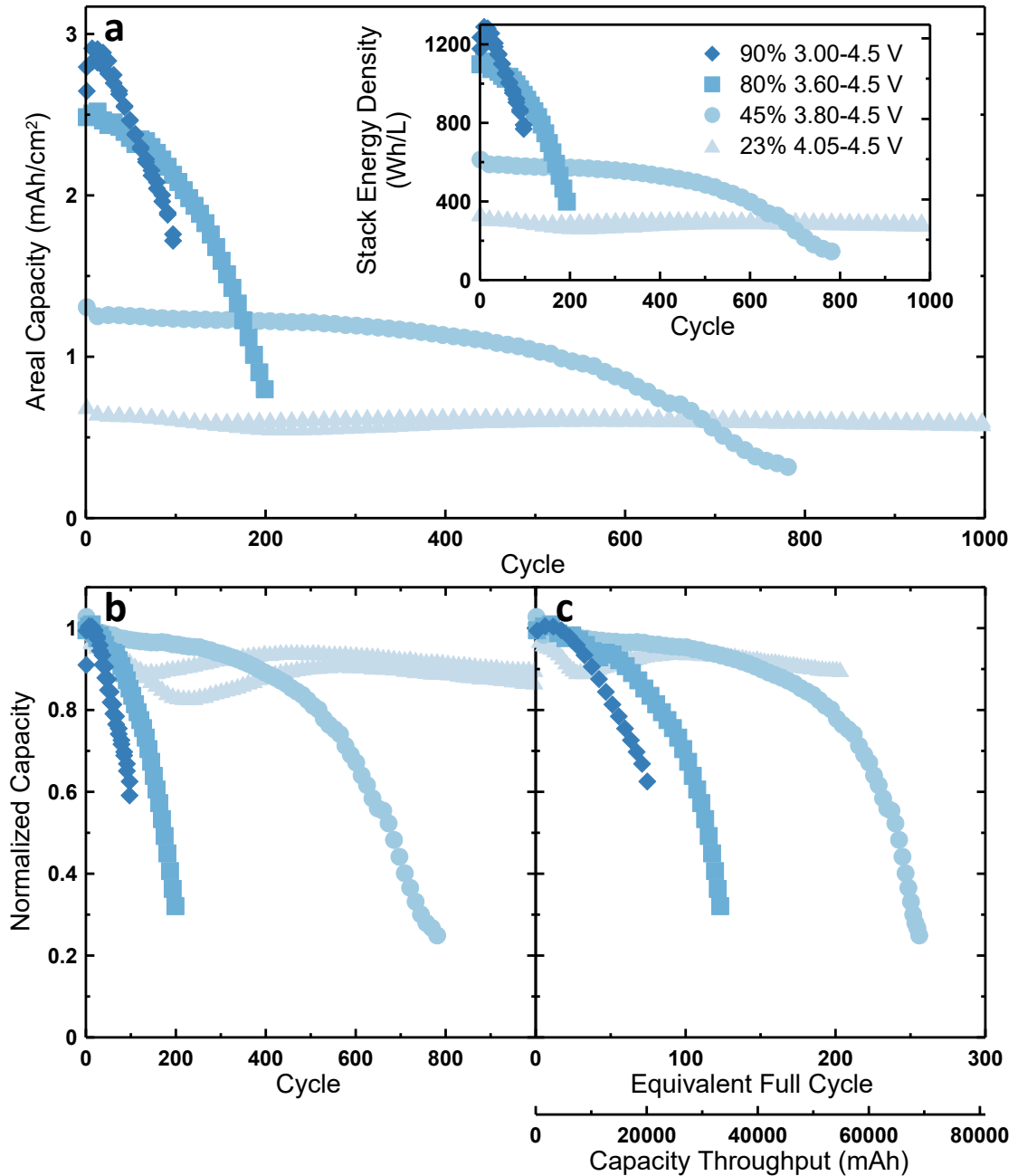


**Figure 5.13 | Depth of discharge test.** **a**, Areal capacity vs cycle and volumetric stack energy density vs cycle (inset) for cells cycled from 4.5 V down to different lower cut-off voltages and corresponding depths of discharge as indicated in the legend. **b-c**, Normalized capacity vs cycle (**b**) and normalized capacity vs equivalent full cycle and capacity throughput (**c**). One equivalent full cycle has the same capacity throughput as a single 100% DoD cycle. NMC532 anode-free cells were cycled at C/5 D/2 at 40 °C under high pressure (1200 kPa) with 1.4 M LiDFOB 0.4 M LiBF<sub>4</sub> FEC:DEC 1:2 electrolyte.

**Figure 5.13** shows the cycling performance for cells tested with different depths of discharge. The upper cut-off voltage was 4.5 V for all experiments and the lower cut-off voltages tested were 3.0 V, 3.6 V, 3.8 V and 4.05 V, corresponding to DoDs of 90, 80, 45 and 23% and Li excesses of 0.11, 0.25, 1.2 and 3.3. These depths of discharge correspond to a cycled areal capacity (and lithium reservoir thickness) of, from highest to lowest DoD, 2.75 mAh/cm<sup>2</sup> (1.7 μm), 2.57 mAh/cm<sup>2</sup> (2.5 μm), 1.39 mAh/cm<sup>2</sup> (8.2 μm) and 0.71 mAh/cm<sup>2</sup> (11.5 μm). These values are shown in **Figure 5.12b** and **Table 5.2**.

**Figure 5.13a** shows the cycling results plotted as areal capacity vs cycle. Since the areal capacity will affect the cell energy density, the stack volumetric density is shown for context in the inset. **Figure 5.13b** shows normalized capacity vs cycle. The deepest DoD down to 3.0 V results in a 40% capacity loss in 100 cycles. The same capacity loss occurs after over 160 cycles at 80% DoD to 3.6 V, and over 630 cycles at 45% DoD to 3.8 V. The shallowest DoD discharging only to 4.05 V experiences only a 10% capacity loss through 1000 cycles which is not surprising given a Li excess of 3.3. Clearly, limiting the depth of discharge (increasing Li excess) has a significant positive impact on cycle life. This can be attributed to having a larger lithium reservoir to replenish lost lithium. However, the lower areal capacity being cycled might also be contributing to this positive effect; cycling less lithium with every charge-discharge may mitigate lithium loss to parasitic reactions and mechanical isolation.

To try to deconvolute the effects of lowered areal capacity and the Li excess, this data was plotted vs equivalent full cycle (**Figure 5.13c**). The number of equivalent full cycles was calculated by taking the rolling sum of discharge capacity divided by the first charge capacity (~270 mAh). This measures how many cycles would have accrued if cycled at 100% DoD. In other words, this is a normalized capacity throughput. Therefore, the capacity throughput can be calculated by multiplying the number of equivalent full cycles by the first charge capacity of 270 mAh, as displayed in the bottom axis of **Figure 5.13c**. Plotting equivalent full cycles provides a head-to-head comparison of total amount of lithium cycled between the different DoDs. For example, it takes about four 23% DoD cycles to accrue one equivalent full cycle. If the 23% DoD cells were able to accumulate

over 1000 normal cycles in comparison to the 100 cycles achieved by the 90% DoD cells only because they were cycling less lithium per cycle at a lower areal capacity—*i.e.* if only the total amount of lithium cycled determined cell lifetime—then a cell cycling with a quarter of the areal capacity should only be four times better vs cycle (**Figure 5.13b**), and should be equivalent when plotted vs equivalent full cycles (**Figure 5.13c**). However, this is not the case. **Figure 5.13c** shows that when plotted vs equivalent full cycles, there is still a significant benefit for cells cycled to a lower depth of discharge. The achievable lithium throughput is increased at lower DoDs.

### 5.3.2 Lithium Utilization

Operating with higher areal capacities may be detrimental to cycle life due to generating more lithium surface area concomitant with cycling a larger volume of lithium. More lithium-electrolyte parasitic reactions facilitate lithium inventory loss as well as accelerate electrolyte degradation. Additionally, higher volumes of lithium stripping can increase the likelihood of forming mechanically isolated dead lithium.<sup>123</sup> To further examine the impact of cycling with different areal capacity and deconvolute this effect from the Li excess, cells with the same Li excess were tested with different areal capacities in **Figure 5.14a**. This was done by cycling to different upper cut-off voltages while maintaining same lower cut-off voltage of 3.0 V, corresponding to a Li excess of 0.11 and a 1.7  $\mu\text{m}$  thick lithium reservoir. These capacity vs cycle data for cells cycled with a fixed, small lithium reservoir and different upper cut-off voltages of 4.33, 3.81 and 3.74 V are plotted in red in **Figure 5.14a**, overlaid on top of cells with similar areal capacities and larger lithium reservoirs in blue for comparison. **Figure 5.14a** shows that despite similar areal capacities, the cells with smaller lithium reservoirs plotted in red perform worse than the cells with larger lithium reservoirs in blue. This suggests that the magnitude of the Li excess impacts the cycle life more than the cycled areal capacity, at least for areal capacities less than 3  $\text{mAh}/\text{cm}^2$  tested here. Although it should be noted that this is not a perfect apples-to-apples comparison since the different upper cut-off voltages of cells tested may also affect performance. However, lithium-lithium symmetric cells cycling different areal capacities support this finding.<sup>165</sup>

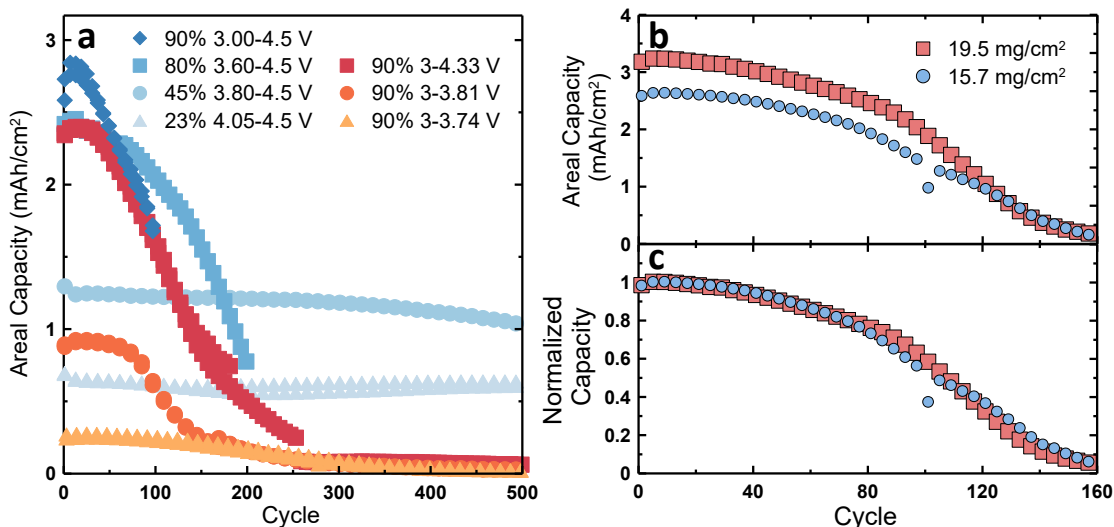


**Figure 5.14 | Impact of areal capacity vs lithium reservoir size.** **a**, Areal capacity vs cycle for cells cycled with different areal capacities under a fixed 90% DoD (small lithium reservoir, in red) and with limited DoDs (larger lithium reservoirs, in blue). The DoDs and voltage ranges are indicated in the legend. **b-c**, Cells cycled under the same conditions (3.6-4.5 V, 80% DoD) otherwise identical except for the positive electrode loading (19.5 vs 15.7 mg/cm<sup>2</sup>) resulting in a 20% difference in areal capacity, plotted as areal capacity (**b**) and normalized capacity (**c**) vs cycle. NMC532 anode-free cells were cycled at C/5 D/2 at 40 °C under high pressure (1200 kPa) with 1.4 M LiDFOB 0.4 M LiBF<sub>4</sub> FEC:DEC 1:2 electrolyte.

A perfect apples-to-apples comparison would be testing two cells under the same conditions—with the same depth of discharge, Li excess and voltage range—but with different areal capacity. This was done in **Figure 5.14b-c** which show cycling results for two cells otherwise identical except for the positive electrode loading—19.5 vs 15.7 mg/cm<sup>2</sup>. These loadings correspond to initial areal capacities of 3.2 vs 2.6 mAh/cm<sup>2</sup>, or a 20% difference in lithium capacity being cycled. **Figure 5.14b** shows the areal capacity vs cycle and **Figure 5.14c** shows the normalized capacity vs cycle. Comparing the normalized capacity retention, the performance of these two cells with different areal capacities are virtually identical. Unfortunately, anode-free pouch cells with only a 20% difference in positive electrode loading and areal capacity were available to test in this way. A more robust test would involve pouch cells with areal capacities that varied by an order of magnitude. In any event, these results suggest that areal capacity may not have as

significant an effect on the performance of lithium metal cells as has more conventionally been thought, at least for areal capacities less than 3 mAh/cm<sup>2</sup>.

**Figure 5.13** and **Figure 5.14** indicate that limiting the depth of discharge extends cycle life by providing a larger Li excess. **Table 5.2** listed the capacity of the lithium reservoir for each DoD. These anode-free cells should not exhibit capacity fade via lithium inventory loss until the lithium reservoir is depleted. For example, using our standard voltage range of 3.60-4.5 V (80% DoD), there is a 0.52 mAh/cm<sup>2</sup> lithium reservoir formed. Therefore, 45 mAh (over the entire 86.58 cm<sup>2</sup> area cell) of lithium inventory loss via SEI formation and mechanical lithium isolation can occur until this reservoir is depleted and capacity loss is observed. This is why lithium metal cells built with thick lithium foils and significant lithium reservoirs (>100 μm, 20 mAh/cm<sup>2</sup>) can exhibit seemingly stable cycling for hundreds of cycles even despite lower cycling efficiencies than the dual-salt electrolyte system used here. Beyond replenishing lost lithium inventory, Fang *et al.* have found that plating lithium on top of a lithium reservoir is beneficial for maintaining a compact lithium morphology.<sup>85</sup> Lithium plating on lithium has a lower overpotential than lithium plating on copper. Therefore, a lithium reservoir improves lithium nucleation.

Limiting the depth of discharge thus improves cycle life for the reasons described here. However, if one's goal is to reveal the “true” cycling efficiency of lithium metal with anode-free cells, researchers should cycle with a high DoD down to a lower cut-off voltage of 3.0 V or lower.

## 5.4 Optimized Cycling Conditions

### 5.4.1 Intermittent High DoD Protocol

Now that we have determined optimal cycling conditions for anode-free cells with dual-salt electrolyte—cycling at 20 °C with hot formation, using an asymmetric slower charge protocol (C/5 D/2) with a limited depth of discharge—we can start developing different cycling protocols to take advantage of these synergies. **Figure 5.13** shows that there is a compromise to be made between energy density and cycle life when using limited depths



of discharge. Between 80% and 45% DoD, there should be an intermediary depth of discharge that will provide a longer lifetime than 80% DoD while delivering a higher energy density than 45% DoD. To this end, we developed a specialized intermittent high DoD protocol. Cells were cycled for the most part at a limited depth of discharge (50% DoD; 3.75-4.5 V) with intermittent high depth of discharge (80%; 3.60-4.5 V) cycles. The protocol repeats 10 limited DoD cycles followed by 2 high DoD cycles. The limited DoD voltage range was selected to deliver a stack energy density comparable to a lithium-ion cell with the same cathode (~700 Wh/L). The high DoD voltage range was selected as a compromise between delivering the highest stack energy density while leaving a small lithium reservoir to maximize cycle life. This intermittent protocol was inspired by the compromise of silicon-graphite composite electrodes. Silicon electrodes deliver higher energy density but lower lifetime than graphite electrodes. With silicon-graphite composite electrodes, it is possible to achieve long lifetime and high energy density. Similarly, with this specialized protocol, we utilize a limited depth of discharge to enable longer lithium metal cycle life while intermittently harnessing the high energy density of anode-free cells with a deep discharge.

**Figure 5.15** shows the cycling performance of cells subjected to this specialized intermittent high DoD protocol, both as a function of cycle (**Figure 5.15a**) and equivalent full cycle (**Figure 5.15b**). This was tested both at 40 °C as well as at 20 °C after hot formation. For comparison, the data for excellent lithium-ion cells with the same NMC532 positive electrode cycling at 40 °C and 20 °C are included.<sup>21</sup> The intermittent high DoD cycles begin at a stack energy density of about 1200 and 1000 Wh/L for the 40 °C and 20 °C anode-free tests, highlighted in the figure as the 3.60-4.5 V cycles. The limited DoD cycles begin at a stack energy density comparable to the lithium-ion cell at about 700 Wh/L. At 40 °C, the intermittent protocol sustains an energy density higher than lithium-ion during the high DoD cycles for over 300 total (high DoD + low DoD) cycles. At 20 °C, a higher energy density is sustained for over 400 total cycles. Over these 300 and 400 cycles at 40 °C and 20 °C, the low DoD cycles maintained a comparable stack energy density to the lithium-ion cells. **Figure 5.15b** shows that this intermittent protocol sustains approximately

200 and 260 equivalent full cycles at 40 °C and 20 °C, respectively; 100 and 160 more equivalent full cycles than the 80% DoD cells shown in **Figure 5.13c**.

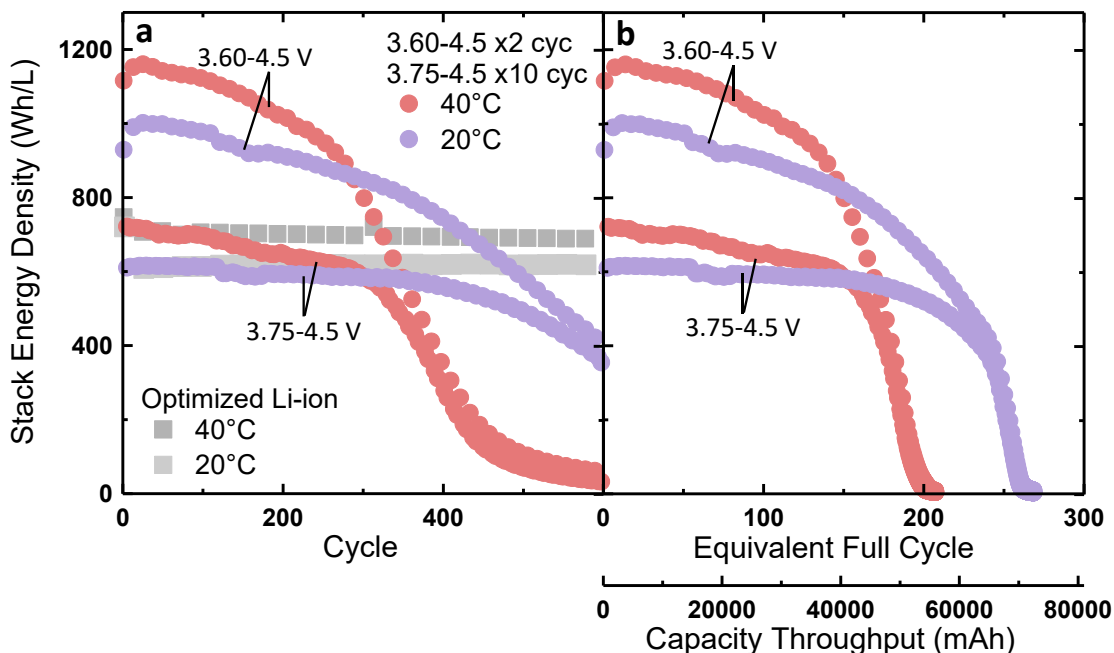


**Figure 5.15 | Specialized intermittent high DoD protocol.** a-b, Stack energy density vs cycle (a) and stack energy density vs equivalent full cycled and capacity throughput (b) for cells cycled with an intermittent high depth of discharge protocol. This protocol consists of ten limited depth of discharge (3.75-4.5 V) cycles are followed by two high depth of discharge (3.60-4.5 V) cycles. NMC532 anode-free cells were cycled at 20 °C with hot formation and 40 °C at C/5 D/2 under high pressure (1200 kPa) with 1.4 M LiDFOB 0.4 M LiBF<sub>4</sub> FEC:DEC 1:2 electrolyte. Optimized lithium-ion cells cycled at 40 °C and 20 °C are shown for comparison. The electrolyte used in the lithium-ion cell was 1.2 M LiPF<sub>6</sub> EC:EMC 3:7 + 2% VC 1% DTD.

The specialized intermittent high DoD protocol shows that it is possible to achieve a compromise between energy density and lifetime with anode-free lithium metal cells. The lifetime was extended by using a small lithium reservoir formed *in-situ* with a limited depth of discharge. This method is superior to conventional lithium metal cells in two ways: lithium foils are not required during cell construction, and it is possible to form an ultra thin lithium reservoir *in-situ* (here, ~7 μm) to maintain a practical energy density, whereas even thin lithium foils 50 μm and thicker will yield lithium metal cells with an energy density less than lithium-ion cells. Furthermore, the high energy density promised by

anode-free cells can still be delivered during the high DoD cycles. This intermittent protocol is likely more practical than continuous high depth of discharge cycles since many battery applications do not operate with a deep discharge with every cycle. For example, many drivers use their vehicles for a short commute for most of the week and only drive the full range of their vehicle periodically during long trips. Smart *et al.* showed in a study of electric vehicle driving behaviour that only 1% of daily trips were longer than 325 km on average.<sup>166</sup> This intermittent protocol could sustain 325 km trips with the low DoD ~700 Wh/L cycles while also capable of long >400 km trips with the high DoD ~1200 Wh/L deep discharge cycles.

#### 5.4.2 Concluding Remarks

It is worth taking a moment to note and appreciate some of the lucky breaks involved throughout our work with anode-free cells as we came to understand the impact of different cycling conditions. We started our tests cycling at 40 °C for no other reason than temperature box availability. Fortunately, it turned out that cycling cells with dual-salt electrolyte at 40 °C significantly improved their performance, enabling a lifetime of 80 cycles compared to only 20 cycles at 20 °C. Another equipment limitation influenced our initial selection of 3.6 V for the lower cut-off voltage. The slow response time of the Moli charger setup coupled with the rapid degradation of anode-free cells conspired to easily trigger the low voltage alarm when a lower cut-off voltage lower than 3.6 V was used. It was only later did we realize that this improved lifetime by limiting the depth of discharge to 80%. If we had originally cycled at 20 °C or at 90% depth of discharge, we may have been discouraged by even shorter lifetimes. These lucky breaks are sometimes the nature of scientific discovery.

We have shown how depth of discharge, temperature, and charge-discharge rate all play an important role on the performance of anode-free cells. When the optimal conditions are selected, the lifetime of anode-free cells with dual-salt electrolyte can be extended to 200 cycles. This is encouraging. However, it is important to frame the practicality of using these optimized conditions by considering their application in the field.

There should be no practical limitations to taking advantage of limited depth of discharge to improve the lifetime of anode-free cells. The lower cut-off voltage limit, which determines the depth of discharge, is controlled by the battery management system used for all lithium-ion cells. Therefore, a limited DoD can be simply programmed in, and users would notice nothing except for increased lifetime. We have shown that limiting the DoD too much can result in cell energy densities that are lower than lithium-ion cells; however, with the correct selection of depth of discharge, a good compromise between energy density and increased longevity can be achieved.

As for temperature, no one controls the weather. Ideally, the batteries in an electric vehicle would operate just as effectively at  $-40\text{ }^{\circ}\text{C}$  in Alberta, Canada as they would at  $+40\text{ }^{\circ}\text{C}$  in Arizona, USA and everywhere in between. The temperature of cells in a battery pack can be controlled by heating and cooling elements often included in electric vehicle battery packs. It was our intention to ensure “room temperature”  $20\text{ }^{\circ}\text{C}$  operation of anode-free cells was viable as this is likely the most common ambient and pack-controlled operating temperature. We showed that this was made possible via the implementation of a hot formation protocol. This is no problem from the standpoint of practical implementation as formation steps are already used by original equipment manufacturers for lithium-ion cells. However, we showed that extended operation at  $40\text{ }^{\circ}\text{C}$  is sometimes worse than  $20\text{ }^{\circ}\text{C}$  operation after hot formation (**Figure 5.4**). Moreover, significant gas generation during cycling—which can be overcome with  $20\text{ }^{\circ}\text{C}$  operation after hot formation<sup>45</sup>—would be an issue with extended  $40\text{ }^{\circ}\text{C}$  operation owing to parasitic reactions, particularly at high voltage.<sup>167</sup> Although the battery pack can be cooled during operation, extended stints at high temperature may occur while the pack is idle, for example, when an electric vehicle is not running. As for colder temperatures below  $20\text{ }^{\circ}\text{C}$ , this is not something we have explored in this work.

Optimized charge-discharge rates are probably the most concerning from a practical point of view. Charging slow and discharging fast may be the best for extending lifetime, but this is often contradictory to what consumers want—fast charge and the ability to discharge over the course of an entire day. For electric cars, the desire for fast charge under 15

minutes (4C), mimicking the experience of gassing up an internal combustion car, may be mitigated by battery packs with high energy density cells that deliver long >500 km driving ranges. If the driving range is long enough such that the car does not need to be charged mid-journey, then a long charge time may be less of an inconvenience as consumers can just charge at home overnight. Although the charge rate can be entirely controlled by the battery management system, this is less true for the discharge rate. Maximum discharge currents can be imposed, but ultimately, the discharge will be determined by how consumers use the product. So, although charge-discharge rates can be optimized in the lab, in practice, you cannot control how a consumer will use a battery. Moving forward, one of the biggest challenges for lithium metal cells with liquid electrolytes will be successful operation independent of optimized asymmetric slower charge protocols.

## Chapter 6: Different Positive Electrodes for Anode-Free Cells

Our first foray into the anode-free cell design utilized an excellent single crystal  $\text{LiNi}_{0.5}\text{Mn}_{0.3}\text{Co}_{0.2}\text{O}_2$  (NMC532) positive electrode known to facilitate long lifetime “million mile” lithium-ion cells.<sup>21,168</sup> However, there are a number of other positive electrode materials of interest. For example,  $\text{LiNi}_{0.8}\text{Mn}_{0.1}\text{Co}_{0.1}\text{O}_2$  (NMC811) delivers a higher specific capacity and utilizes less cobalt, which is beneficial from both a cost and humanitarian point of view since ethical sourcing of cobalt is challenging.<sup>16,169</sup> There is also a desire to reduce the utilization of nickel due to cost and supply concerns. To that end,  $\text{LiFePO}_4$  (LFP) electrodes, based on abundant and low-cost iron and contain no nickel or cobalt are becoming more popular.<sup>17</sup> LFP also exhibits improved safety in comparison to NMC materials.<sup>16,18</sup> Unfortunately, LFP electrodes deliver a smaller specific capacity and a lower voltage, thereby reducing the energy density of LFP-based cells. From our anode-free point of view, LFP is also particularly interesting because it does not exhibit a significant “irreversible capacity”. As a result, the *in-situ* lithium excess demonstrated in Chapter 5 can be largely avoided, facilitating high depth of discharge cycling. Similarly,  $\text{LiCoO}_2$  (LCO) does not exhibit a significant positive electrode “irreversible capacity”. LCO is used in most portable electronics today, but the high cobalt content, high cost, and worse safety than NMC materials has driven the market away from using LCO in electric vehicles.<sup>1</sup> For our purposes, since depth of discharge plays such a strong role in the lifetime of anode-free cells, studying the performance of LFP and LCO based anode-free cells should be instructive.

In addition to the NMC532 anode-free cells we have studied to this point, NMC811, LFP, and LCO anode-free pouch cells were obtained for testing, as detailed in **Table 3.1**. In this chapter, we study the performance of these anode-free cells with different positive electrodes. This was done first with our control dual-salt  $\text{LiDFOB}/\text{LiBF}_4$  electrolyte. Later in this chapter, we explore the performance of different electrolyte chemistries and more optimized cycling conditions such as hot formation and high pressure cycling.

## 6.1 Comparison of NMC532, NMC811, LCO, & LFP Anode-Free Cells

### 6.1.1 Energy Density

Since the virtue of anode-free cells is high energy density, it is important to determine the energy density that each positive electrode chemistry can deliver and compare this to a baseline lithium-ion cell. **Figure 6.1a** and **b** show the stack volumetric energy densities and specific energy densities of anode-free cells with LFP, NMC532, LCO, and NMC811 positive electrodes compared to a lithium-ion cell with an NMC532 positive electrode. The energy density of LFP anode-free cells is similar to NMC532 Li-ion cells; the benefit to of storing capacity as lithium metal is counterbalanced by the lower specific capacity and voltage of the LFP positive electrode. NMC532, LCO, and NMC811 anode-free cells all deliver a significantly increased energy density compared to the NMC532 Li-ion cell. The benefit to volumetric energy density is greater than the benefit to specific energy density.

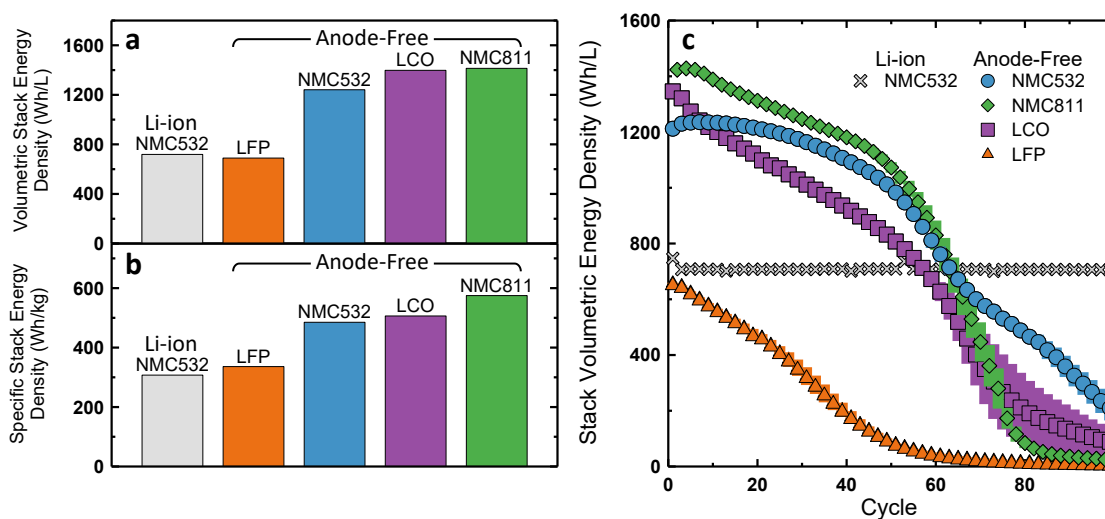


**Figure 6.1 | Energy Density Comparison.** a-b, Stack energy density calculated by volume (a) and by mass (b) for anode-free lithium metal cells with  $\text{LiFePO}_4$  (LFP),  $\text{LiNi}_{0.5}\text{Mn}_{0.3}\text{Co}_{0.2}\text{O}_2$  (NMC532),  $\text{LiCoO}_2$  (LCO), and  $\text{LiNi}_{0.8}\text{Mn}_{0.1}\text{Co}_{0.1}\text{O}_2$  (NMC811) positive electrodes compared to a conventional Li-ion cell with an NMC532 positive electrode. c, Stack volumetric energy density vs cycle for anode-free cells cycled to ~90% depth of discharge compared to a conventional Li-ion cell. Anode-free cells were cycled at C/5 D/2 at 40 °C with 0.6 M LiDFOB 0.6 M LiBF<sub>4</sub> FEC:DEC 1:2 electrolyte. Li-ion cells were cycled at C/3 D/3 at 40 °C with 1.2 M LiPF<sub>6</sub> EC:EMC 3:7 + 2%VC 1%DTD electrolyte. Error bars represent the standard deviation of duplicate cells.

As an initial comparison of cycling performance, **Figure 6.1c** shows the stack volumetric energy density vs cycle for each of these cells tested to ~90% depth of discharge with dual-salt LiDFOB/LiBF<sub>4</sub> electrolyte. The stack volumetric energy density begins at about 1400 Wh/L for NMC811 and LCO anode-free cells, 1200 Wh/L for NMC532 anode-free cells, 700 Wh/L for LFP anode-free cells, and 700 Wh/L for conventional NMC532 Li-ion cells. The NMC811, LCO, and NMC532 anode-free cells all deliver a higher energy density than the Li-ion cell for about 70 cycles. Although the ultimate lifetime is quite similar, the cycling behaviour exhibits subtle differences. The NMC532 cells show the most stable performance through 50 cycles before there is more significant energy fade. The initial energy fade of NMC811 cells is larger, and then the drop after 50 cycles is more significant as well. The LCO cells show the most linear energy fade through 60 cycles before more rapid loss begins. These differences may be attributed to unique interactions with the different positive electrode materials. However, the slightly different depths of discharge and areal capacities should not be discounted either—this will be addressed shortly. The LFP cells exhibit the most severe energy fade of all anode-free chemistries. Although some electrolyte formulations have successfully enabled lithium metal cycling with LFP electrodes,<sup>48</sup> dual-salt electrolyte is not one of them. Even with more successful electrolytes, the low energy density LFP anode-free cells deliver begs the question of the virtue of this cell design. With a lower cycle life and energy density on par with Li-ion cells, the only argument that can be made is for lower cost.

### 6.1.2 Cycling with Different Voltage Limits

Anode-free cells tested in **Figure 6.1c** were cycled with a targeted depth of discharge of 90% so that each chemistry could be compared with the same lithium reservoir capacity. However, the depth of discharge (DoD) is determined by the lower cut-off voltage (LCV), and LCVs chosen here result in a  $90 \pm 5\%$  DoD. The first charge-discharge voltage curves must be studied to determine the precise depth of discharge facilitated by different LCVs. **Figure 6.2** shows the first cycle voltage curves for each positive electrode chemistry cycled under typical C/5 D/2 charge-discharge rates (solid lines) as well as at C/10 D/10 (dashed lines). The vertical gray dotted lines denote minimum and maximum capacities delivered



between a deep discharge down to 1.2 V up to the typical upper cut-off voltages (UCVs) for each electrode chemistry. The horizontal gray dotted lines show the range of capacity for the different depths of discharge tested in this work; 90 and 80% DoD are specifically highlighted. The areal capacity, specific capacity, and depth of discharge for the different cycling ranges shown in **Figure 6.2** are detailed in **Table 6.1**. In **Table 6.1**, depth of discharge is calculated in two different ways: normalized to the first charge capacity (the method used throughout this work) and normalized to the first discharge capacity using a deep discharge to 1.2 V. Although the latter is a more accurate calculation, the former, which systematically underestimates DoD because of lithium inventory lost during the first charge, was used for simplicity.

For the ~90% DoD tests, the lower cut-off voltages used are 3.0 V for NMC532 and NMC811, 3.65 V for LCO, and 2.95 V for LFP anode-free cells. These LCVs result in depths of discharge—calculated normalized to the first charge capacity—of 85.8, 91.8, 94.4 and 94.6%, respectively. For the ~80% DoD tests, the lower cut-off voltages used are 3.6 V for NMC532, 3.55 V for NMC811, and 3.86 V for LCO (80% DoD is not possible for LFP by limiting the LCV). This results in depths of discharge of 80.1, 83.4, and 76.8%, respectively. Therefore, when we refer to the “90%” and “80%” DoD tests, it is important to note that these are approximations.

**Figure 6.3** shows the cycling results for the different anode-free chemistries cycled to different voltage ranges. The NMC532 results presented here are different from those presented in Section 5.3 since they are using a lower concentration dual-salt electrolyte and are cycled under low pressure. Beyond testing different lower cut-off voltages and DoDs, a few different upper cut-off voltages were tested. The control UCVs selected were 4.5 V for NMC532, 4.4 V for NMC811 and LCO, and 3.7 V for LFP. In addition, 4.3 V was tested for NMC532; 4.5 V and 4.14 V were tested for NMC811, and 4.2 V was tested for LCO.

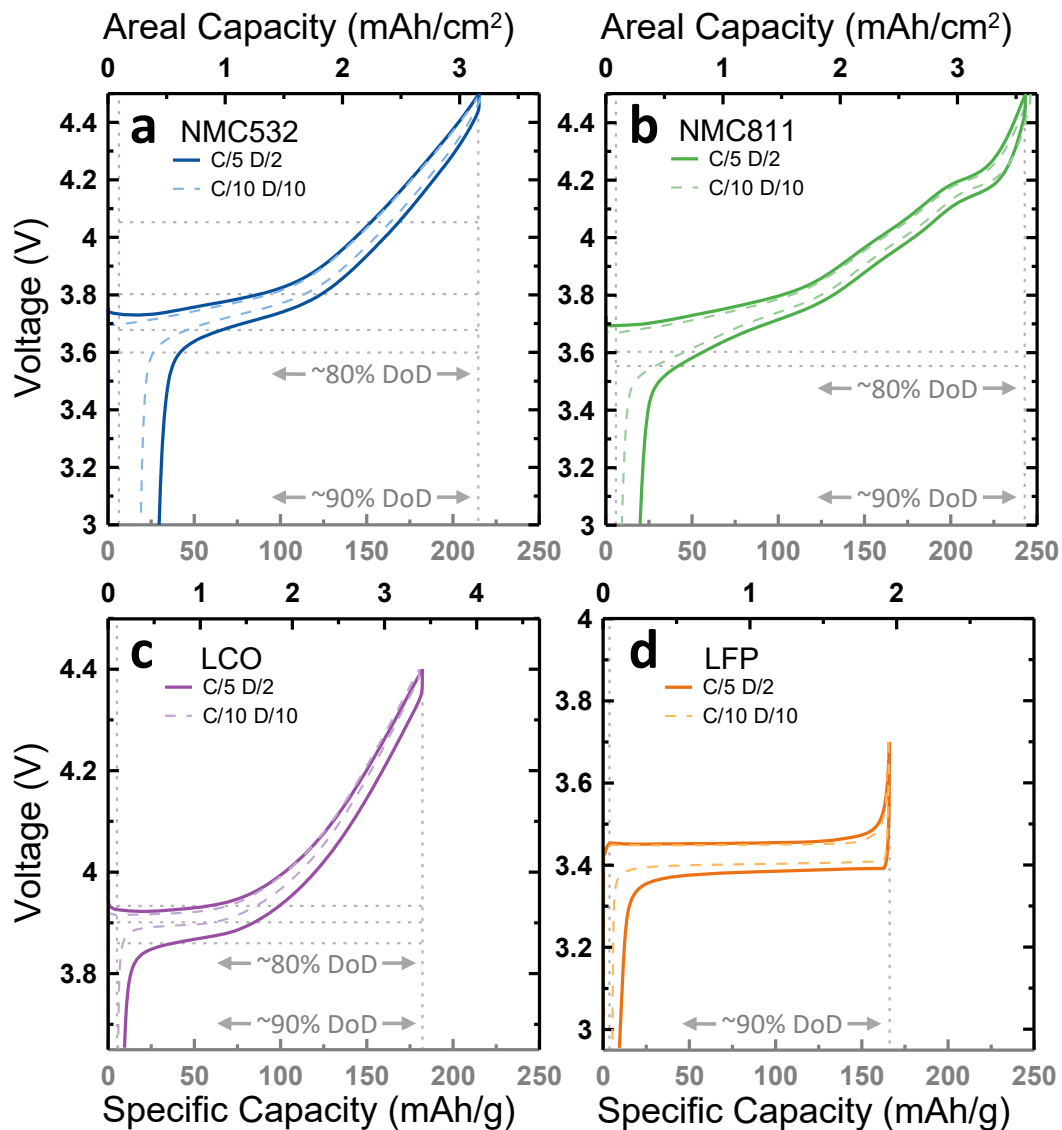


**Figure 6.2 | Voltage profiles. a-d,** First charge-discharge voltage vs areal capacity (top axes, black) and specific capacity (bottom axes, grey) for anode-free cells with NMC532 (a), NMC811 (b), LCO (c) and LFP (d) positive electrodes. Dotted lines indicate the capacity range cycled for different lower cut-off voltages in this work; 90% and 80% depth of discharge are specifically highlighted. Cells were charged and discharged at C/5 D/2 (solid lines) and C/10 D/10 (dashed lines) at 40 °C with 0.6 M LiDFOB 0.6 M LiBF<sub>4</sub> FEC:DEC 1:2 electrolyte.

**Table 6.1:** Different depth of discharge cycling conditions for the NMC532, NMC811, LCO, and LFP anode-free cells tested in this work.

	1st charge (4.5 V)	1st discharge (1.2 V)	3.0 V	3.6 V	3.68 V	3.8 V	4.05 V
<b>NMC532</b>							
Areal Capacity (mAh/cm <sup>2</sup> )	3.16	3.06	2.71	2.53	2.22	1.35	0.68
Specific Capacity (mAh/g)	214.8	207.8	184.4	172.3	150.8	91.8	46.1
DoD from 1st dschg (%)		100.0	88.7	82.9	72.6	44.2	22.2
DoD from 1st chg (%)	100.0	96.7	85.8	80.1	70.1	42.7	21.4
	1st charge (4.4 V)	1st discharge (1.2 V)	3.0 V	3.55 V	3.6 V		
<b>NMC811</b>							
Areal Capacity (mAh/cm <sup>2</sup> )	3.56	3.48	3.27	2.97	2.73		
Specific Capacity (mAh/g)	242.2	236.3	222.3	201.9	185.5		
DoD from 1st dschg (%)		100.0	94.0	85.5	78.5		
DoD from 1st chg (%)	100.0	97.6	91.8	83.4	76.6		
	1st charge (4.4 V)	1st discharge (1.2 V)	3.65 V	3.86 V	3.9 V	3.93 V	
<b>LCO</b>							
Areal Capacity (mAh/cm <sup>2</sup> )	3.41	3.31	3.22	2.68	1.82	1.54	
Specific Capacity (mAh/g)	182.4	176.9	172.3	143.4	97.3	82.4	
DoD from 1st dschg (%)		100.0	97.4	81.0	55.0	46.6	
DoD from 1st chg (%)	100.0	97.0	94.4	78.6	53.3	45.2	
	1st charge (3.7 V)	1st discharge (1.2 V)	2.95 V				
<b>LFP</b>							
Areal Capacity (mAh/cm <sup>2</sup> )	1.96	1.91	1.85				
Specific Capacity (mAh/g)	166.0	162.1	157.0				
DoD from 1st dschg (%)		100.0	96.9				
DoD from 1st chg (%)	100.0	97.6	94.6				

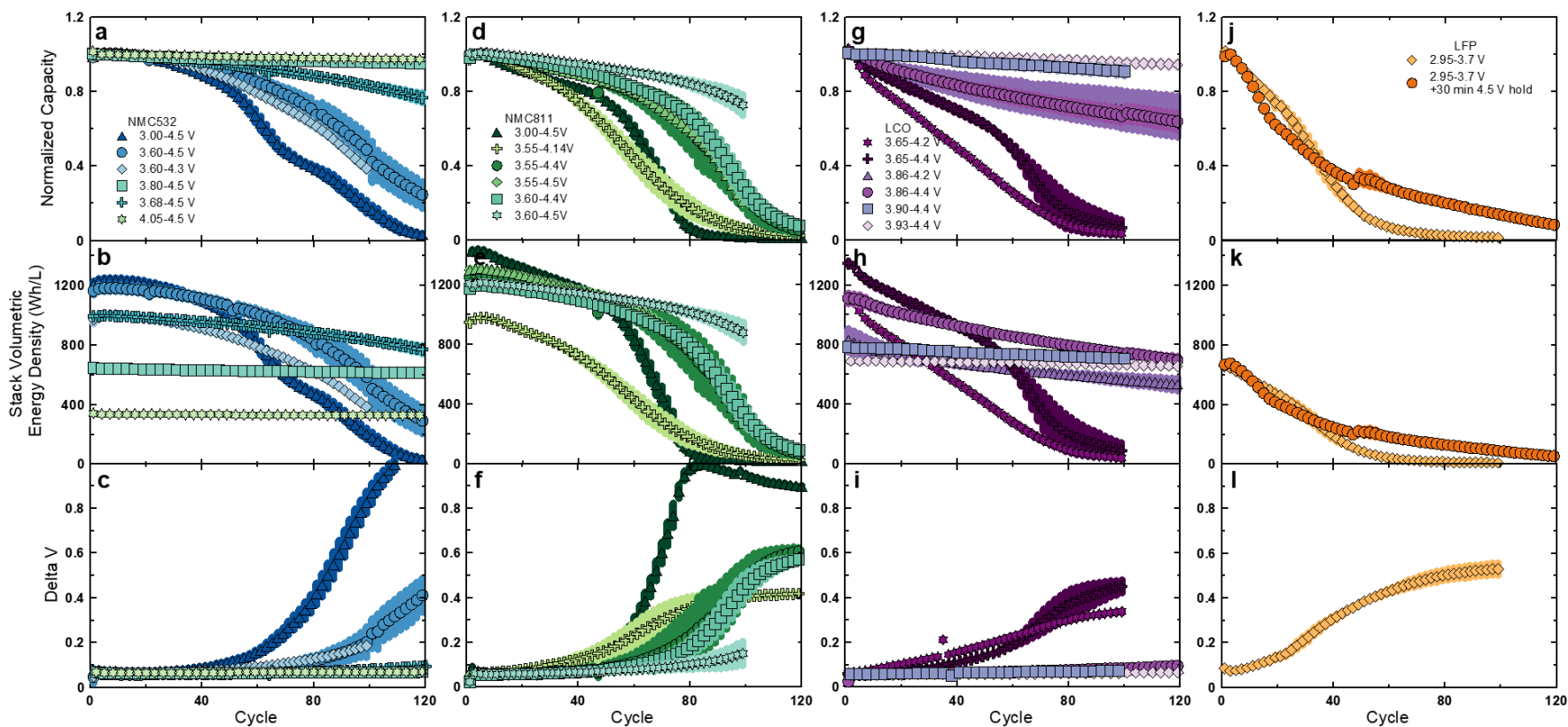


**Figure 6.3 | Voltage range and depth of discharge performance.** a-c, NMC532; d-f, NMC811; g-i, LCO; j-l, LFP anode-free cycling data plotted as normalized capacity (first row), stack volumetric energy density (second row), and delta V (third row) vs cycle for different voltage ranges and depths of discharges. The cycling conditions (areal and specific capacity, depth of discharge) of the various voltage ranges are listed in **Table 6.1**. Cells were cycled at C/5 D/2 and 40 °C with 0.6 M LiDFOB 0.6 M LiBF<sub>4</sub> FEC:DEC 1:2 electrolyte. Error bars represent the standard deviation of duplicate cells.

Generally, the 90% DoD tests performed the worst. Although they provide the highest stack volumetric energy density (**Figure 6.3**, middle row), they result in the fastest capacity fade (**Figure 6.3**, top row) and delta V growth (**Figure 6.3**, bottom row). This is expected since high depths of discharge result in correspondingly low capacity lithium reservoirs. When lower UCVs are used compared to control, similar or worse cycling results. For example, 3.55-4.14 V for NMC811 and 3.65-4.2 V for LCO result in worse capacity retention. This may be attributed to fewer synergistic parasitic reactions.

Limiting the depth of discharge below 80% facilitates the best cycling results for NMC532, NMC811, and LCO electrode chemistries. NMC532 cells cycling between 3.68-4.5 V (72% DoD) and NMC811 cells cycling between 3.60-4.5 V (78% DoD) sustain 100 cycles to ~80% capacity retention, about 20 cycles better than the 80% DoD tests. Although this reduces the energy density of NMC532 cells by some 200 Wh/L, the energy density of NMC811 cells is unaffected. Therefore, 3.60 V should be used more as a lower cut-off voltage for NMC811 tests in future endeavors since it benefits lifetime without depreciating energy density. Depths of discharge below 50% tested for NMC532 and LCO result in no significant capacity loss over 120 cycles. Again, this is expected due to the correspondingly large lithium reservoirs and comes at a cost of significantly reduced energy density. Overall, the effects of depth of discharge are consistent with what was previously demonstrated in Chapter 5.

Due to the flat voltage curve of LFP, different UCVs and LCVs cannot be easily cycled. Instead, to try to incorporate time at higher voltage, a protocol was tested in which LFP anode-free cells were held at 4.5 V for 30 minutes at the end of every charge. This was tested since we have shown that synergistic parasitic reactions occur at high voltage in NMC532 cells.<sup>46</sup> Unfortunately, this protocol only marginally improves cycling. Most capacity, over 60%, is still lost by cycle 40. A lifetime of only 20 cycles to 80% capacity is achieved with LFP anode-free cells with dual-salt electrolyte.

### 6.1.3 80% Depth of Discharge Analysis

**Figure 6.3** showed some significant differences between the 80% DoD performance between different positive electrode chemistries—although this may be hard to parse amidst all the other data. NMC532 and NMC811 deliver similar lifetime, but the “knee point” where the capacity begins to trend concave down is steeper for NMC811. Surprisingly, LCO performs significantly better, with a more ideal concave up capacity fade resulting in a capacity retention of about 75% after 120 cycles, compared to NMC532 and NMC811 which deliver almost 0% capacity after 120 cycles. Since 80% DoD facilitates a good compromise between longevity and energy density, delivering about 1200 Wh/L for NMC532, NMC811, and LCO anode-free cells, 80% DoD was chosen as the control cycling condition to study further. For LFP cells, since we could not achieve 80% DoD via tuning the LCV, only the 90% DoD condition was studied.

**Figure 6.4** presents an extensive analysis of the nominal cycling conditions for the different anode-free positive electrode chemistries—80% DoD for NMC532 (3.6-4.5 V), NMC811 (3.55-4.4 V), LCO (3.86-4.4 V), and 90% DoD for LFP (2.95-3.7 V) with dual-salt electrolyte cycled at C/5 D/2 and 40 °C. NMC532 data is shown in blue (**Figure 6.4a,b**), LCO in purple (**Figure 6.4c,d**), NMC811 in green (**Figure 6.4e,f**), and LFP data is shown in orange (**Figure 6.4g,h**). The cycling data are shown in the first and third columns with capacity (circles, left axes) and delta V (light diamonds, right axes) vs cycle. The voltage vs capacity discharge curves are shown in second and fourth columns.

At the end of nominal LCV-UCV cycling, a deep discharge was performed to quantify the remaining active lithium inventory. This consisted of a constant current discharge down to 1.2 V with a constant voltage hold at 1.2 V until the current dropped to C/20. This protocol ensures that all remaining active lithium inventory which can be discharged is discharged. Since a deep discharge may hinder future cycling, cells were not continued cycling after a deep discharge. As a result, many duplicate cells had to be run to get data for deep discharges as a function of cycle. For NMC532, duplicate cells were run for 1 cycle, 20, 50, 80, 100, and 200 cycles. For LCO, NMC811, and LFP, duplicate cells were run for 1

cycle, 50, 100, and 200 cycles. The capacity of the deep discharges are shown in dark circles with a black outline and appear above the nominal discharge capacity vs cycle data. The gap between the deep discharge and the nominal discharge data represents the capacity of the lithium reservoir and the capacity inaccessible at the typical discharge LCV due to kinetic hinderance. The very first charge capacity is shown in a gray square for each electrode chemistry. The difference between the first charge capacity and the first deep discharge capacity corresponds to the lithium inventory lost during the first cycle.

The voltage vs capacity curves of the deep discharge cycles are shown in **Figure 6.4b,d,f,g**. The top panels show the entire deep discharge down to 1.2 V, and the bottom panels show the same data cut-off to the nominal lower cut-off voltage—the difference between these is the capacity of the lithium reservoir and the capacity inaccessible at the typical discharge LCV due to kinetic hinderance. The gray vertical dotted line spanning both panels denote the end capacity for the typical LCV—any capacity beyond this line corresponds to capacity of the lithium reservoir and inaccessible capacity due to kinetic hinderance.

For NMC532, the difference between the normal and deep discharge at cycle 1 is about 50 mAh (**Figure 6.4a**), corresponding to a lithium excess of approximately  $\frac{50 \text{ mAh}}{260 \text{ mAh}} = 0.19$ . **Figure 6.4b** shows that most of this lithium reservoir is capacity from the 1.5 V voltage plateau; however, some capacity between 3.6-3.0 V also contributes. By cycle 50, this lithium reservoir has been mostly all consumed. After cycle 100, the gap between the normal and deep discharges increases again, but now this is due to increased kinetic hindrance resulting from resistance growth demonstrated by increasing delta V. This analysis reveals a surprising disparity between the capacity of the deep discharges compared with the normal discharges. Unlike normal cycling which exhibits a concave down capacity fade, the deep discharges show a linear capacity loss. This indicates that the rate of lithium inventory loss is relatively constant throughout cycling, and the increased capacity fade observed is a result of resistance growth. By fitting the deep discharge capacity vs cycle data with a straight line, the rate of lithium inventory loss for NMC532 anode-free cells with dual-salt electrolyte (cycling under the conditions described in the caption of **Figure 6.4**) is 1.15 mAh/cycle.

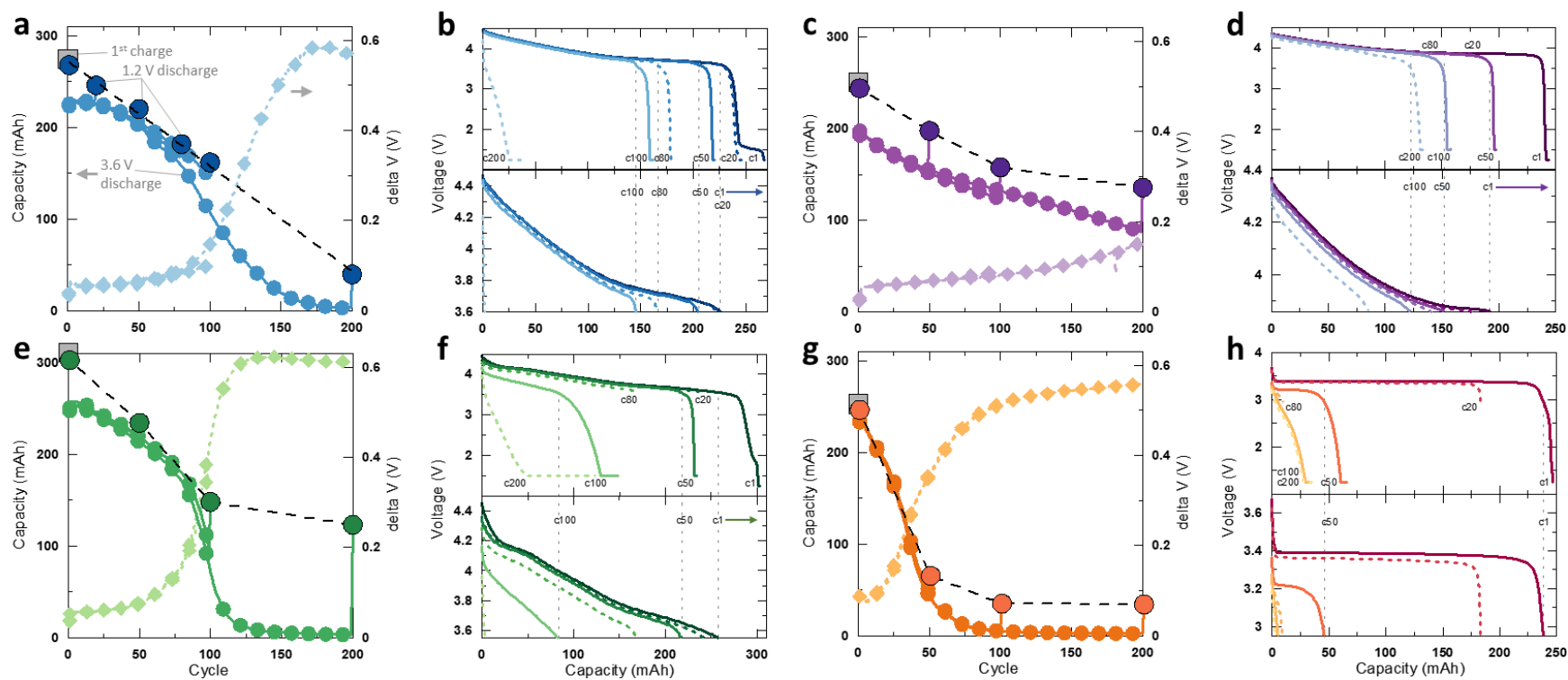


**Figure 6.4 | 80% DoD lithium inventory loss. a-b, NMC532; c-d, LCO; e-f, NMC811; g-h, LFP anode-free cycling data.** The first and third columns show capacity vs cycle (left axes) and delta V (right axis). Nominal LCV-UCV cycling data is shown in symbols without outlines (circles for capacity and diamonds for delta V). Capacity data from a deep discharge down to 1.2 V are displayed by circles with black outlines. The second and fourth columns show the voltage profiles plotted from the upper cut-off voltage down to 1 V (top panels) and from the upper cut-off voltage down to the lower cut-off voltage during nominal cycling (bottom panels). Vertical gray dotted lines show where the deep discharges and normal discharges line up. Cells were cycled between 3.6-4.5 V (NMC532), 3.55-4.4 V (NMC811), 3.86-4.4 V (LCO), and 2.95-3.7 (LFP) at C/5 D/2 at 40 °C with 0.6 M LiDFOB 0.6 M LiBF<sub>4</sub> FEC:DEC 1:2 electrolyte.



NMC811 (**Figure 6.4e-f**) exhibits a similar behaviour to NMC532. However, several important distinctions can be observed. First, the low voltage plateau contributes less to the capacity of the initial lithium reservoir—most of this capacity appears between 3.55-3.0 V. Through 50 cycles, the lithium reservoir is mostly depleted, just as with NMC532. The next distinction appears in the cycling behaviour after 100 cycles as the gap between the normal and deep discharges becomes more significant than with NMC532. This is a result of more dramatic  $\Delta V$  growth exhibited by NMC811 cells. Finally, the lithium inventory loss shown by the capacity fade of the deep discharges is not linear through 200 cycles as it was for NMC532. This is a consequence of the increased kinetic hindrance suffered by NMC811 cells—as the  $\Delta V$  soars after 100 cycles, lithium capacity becomes more difficult to access. Practically, this means that after 100 cycles, most of the remaining lithium inventory is not being cycled, and therefore degradation is not occurring. The linear region over the first 100 cycles exhibits a rate of lithium inventory loss of 1.58 mAh/cycle. Beyond a higher rate of lithium inventory loss, the most important distinction to be made is that NMC811 anode-free cells suffer from more severe resistance growth than NMC532 cells. This is not particularly surprising since impedance growth in NMC811 materials cycled to high voltage is a problem for NMC811 lithium-ion cells as well.

We previously highlighted the stark difference in capacity retention of LCO cells compared to NMC532 and NMC811. This is again demonstrated in **Figure 6.4c**. A similar initial lithium excess of approximately  $\frac{50 \text{ mAh}}{250 \text{ mAh}} = 0.2$  is present. However, almost none of this lithium reservoir originates from a low voltage plateau. Therefore, a higher lower cut-off voltage of 3.86 V was necessary to achieve a DoD of 80%; most of the lithium excess is thus stored between 3.86-3.0 V, shown in the top panel of **Figure 6.4d**. As a result, the shape of the voltage curve toward the end of discharge for the normal lower voltage cut-off (bottom panel of **Figure 6.4d**) is much flatter than the shape of the voltage curves toward the normal discharge cut-offs for NMC532 and NMC811. Surprisingly, unlike with NMC532 and NMC811, the lithium reservoir of LCO anode-free cells is not depleted during cycling—a relatively constant gap between the deep and normal discharges of ~50 mAh exists throughout 200 cycles. Conventionally, one might believe that any lithium

excess must be depleted before capacity fade is observed, and that this would result in a slower initial capacity loss and concave down capacity fade as is the case for NMC532 and NMC811. However, this is clearly not true for LCO cells which exhibit a concave up capacity fade. Again, one might believe that the benefit of an 80% DoD is that the resultant lithium excess can replenish lithium inventory lost during cycling. Although this is not the case for LCO, the 80% DoD does clearly benefit performance somehow, as demonstrated by the dramatic improvement in capacity retention in comparison to LCO cells running at 90% DoD in **Figure 6.3**. Perhaps the benefit of the limited depth of discharge in this case can be largely attributed to the improved cycling efficiency of plating and stripping lithium on top of a lithium reservoir as demonstrated by Fang *et al.*<sup>85</sup> However, why the lithium reservoir is not depleted during cycling is still mysterious. Regardless, this results in a lessened rate of lithium inventory loss over the first 100 cycles of 0.91 mAh/cycle. Moreover, the delta V growth is much less severe for LCO anode-free cells compared to NMC532 and NMC811. As a result, the dramatic capacity fade exhibited by the NMC cells toward the end of life during nominal cycling is avoided with LCO, facilitating a longer lifetime.

LFP anode-free cells exhibit the worst performance. **Figure 6.4g** shows that almost all capacity is lost through 50 cycles with a massive rate of lithium inventory loss of 3.65 mAh/cycle. The fact that this lithium inventory loss is much greater than for the other positive electrode chemistries indicates that dual-salt electrolyte is not compatible with LFP anode-free cells. After 20 cycles and most lithium inventory has been lost, the delta V soars. As a result, the remaining lithium inventory cannot be accessed during nominal cycling. About 30 mAh of capacity can still be accessed through a deep discharge after 200 cycles since it is not being aged due to this kinetic hinderance.

A head-to-head comparison of NMC532, NMC811, LCO, and LFP anode-free cells is presented in **Figure 6.5**. The normalized capacity vs cycle (**Figure 6.5a**) shows similar performance of NMC532, NMC811, and LCO cells to 80% capacity retention through 80 cycles. However, the shape of the fade curves distinguishes their performance after extended cycling through 200 cycles: the NMC electrodes feature concave down fade

curves, with a more dramatic loss exhibited by NMC811 because of more severe resistance growth while LCO features a more ideal concave up fade, resulting longer extended lifetime. **Figure 6.5b** shows the fractional lithium inventory vs cycle, calculated by normalizing the 1.2 V deep discharge capacities. The similarity in shape for LCO and LFP results between normal cycling and the deep discharges (**Figure 6.5a** and **b**) indicate that these cells experience capacity fade primarily because of lithium inventory loss. In contrast, there is a large resistive contribution for NMC532 and NMC811, particularly toward the end of life, demonstrated by the delta V growth in **Figure 6.5f**. **Figure 6.5b** shows that LCO exhibits the slowest rate of lithium inventory loss, with NMC532 close behind and NMC811 showing a yet larger inventory loss. LFP cells exhibit the largest lithium inventory loss.

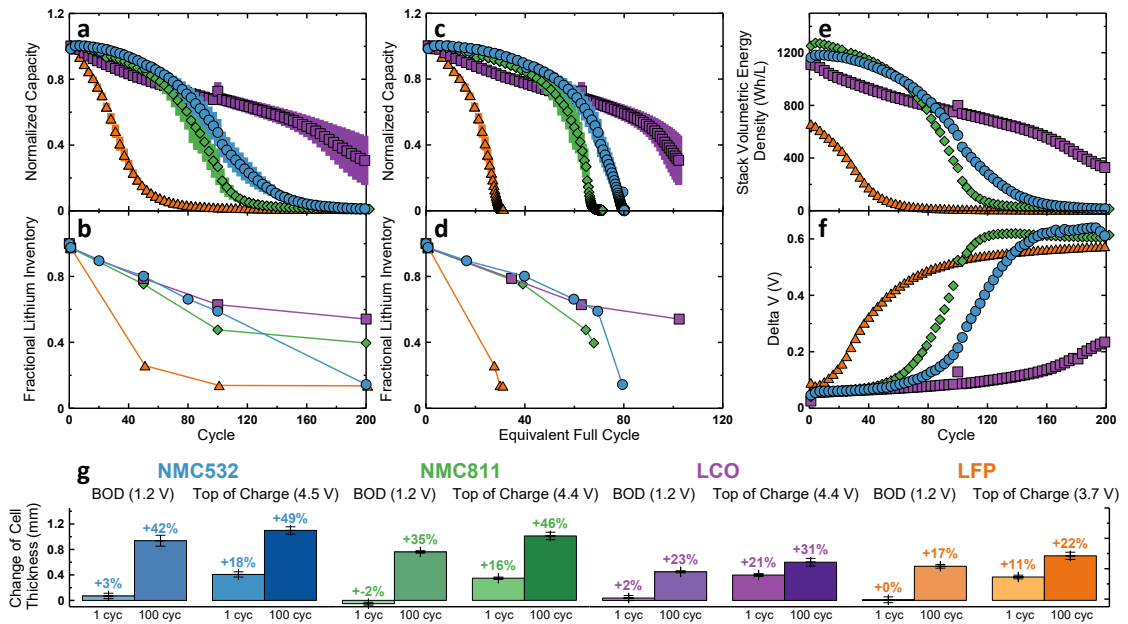


**Figure 6.5 | Positive electrode cycling comparison.** **a-f**, Cycling data for anode-free NMC532, NMC811, LCO, and LFP cells. Normalized capacity (**a**) and fractional lithium inventory (**b**) vs cycle; normalized capacity (**c**) and fractional lithium inventory (**d**) vs equivalent full cycle; stack volumetric energy density (**e**) and delta V (**f**) vs cycle are shown. **g**, Change in cell thickness in the fully discharged (bottom of discharge, BOD) and in the fully charged (top of charge, TOC) state after 1 and 100 cycles. Cells were cycled between 3.6-4.5 V (NMC532), 3.55-4.4 V (NMC811), 3.86-4.4 V (LCO), and 2.95-3.7 (LFP) at C/5 D/2 and 40 °C with 0.6 M LiDFOB 0.6 M LiBF<sub>4</sub> FEC:DEC 1:2 electrolyte.

Plotting performance metrics vs cycle is convenient. For cells of the same build, it is a perfect comparison. However, here, the different positive electrode chemistries are cycling slightly different areal capacities and depths of discharge. Another way to present this data is to plot it versus equivalent full cycle—a capacity throughput normalized to the first charge capacity. The number of equivalent full cycles is a measure of how many 100% depth of discharge cycles have accrued. The normalized capacity vs equivalent full cycle is shown in **Figure 6.5c**. Under these conditions, anode-free LFP cells sustain about 30 equivalent full cycles; 65 for NMC811, 80 for NMC532, and over 100 equivalent full cycles are sustained for LCO. The fractional lithium inventory vs equivalent full cycle is shown in **Figure 6.5c**. An additional head-to-head comparison taking into account the effect of areal capacity and depth of discharge is the stack volumetric energy density, which is plotted vs cycle in **Figure 6.5e**.

Another performance metric to consider is the thickening of anode-free cells. In Section 4.1.1, we showed that anode-free cells experience a reversible and irreversible volume expansion due to lithium plating and stripping and the accumulation of dead lithium. We were able to observe this via proxy pressure measurements of the pouch cells expanding against a pressure sensor. Equally, the thickness can be directly measured via a linear gauge. Ideally, from a practical standpoint, increasing thickness should be minimized. Moreover, we have correlated cell degradation to irreversible thickening; therefore, this measurement is another gauge of cell performance. **Figure 6.5g** shows the change of thickness of anode-free cells after 1 and 100 cycles in the fully discharged state (bottom of discharge, BOD, hatched bars) and in the fully charged state (top of charge, TOC, solid bars). **Figure A.18** shows the change in cell thickness after 100 cycles at the TOC vs number of equivalent full cycles completed.

After a single charge (1 cyc top of charge), all the anode-free cell chemistries expand by about 20%. This is a result of lithium from the positive electrodes plating on the bare copper current collectors. After a single cycle (1 cyc BOD), the change in thickness corresponds to irreversible volume expansion due to the formation of dead lithium (SEI growth and mechanically isolated lithium). Unfortunately, the resolution of our measurements is

similar to the small irreversible thickness after 1 cycle—on the order of a couple of percent. After 100 cycles, the thickness in the fully charged and discharged states are almost equal within each cell chemistry; the irreversible expansion due to the accumulation of dead lithium dwarfs the reversible expansion of cycled lithium after cell aging. NMC532 and NMC811 cells more than double in thickness in the fully charged state after 100 cycles. LFP cells also double in thickness. LCO cells again stand in stark contrast, exhibiting much less irreversible thickness growth in the charged state through 100 cycles.

The significant and frankly impractical thickening of NMC532 and NMC811 cells after 100 cycles is likely exacerbated by the severe resistance growth they experience. In Section 5.2.2 and **Figure 5.11**, we argued that strong concentration gradients result in worsened lithium plating morphology. Increased resistance will enhance the formation of electrolyte concentration gradients. Therefore, this kinetic hindrance impedes ionic transport and uniform lithium plating. LCO cells which do not exhibit severe resistance growth consequently do not experience significant irreversible thickening. This behaviour motivates a future study analyzing the lithium morphology as a function of cycle for LCO anode-free cells to observe if indeed a dense lithium microstructure is maintained longer than with NMC532 through cell aging.

Throughout this section, anode-free cells have been cycled with C/5 D/2 charge-discharge rates. We tested some additional rates for the different positive electrode chemistries in **Figure A.19**. As we showed for NMC532 in Chapter 5, symmetric cycling protocols (C/5 D/5) perform worse than the asymmetric slower charge protocol (C/5 D/2).

#### 6.1.4 Safety

We characterized the safety of anode-free cells with different positive electrodes with smart nail penetration tests shown in **Figure 6.6**. Interestingly, after 20 cycles (**Figure 6.6a**), no significant difference in the temperature vs time evolution of penetrated cells was observed between the different positive electrode chemistries. This is somewhat surprising since NMC811 and LCO positive electrodes are known to be more volatile than NMC532, and all of these electrodes are more volatile than LFP—especially at high voltage, as tested

here.<sup>\*16,18</sup> Apparently, the differences in positive electrode volatility do not significantly impact the safety of anode-free cells after 20 cycles.

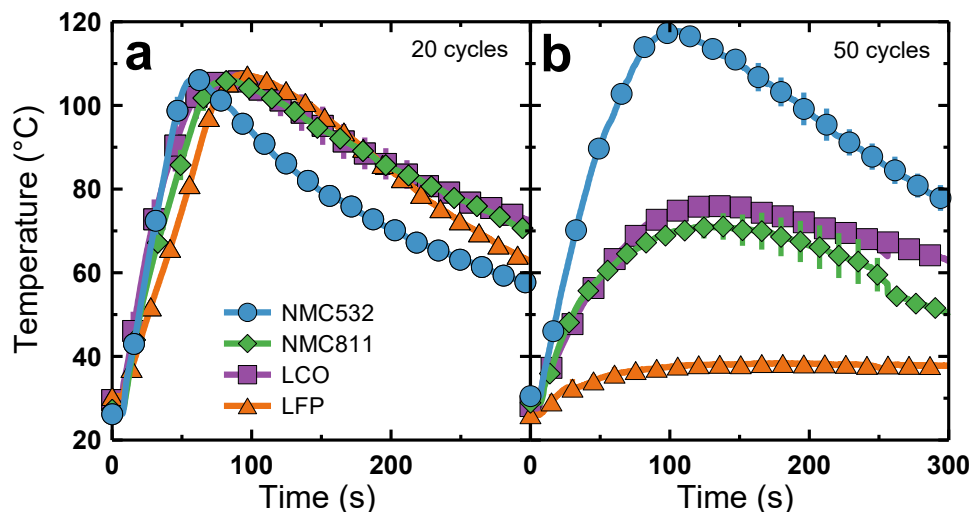


**Figure 6.6 | Positive electrode safety. a-b**, Smart nail penetration tests of anode-free cells with different positive electrodes performed after 20 cycles (a) and 50 cycles (b). Penetrations were performed on cells at the top of charge with a controlled speed of 0.5 mm/s to a depth of 2.5 mm. Cells were cycled between 3.6-4.5 V (NMC532), 3.55-4.4 V (NMC811), 3.65-4.4 V (LCO), and 2.95-3.7 (LFP) at C/5 D/2 and 40 °C with 0.6 M LiDFOB 0.6 M LiBF<sub>4</sub> FEC:DEC 1:2 electrolyte. The error bars show the standard deviation between pair measurements.

Cells aged to 50 cycles were also tested, shown in **Figure 6.6b**. Here, a significant difference in the temperature vs time signals are observed. However, the intrinsic safety of the positive electrode chemistries is probably not the cause of this disparity since the ranking is not what we would expect with NMC532 cells exhibiting the highest temperatures. Instead, this disparity is likely a result of the remaining capacity available to generate heat during a short circuit uncontrolled discharge. NMC811 cells cycled to 80%

---

\*NMC811 and LCO cells were tested at 4.4 V, NMC532 cells were tested at 4.5 V, and LFP cells tested at 3.7 V.

DoD and LCO cells cycled to 90%<sup>†</sup> DoD, tested here, have worse capacity retention than NMC532. As a result, less capacity is available for discharge and less heat is generated during the nail penetration. LFP cells have an even worse capacity retention, with only about 30% remaining lithium inventory available for discharge, resulting in the smallest temperature signal. None of these tests result in thermal runaway. Overall, the positive electrode chemistry does not appear to significantly impact the safety of the small 250 mAh anode-free pouch cells cycled with dual-salt electrolyte.

## 6.2 Degradation Analysis

For further insight into the degradation of anode-free cells with different positive electrodes, in depth impedance and electrolyte analysis was performed for cells aged under nominal cycling conditions—80% DoD for NMC532 (3.6-4.5 V), NMC811 (3.55-4.4 V), LCO (3.86-4.4 V), and 90% DoD for LFP (2.95-3.7 V) cycled at C/5 D/2 at 40 °C with dual-salt electrolyte.

### 6.2.1 Impedance Growth

We have identified that resistance growth plays a strong role in the degradation of anode-free cells, particularly for cells with NMC532 and NMC811 electrodes. In contrast, the resistance growth is much more subdued in anode-free cells with LCO electrodes. To identify the sources of this behaviour, electrochemical impedance spectroscopy (EIS) was performed on cells as a function of cycling using a frequency response analyzer (FRA) system. **Figure 6.7** shows the Nyquist impedance spectra for each electrode chemistry; the first column shows a magnified view of the first few spectra, and the second column shows the entire series. Note that the x-axes are not the same scale for the different positive electrodes. **Figure A.20** shows the cycling results of these FRA tests.

---

<sup>†</sup> Unlike the previous section which showed the best performance for LCO cells cycled to 80% DoD (3.86-4.4 V), the LCO cells used in these safety tests were cycled to 90% DoD (3.65-4.4 V) which exhibited significantly worse performance as shown in **Figure 6.3**.

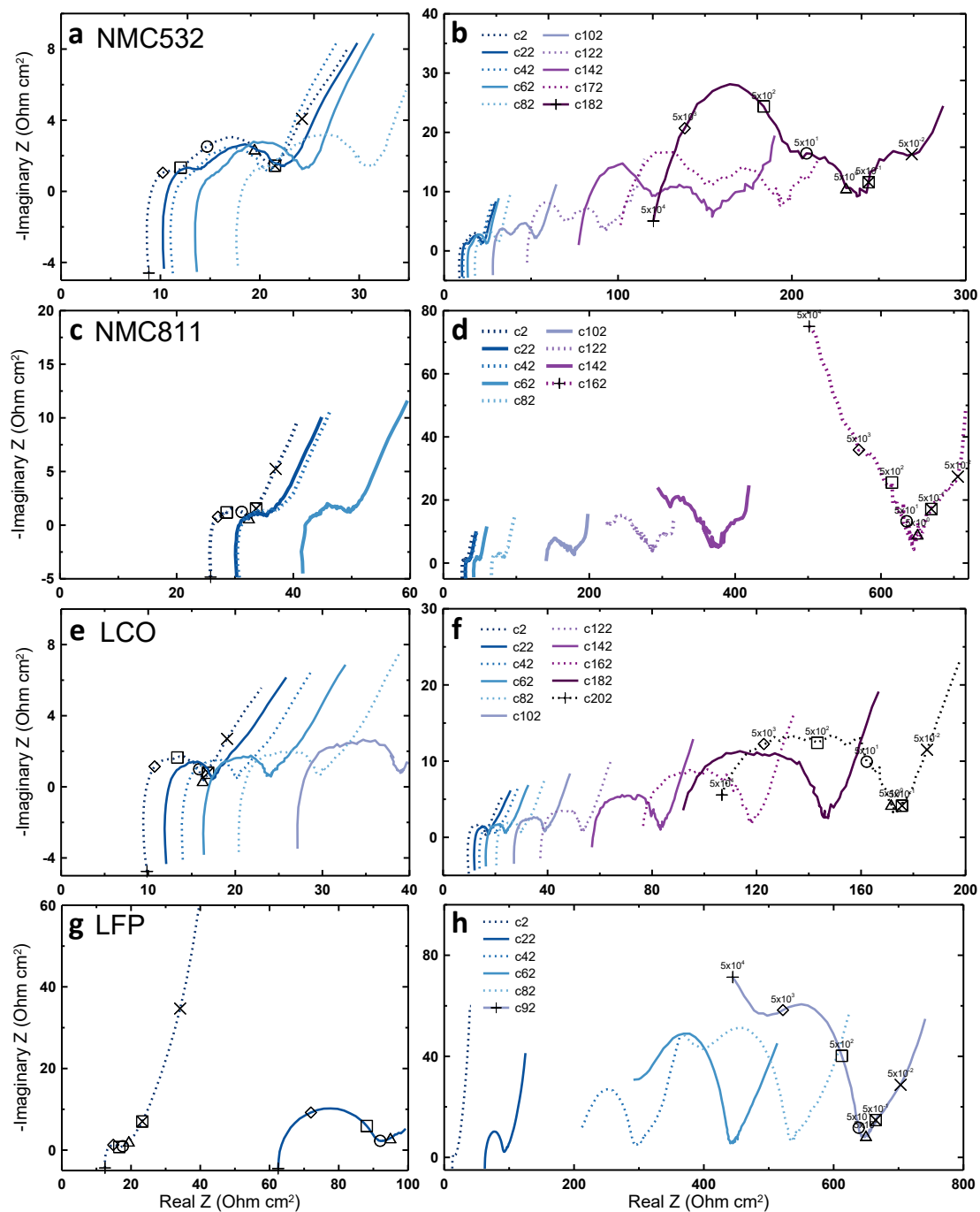


**Figure 6.7 | Positive electrode EIS.** a-b, NMC532; c-d, NMC811; e-f, LCO; g-h, LFP anode-free EIS spectra as a function of cycle. The first column shows a magnified view of the first few Nyquist plots; the entire series is shown in the second column. The Real Z x-axes are not equal for each panel. The first and last EIS spectra have symbols appearing at each frequency decade between  $5 \times 10^4 - 5 \times 10^{-2}$  Hz.



In **Figure 6.7**, the EIS spectra for every 20 cycles is shown, alternating between dashed and solid lines for clarity. Symbols appearing at each frequency decade from  $5 \times 10^4$ - $5 \times 10^{-2}$  Hz are also included for the first and last EIS spectra. Looking at the uncropped view in the second column, considering the different x-axis scales, LFP and NMC811 cells show the most dramatic impedance growth; NMC532 cells exhibit less impedance growth, and LCO cells show the least impedance growth. The same ranking is observed for the growth in solution resistance ( $R_s$ ), the real Z shift from zero, but it is worth noting the contrast between the massive  $R_s$  growth of LFP compared to the relatively minimal  $R_s$  growth of LCO.

For a quantitative analysis of the contributions to impedance growth, the EIS spectra were fit with using the RelaxIS 3 software suite. These fits are shown in **Figure A.21-Figure A.24**. Impedance spectra with two semi-circular humps (*i.e.* for NMC532, NMC811) were fit with an equivalent circuit model consisting of a resistor corresponding to the solution resistance ( $R1 = R_s$ ), two R-CPE circuits corresponding to the two charge transfer semi-circles ( $R2 + R3 = R_{ct}$ ), and a Warburg impedance element for solid-state diffusion. This circuit model is shown in **Figure 6.8f**. It is less obvious for the LCO spectra that there are two distinct semi-circular humps; however, the flatter spectra shape shown in **Figure 6.7e** and **f** are better fit with two semi-circles than just one, so this circuit model was also used for LCO. Only one discernable semi-circle is observed for the LFP spectra, so they were fit using an equivalent circuit model consisting of a single R-CPE circuit as shown in **Figure A.24**. The shape of the NMC811 and LFP spectra begin to change dramatically after significant impedance growth at around cycle 122 and cycle 62, respectively. Instead of a semi-circle ending at a minimum at high frequency, these spectra end with a maximum at high frequency, morphing into a lopsided W or V shape. This appears to be the result of an emergent high frequency ( $> 5 \times 10^4$  Hz) semi-circle, as confirmed with *ex-situ* EIS measurements performed on an aged NMC811 tested to 700 kHz (**Figure A.25**). It is not clear what the cause of this high frequency semi-circle is, but it seems to show up after significant cell degradation and severe impedance growth. Regardless, since this semi-circle is not entirely captured in the 50 kHz-10 mHz frequency range of the FRA experiments, once this semi-circle becomes dominant in the Nyquist curves, reliable fits

cannot be made. Therefore, fits for NMC811 cells were only performed to cycle 122, and fits for LFP cells were only performed to cycle 92. An example fit for the second cycle of NMC532 is shown in **Figure 6.8f**. The contribution of each circuit element is shown in different colours underneath the fitted data.

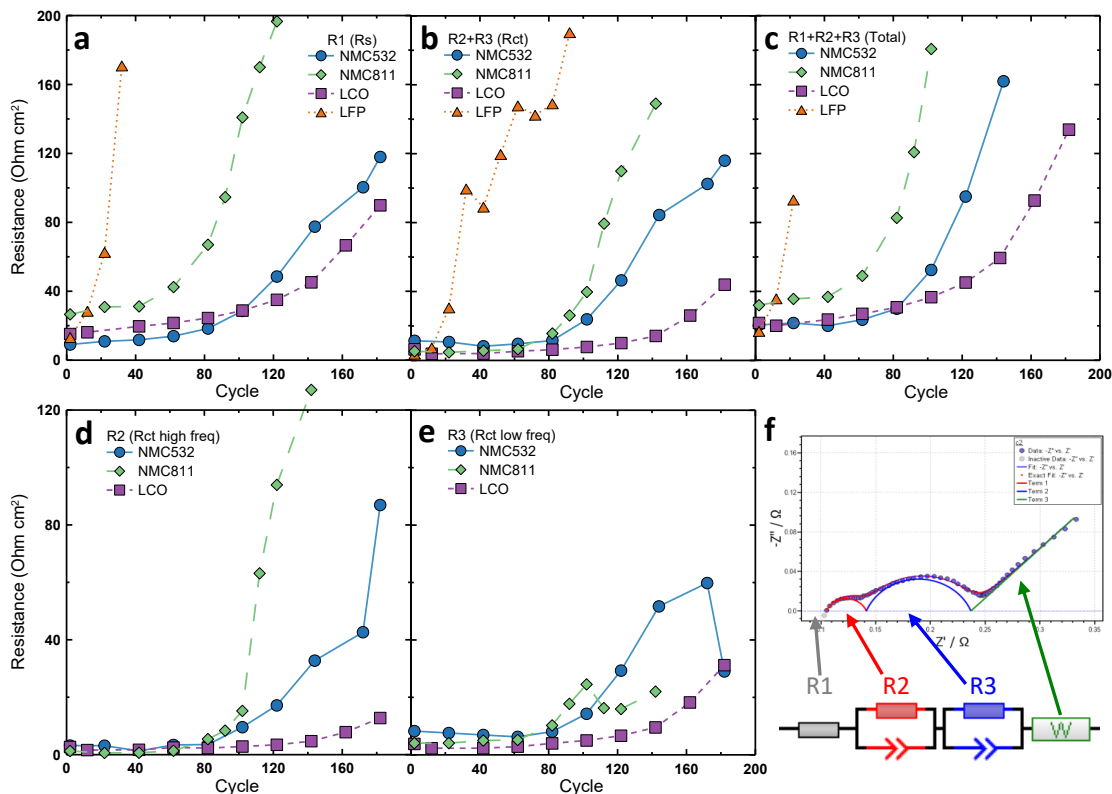


**Figure 6.8 | EIS fit parameters.** a-e, Equivalent circuit fit parameters vs cycle for EIS measurements of aged anode-free cells with different positive electrodes. The solution resistance ( $R_s = R1$ , a), charge transfer resistance ( $R_{ct} = R2 + R3$ , b), total resistance ( $R1 + R2 + R3$ , c), high frequency charge transfer resistance ( $R2$ , d), and low frequency charge transfer resistance ( $R3$ , e) are shown. f, Example EIS data (circles) that has been fit (solid lines); the individual contributions of each circle elements are shown beneath in colour. Cells were cycled between 3.6-4.5 V (NMC532), 3.55-4.4 V (NMC811), 3.86-4.4 V (LCO), and 2.95-3.7 (LFP) at C/5 D/2 and 40 °C with 0.6 M LiDFOB 0.6 M LiBF<sub>4</sub> FEC:DEC 1:2 electrolyte.

**Figure 6.8a-e** show the extracted parameters from the EIS fits. **Figure 6.8a** shows the solution resistance ( $R_s$ , or  $R1$  in the equivalent circuit model). As previously noted, LCO cells show the slowest rate of  $R_s$  growth, with NMC532 not far behind. NMC811 cells

show a similarly stable solution resistance for the first 40 cycles, but after 40 cycles a severe  $R_s$  growth ensues. For LFP, there is an immediate severe solution resistance growth. We have previously demonstrated that the solution resistance of anode-free cells grows due to salt depletion and electrolyte dry-out resultant of uncontrolled lithium morphology degradation.

The total charge transfer resistance ( $R_{ct}$ )— $R_2 + R_3$  for NMC532, NMC811, and LCO cells fit with two R-CPE circuits and just  $R_2$  for LFP fit with one R-CPE circuit—is shown in **Figure 6.8b**. NMC532, NMC811, and LCO cells exhibit a stable  $R_{ct}$  for about 60 cycles before significant growth develops, again with the ranking LCO < NMC532 < NMC811. The charge transfer resistance of LFP cells begin to soar after just 10 cycles. The total resistance ( $R_s + R_{ct} = R_1 + R_2 + R_3$ ) is plotted in **Figure 6.8c**. These parameters are also plotted vs equivalent full cycle in **Figure A.26**. It should be noted that the performance of the LCO cell cycling with the FRA protocol, shown in **Figure A.20**, performs worse than LCO cells cycling normally, shown in **Figure 6.5**. However, even with worse FRA cycling, the LCO cell still ekes out a better lifetime than the other positive electrode chemistry and maintains a lower delta V for longer. This is probably the “worse case” cycling behaviour as opposed to the average as shown in **Figure 6.5**.

To try to understand the contributions to the two charge transfer semi-circles observed for NMC532, NMC811, and LCO cells—and perhaps to deconvolute the positive and negative electrode contributions—the impedance spectra of symmetric cells built from electrodes extracted from NMC532 anode-free cells were analyzed in **Figure A.27**. Unfortunately, through this analysis we learned that the positive and negative electrode contributions cannot be neatly deconvoluted since they overlap at low frequencies. However, the high frequency semi-circle appears to be solely attributed to the lithium metal negative electrode. A more robust analysis of symmetric cells built from aged cells retrieved from each positive electrode chemistry should be performed in the future for a better insight into the charge transfer resistance contributions.

The high and low frequency contributions to the charge transfer resistance ( $R_2$  and  $R_3$  in the equivalent circuit model) are plotted vs cycle in **Figure 6.8d** and **e**. This shows that the major differences in  $R_{ct}$  appear at high frequency (**Figure 6.8d**) and thus are attributed to impeded charge transfer of the lithium negative electrode. The low frequency (**Figure 6.8e**)  $R_{ct}$  growth does also show some difference between the positive electrode chemistries; therefore, the impedance at the positive electrode may also be contributing to rising charge transfer resistance, but certainly less so than the negative lithium electrode.

**Figure 6.7** and **Figure 6.8** demonstrate significant disparity in impedance growth between anode-free cells with different positive electrodes. LCO cells clearly exhibit a lower impedance growth compared to the other cell chemistries. As discussed in section 4.2.3, there is a feedback loop between resistance growth, morphology degradation, and cell failure since resistance growth contributes to worsening morphology which then precipitates failure. The relatively low impedance growth of LCO cells thus explains the minimal thickness expansion of these cells demonstrated in **Figure 6.5g**.

### 6.2.2 Salt Depletion

At least half of the resistance growth of aged anode-free cells is resultant of increased solution resistance, as shown in **Figure 6.8a**. Since we know salt depletion, a source of  $R_s$  growth, is a failure mode for NMC532 anode-free cells with dual-salt electrolyte, investigating electrolyte degradation in each positive electrode chemistry was an obvious next step. Therefore, we extracted electrolyte from aged anode-free cells and performed liquid NMR analysis to quantify the LiDFOB and LiBF<sub>4</sub> salt concentrations. Since salt depletion is a result of parasitic reactions between the electrolyte and electrode materials, the amount of salt consumption should be related to the amount of capacity cycled. Therefore, salt concentration is plotted vs equivalent full cycle in **Figure 6.9**. This is also plotted vs cycle in **Figure A.28**.

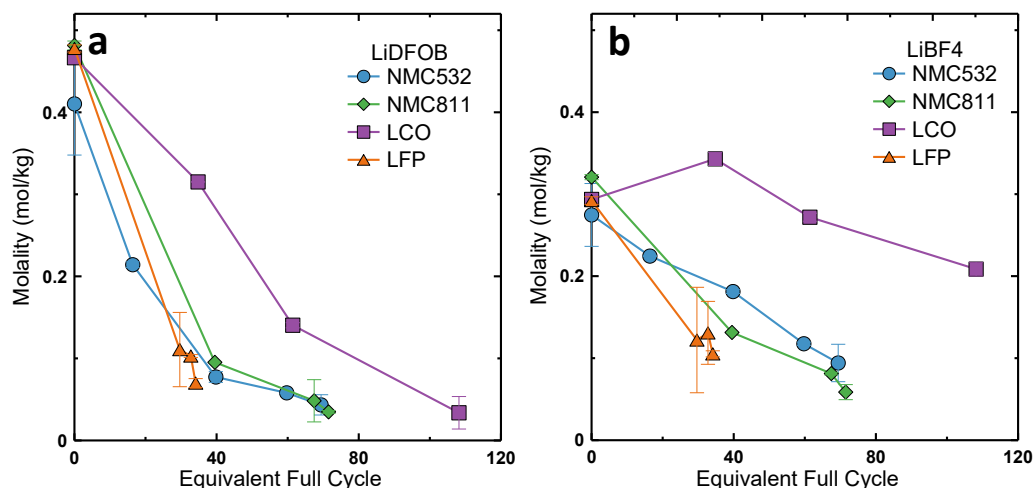


**Figure 6.9 | Positive electrode salt depletion. a-b,** LiDFOB (a) and LiBF<sub>4</sub> (b) salt concentration vs equivalent full cycle as measured via liquid NMR of extracted electrolyte from cycled anode-free cells. The error bars show the standard deviation of duplicate measurements. Cells were cycled between 3.6-4.5 V (NMC532), 3.55-4.4 V (NMC811), 3.86-4.4 V (LCO), and 2.95-3.7 (LFP) at C/5 D/2 and 40 °C with 0.6 M (0.52 mol/kg) LiDFOB 0.6 M (0.52 mol/kg) LiBF<sub>4</sub> FEC:DEC 1:2 electrolyte.

The molarity of dual-salt electrolyte is 0.6 M LiDFOB 0.6 M LiBF<sub>4</sub>. This corresponds to a molality, as plotted in **Figure 6.9**, of 0.52 mol/kg LiDFOB 0.52 mol/kg LiBF<sub>4</sub>. However, the initial concentrations we observe are only about 0.43 mol/kg LiDFOB (**Figure 6.9a**) and 0.3 mol/kg LiBF<sub>4</sub> (**Figure 6.9b**). This is not an insignificant difference from the expected values. Therefore, one must conclude that quantifying lithium salt concentrations using this method is not particularly accurate. However, since these differences appear to be systematic, we believe that this method is precise and that the changes in molality observed are meaningful.

As expected, salt depletion occurs in each anode-free cell chemistry. LiDFOB is consumed at a faster rate compared to LiBF<sub>4</sub>. The rate of salt depletion is similar for NMC532, NMC811, and LFP cells, but it is significantly less for LCO. Surprisingly, LCO cells exhibit about half the rate of LiDFOB loss and about one third the rate of LiBF<sub>4</sub> loss. This slowed rate of salt depletion accounts for, in part, the lower solution resistance growth observed for LCO cells. It is not clear what the cause of this behaviour might be. Through electrolyte analysis of cycled NMC532 symmetric cells in Section 4.2.2, we showed that

both LiDFOB and LiBF<sub>4</sub> are consumed by the negative lithium electrode, whereas the positive electrode consumed LiDFOB while producing LiBF<sub>4</sub>. Since the negative electrode chemistries are the same (both cycling lithium metal), one might naïvely assume that the contributions to salt consumption by the negative electrode should be the same. In this case, a lowered rate of LiDFOB consumption could be attributed to the positive LCO electrode not facilitating the conversion of LiDFOB to LiBF<sub>4</sub>. However, this does not account for a reduced rate of LiBF<sub>4</sub> consumption, since LiBF<sub>4</sub> was only shown to be consumed on the lithium negative electrode. Therefore, one might conclude that a more sophisticated form of crosstalk is going on, whereby the presence of the LCO positive electrode in the cell slows the rate of LiBF<sub>4</sub> consumption on the lithium metal negative electrode. A simpler explanation might be that a lower surface area lithium morphology in LCO cells results in less salt consumption. More experimental evidence—such as electrolyte analysis from cycled symmetric cells and morphological analysis of lithium extracted from LCO cells—is required to further elucidate this behaviour.

Although salt depletion contributes to the rise of solution resistance, it is not the sole cause of increases in the ohmic resistance. This is clearly demonstrated by the fact that NMC532, NMC811, and LFP cells exhibit similar salt depletion but very different solution resistance growth. This indicates that the other contributor to solution resistance growth—electrolyte dry out due to lithium morphology degradation—must play a significant role here. In particular, electrolyte dry-out likely causes the severe solution resistance growth observed toward the end of life.

### 6.3 Additional Cycling Results

So far, we have benchmarked anode-free cells with different positive electrodes using our dual-salt electrolyte and control cycling conditions. Now, we test the performance of different electrolyte formulations as well as the impact high pressure cycling and hot formation on each cell chemistry.

### 6.3.1 Different Electrolytes & Optimized Cycling Conditions

**Figure 6.10** shows cycling performance plotted as stack volumetric energy density vs cycle for NMC532 anode-free cells. We have already explored different electrolyte chemistries for NMC532 in Section 4.1.2. However, we had only shown the impact of increased mechanical pressure and hot formation on cells with dual-salt electrolyte. These data are replotted **Figure 6.10a,c** to be compared now with results for cells utilizing the successful localized high concentration (LHC) electrolyte<sup>47</sup> cycled under increased mechanical pressure (**Figure 6.10b**) and with hot formation (**Figure 6.10d**).

**Figure 6.10b** shows that cells with LHC 1.73 M LiFSI DME:TTE electrolyte do not benefit from high pressure as their dual-salt counterparts do. In **Figure 6.10d**, a similar rate of energy fade is observed cycling at 20 °C after hot formation as with 40 °C cycling—demonstrating that hot formation is also successful for this electrolyte chemistry. However, the already depressed energy density delivered by this LHC electrolyte at 40 °C is further reduced to 800 Wh/L at 20 °C. We have previously identified the transport limitations in this electrolyte system, resulting in a reduced reversible capacity and thereby decreasing the energy density. Cycling at 20 °C further reduces the reversible capacity because of diminished diffusion kinetics at lower temperature, both in solid state and in the electrolyte. Nevertheless, cells with LHC electrolyte exhibit a stable energy fade, only resulting in worse lifetime than dual-salt electrolytes because of their reduced initial energy density. Lifetime, defined here as the number of cycles that cells deliver a higher energy density than comparator Li-ion cells, is about 160 cycles for cells with LHC electrolyte compared to 200 cycles for the best dual-salt electrolyte results.

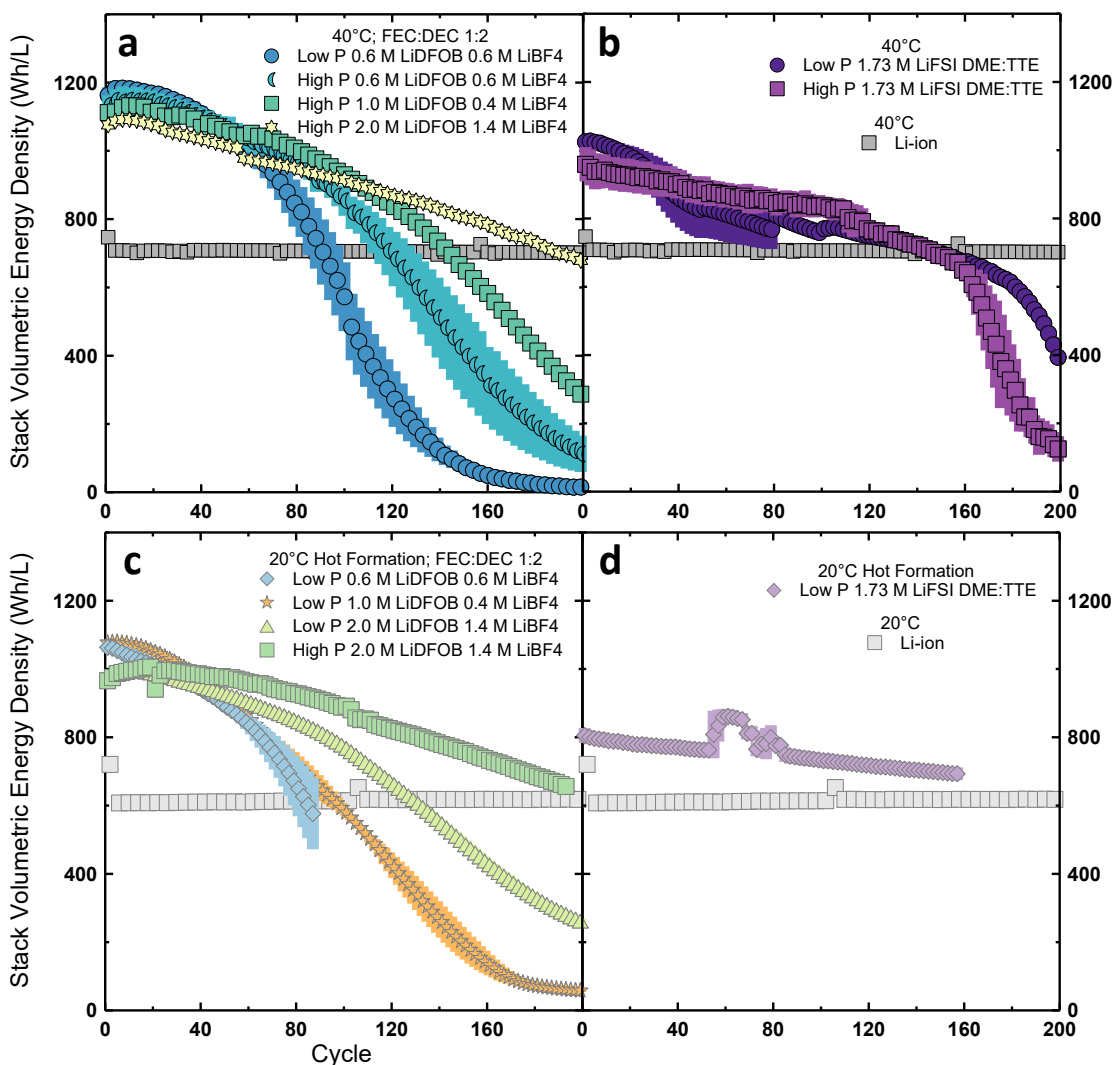


**Figure 6.10 | NMC532 electrolyte study. a-d,** Cycling performance of NMC532 anode-free cells at 40 °C (a,b) and 20 °C after hot formation (c,d) compared with NMC532 Li-ion cells. Anode-free cells were cycled between 3.6-4.5 V at C/5 D/2 at low pressure (Low P, 200 kPa) and high pressure (High P, 1200 kPa). Li-ion cells were cycled between 3.0-4.3 V at C/3 D/3 with 1.2 M LiPF<sub>6</sub> EC:EMC 3:7 + 2%VC 1%DTD electrolyte. Error bars represent the standard deviation of duplicate cells.

**Figure 6.11** shows the performance NMC811 anode-free cells tested with different electrolytes under different cycling conditions. **Figure 6.11a** shows dual-salt electrolyte formulations tested under high and low mechanical pressure. As with NMC532, increasing the salt concentrations of LiDFOB and LiBF<sub>4</sub> as well as cycling under higher mechanical pressure improves lifetime. At high pressure, the 1.6 M/0.8 M and 2.0 M/1.4 M



LiDFOB/LiBF<sub>4</sub> formulations exhibit similar performance, indicating that the former is sufficient to overcome salt depletion through 200 cycles. The energy fade is more linear compared to the classic 0.6 M/0.6 M formulation, indicating that severe resistance growth has also been largely overcome. Nevertheless, there is a more significant rate of lithium inventory loss compared to NMC532 since a lifetime of only 140 cycles is delivered compared to 200 cycles for NMC532 anode-free cells.

**Figure 6.11b** shows the performance of non-dual-salt electrolytes in NMC811 anode-free cells. Again, the LHC 1.73 M LiFSI DME:TTE electrolyte shows more stable cycling at a lower initial energy density. Despite this lowered energy density, the LHC electrolyte is more successful than dual-salt electrolytes in NMC811 anode-free cells, enabling an energy density higher than the NMC532 Li-ion comparator for 170 cycles. The FDMB-based electrolytes (two batches of FDMB were received and tested) show significantly worse energy retention. This electrolyte formulation also exhibits transport limitations, decreasing the initial energy density delivered.

NMC811 cells with dual-salt electrolytes tested at 20 °C with hot formation at both high and low pressure are shown in **Figure 6.11c**. Hot formation is mostly successful at facilitating similar lifetimes as 40 °C cycling. However, the highest concentration dual-salt cells tested under pressure only exhibit a cycle life of about 120 cycles, compared with 140 cycles at 40 °C. **Figure 6.11d** shows results for NMC811 cells with LHC electrolyte tested after hot formation. The reduced energy density due to lower temperature cycling coupled with inherent electrolyte transport limits and 4.3 V operation results in an energy density nearly on par with comparator NMC532 Li-ion cells. With 4.5 V operation, a lifetime of 120 cycles is enabled, with a more dramatic energy fade occurring afterwards—a behaviour not observed with 4.3 V operation. Additional cycling results for NMC811 cells with different electrolyte formulations tested between different voltage ranges are shown in **Figure A.29**.

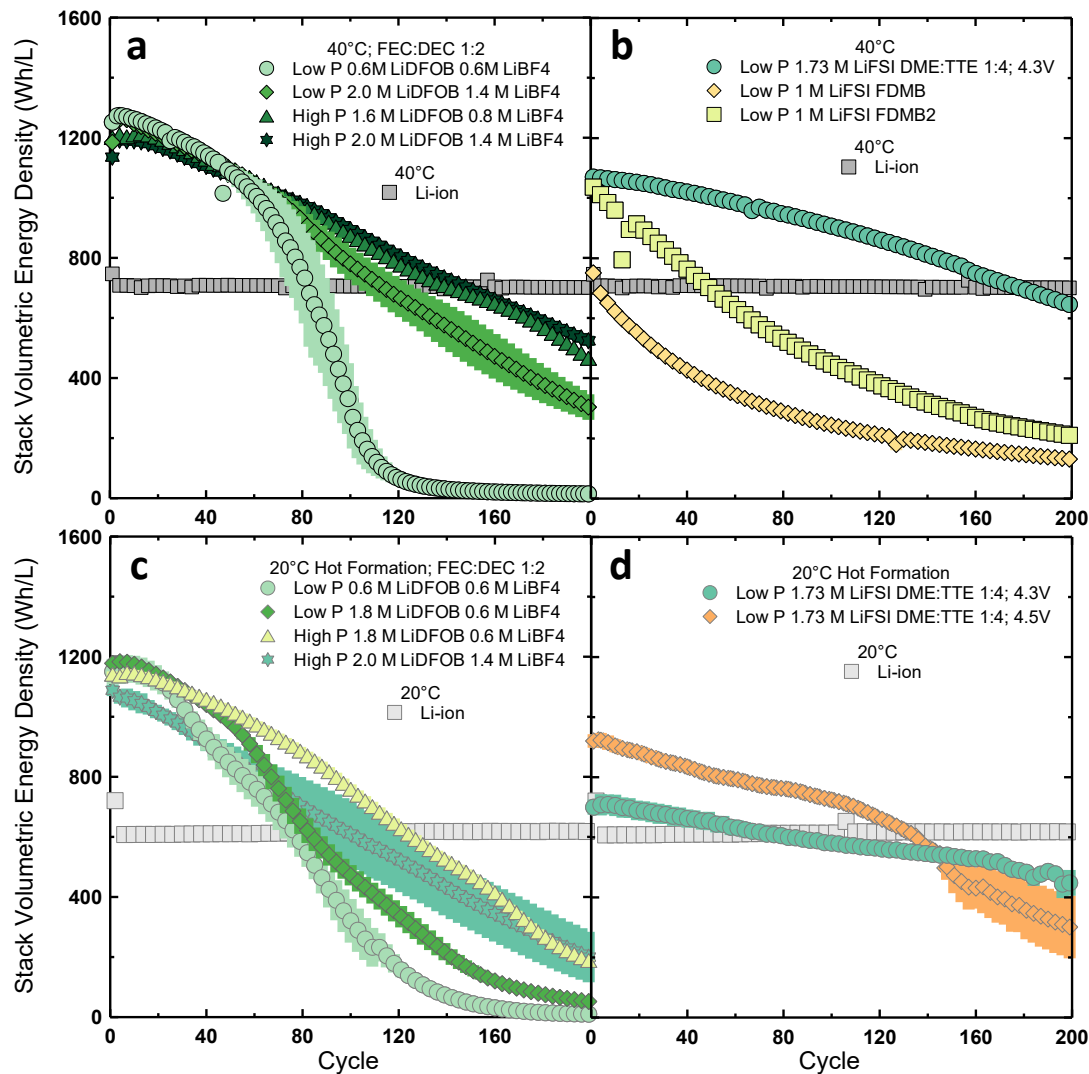


**Figure 6.11 | NMC811 electrolyte study.** a-d, Cycling performance of NMC811 anode-free cells at 40 °C (a,b) and 20 °C after hot formation (c,d) compared with NMC532 Li-ion cells. Anode-free cells were cycled between 3.55-4.4 V (with exception of the different UCVs listed in the legend) at C/5 D/2 at low pressure (Low P, 200 kPa) and high pressure (High P, 1200 kPa). Li-ion cells were cycled between 3.0-4.3 V at C/3 D/3. Error bars represent the standard deviation of duplicate cells.

Overall, the LHC electrolyte results in more stable cycling than dual-salt formulations in NMC anode-free cells. However, the lowered energy density—which may facilitate slowed degradation due to the creation of a larger lithium reservoir—results with lifetimes comparable to dual-salt formulations. The safety of the LHC electrolyte system must also

continue to be scrutinized, as we showed violent thermal runaway events for NMC532 anode-free cells with this electrolyte in Section 4.3.

**Figure 6.12** shows cycling results for LCO anode-free cells. The performance of different dual-salt formulations tested under low pressure are shown in **Figure 6.12a**. The 1.6 M LiDFOB 0.8 M LiBF<sub>4</sub> formulation shows the longest lifetime of 190 cycles. Testing two 0.6 M/0.6 M formulations with the addition of TFEC solvent show similar performance to the control FEC:DEC solvent mixture. **Figure 6.12b** shows the performance of LHC and FDMB electrolytes. Again, a familiar trend re-emerges of a stable energy fade but at a lower initial energy density. However, the depressed energy density is even more significant than in NMC cells, resulting in energy densities on par or lower than the NMC532 Li-ion cell comparators from the beginning of cycling.

**Figure 6.12c** shows the impact of high pressure cycling on LCO cells with dual-salt electrolyte. A significantly improved energy retention is enabled, but the energy density is decreased by about 300 Wh/L—a behaviour not exhibited by NMC cells. The 20 °C results in **Figure 6.12d** show similarly depressed energy densities not observed under the same conditions for NMC cells with dual-salt electrolytes. To understand what is going on here, one needs only to consider the shape of the voltage curve of LCO cells discharged to 3.86 V, shown in **Figure 6.4d**. Unlike with the NMCs, the LCO voltage curve is very flat towards the end of discharge. Since increased cell resistance acts to shift the discharge voltage curve downward, cells with a flat voltage curve towards the end of discharge are highly susceptible to impedance growth as a significant portion of capacity is cut off with even the slightest downward shift. The highly sloped NMC532 and NMC811 voltage curves at the end of discharge result in very little capacity being cut off, at least for small initial increases to cell resistance. Therefore, anything that results in increased cell resistance—increased pressure, electrolyte transport limitations (LHC and FDMB electrolytes), reduced electrode kinetics (lower temperature operation)—will have a significant detriment to the reversible capacity and energy density delivered by anode-free LCO cells cycled to 3.86 V.

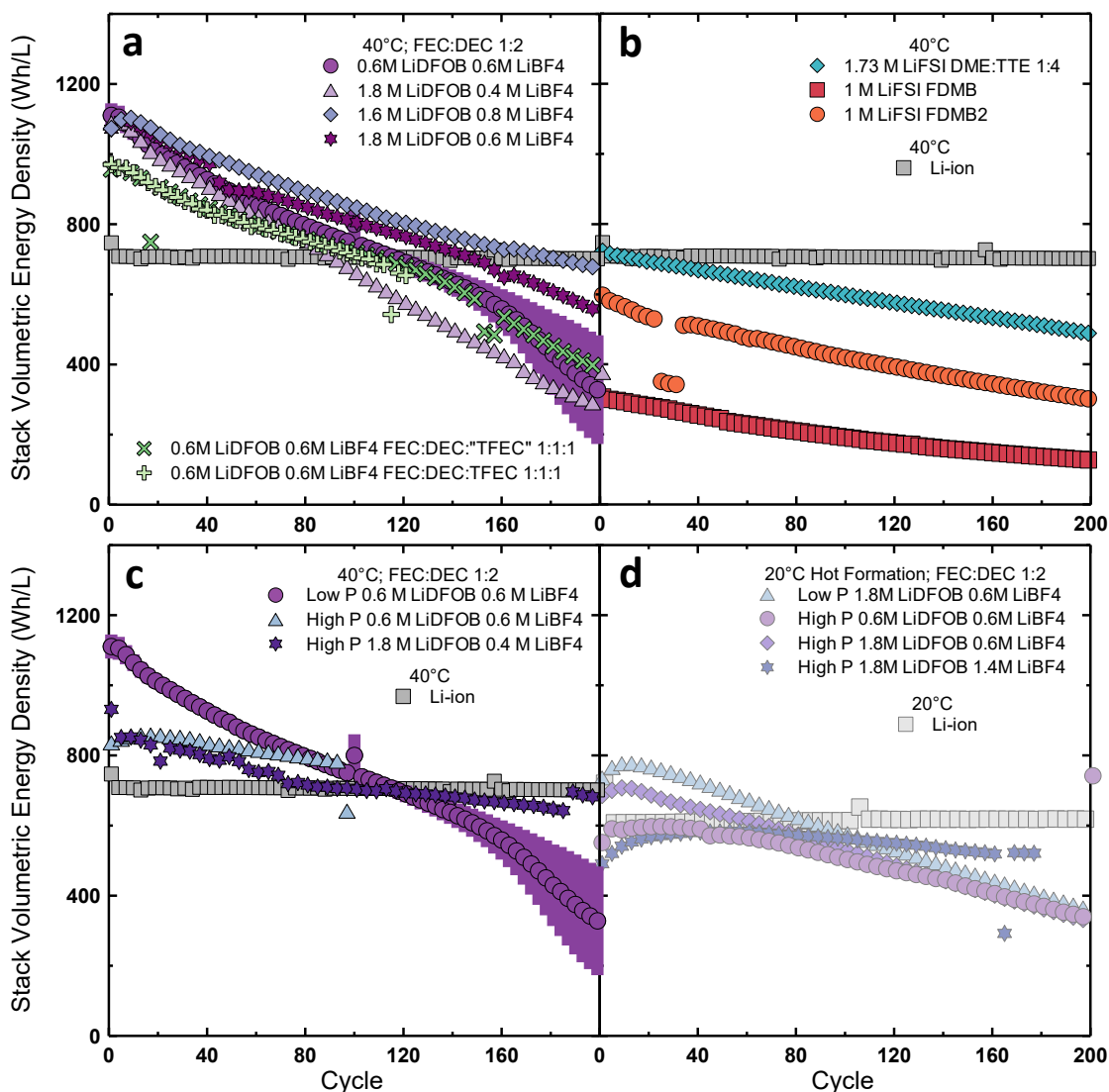


**Figure 6.12 | LCO electrolyte study. a-d,** Cycling performance of LCO anode-free cells at 40 °C (a-c) and 20 °C after hot formation (d) compared with NMC532 Li-ion cells. Anode-free cells were cycled between 3.86-4.4 V at C/5 D/2 at low pressure (Low P, 200 kPa) and high pressure (High P, 1200 kPa). Li-ion cells were cycled between 3.0-4.3 V at C/3 D/3 with 1.2 M LiPF<sub>6</sub> EC:EMC 3:7 + 2%VC 1%DTD electrolyte. Error bars represent the standard deviation of duplicate cells.

**Figure 6.13** shows cycling results for LFP anode-free cells. Remember that the NMC532 Li-ion cell comparators deliver an energy density of about 700 Wh/L; therefore, the LFP results here already begin at a deficit. Carbonate-based electrolyte blends are shown in **Figure 6.13a**. We have previously shown how dual-salt LiDFOB/LiBF<sub>4</sub> electrolyte is not successful in LFP anode-free cells. In stark contrast to NMC532 cells, 1.0 M LiPF<sub>6</sub> results

in the same performance as 0.6 M LiDFOB 0.6 M LiBF<sub>4</sub> electrolyte. Single-salt 1.2 M LiDFOB electrolyte, although still performing very poorly, extends cycle life similarly to 1.4 M LiDFOB 0.4 M LiBF<sub>4</sub> and 1.0 M LiDFOB 0.4 M LiBF<sub>4</sub>. This reveals a couple of things. The presence of LiBF<sub>4</sub> seems to provide no discernible benefit to cycle life, despite being consumed at a similar rate as in NMC cells as shown in **Figure 6.9**. Nevertheless, the increased salt concentrations do slightly benefit performance. This is likely because of the severe impedance growth exhibited in LFP anode-free cells—increasing the salt concentrations can act to mitigate kinetic hinderance. If this is the case, then increased LiPF<sub>6</sub> concentrations should also somewhat increase cycle life. Regardless, unlike in NMC532 anode-free cells, there does not appear to be a synergistic decomposition of LiDFOB and LiBF<sub>4</sub> that improves lithium reversibility in LFP anode-free cells.

Since ether-based electrolytes have been shown to be more successful in LFP anode-free cells due to their low operating potential,<sup>29</sup> many different ether electrolytes were tested in **Figure 6.13b**. A variety of LHC electrolytes with different solvents and diluents were tested. However, none more successful were found than the 1.73 M LiFSI DME:TTE electrolyte. Although an extended stable cycling performance is exhibited, the quick initial energy fade still results in an energy density of just 400 Wh/L after 50 cycles. The FDMB electrolytes performed similarly to the dual-salt electrolytes.

**Figure 6.13c** shows results for LFP cells with dual-salt and LHC electrolyte tested under low and high pressure. High pressure cycling does not significantly improve the performance of 0.6 M LiDFOB 0.6 M LiBF<sub>4</sub> electrolyte. However, cells with 1.73 M LiFSI DME:TTE 1:4 LHC electrolyte are benefitted by high pressure cycling, extending their lifetime to 120 cycles to 400 Wh/L. **Figure 6.13d** shows that the best carbonate-based electrolyte results are achieved 20 °C after hot formation at high pressure with a high concentration dual-salt electrolyte formulation.

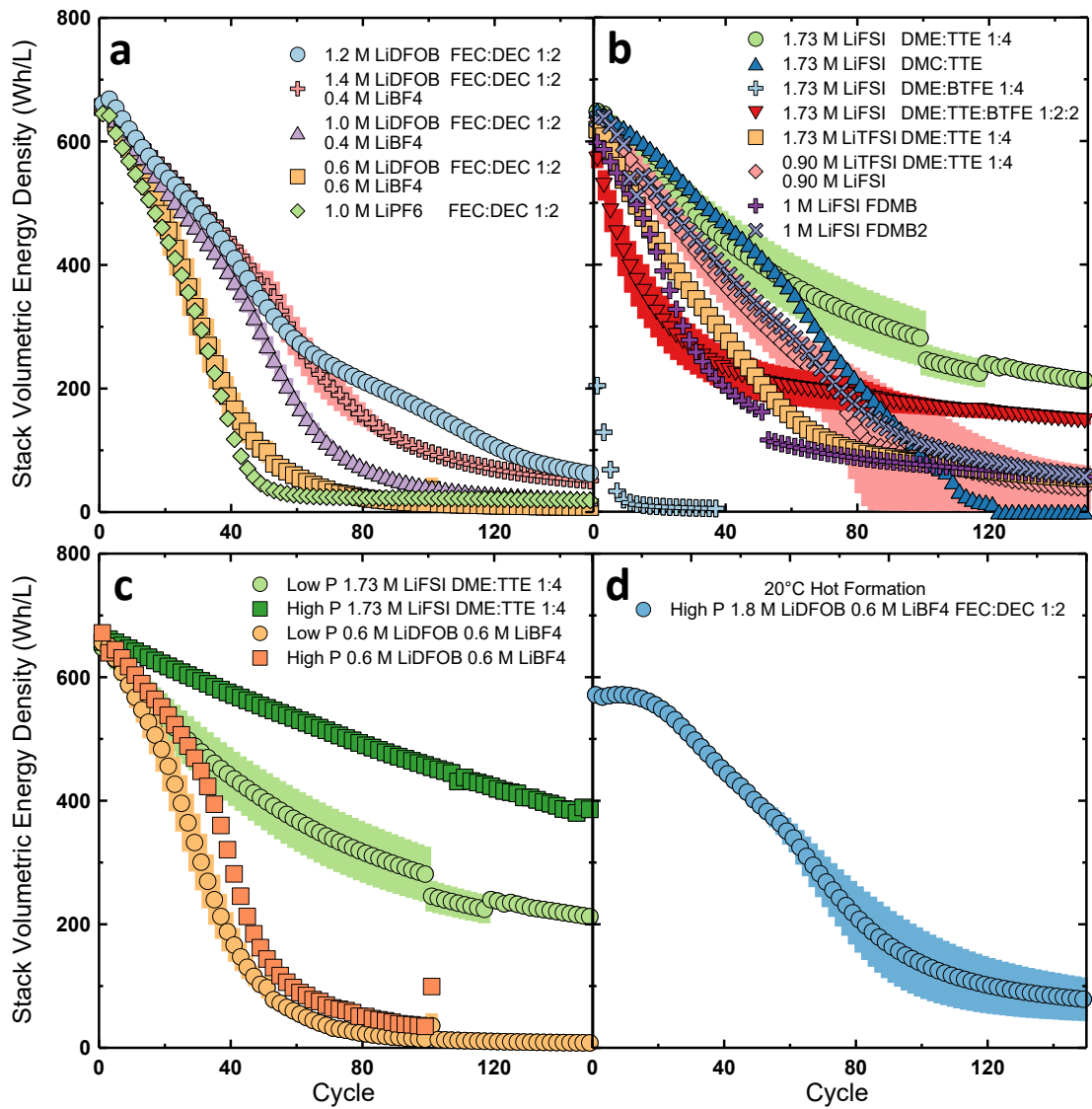


**Figure 6.13 | LFP electrolyte study. a-d,** Cycling performance of LFP anode-free cells at 40 °C (a-c) and 20 °C after hot formation (d). Anode-free cells were cycled between 2.95-3.7 V at C/5 D/2 at low pressure (Low P, 200 kPa) and high pressure (High P, 1200 kPa). Error bars represent the standard deviation of duplicate cells.

6.3.2 Cycle-Store

Another performance metric batteries need to satisfy is quiescent storage ability. In real life, batteries are not constantly cycled as our tests have simulated. Batteries need to be able to last on a shelf without degrading. In other words, beyond cycle life, calendar life is important. Moreover, a more realistic use profile of a battery-powered device may be a few

cycles followed by a period of inactivity. To better simulate this type of use profile and to gauge the storage ability of anode-free cells, we employed a cycle-store protocol in which cells were alternatively cycled and rested at open circuit voltage. We were concerned about the storage prospects of cells with dual-salt electrolyte because of the parasitic reactions which result in salt decomposition in this electrolyte—particularly at high voltage.<sup>167</sup> More recently, a paper from Stanford suggested that lithium metal electrodes may have a fatal flaw as they claimed to show that lithium metal loses at least 2-3% of its capacity after only 24 hours of aging, regardless of electrolyte chemistry.<sup>150</sup> Therefore, we set out to investigate storage performance and to determine if parasitic reactions at high voltage or if inherent calendar degradation of lithium metal may be inhibiting to realistic operation of anode-free cells with dual-salt electrolyte.

**Figure 6.14** shows cycle-store results for anode-free cells with NMC532, NMC811, and LCO positive electrodes. The cycle-store protocol consisted of repeating 10 cycles followed by a 74-hour open-circuit rest. Two open-circuit voltages were tested during the rest period: resting at the upper cut-off voltage at the top of charge (4.5 V for NMC532, 4.4 V for NMC811 and LCO) and resting at 4.0 V at about 50-60% state of charge. The top of charge rest was an aggressive test meant to exacerbate parasitic reactions—if degradation at high voltage storage was going to be a problem, it would be revealed with this protocol.

**Figure 6.14a-c** shows these results plotted vs cycle. First, we observe that storing at top of charge (circles) vs storing at 4.0 V (squares) results in the same lifetime—high voltage storage is not an issue cycling under these conditions. Moreover, these cycle-store results exhibit almost the same capacity retention as conventional cycling results (circles). Only the NMC811 cycle-store cells perform worse than conventional cycling, with lifetime shortened by ~20 cycles. Plotting these results vs time (**Figure 6.14d-e**) shows that cycle-store cells actually exhibit a longer calendar life than cells cycled normally. These results clearly indicate that lithium metal is not particularly susceptible to calendar aging and certainly is not losing 2-3% capacity for every 24 hours of storage.

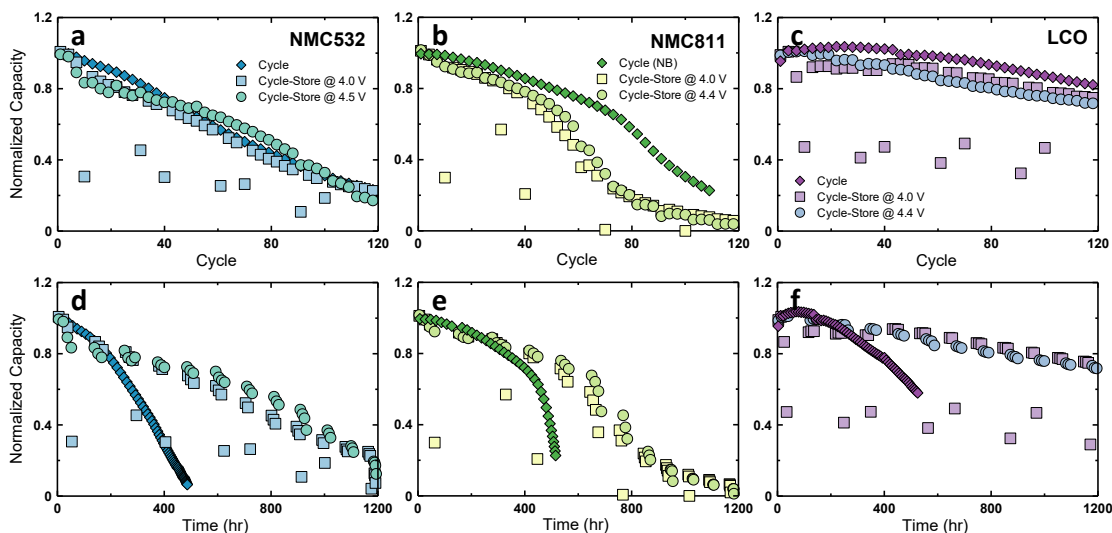


**Figure 6.14 | Cycle-store testing.** a-f, Normalized capacity vs cycle (a-c) and normalized capacity vs time (d-c) for NMC532, NMC811, and LCO anode-free cells tested with a cycle-store protocol. The storage period was 3 days and occurred every 10 cycles at the open circuit voltages listed in the legend. Cells were cycled between 3.6-4.5 V (NMC532), 3.55-4.4 V (NMC811), and 3.86-4.4 V (LCO) at C/5 D/2 and high pressure (1200 kPa) at 20 °C after hot formation with 0.6 M LiDFOB 0.6 M LiBF<sub>4</sub> FEC:DEC 1:2 electrolyte.

It is interesting that lithium metal is not intrinsically vulnerable to this cycle-store protocol as this somewhat contradicts conventional wisdom. SEI growth is conventionally thought to be a dominant degradation mode for lithium metal since significant capacity loss to electrolyte-lithium reactions were assumed to occur with every cycle due to the large volume change of cycled lithium constantly breaking and reforming the SEI. In this case, any time-dependant SEI growth would be exacerbated during storage periods between cycles. However, more recently, quantification of inactive lithium has shown that mechanically isolated lithium was the more significant mode of lithium inventory loss.<sup>71</sup> There is no reason to believe that more lithium would become mechanically isolated or that the lithium microstructure should worsen during storage. In this paradigm, cycle-store should not be any more harmful than conventional cycling, and this bears out in the data shown in **Figure 6.14**.

It should also be noted that although we showed here that high voltage storage did not significantly exacerbate parasitic reactions to harm dual-salt containing cells, these tests



were performed under favorable conditions. In Section 5.1 we learned that parasitic reactions with dual-salt electrolyte are tamed at lower temperature. Therefore, we performed these cycle-store tests at 20 °C after hot formation. Although in general this may be a more realistic cycling condition, anode-free cells might face high temperature storage if they were deployed in the field. Increased parasitic reactions may be more harmful during storage at higher temperatures.

### 6.3.3 Concluding Remarks

In this chapter, we set out to explore how the performance of anode-free cells with different positive electrodes might diverge. Indeed, we found significant differences between NMC532, NMC811, LCO, and LFP anode-free cells. In particular, impedance growth suffered by these cell chemistries varied, resulting in the shortest lifetime for NMC811 and the longest lifetime for LCO anode-free cells. Moreover, the positive electrode chemistries exhibited disparate compatibility with different electrolyte formulations.

Although LCO anode-free cells were originally intended as a test vehicle, we found that they exhibited some of the best performance of all the anode-free cells tested in this work to 80% depth of discharge. This is a result of lower impedance growth as well as a still mysterious suspected crosstalk between lithium metal and the LCO positive electrode. As discussed in the introduction, there are economic and ethical concerns regarding the use of significant portions of cobalt present in LCO electrodes. Therefore, LCO anode-free cells are unlikely to be deployed in any large-scale application such as for electric vehicles. But perhaps this chemistry may find a home in more niche markets that value energy density more than lifetime. For example, the drone I own for areal photography employs an LCO Li-ion cell battery. I would happily trade this for an LCO anode-free cell that would enable extended operating range even if I could only use it one hundred times.

Alternatively, instead of having to use LCO positive electrodes in anode-free cells, continued research may elucidate the mechanism that facilitates improved performance which we may be able to harness in other ways. One simple solution may be to build composite positive electrodes with small portions of LCO. Composite LCO-NMC positive

electrodes have been employed in the past to advantage the beneficial crosstalk of one electrode chemistry to improve the other<sup>170</sup> (although in this case it was the presence of NMC that improved the LCO). Perhaps the presence of small portions of LCO in composite NMC electrodes may impart the longer lifetime enabled by pure LCO electrodes in anode-free cells. Regardless, the promising performance of LCO anode-free cells merit further investigation.

## Chapter 7: Hybrid Lithium-Ion/Lithium Metal Cells

Increased energy density is the promise of lithium metal cells. However, as we have shown in this thesis, this benefit comes at the cost of longevity. The lifetime of cells cycling lithium metal is much reduced in comparison to conventional lithium-ion cells with graphite negative electrodes. In Section 5.4, we explored the idea of making a compromise between energy density and lifetime by tuning the depth of discharge. This compromise is based off the concept of silicon-graphite composite negative electrodes which are in commercial use today. Silicon negative electrode materials are similar to lithium metal in that they deliver a higher energy density but result in accelerated capacity fade due to enhanced lithium inventory loss from SEI growth and mechanical degradation. Therefore, a compromise between energy density and lifetime is made by partial incorporation of silicon (*e.g.* 10% by weight) into conventional graphite negative electrodes. The energy density of this silicon-graphite composite is larger than graphite alone, while the large volume expansion of silicon—the primary catalyst of enhanced lithium inventory loss—is mitigated by the surrounding matrix of graphite, thereby enabling long lifetime. Moreover, the delithiation potential of silicon is higher than graphite. This means that silicon component will only be accessed during a deep discharge, further benefiting longevity since aging of the silicon component will only occur during cycles with a deep discharge.

The successful application of silicon composite electrodes led us to question whether this concept could be translated to lithium metal. That is, can we achieve a compromise between energy density and longevity by implementing hybrid graphite/lithium metal negative electrodes? In hindsight, the similarities between silicon and lithium metal make this an obvious approach to try. At the same time, this is almost a crazy idea since lithium plating on graphite is normally considered a fatal degradation mode for lithium-ion cells, and here we are suggesting doing this purposefully. However, our new insights into successful electrolyte chemistries for reversibly cycling lithium metal now make this idea more viable.

This work was performed on the hybrid lithium-ion/lithium metal “semi anode-free” pouch cells with NMC532 positive electrodes detailed in **Table 3.1**. This work was previously published in Ref.<sup>171‡</sup>

## 7.1 Hybrid Graphite/Lithium Metal Electrodes

Hybrid lithium-ion/lithium metal cells were built like conventional lithium-ion cells but with a thin graphite coating (5.07 mg/cm<sup>2</sup> instead of 9.93 mg/cm<sup>2</sup>). Normally, the capacity of the positive and negative electrodes are balanced such that the graphite negative electrode reaches full capacity only when the desired upper cut-off voltage of the full cell is reached. Instead, these cells were designed such that the graphite electrode reaches full capacity at a voltage below the desired upper cut-off. Charging beyond this point results in the remaining capacity being plated as lithium metal on top of graphite. This is schematically shown in **Figure 7.2**. Since capacity is stored both in lithiated graphite as well as in metallic lithium, the energy density of the hybrid graphite/lithium metal electrode is higher than a pure graphite electrode but lower than a pure lithium metal electrode. At the top of charge (4.4 V) the hybrid cell stack is ~20% thinner and ~15% lighter than the conventional lithium-ion design. The hybrid cell thus offers an intermediate energy density, less than anode-free, but greater than lithium-ion. Due to the increased average voltage and decreased stack thickness and weight, the hybrid format boasts volumetric and specific energy densities 25% and 20% greater, respectively, than conventional lithium-ion cells.

---

<sup>‡</sup> C. Martin, M. Genovese, A.J. Louli, R. Weber, J.R. Dahn, Cycling Lithium Metal on Graphite to Form Hybrid Lithium-Ion/Lithium Metal Cells, *Joule*. **4** (2020) 1296–1310.

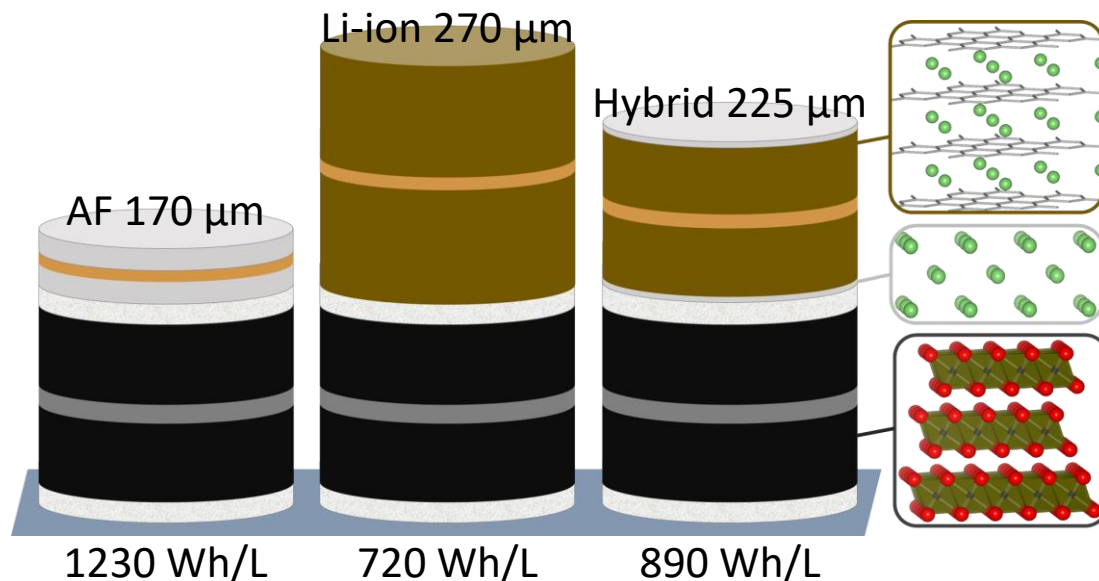


**Figure 7.1 | Hybrid lithium-ion/lithium metal cells.** Comparison of cell stacks for anode-free (AF, left), lithium-ion (center), and hybrid lithium-ion/lithium metal (right) cells. The stack thickness and energy densities are displayed at the top and bottom. The atomic structures of the active materials are also included; the gold-coloured layer represents lithiated graphite, the silver-coloured layer represents lithium metal, and the black coloured layer represents NMC532.

To demonstrate the electrode balancing and determine how much capacity is stored in the thin graphite electrode and how much capacity is stored as plated lithium metal, differential voltage ( $dV/dQ$ ) analysis was performed. **Figure 7.2a** shows the measured voltage profile for the hybrid cell (green) along with its corresponding differential voltage curve (blue). For this analysis, the full cell differential voltage curve is fit with a linear combination of the positive electrode (orange) and negative electrode (pink) voltage curves.<sup>172,173</sup> The fit is shown in light purple and agrees well with the measured  $dV/dQ$  vs  $Q$  curve. Beyond the conventional features corresponding to graphite staging, the full cell  $dV/dQ$  curves show a large peak at approximately 140 mAh. This corresponds to the capacity at which the potential of the negative electrode falls to 0.0 V indicating that the graphite is fully lithiated and subsequent capacity will be plated as lithium metal on the graphite surface. At this point, a noticeable inflection in the full cell voltage curve at approximately 3.85 V. This information is summarized in the full and half-cell voltage curves shown in **Figure 7.2b**.

The capacity of the hybrid cells when charged to 4.4 V is 230 mAh. The graphite component stores 140 mAh of capacity. Therefore, the remaining 90 mAh ( $1 \text{ mAh/cm}^2$ ) is plated as lithium metal.

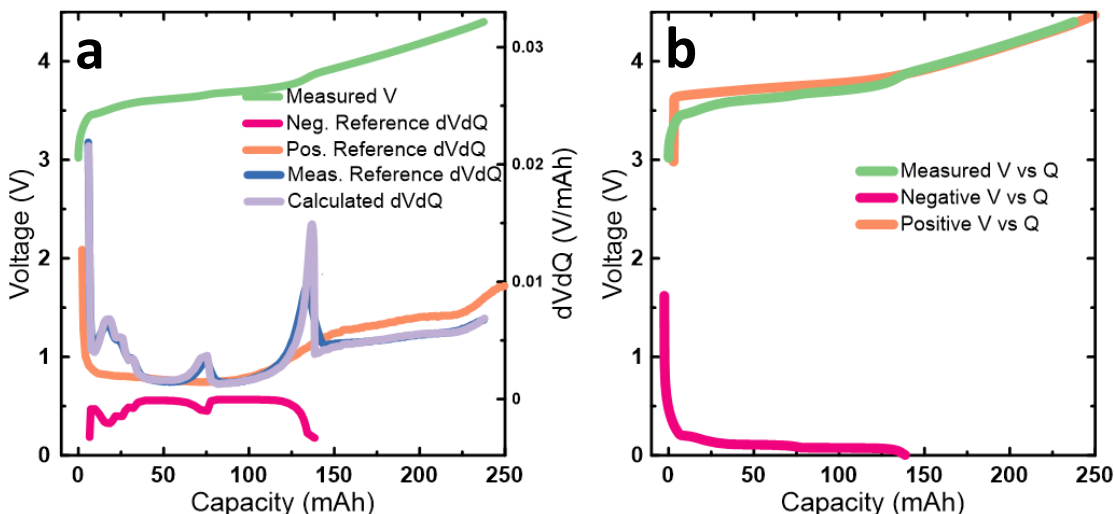


**Figure 7.2 | Differential voltage analysis.** **a**, Voltage (left axis) and  $dV/dQ$  (right axis) vs capacity for the second charge to 4.4 V of a hybrid cell. **b**, Voltage vs capacity for the second charge of hybrid cell and the constituent graphite negative and NMC532 positive electrodes. Hybrid cells were charged at  $C/20$  at  $40^\circ\text{C}$  with 1 M LiDFOB 0.4 M  $\text{LiBF}_4$  FEC:DEC 1:2 electrolyte.

## 7.2 Performance of Hybrid Cells

### 7.2.1 Conventional Cycling

Hybrid cells were cycled with three different electrolytes. Two lithium-ion electrolytes with 1.5 M  $\text{LiPF}_6$  EC:EMC:DMC 25:5:70 were tested with different additive combinations—2% VC (2VC) and 2% FEC + 1% LFO (2F1L). These formulations represent standard and optimized lithium-ion electrolytes.<sup>174</sup> A dual-salt electrolyte blend, 1 M LiDFOB 0.4 M  $\text{LiBF}_4$  FEC:DEC 1:2 (LDBF), which we have shown is quite good for cycling lithium metal, was also tested. These electrolytes were selected to evaluate if hybrid cells performed best using electrolytes optimized for graphite or lithium metal negative electrodes. **Figure 7.3** shows that the latter is certainly the case. Hybrid cells with lithium-ion electrolytes exhibit rapid capacity loss; by 80 cycles, most of the capacity stored as

lithium metal (above 140 mAh, shown with the dotted line) is no longer available. In contrast, capacity is sustained much better for cells with LDBF electrolyte.

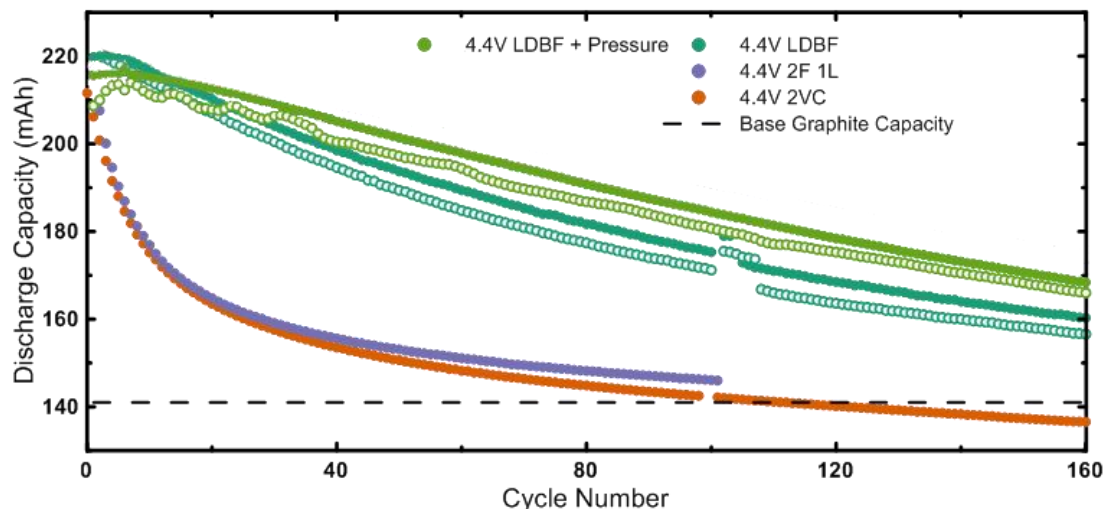


**Figure 7.3 | Hybrid cell electrolyte test.** Capacity vs cycle for hybrid cells tested with different electrolytes optimized for Li-ion cells (2VC, 2F1L) and lithium metal cells (LDBF). NMC532 hybrid cells were cycled between 3.0-4.4 V at C/5 D/2, 40 °C, and low pressure (200 kPa) and high pressure (+Pressure, 1200 kPa). The dotted line shows the capacity of the graphite component of the hybrid cells. Pair cells are shown with open and closed circles. The electrolytes used were 2VC = 1.5 M LiPF<sub>6</sub> EC:EMC:DMC 25:5:70 + 2% VC; 2F1L = 1.5 M LiPF<sub>6</sub> EC:EMC:DMC 25:5:70 + 2% FEC 1% LFO; LDFB = 1 M LiDFOB 0.4 M LiBF<sub>4</sub> FEC:DEC 1:2.

The rapid capacity loss of hybrid cells with lithium-ion electrolytes is consistent with our previous tests using these conventional electrolytes in anode-free cells. Lithium metal cannot be reversibly cycled in these electrolytes. Cells with both 2VC and 2F1L formulations lose over 50% of their lithium metal capacity in just 15 cycles. The capacity fade then slows down significantly; the capacity does not plummet to zero as with anode-free cells. That is because below 140 mAh, only the graphite component of the hybrid electrode is cycling capacity. **Figure 7.3** shows that after all the lithium metal capacity is lost to SEI growth and mechanical isolation, the graphite component can still be accessed and cycled. However, cells with 2VC still show appreciable capacity fade even after all the lithium capacity is lost beyond cycle 100. It is no wonder lithium plating is considered a fatal degradation mode for lithium-ion cells. In contrast, cells with dual-salt 1 M LiDFOB

0.4 M LiBF<sub>4</sub> (LDFB) electrolyte retain 50% of the capacity delivered by lithium metal component for 80 cycles, and hybrid cells with dual-salt electrolyte tested under high pressure sustain 50% of their lithium metal capacity for 120 cycles. Of their total capacity, this corresponds to a capacity retention of 80% after 160 cycles. **Figure A.30a** shows that this performance is also maintained at 20 °C after hot formation. As is always the case for lithium metal, differences in capacity retention can be correlated to the morphology of lithium plated under these different conditions.

**Figure 7.4** shows images of lithium plated in hybrid cells under low pressure after one charge. **Figure 7.4a** is an optical image of a hybrid negative electrode formed in dual-salt electrolyte. The negative electrodes in the pouch cells tested are slightly oversized relative to the positive electrode (2.8 vs 2.6 mm wide). As a result, there is a ~1 mm “overhang” region on both edges of the negative electrode that are not directly opposite a positive electrode. In **Figure 7.4a**, regions of the electrode directly opposite the positive electrode show a silver-coloured layer of lithium with good coverage of the graphite underneath. The overhang regions show no plated lithium, as expected. However, the overhang is gold in colour, which is indicative of lithiated graphite. Lithium must have diffused into the overhang region during the first charge. **Figure 7.4b-d** show the lithium microstructure plated in the 2VC, 2F1L lithium-ion electrolytes as well as in the dual-salt electrolyte. The lithium morphology generated in the dual-salt electrolyte is dense and compact, as expected. The lithium morphology formed in the lithium-ion electrolytes is more porous. This will result in enhanced lithium inventory loss and explains why hybrid cells with these electrolytes quickly lose their lithium metal capacity. FEC, which we have shown is beneficial to the lithium microstructure in anode-free cells, slightly benefits the morphology of the 2F1L formulation since it is present at 2%.



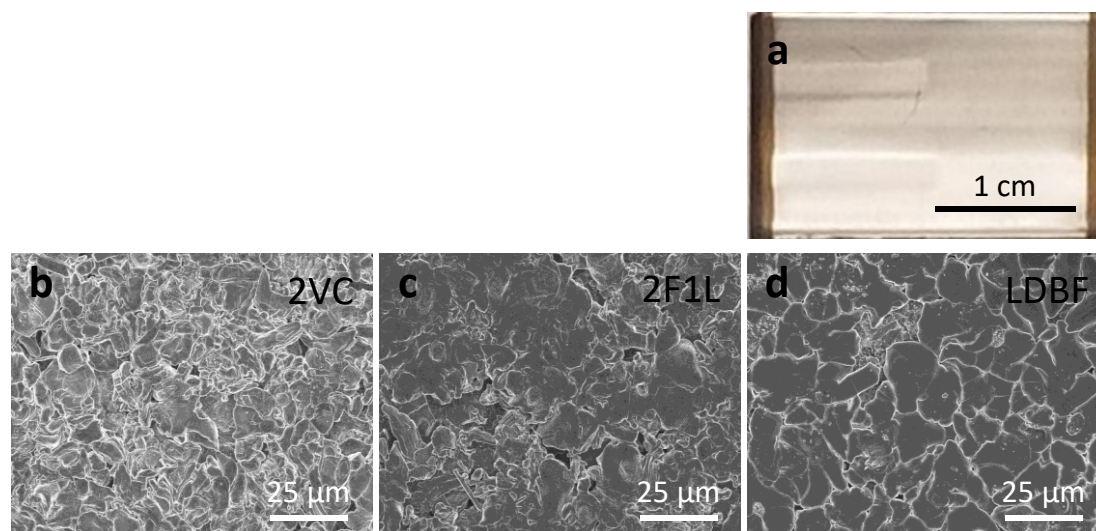


**Figure 7.4 | Hybrid cell lithium morphology.** a-d, Optical picture (a) and SEM images (b-d) of lithium metal plated on top of graphite retrieved from hybrid lithium-ion/lithium metal cells after one charge to 4.4 V. The lithium morphology was formed in dual-salt 1 M LiDFOB 0.4 M LiBF<sub>4</sub> FEC:DEC 1:2 (LDBF, a,d), 1.5 M LiPF<sub>6</sub> EC:EMC:DMC 25:5:70 + 2% VC (2VC, b), and 1.5 M LiPF<sub>6</sub> EC:EMC:DMC 25:5:70 + 2% FEC 1% LFO (2F1L, c). Hybrid cells were charged at C/5 and 40 °C under low pressure.

For further degradation analysis, aged hybrid cells with dual-salt electrolyte were analyzed with dVdQ analysis after 50 cycles to evaluate the changes since the first charge. **Figure 7.5** shows that the graphite capacity contribution of the negative electrode remains approximately 140 mAh, while the lithium metal contribution has shrunk from 90 mAh after the first cycle to just 60 mAh here. The dVdQ feature indicating the onset of lithium metal plating, the peak at around 140 mAh in **Figure 7.5a**, has shifted such that it occurs at a full cell voltage of 4.05 V in comparison to 3.85 V after the first cycle. This is a result of electrode “slippage”—in both **Figure 7.5a** and **b**, it can be observed that the negative electrode voltage curve has shifted or slipped relative to positive electrode voltage curve. After the first charge in **Figure 7.2**, the positive and negative electrode voltage curves showed good alignment around 0 mAh. After 50 cycles, the negative electrode voltage curve has slipped by 30 mAh. This is an indication of lithium inventory loss,<sup>147,175,176</sup> likely attributed to SEI growth and mechanical isolation of the lithium metal component. These results also demonstrate that the voltage at which plating begins will continually shift

higher with cycling as more lithium metal capacity is lost and the relative positive-negative electrode slippage increases.

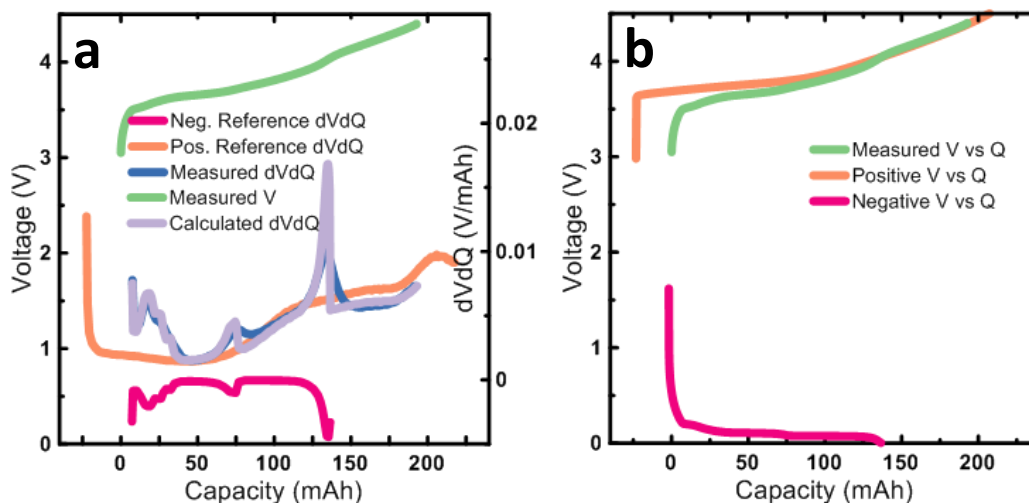


**Figure 7.5 | Differential voltage analysis of aged cells. a,** Voltage (left axis) and  $dV/dQ$  (right axis) vs capacity for the 50<sup>th</sup> charge to 4.4 V of a hybrid cell. **b,** Voltage vs capacity for the 50<sup>th</sup> charge of hybrid cell and the constituent graphite negative and NMC532 positive electrodes. Hybrid cells were cycled between 3.0-4.5 V at C/5 D/2 and 40 °C under low pressure with 1 M LiDFOB 0.4 M LiBF<sub>4</sub> FEC:DEC 1:2 electrolyte. The final cycle used for dVdQ analysis shown here was performed at C/20.

### 7.2.2 Specialized Cycling

**Figure 7.3** showed results testing hybrid cells with a conventional protocol cycling between 3.0-4.4 V, with every cycle utilizing both the graphite and lithium metal components to their full capacity. Under these conditions, hybrid cells had a capacity retention of 80% to 160 cycles. However, this hybrid electrode concept was based on the analogy to silicon/graphite composite electrodes which show increased lifetime when the silicon component is not utilized with every cycle—just for cycles with a deep discharge. Therefore, in the same vein, we implemented a specialized cycling protocol that would only intermittently take advantage of the lithium metal capacity in the hybrid electrode. During these partial cycles, the hybrid cells would not be charged to 100% such that lithium plating did not occur. The cells would then operate as conventional lithium-ion cells for

most cycles, while periodically accessing the lithium metal capacity with a “boosted” charged to 4.4 V.

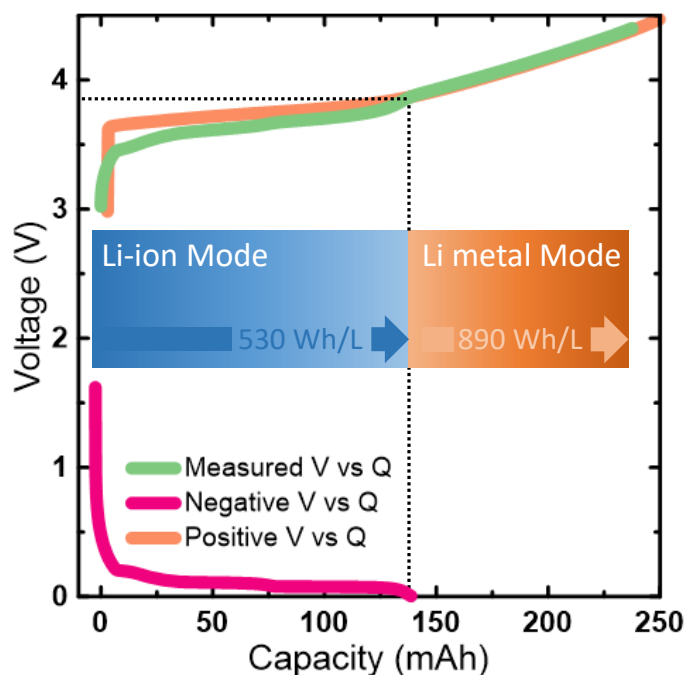


**Figure 7.6 | Dual mode operation of hybrid cells.** Voltage vs capacity for the first charge of a hybrid cell and the constituent graphite negative and NMC532 positive electrodes. Via a partial charge, hybrid cells operate in “Li-ion mode” to an energy density of 530 Wh/L when only the graphite component is used. When charged to 100%, hybrid cells operate in “Li metal mode” to an energy density of 890 Wh/L when lithium is plated on top of graphite.

Utilizing the full capacity of both the graphite and lithium metal components, hybrid cells deliver an energy density of 890 Wh/L, about 20% higher than lithium-ion cells. If an electric vehicle with a conventional lithium-ion battery has a range of 400 km, then hybrid cells could enable a range of 480 km. By capping the upper cutoff voltage of hybrid cells to operate in lithium-ion mode, the average cell voltage and delivered capacity will decrease. As a result, operating a hybrid cell in lithium-ion mode delivers an energy density of 530 Wh/L, about 25% less than a conventional lithium-ion cell. This would result in a range of 300 km. In a study of driving behaviour for EVs, Smart *et al.*<sup>166</sup> showed that only 1% of daily trips are longer than 325 km on average. Therefore, operating hybrid cells most

of the time in lithium-ion mode enabling a range of 300 km, while periodically using the lithium metal portion for long > 400 km trips, as mimicked by this testing protocol, should be viable for most drivers. **Figure 7.6** shows how operating in “Li-ion mode” and “Li metal mode” correspond to the voltage curves of hybrid cells.

4.0 V was chosen for the voltage corresponding to the average onset voltage of lithium plating between 0 and 50 cycles, since we showed this voltage does not remain fixed as discussed previously. Therefore, this specialized protocol cycles between 3.0-4.0 V for Li-ion mode (cycling very little or no lithium metal capacity, depending on the cycle number) and cycled between 3.0-4.4 V for Li metal mode (cycling both the graphite and full lithium metal capacity). The breakdown of Li-ion mode cycles to Li metal mode cycles was either 10:1 or 10:5 as indicated in the legend of **Figure 7.7**. These protocols were tested for both dual-salt 1 M LiDFOB 0.4 M LiBF<sub>4</sub> FEC:DEC 1:2 (LDBF) and 1.5 M LiPF<sub>6</sub> EC:EMC:DMC 25:5:70 + 2% FEC 1% LFO (2F1L) electrolytes.

**Figure 7.7** shows the results for hybrid cells tested with this specialized Li-ion mode/Li metal mode protocol. After almost 400 cycles, hybrid cells tested with dual-salt electrolyte under high pressure with the 10/1 protocol have lost very little of the original graphite capacity after cycling the lithium metal capacity ~40 times. The plating and stripping of lithium metal multiple times on top of the graphite does not appear to be severely inhibiting the capacity of the graphite portion of the anode. In this way, the cell can operate reasonably well in “lithium-ion mode” with periodic cycles accessing the lithium metal capacity. **Figure A.30b** shows that this protocol is also enabled at 20 °C after hot formation. **Figure 7.7** shows the cells that charged with the 10/5 protocol exhibit significant loss of the graphite capacity, demonstrating the problem with using a static 4.0 V upper cut-off voltage for Li-ion mode operation. This is a result of the negative electrode slippage discussed previously. The voltage at which the graphite reaches its maximum capacity rises as the cells are cycled, and thus these cycles to 4.0 V fail to access the full capacity after a certain number of cycles. This observation also strengthens the theory that the slippage of the negative electrode is due to loss of lithium metal capacity, as the 10/1 cells do not exhibit this slippage as dramatically. In practice, the charging end condition for the graphite region

may need to be based on capacity rather than voltage to have more precise control over the hybrid anode.

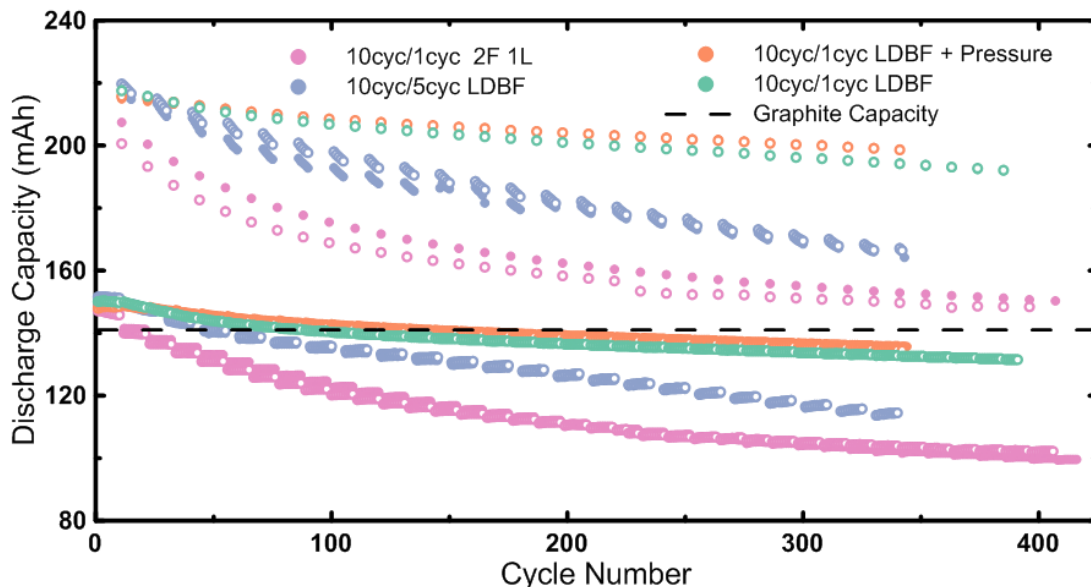


**Figure 7.7 | Specialized hybrid cycling protocol.** Capacity vs cycle for hybrid cells tested with a protocol that cycled most of the time between 3.0-4.0 V in Li-ion mode (~140 mAh) with intermittent 3.0-4.4 V Li metal mode (~220 mAh) cycles. The ratio of Li-ion to Li metal mode cycles was either 10cyc/1cyc or 10cyc/5cyc as detailed in the legend. NMC532 hybrid cells were cycled at C/5 D/2, 40 °C, low pressure (200 kPa) and high pressure (+Pressure, 1200 kPa). The dotted line shows the capacity of the graphite component of the hybrid cells. Pair cells are shown with open and closed circles. The electrolyte used were 2F1L = 1.5 M LiPF<sub>6</sub> EC:EMC:DMC 25:5:70 + 2% FEC 1% LFO; LDFB = 1 M LiDFOB 0.4 M LiBF<sub>4</sub> FEC:DEC 1:2.

**Figure A.31** shows the capacity retention of just the Li metal mode cycles from **Figure 7.7** plotted with the results from the conventional cycling protocol from **Figure 7.3** for comparison. The Li metal mode cycles track similarly to the capacity retention of hybrid cells cycled exclusively between 3.0-4.4 V. These results suggest that hybrid cell contains a certain number of 100% utilization cycles which can be utilized periodically among many hundreds of cycles of the graphite anode.

We have shown that dual-salt electrolyte optimized for cycling lithium metal is required to successfully operate hybrid cells. A question then is if the dual-salt electrolyte might hinder

the performance of the graphite component or if it can adequately passivate graphite for long term cycling in Li-ion mode. To this end, we tested dual-salt electrolyte in a conventional lithium-ion cells and compared it to the performance of an optimized Li-ion electrolyte, shown in **Figure 7.8**. Li-ion cells with dual-salt (LDBF) electrolyte lose 3% capacity after 500 cycles. The optimized lithium-ion electrolyte (1.2 M LiPF<sub>6</sub> EC:EMC 3:7 + 2% VC 1% DTD)<sup>21</sup> results in just 2% capacity loss under the same conditions—slightly better than dual-salt. Nevertheless, dual-salt electrolyte performs well in Li-ion cells. Therefore, we conclude that this electrolyte optimized for cycling lithium metal does not negatively affect the underlying graphite capacity in hybrid cells. An additional test was performed in which hybrid cells were cycled in Li metal mode 60 times and then cycled in Li-ion mode only accessing the graphite capacity for a further 440 cycles (**Figure A.32**). Negligible capacity loss was observed after 440 cycles in lithium-ion mode, reaffirming again that the cycling of lithium metal in hybrid cells does not have a negative impact on the graphite cycle life with dual-salt electrolyte.

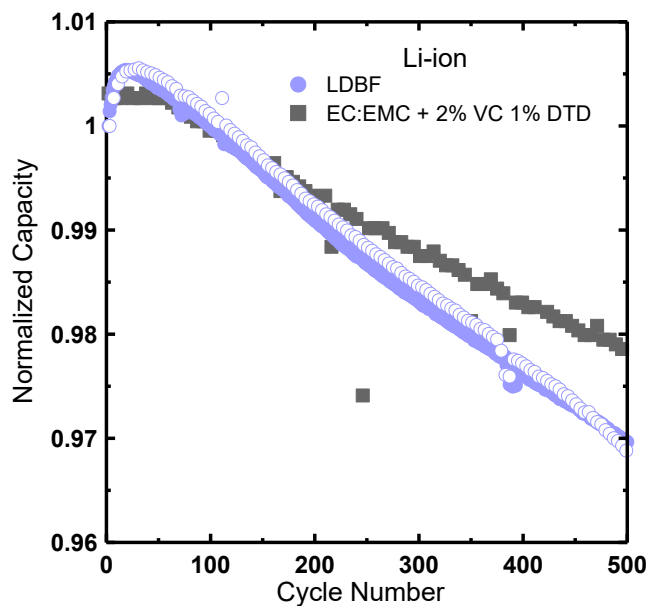


**Figure 7.8 | Lithium metal electrolyte in a Li-ion cell.** Normalized capacity vs cycle for conventional Li-ion cells tested with an optimized Li-ion electrolyte (1.2 M LiPF<sub>6</sub> EC:EMC 1:2 + 2% VC 1% DTD) and with a dual-salt electrolyte optimized for cycling lithium metal (LDBF, 1 M LiDFOB 0.4 M LiBF<sub>4</sub> FEC:DEC 1:2). Li-ion cells were cycled between 3.0-4.3 V at C/3 D/3 and 40 °C. Pair cells are shown with open and closed circles.

### 7.2.3 Concluding Remarks

In this chapter, we explored the concept of hybrid graphite/lithium metal negative—a novel concept we first published in Ref.<sup>171</sup> Although a cell design based on purposefully plating lithium metal on graphite had not been tried before, this concept was inspired by the compromise between energy density and longevity that is made with silicon/graphite composite electrodes that are on the market today. We showed that an electrolyte optimized for cycling lithium metal is required for successful operation of these hybrid lithium-ion/lithium metal cells otherwise the capacity delivered by the lithium metal component is quickly lost. We also demonstrated that cells can be successfully operated in “Li-ion mode”, cycling just the graphite component for hundreds of cycles, with intermittent “Li metal mode” cycles interspersed where the full lithium metal capacity is accessed.

Moving forward, the challenge for these hybrid cells will be developing electrolytes that are optimized for simultaneous graphite and lithium metal passivation. Furthermore, other critical performance metrics, such as safety, need to be investigated. The work presented here is just the first foray into this new negative electrode concept. The success of silicon/graphite composite electrodes indicates that there is certainly a market for cells with improved energy density at the cost of cycle life. As better electrolytes for cycling lithium metal are developed, hybrid cells will become even more attractive. Therefore, hybrid lithium-ion/lithium metal cells may have an exciting future if researchers continue pushing this concept further.

## Chapter 8: Conclusions

In this thesis we endeavoured to describe the life and death of anode-free lithium metal cells with liquid electrolytes. Motivated by their massive energy density but humbled by their rapid degradation, we worked to attain the best performance from these cells through several mechanical, electrolyte, cycling, and design solutions. Now we will outline future work that would be useful to deliver additional insight and hopefully lead to further improvements. Finally, we discuss our outlooks for this technology moving forward.

### 8.1 Future Work

#### 8.1.1 Natural Next Steps

Throughout this thesis we have identified sections that would benefit from additional experimentation. These are obvious next steps that could be taken on in future work on anode-free cells.

We demonstrated that electrolyte degradation played a significant role in the failure of anode-free cells with dual-salt LiDFOB/LiBF<sub>4</sub> electrolyte and quantified salt depletion using liquid NMR analysis from electrolyte extracted from cycled cells. Cells were originally filled with 0.6 M LiDFOB 0.6 M LiBF<sub>4</sub> corresponding to molalities of 0.52 mol/kg LiDFOB 0.52 mol/kg LiBF<sub>4</sub>; however, electrolyte extracted immediately after filling without aging were only measured to have 0.43 mol/kg LiDFOB and 0.3 mol/kg LiBF<sub>4</sub>. This was consistent between multiple cells filled with electrolyte from different batches—in other words, this was not a result of an error in the electrolyte recipe. Therefore, we concluded that there is a systematic error in the NMR analysis leading to inaccurate but precise measurements such that the trends of salt loss observed were real. We observed about a 0.4 mol/kg loss of LiDFOB salt concentration during cycling. But this leads to the question: is there 0.12 m (0.52 m – 0.4 m) LiDFOB remaining or is there just 0.03 m (0.43 m – 0.4 m) LiDFOB remaining? It would be useful to know if the LiDFOB was entirely depleted or if there was just an insufficient concentration remaining to sustain its beneficial impact. The NMR analysis could be improved via the introduction



of an internal standard—an inert chemical added at a known quantity to the electrolyte with which the NMR peaks of the LiDFOB and LiBF<sub>4</sub> salt components could be measured against. We have not done this because we had not found an internal standard that was inert to dual-salt electrolyte. However, no doubt a suitable internal standard could be found.

To combat salt depletion, we increased the concentrations of LiDFOB and LiBF<sub>4</sub> to facilitate longer lifetime. Our longest lifetime was achieved with a 2.0 M LiDFOB 1.4 M LiBF<sub>4</sub> recipe, but heating and stirring of the electrolyte was necessary at these concentrations to achieve full salt dissolution. Moreover, this recipe resulted in a lowered reversible capacity due to worse electrolyte kinetics, presumably because of increased viscosity lowering the ionic conductivity. Ideally, a more optimized dual-salt recipe that is sufficient to extend lifetime without these added detriments could be found. We explored several concentrations between the initial dual-salt recipe of 0.6 M/0.6 M and the high concentration 2.0 M/1.4 M recipe; however, an investigation of a systematic matrix of salt combinations would likely result in a more optimized formulation.

The safety of high concentration dual-salt electrolyte should also be investigated. We showed that the safety of anode-free cells dual-salt 0.6 M LiDFOB 0.6 M LiBF<sub>4</sub> electrolyte was superior to cells with other electrolytes from the literature, but we have not yet performed nail tests on cells with higher LiDFOB and LiBF<sub>4</sub> concentrations. We found that cells with high concentration 4 M LiFSI electrolyte were highly volatile. It may be the case that increased LiDFOB and LiBF<sub>4</sub> concentrations could worsen the safety prospects of dual-salt cells. This would be easily determined via nail tests of cells aged with 2.0 M LiDFOB 1.4 M LiBF<sub>4</sub> electrolyte. Nail tests to determine the safety prospects of hybrid lithium-ion/lithium metal cells should also be performed.

Reversible lithium metal plating and stripping hinges on avoiding a mossy deposition morphology. A dense lithium microstructure is a key indicator of efficient deposition which will facilitate long cycle life. In this work, we performed extensive SEM analysis to qualitatively inspect the lithium morphology that evolved in anode-free cells. However, we observed significant heterogeneity of the lithium deposits over the ~80 cm<sup>2</sup> area of the

lithium electrode extracted from pouch cells. Often, both regions of denser lithium plating as well as regions of mossier lithium could be identified in a single sample just by focusing on different areas. In an effort to be as fair as possible, we have always compared the best lithium morphologies observed from each sample since the “average” morphology would be impossible to judge. A more quantitative assessment of lithium morphology would be preferable. Weber *et al.* showed that argon Brunauer-Emmett-Teller (BET) surface area measurements are potentially a good way to do this.<sup>177</sup> Instead of just qualitatively comparing lithium microstructures with SEM images only spanning hundreds of microns, the surface area of entire 80 cm<sup>2</sup> lithium electrodes can be quantified. This will effectively average out both the “good” and “bad” regions of the lithium morphology that are observed via SEM.

When we were investigating the effect of pressure on lithium cyclability, we found that the application of high pressures >1700-2300 kPa resulted in a faster increase in cell resistance. We speculated that this may have been a result of worse mass transport through the separator due to the internal porosity being crushed at high pressure. Ultimately we did not pursue this further since we concluded that lower pressures around 1200 kPa were sufficient for benefiting the performance of anode-free cells. Nevertheless, the potential impact of mechanical pressure on polyolefin separators is an outstanding issue. Other studies have shown that pressures of 10,000 kPa and above do result in significant separator strain,<sup>178</sup> but more work at lower pressures between 1000-10,000 kPa is required. One particularly interesting experiment would be to investigate the performance of cells with polyethylene separators vs cells with polypropylene separators. The pore structure of polyethylene is quite random, with a collection of both vertical and horizontal pores (with respect to the gap between electrodes). In this case, the horizontal pores would be more liable to being crushed by a compressive stress. In contrast, the pores in polypropylene separators are primarily vertical<sup>16</sup> and thus would be less liable to being crushed. Comparing the performance of cells with these distinct pore morphologies under pressure would be instructive.

Our study of anode-free cells with different positive electrodes revealed some interesting behaviour that merit further investigation. The bulk of our NMC811 anode-free tests were cycled between 3.55-4.4 V, but we showed that a slightly lower depth of discharge between 3.6-4.4 V resulted in a significant improvement to lifetime without significantly decreasing energy density. Future studies with NMC811 anode-free cells should employ a 3.6 V lower cut-off voltage for improved performance.

All positive electrode chemistries suffered from varying degrees of significant impedance growth. The interpretation of these impedance results would be benefited from an analysis of symmetric cells built from aged anode-free cells of each chemistry. Cells after 1 cycle and 100 cycles, for example, should be deconstructed to make positive and negative symmetric cells. This would facilitate a robust analysis of the contributions to the charge transfer resistance and elucidate whether impedance growth at the positive electrode was a significant factor distinguishing the performance of NMC532, NMC811, LCO, and LFP anode-free cells. Moreover, we showed that cells with different positive electrodes exhibited different degrees of increased solution resistance despite showing similar rates of salt depletion. We speculated that this is likely a result of differences in electrolyte dry-out. This should be confirmed using ultrasonic transmission mapping of aged cells.

There are still several unanswered questions with respect to the performance of LCO anode-free cells. For example, why the lithium excess when cycled at 80% DoD is not depleted during cycling? Also, the relatively small increase in solution resistance and cell thickness indicates that the lithium morphology in LCO cells remains more compact during aging. This should be investigated with SEM—or BET—as a function of cycle. Moreover, the electrolyte analysis of aged LCO cells exhibited less LiBF<sub>4</sub> consumption than other chemistries. This is peculiar because we showed that LiBF<sub>4</sub> was only consumed on the lithium metal negative electrode in NMC532 cells. The same lithium metal is being cycled in LCO cells; the fact that the positive electrode chemistry affects reactions with the negative electrode may indicates that there are more sophisticated crosstalk reactions going on whereby the presence of the LCO electrode impacts the consumption of LiBF<sub>4</sub> on lithium metal. However, this may also just be a result of less parasitic reactions if the LCO

morphology is indeed much more compact. Electrolyte analysis of cycled LCO symmetric cells, like we performed for NMC532, would help elucidate this behaviour.

Finally, we showed throughout this work the massive impact of electrolyte chemistry on performance of anode-free cells. Between all the various strategies to benefit performance, our most significant improvement to lifetime was achieved through the development of the LiDFOB/LiBF<sub>4</sub> dual-salt electrolyte chemistry. But there are still many different solvents and lithium salts to try, not to mention the innumerable combinations that could be tested. Out of all these possible combinations, it seems unlikely that our dual-salt recipe is the best possible liquid electrolyte formulation for lithium metal cycling. Through a combination of an increased understanding in what makes a good electrolyte, a lot of work, and some luck, improvements to lifetime will undoubtedly be unlocked through further innovations in electrolyte chemistry.

#### 8.1.2 Tangential Efforts

Beyond a simple continuation of the work presented in this thesis, more divergent strategies should be considered. One strategy for improving lithium plating efficiency which we had not explored yet is the plating substrate. This was largely because our tests were performed on as-received pouch cells—the current collector was effectively dictated by the manufacturer. We could have requested cells with different current collectors, but as cells are shipped in batches of 1000, it is not feasible to be testing different substrates at this scale. Instead, coin cells are the obvious testing platform. Genovese *et al.* previously demonstrated that a Zn coated copper current collector improved the lifetime of anode-free cells 1 M LiPF<sub>6</sub> FEC:TFEC electrolyte.<sup>108</sup> Lee *et al.*, researchers from Samsung working with a sulfide solid electrolyte, demonstrated impressive anode-free performance of their solid-state cell which employed a Ag-C current collector coating which facilitated improved lithium plating. In fact, Lee *et al.* showed that lithium surprisingly plated underneath the Ag-C layer which acted as a shield separating the lithium from the electrolyte.<sup>43</sup> Inspired by both the works of Genovese *et al.* and Lee *et al.*, we performed

some preliminary work trying to replicate these current collector modifications and apply them in anode-free coin cells with dual-salt electrolyte.

The Ag-C coating with prepared as a slurry with a ratio of 1:3 nano-silver power to super S carbon mixed with 20% polyvinylidene fluoride (PVDF) binder and an N-Methyl-2-pyrrolidone (NMP) solvent. The Ag-C mixture was cast on to a copper current collector and calendared to a thickness of  $\sim 14 \mu\text{m}$ . The Zn coating was prepared via sputtering  $0.5 \text{ mg/cm}^2$  ( $\sim 700 \text{ nm}$ ) of Zn on a copper current collector. The result for anode-free cells built with these modified current collectors compared with typical anode-free cells with bare Cu current collectors are shown in **Figure 8.1**. Unfortunately, the modified current collectors were not any better than the bare Cu controls.

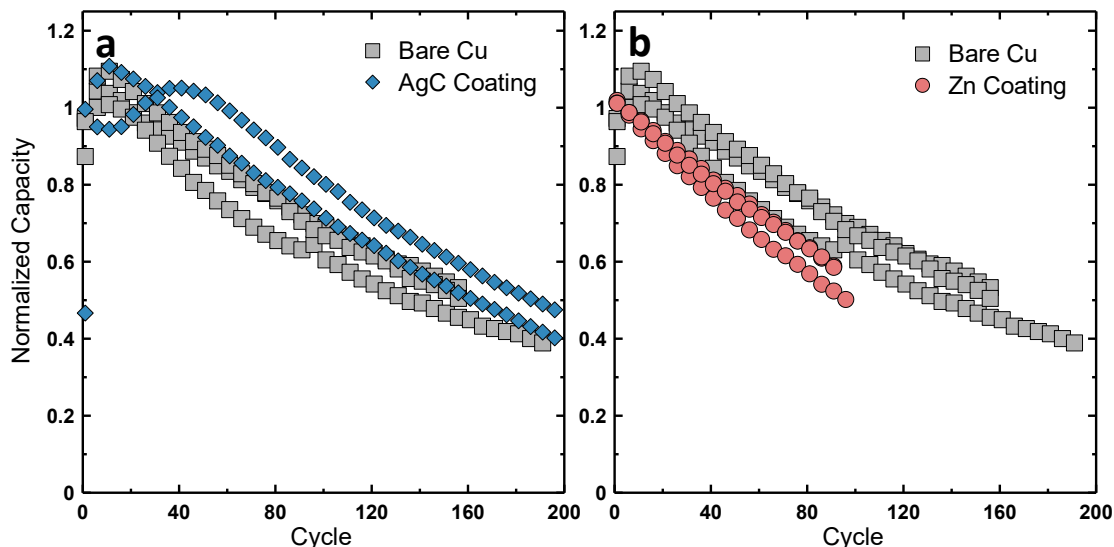


**Figure 8.1 | Current collector modification.** a-b, Normalized capacity vs cycle of anode-free cells with modified copper current collectors; an Ag-C coated current collector (a) and a Zn coated current collector (b). Control cells with a bare copper (Cu) current collector are shown for comparison. NMC532 anode-free coin cells were cycled between 3.6-4.5 V at C/5 D/2 and 40 °C and contained 0.6 M LiDFOB 0.6 M LiBF<sub>4</sub> FEC:DEC 1:2 electrolyte.

There are a couple of potential explanations for why these modified current collectors did not help. First, we showed in Section 5.3 that lithium plating will only occur on the bare current collector once, and then subsequently on the lithium reservoir created by the

“irreversible” capacity of  $\text{Li}_x\text{MO}_2$  type cathodes. So although the first nucleation may be improved, there will not be a benefit from plating on this modified surface every cycle. Second, if the benefit of these modified substrates is improved lithium nucleation, and dual-salt electrolyte is also beneficial by tuning the SEI to improve lithium nucleation, then combining the individual benefits from these strategies should not be expected to stack. Moreover, due to the coin cell format, it is very challenging to build cells with a lean  $<3$  g/Ah loading of electrolyte; the loading in these coin cells is closer to 100 g/Ah. Operating with such an excess of electrolyte also improves performance, as can be noticed from the capacity fade curves exhibited in **Figure 8.1** compared to pouch cell results. Therefore, potential benefits from the current collector modifications may be drowned out by the benefits of an excessive volume of a good electrolyte.

One strategy to improve lifetime we presented in this thesis was to operate at lower depths of discharge to create a small lithium reservoir. By forming the lithium reservoir *in-situ*, the downfalls of handling lithium foil during cell construction are avoided. Furthermore, it is possible to form a very limited lithium excess electrochemically so as to not significantly hurt energy density. Other methods to electrochemically introduce a lithium excess should also be considered. One such clever method was recently demonstrated by Qiao *et al.* by introducing  $\text{Li}_2\text{O}$  on the NMC811 positive electrode. The  $\text{Li}_2\text{O}$  acts as a “sacrificial agent”, decomposing during the first charge and adding to the lithium inventory of the cell.<sup>179</sup> Until more sophisticated methods of improving lithium cycling efficiency are discovered, methods to overcome low cycling efficiency via the introduction of limited lithium excess will be necessary to extend lifetime.

In theory, solid electrolytes should improve lithium cycling efficiency by eliminating lithium-electrolyte parasitic reactions. However, in practice, solid electrolytes can still react with lithium metal and with charged positive electrode materials. As a result, beyond simply replacing the liquid electrolyte, implementing a solid electrolyte requires a series of solutions for all the issues that arise between the various interfaces and interphases in a cell.<sup>114</sup> The recent efforts from Samsung which demonstrated a long lasting anode-free cell employing a sulfide-based solid electrolyte are very promising. This cell utilized a

Li<sub>6</sub>PS<sub>5</sub>Cl solid electrolyte with a Li<sub>2</sub>O-ZrO<sub>2</sub> coating to protect the positive electrode and a Ag-C layer to passivate the lithium metal.<sup>43</sup> Our lab has begun to try to replicate this approach. It is certainly possible that lifetime of thousands of cycles may never be realized with liquid electrolytes for anode-free cells, so efforts to tackle the challenges of implementing practical solid electrolytes must also be explored.

## 8.2 Outlooks

To date, we have demonstrated impressive progress increasing the lifetime of anode-free cells with liquid electrolytes. By introducing a dual-salt LiDFOB/LiBF<sub>4</sub> electrolyte in combination with cycling under high mechanical pressure, 80% depth of discharge, an asymmetric slower charge protocol, and hot formation, we have extended the cycle life of anode-free cells to 200 cycles. This seemed like an unlikely prospect just 3 years ago when we could only achieve between 1 and 20 cycles with conventional electrolytes. The prospect for the next 200 cycles—improving lifetime even further—seems just as daunting if not even more so.

This exciting progress notwithstanding, it is important to keep our anode-free results in context. Optimized lithium-ion cells can cycle very efficiently for 1000 cycles and beyond, as shown in **Figure 8.2**. The compromise of lifetime for a significant boost of energy density that anode-free cells deliver may be currently suitable for some applications; for example, 200 cycles is sufficient for areal drones. However, a lifetime of at least 800 cycles is required for electric vehicles. Therefore, the 200 cycles we have enabled for anode-free cells is still a far cry away from practical electric vehicle applications as well as the prospect of launching flying taxis off the ground.

In the continued effort for improving performance, we believe that developments of electrolyte chemistry will be the largest driving force extending lifetime. Novel strategies like localized high concentration electrolytes have already demonstrated significant promise. However, we demonstrated here that for our best-yet dual-salt electrolyte, the longevity it enabled was a result of the decomposition of the electrolyte salts. The fact that the mechanism which facilitated the stabilization of the lithium anode was the electrolyte's

own decomposition leads us to a fundamental question: do liquid electrolytes have to be bad to be good? That is to say, is the decomposition of liquid electrolyte required to facilitate good cyclability? If the cause of good cyclability is intrinsically linked to its own failure, then achieving a long 800 cycle life will be extremely challenging. This is why solid electrolytes are currently viewed as the most likely strategy to enable long lasting lithium metal cells.

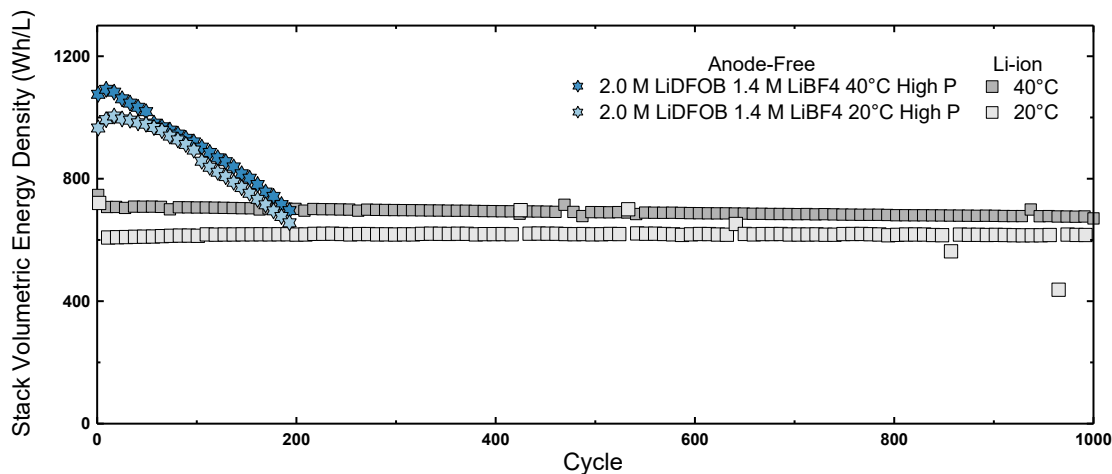


**Figure 8.2 | Anode-free vs Li-ion cells.** Comparison of the lifetime of our best anode-free cell results with optimized lithium-ion cells. Anode-free cells were cycled between 3.6-4.5 V at C/5 D/2 at high pressure (High P, 1200 kPa) at 40 °C and 20 °C after hot formation. Li-ion cells were cycled between 3.0-4.3 V at C/3 D/3 at 40 °C and 20 °C with 1.2 M LiPF<sub>6</sub> EC:EMC 3:7 + 2%VC 1%DTD electrolyte. Both anode-free and Li-ion cells utilized the same NMC532 positive electrode.

More than just lifetime, cycling rates and safety will be enduring challenges. We achieved 200 cycles using an optimized asymmetric slower charge protocol. On the contrary, most battery applications demand fast charging capability. Perhaps the desire for fast charge will be overcome by high energy density—a 15 minute fast charge for a vehicle with a 500 km range probably isn't necessary most of the time. Regardless, improving the rate capability will be challenging due to the intrinsic difficulty of efficient fast plating and slow stripping of lithium metal. Perhaps electrolytes with higher transference numbers can mitigate the formation of detrimental concentration gradients to enable faster charge rates. As for safety, we have shown that thermal runaway can be prevented by some electrolytes, at least



in our small 250 mAh pouch cells. The safety of larger cells even with the safest electrolytes will be more challenging. Beyond electrolyte formulations, the safety of anode-free cells also depends on how they have been aged. Cells which develop a mossy lithium morphology will be more volatile. Of course, if we could maintain a compact lithium morphology over hundreds of cycles, many of the woes of the lithium metal anode would be solved. There is no doubt that acceptable safety will be critical for any attempt at commercialization.

Despite these challenges I have laid out, anode-free lithium metal cells are attractive because of their high energy density and their simplicity. Even if solid electrolytes are shown to enable long lifetime lithium metal cells, the large-scale manufacturing and roll-to-roll processing of cells with solid electrolytes will need to be demonstrated before they will become a viable mass-market option. In contrast, anode-free cells with liquid electrolytes are compatible with today's well-established cell production lines. By just removing the graphite coating on the copper current collector, the production of anode-free cells will be even cheaper than lithium-ion cells. This will always be the edge for anode-free cells with liquid electrolytes, provided the performance metrics can ultimately be satisfied. As a result, I believe anode-free lithium metal cells with liquid electrolyte present the most *straightforward* path towards unlocking the highest energy density cells for the next generation of energy storage.

## Appendix A Additional Data

### A.1 Chapter 4 Supplementary Data

**Figure A.1** shows a comparison of lithium morphologies which have been reported in the literature (1-5) with the lithium morphology generated in this work with LiDFOB/LiBF<sub>4</sub> dual-salt electrolyte under low and high pressure (6). Each numbered row is a selection of SEM images of plated lithium using a variety of different electrolytes promoted in the literature. These are not head-to-head comparisons since the experimental conditions (electrode chemistry, current density, areal capacity, mechanical pressure, *etc.*) are not all the same. Nevertheless, the SEM images in (1-5) all come from papers which promote the lithium morphology enabled in the electrolyte they are reporting on. Therefore, **Figure A.1** is useful to gauge the state-of-the-art lithium morphology reported in the literature in comparison to what we have achieved in this work. Rows (1-3) show lithium that has been plated after a single charge; row (4) shows lithium after 50 cycles; row (5) shows lithium after 70 cycles. These SEM images have been taken from the following references: row (1)<sup>102</sup>, row (2)<sup>103</sup>, row (3)<sup>47</sup>, row (4)<sup>87</sup>, and row (5)<sup>48</sup>. Our SEM images (6) are pictured after 1 charge, 20 cycles, and 50 cycles, cycled under low pressure (200 kPa) and high pressure (1200 kPa). Note the different scale bars between the various SEM images.

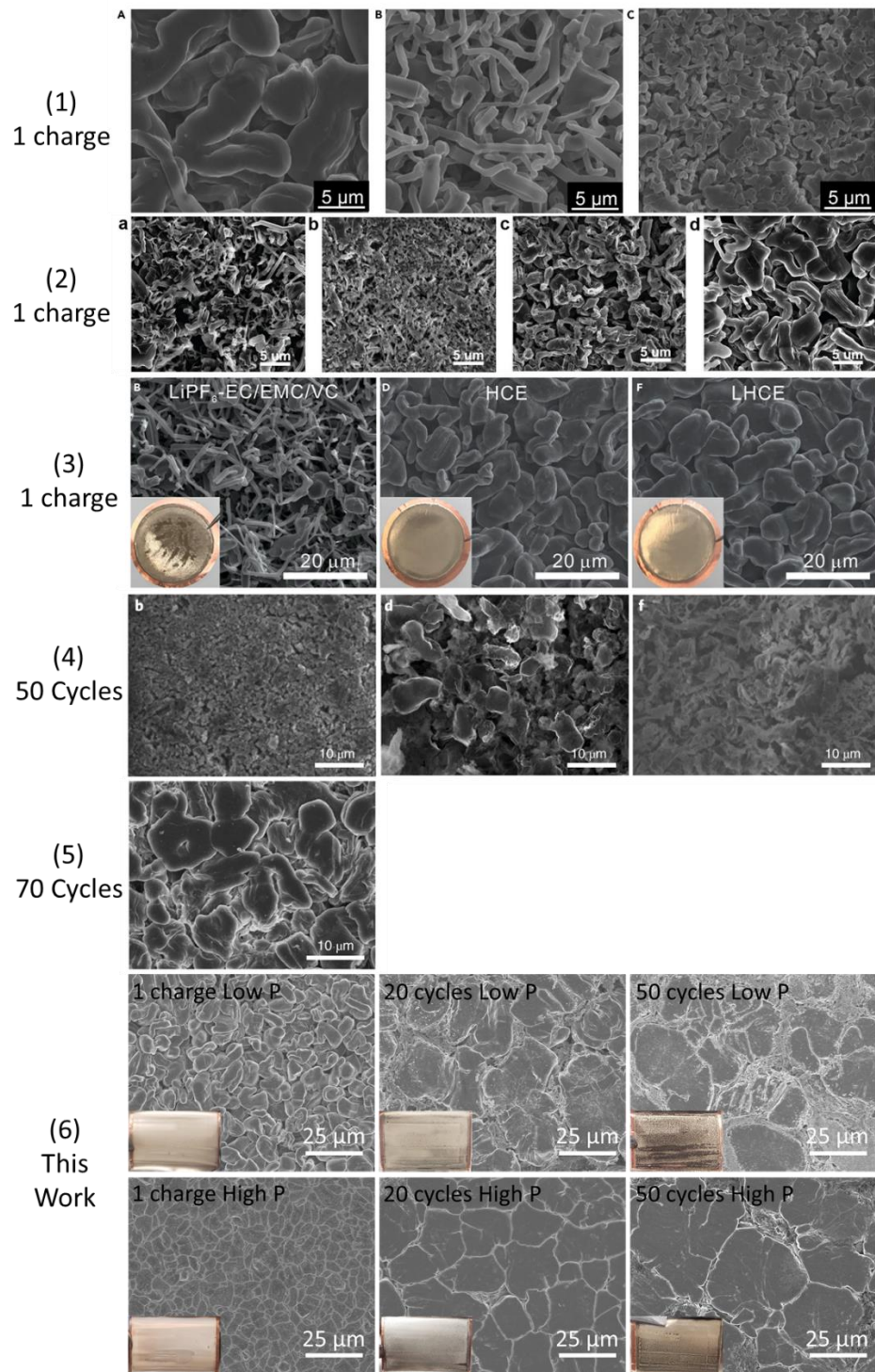


**Figure A.1 | Comparison of lithium morphology.** SEM images of plated lithium images of plated lithium in a variety of electrolytes reported in the literature. The rows numbered (1-5) are SEMs taken from the literature, (1)<sup>102</sup>, (2)<sup>103</sup>, (3)<sup>47</sup>, (4)<sup>87</sup>, and (5)<sup>48</sup>. Row (6) shows the lithium morphology generated in this work with 0.6 M LiDFOB 0.6 M LiBF<sub>4</sub> FEC:DEC 1:2 electrolyte. Not the different scale bars on each SEM image.

**Figure A.2** shows SEM images of plated lithium after one charge (a-d) and after 50 cycles (A-D) for FEC:DEC cells constrained in normal boats at 200 (a, A) and in superboats at 485 kPa (b,B); and for FEC:TFEC cells constrained in normal boats at 200 kPa (c, C) and in superboats at 485 kPa (d,D). After one charge in a normal boat, more void space is observed in the FEC:DEC sample—the plated lithium in the FEC:TFEC sample appears more close packed and nodular. In the superboat constrained at 485 kPa, a significant difference is observed as the plated lithium becomes more close packed for both FEC:DEC (b) and FEC:TFEC (d) samples. The FEC:TFEC sample appears to have less void space and thus the smallest surface area. A low surface area is ideal since this results in less contact with the electrolyte thereby reducing the lithium inventory that is lost to SEI formation.

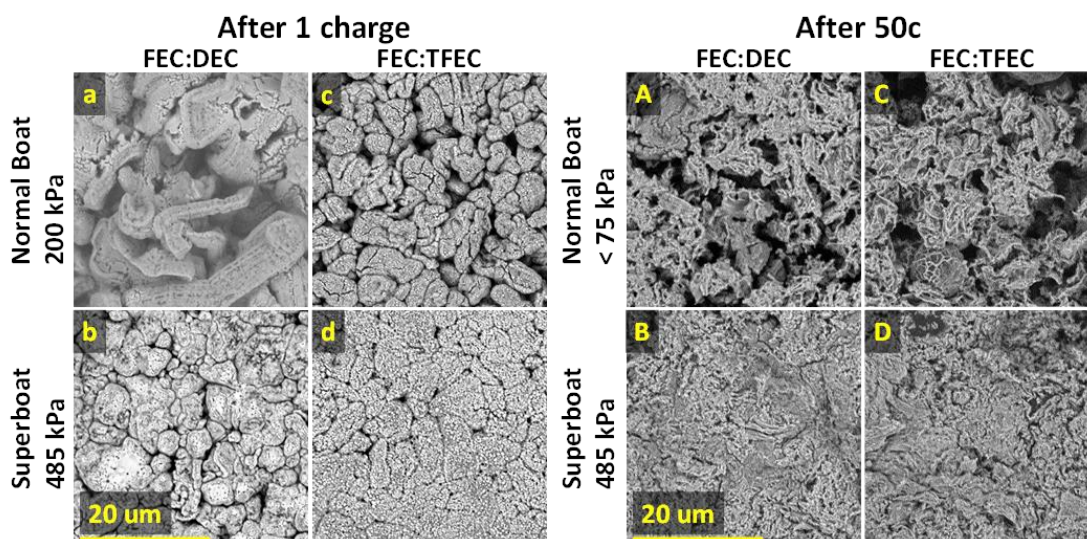


**Figure A.2 | Pressure impact on lithium morphology.** SEM images of plated lithium after one charge (a-d) and after 50 cycles (A-D) for cells containing FEC:DEC electrolyte constrained in normal boats at 200 kPa (a,A) and in surperboats at 485 kPa (b,B) and for cells containing FEC:TFEC electrolyte constrained in normal boats at 200 kPa (c,C) and in superboats at 485 kPa (d,D). Cells contained 1 M LiPF<sub>6</sub> and were cycled between 3.6-4.5 V at C/5 D/2 and 40°C. Anode-free NMC532 cells were used.

After 50 cycles constrained at low pressure 200 kPa in normal boats, the FEC:DEC (A) and FEC:TFEC (C) samples exhibit a significantly more dendritic, mossy structure; the feature size is dramatically reduced and the morphology is very porous with high surface

area. The samples constrained at 485 kPa (B,D) exhibit a morphology that is much less porous, consistent with results which show that higher pressure improves lithium plating efficiency.

**Figure A.3** shows ionic conductivity vs temperature measurements performed for three electrolyte systems, 1 M LiPF<sub>6</sub> with FEC:DEC 1:2 (blue circles), 1 M LiPF<sub>6</sub> FEC:TFEC (green squares), and 1 M LiPF<sub>6</sub> EC:DMC 3:7 (red stars). These measurements performed by Eric Logan using a Mettler Toledo FiveGo conductivity probe. The conductivity cell was immersed in a circulating temperature bath (Thermo Scientific Neslab RTE 7). The temperature bath contained a mixture of ethylene glycol and water. The temperature of the bath was verified in this range using an external thermocouple thermometer (Omega HH802U), found to be accurate to  $\pm 0.5^\circ\text{C}$  between  $0.0^\circ\text{C}$  and  $100.0^\circ\text{C}$ . Conductivity measurements were made at temperatures between  $0^\circ\text{C}$  and  $40^\circ\text{C}$  at intervals of  $10^\circ\text{C}$ . The conductivity cell was allowed to equilibrate for at least one hour before the measurement was recorded. At  $40^\circ\text{C}$ , cells with this electrolyte were cycle at in this work, the FEC:DEC and FEC:TFEC exhibit significantly lower ionic conductivity than conventional EC:DMC electrolyte, with conductivities of 9.2 mS/cm 3.9 mS/cm for FEC:DEC and FEC:TFEC compared to 15 mS/cm for EC:DMC.

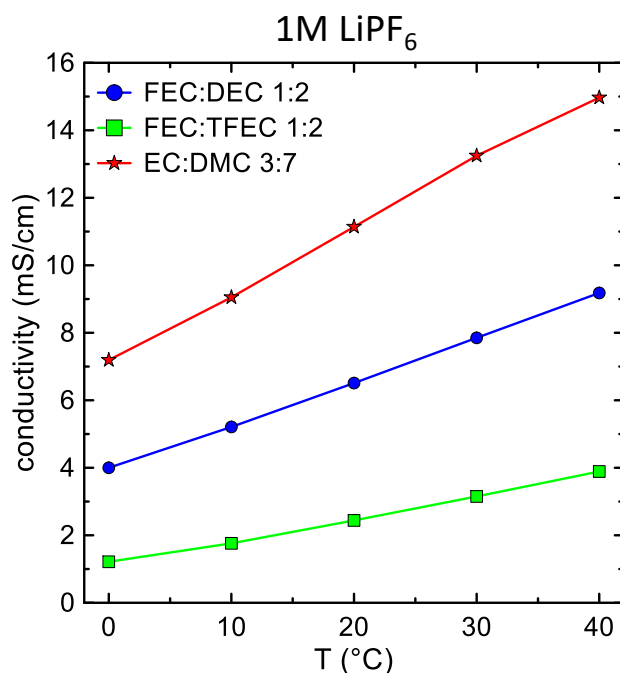


**Figure A.3 | Electrolyte conductivity.** Conductivity vs temperature measurements for electrolyte containing 1 M LiPF<sub>6</sub> salt with FEC:DEC 1:2 solvent (blue circles), FEC:TFEC 1:2 solvent (green squares) and EC:EMC 3:7 solvent (red stars).

**Figure A.4** shows the results for cells with 0.6 M LiDFOB 0.6 M LiBF<sub>4</sub> salt tested with different ether solvent blends. The standard solvent blend, FEC:DEC 1:2, is blended with DME, TTE, and MA. A pure ether solvent blend, DME:TTE 1:4, was also tested. None of these solvent blends exhibited improved performance compared to the control FEC:DEC 1:2 formulation.

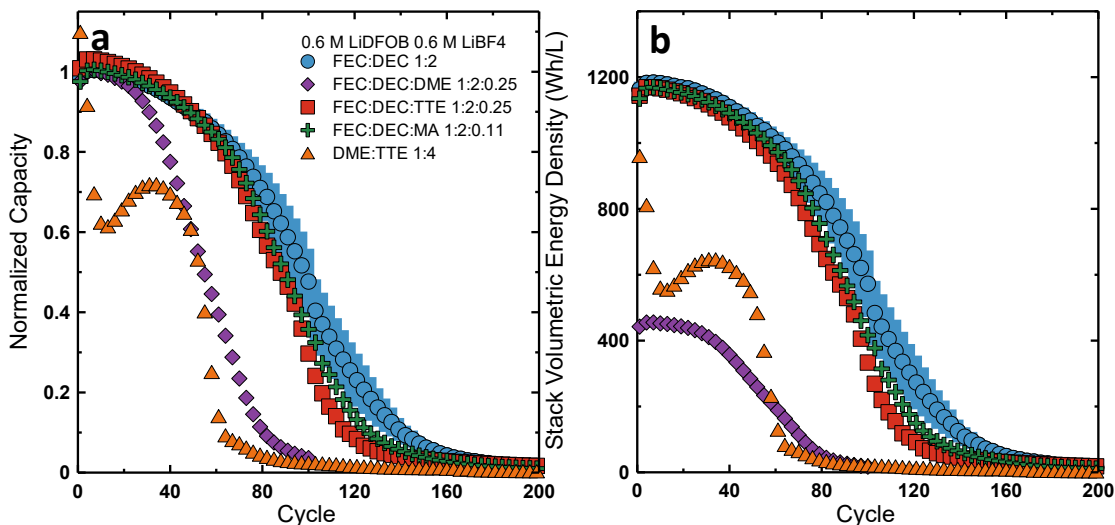


**Figure A.4 | Dual-salt ether solvent test. a-b,** Normalized capacity (a) and stack volumetric energy density (b) vs cycle of anode-free cells with 0.6 M LiDFOB 0.6 M LiBF<sub>4</sub> tested with different ether solvent blends. Cells were cycled under low pressure between 3.6-4.5 V at C/5 D/2 and 40°C. Anode-free NMC532 cells were used. The average of at least two cells are shown here; the error bars are calculated as the standard deviation.



**Figure A.5** shows the results of additional localized high concentration (LHC) electrolyte formulations, as developed by PNNL,<sup>47,103</sup> compared to 0.6 M LiDFOB 0.6 M LiBF<sub>4</sub> electrolyte. The original LHC electrolyte utilized DME solvent and TTE diluent. DMC and BTFE are also substituted for these components in **Figure A.5**, however, they do not successfully improve cycle life.

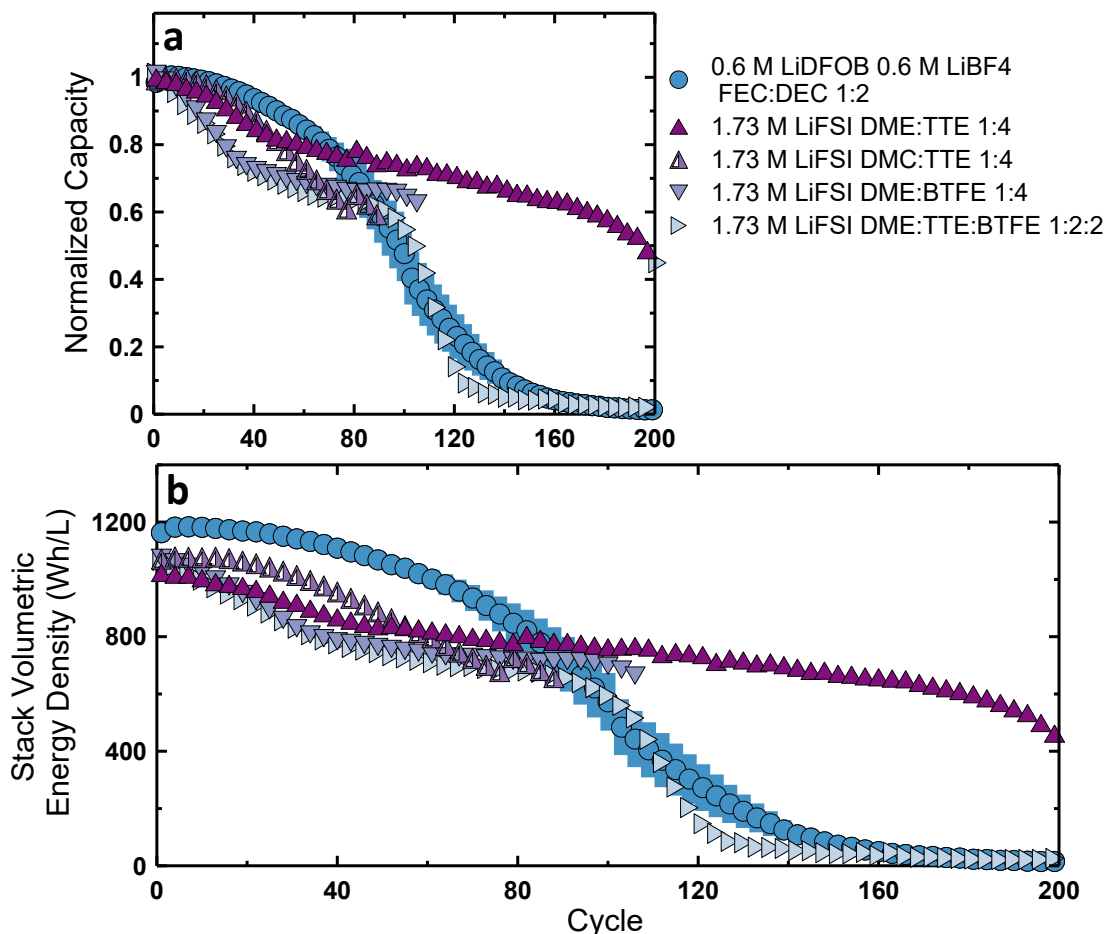


**Figure A.5 | Localized high concentration electrolyte evaluation. a-b,** Normalized capacity (a) and stack volumetric energy density (b) vs cycle of anode-free cells with various localized high concentration electrolyte formulations from the literature. Cells were cycled under low pressure between 3.6-4.5 V at C/5 D/2 and 40°C. Anode-free NMC532 cells were used. The average of at least two cells are shown here; the error bars are calculated as the standard deviation.



**Figure A.6** shows the electrochemical data for cells with dual-salt electrolyte cycled to an upper cut-off voltage of 4.3 V. In comparison to their 4.5 V counterparts, the correlation between the change in behaviour of CE and charge endpoint capacity slippage is slightly delayed to 80 cycles.

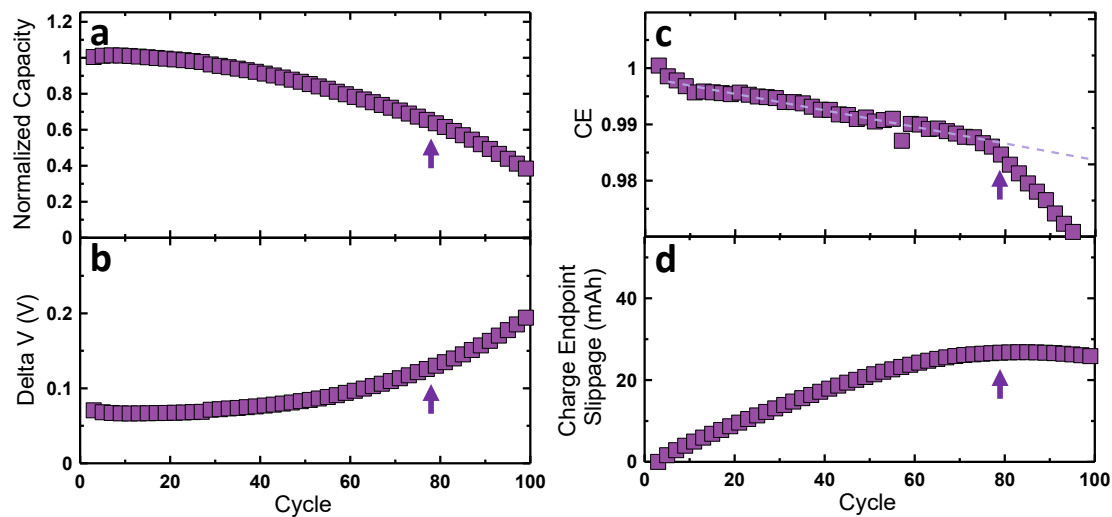


**Figure A.6 | 4.3 V electrochemical analysis. a-d,** Normalized capacity (a), delta V (b), coulombic efficiency (CE, c), and charge endpoint slippage (d) vs cycle of anode-free cells with 0.6 M LiDFOB 0.6 M LiBF<sub>4</sub> FEC:DEC 1:2 electrolyte. Arrows pointing at the data at cycle 80 have been included to guide the eye. Cells were cycled under low pressure between 3.6-4.3 V at C/5 D/2 and 40°C. Anode-free NMC532 cells were used.

To test the voltage-dependence of electrolyte degradation of NMC532 anode-free cells with dual-salt electrolyte, NMR analysis was performed of extracted electrolyte from cells cycled to 4.3 and 4.5 V, shown in **Figure A.7**. LiBF<sub>4</sub> consumption appears to be independent of voltage, whereas the rate of LiDFOB consumption is faster at 4.5 V than 4.3 V.

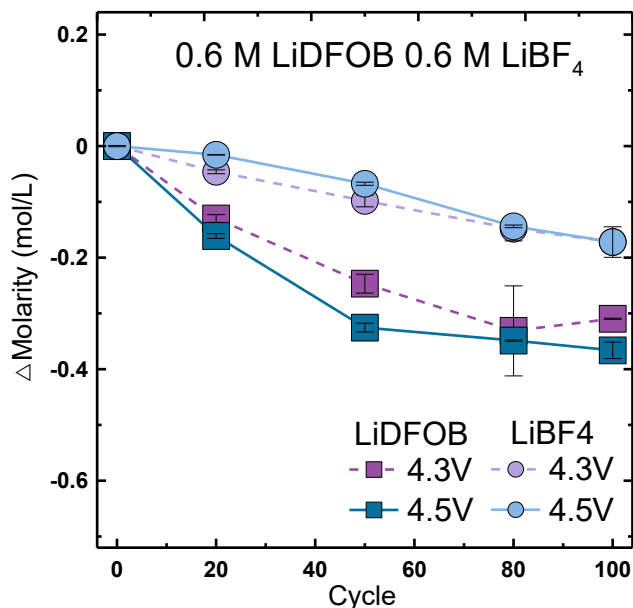


**Figure A.7 | Voltage-dependant electrolyte degradation.** Change in salt concentration molarity vs cycle for anode-free NMC532 full cells with 0.6 M LiDFOB 0.6 M LiBF<sub>4</sub> FEC:DEC 1:2 electrolyte. Cells were cycled under low pressure between 3.6-4.5 V and 3.6-4.3 V at C/5 D/2 and 40°C. Anode-free NMC532 cells were used. Error bars represent the standard deviation of pair cell measurements.

Symmetric coin cells were built from electrodes harvested from pouch cells after being charged once and then discharged to 50% SOC. Symmetric cells were cycled and then their electrolyte was extracted for NMR analysis shown in **Figure 4.11**. **Figure A.8** shows the electrochemical data for symmetric cells cycled with dual-salt electrolyte. Negative-negative symmetric cells were cycled to a fixed capacity of 2.028 mAh. Positive-positive symmetric cells were cycled between -0.92-0.92 V. This voltage range is equivalent to cycling the positive electrodes to potential of 4.5 V vs. Li. The voltage vs time and voltage vs capacity data for these cells are shown in **Figure A.8a-d**. The capacity vs cycle data for

positive-positive symmetric cells are shown in **Figure A.8e**. Positive-positive symmetric cells were also cycled between -0.7-0.7 V to achieve a voltage vs Li of 4.3 V (**Supplementary Fig. 7**).

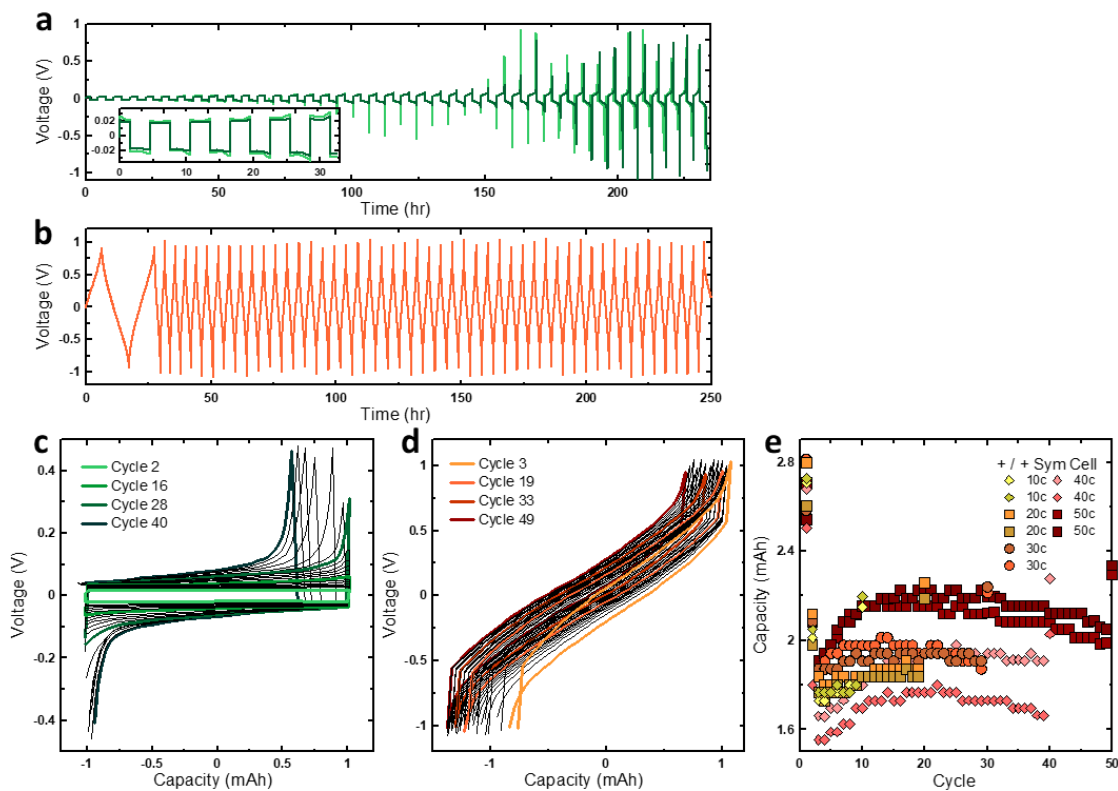


**Figure A.8 | Dual-salt symmetric cell cycling.** **a-b**, Voltage vs time of lithium-lithium (a) and positive-positive (b) symmetric cells with dual-salt electrolyte. **c-d**, Voltage vs capacity of lithium-lithium (c) and positive-positive (d) symmetric cells. **e**, Capacity vs cycle of positive-positive symmetric cells. Cells were cycled with 0.6 M LiDFOB 0.6 M LiBF<sub>4</sub> FEC:DEC 1:2 electrolyte. Positive symmetric cells were cycled to reach 4.5 V vs Li.

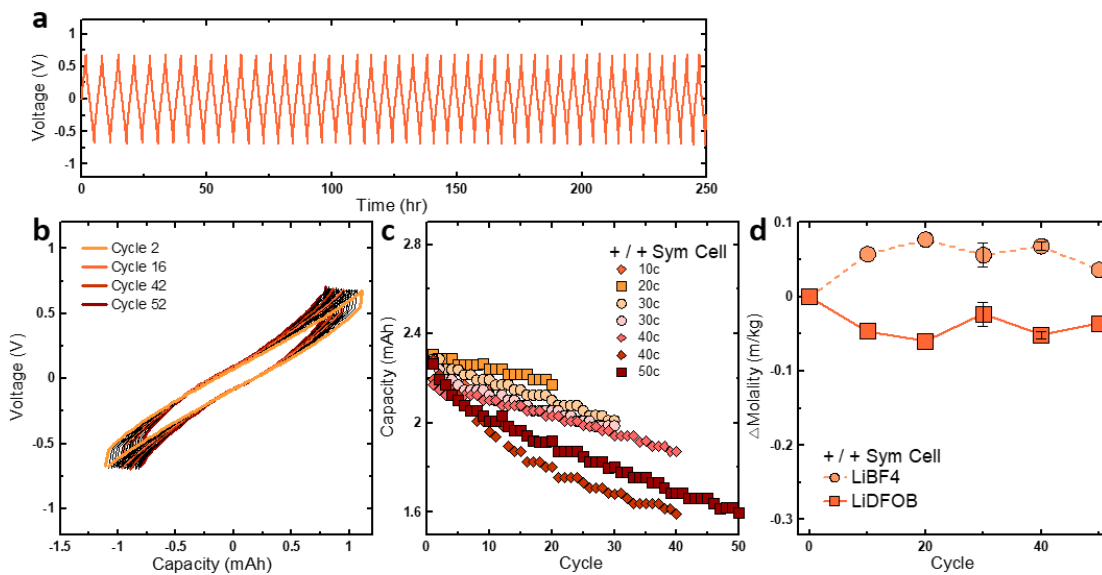


**Figure A.9 | Low voltage positive symmetric cell cycling.** **a**, Voltage vs time of positive-positive symmetric cells with dual-salt electrolyte. **b**, Voltage vs capacity of positive-positive symmetric cells. **c**, Capacity vs cycle of positive-positive symmetric cells. **d**, Molality vs cycle of dual-salt electrolyte determined by NMR. Positive symmetric cells were cycled to reach 4.3 V vs Li.

NMR electrolyte analysis was performed on cells cycled with single-salt 1.2 M LiDFOB FEC:DEC electrolyte to further elucidate the electrolyte degradation mechanism, as shown in **Figure A.10**. In this system with initially no LiBF<sub>4</sub> in the electrolyte, it is observed that LiBF<sub>4</sub> is produced during cycling (**Figure A.10a**), and this occurs at a higher rate at 4.5 V than at 4.3 V, as shown in the inset. In negative symmetric cells (**Figure A.10b**), LiDFOB is shown to be consumed at approximately the same rate as in the dual-salt negative symmetric cells (**Figure 4.11b**), while the concentration of LiBF<sub>4</sub> remains at zero. In positive symmetric cells (**Figure A.10c**), LiDFOB is consumed and LiBF<sub>4</sub> is produced at nearly twice the rate compared to the dual-salt electrolyte cells, suggesting a first-order reaction pathway. The electrochemical data for these symmetric cells are shown in **Figure A.11**.

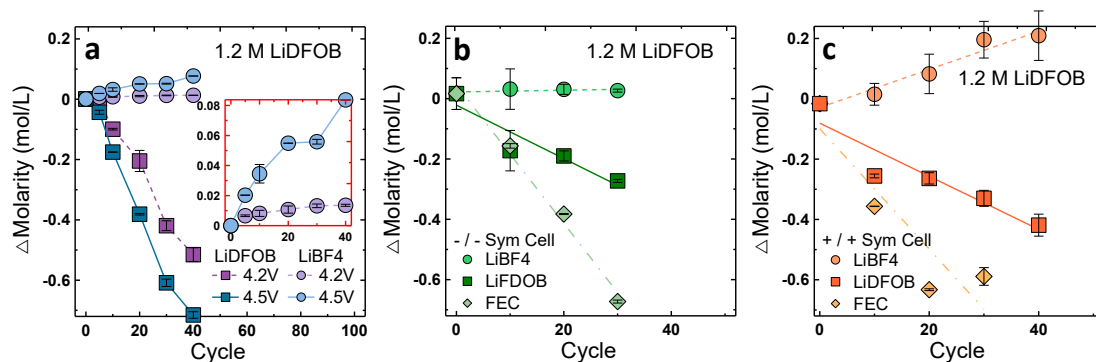


**Figure A.10 | Single-salt electrolyte degradation.** a-c, Change in salt concentration molarity vs cycle for anode-free NMC532 full cells (a), negative Li-Li symmetric cells (b), and positive NMC532-NMC532 symmetric cells with 1.2 M LiDFOB FEC:DEC 1:2 electrolyte. The LiDFOB and LiBF<sub>4</sub> salt components are shown in each panel, as well as the FEC concentration for the symmetric cells (b,c). Cells were cycled under low pressure between 3.6-4.5 V at C/5 D/2 and 40°C. Anode-free NMC532 cells were used. Error bars represent the standard deviation of pair cell measurements.

The electrochemical data for positive-positive symmetric cells built with single-salt LiDFOB electrolyte are shown in **Figure A.11**. Cells were cycled between -0.92-0.92 V to achieve a voltage vs Li. of 4.5 V. The voltage vs time and voltage capacity data are shown in **Figure A.11a** and **c**. The capacity vs cycle data are shown in **Figure A.11b**.

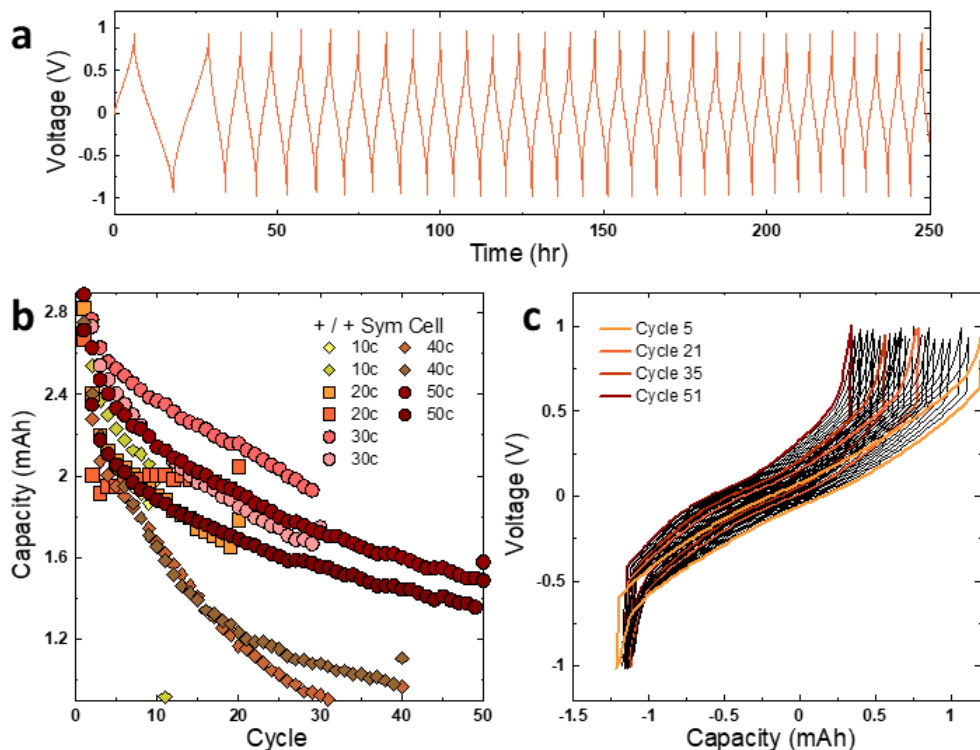


**Figure A.11 | Single-salt positive symmetric cell cycling.** **a**, Voltage vs time of positive-positive symmetric cells with single-salt electrolyte. **b**, Capacity vs cycle of positive-positive symmetric cells. **c**, Voltage vs capacity of positive-positive symmetric cells. Positive symmetric cells were cycled to reach 4.5 V vs Li.

**Figure A.12** shows the evolution of lithium morphology as a function of cycle number for cells cycled under low pressure. SEM images were taken at 3 stages of lithium plating: 100% plating at the top of charge (4.5 V, top row), after most lithium has been stripped away at the bottom of discharge (3.6 V, middle row), and after all active lithium has been stripped away (1.2 V, bottom row). The insets show optical images of the plated lithium.

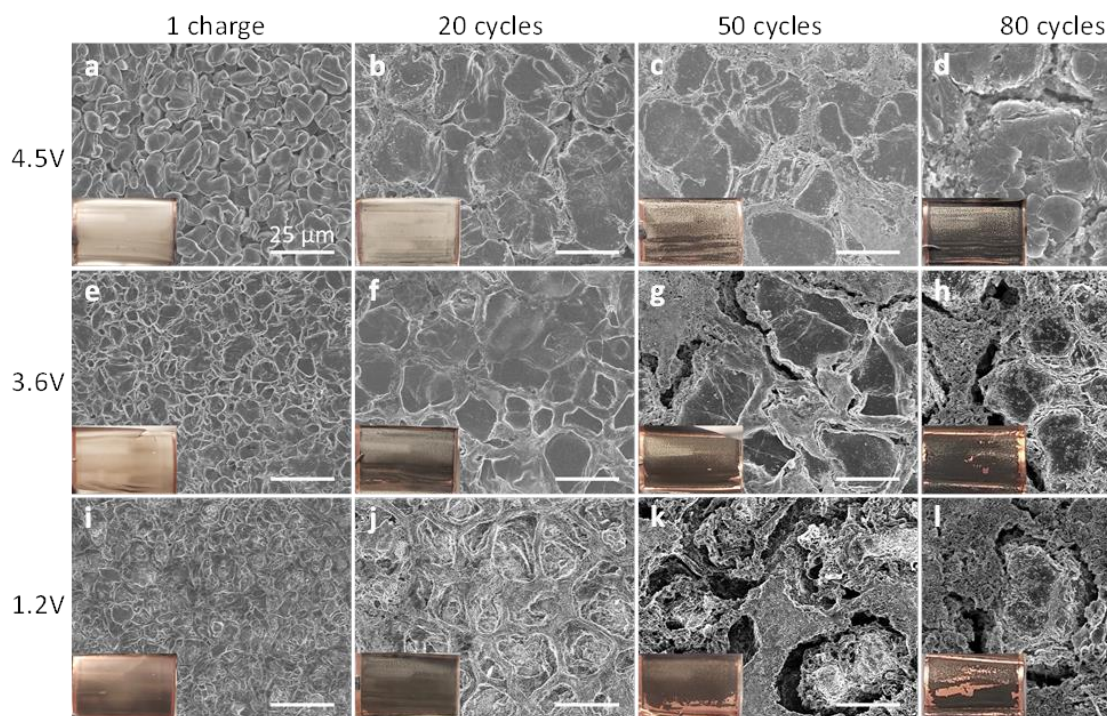


**Figure A.12 | Low pressure morphology degradation.** **a-d**, SEM and optical pictures (insets) of fully plated lithium (4.5 V). **e-f**, Images after most lithium is stripped away (3.6 V). **i-l**, Images after all active lithium is stripped away (1.2 V). Lithium samples were retrieved after 1 charge (a,e,i), 20 (b,f,j), 50 (c,g,k), and 80 (d,h,l) cycles. The insets are optical images of lithium plated on single electrode layer harvested from the pouch cell. Samples were retrieved from cells cycled under low pressure (200 kPa) between 3.6-4.5 V at C/5 D/2 and 40 °C. The electrolyte in the cells was 0.6 M LiDFOB 0.6 M LiBF<sub>4</sub> FEC:DEC 1:2. The scale bars are 25 μm, and the width of the electrodes shown in the insets are 2.6 cm.

**Figure A.13** shows energy dispersive x-ray spectroscopy (EDS) analysis of a lithium sample taken from a cell after 80 cycles constrained under high pressure. **Figure A.13b-e** shows dot maps for fluorine, oxygen, carbon and boron, respectively. Each of these elements are expected to show up in the solid electrolyte interphase (SEI) as electrolyte



decomposition products. The SEI is formed on the surface of lithium metal, therefore, a higher concentration of these decomposition products will be observed in areas with higher surface area. The dot maps show low concentration of these decomposition products on the large lithium grains. In contrast, a high concentration of these elements is observed between the lithium grains, indicating these regions exhibit high surface area.

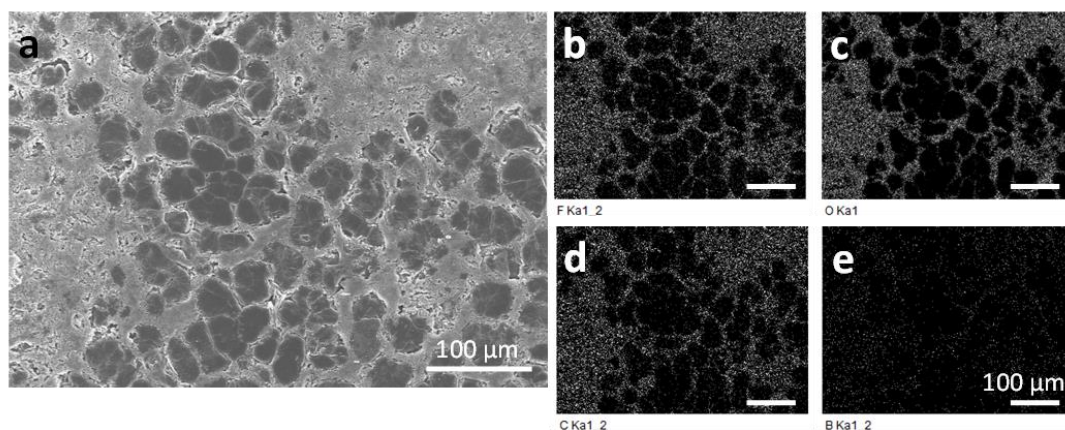


**Figure A.13 | EDS analysis.** **a**, SEM image of plated lithium from a cell cycled with 0.6 M LiDFOB 0.6 M LiBF<sub>4</sub> FEC:DEC 1:2 electrolyte under high pressure after 80 cycles. **b-e**, Fluorine, oxygen, carbon and boron EDS maps. Samples were retrieved from cells cycled between 3.6-4.5 V at C/5 D/2 and 40 °C.

**Figure A.14** shows the normalized capacity, stack volumetric energy density, and delta V vs cycle of the best effort anode-free cells. Applying mechanical pressure, increasing electrolyte volume and increasing LiDFOB and LiBF<sub>4</sub> salt concentrations all improved lifetime. One of the best electrolytes from the literature, the localized high concentration 1.73 M LiFSI DME:TTE 1:4 electrolyte is also included in this comparison.



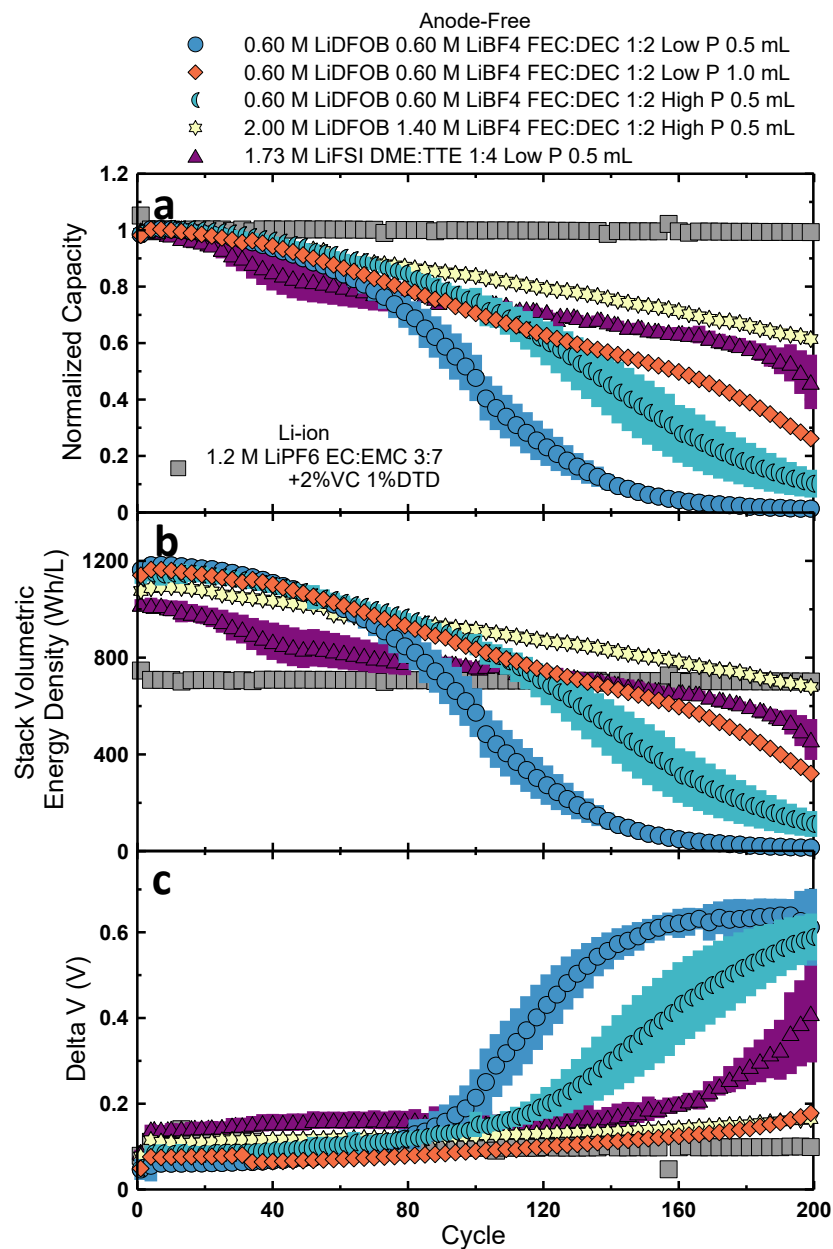


**Figure A.14 | Best effort electrolyte. a-c,** Cycling data of various anode-free cells compared to a Li-ion cell. Normalized capacity (a), stack volumetric energy density (b), and delta V (c) vs cycle. Anode-free Cells were cycled between 3.6-4.5 V at C/5 D/2 and 40°C at low pressure (Low P, 200 kPa) and high pressure (High P, 1200 kPa) as indicated in the legend. The Li-ion cell was cycled between 3.0-4.3 V at C/3 D/3 and 40 °C. The anode-free and Li-ion cells contained the same NMC532 positive electrode. The average of at least two cells are shown; the error bars are calculated as the standard deviation.

## A.2 Chapter 5 Supplementary Data

**Figure A.15** shows the results of all the different rate tests plotted together as a direct comparison. Discharge capacity vs cycle is plotted in **Figure A.15a** to demonstrate the rate dependence of delivered capacity; the first eight cycles are magnified in the inset. **Figure A.15** shows normalized capacity vs equivalent full cycle. This demonstrates the asymmetric slower charge protocol (orange triangles) facilitates the largest capacity throughput.

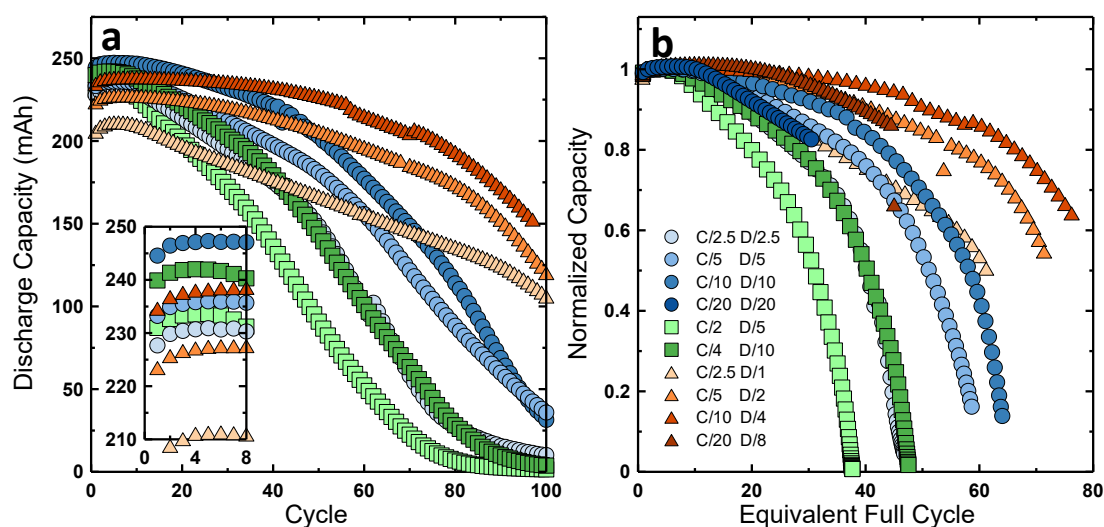


**Figure A.15 | Charge-discharge rate test. a,** Capacity in mAh vs cycle for all charge-discharge rate tests with the inset showing a zoomed in view of the first 8 cycles to clearly show the initial difference in capacity. **b,** Normalized capacity vs equivalent full cycle for all charge-discharge rate tests. The data for each C-rate is the average of two pair cells that were tested. Cells were cycled between 3.6-4.5 V at 40 °C under low pressure with 0.6 M LiDFOB 0.6 M LiBF<sub>4</sub> FEC:DEC 1:2 electrolyte.

The rate dependence on deliverable capacity will impact energy density. Moreover, resistance growth will decrease the deliverable energy; cells which exhibit more severe  $\Delta V$  growth will show more significant energy fade. This is demonstrated in **Figure A.16**.

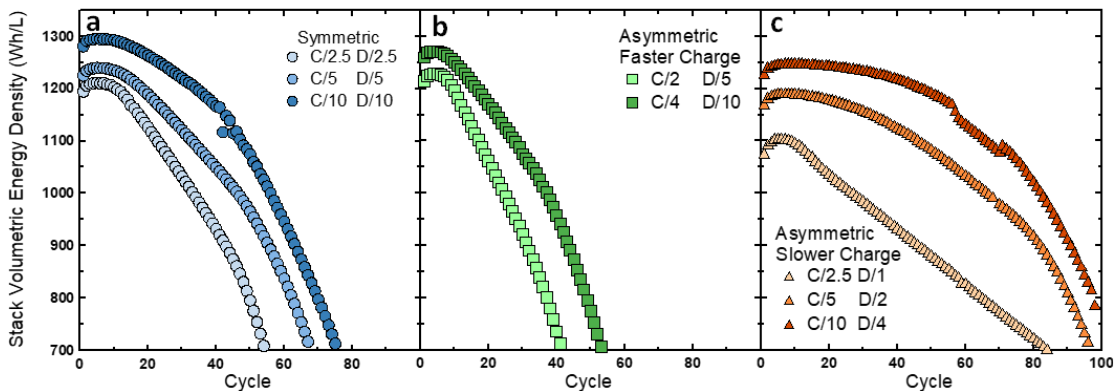


**Figure A.16 | Energy Density of the charge-discharge rate test.** a-c, Stack volumetric energy density vs cycle for cells tested with a symmetric charge-discharge protocol (a), an asymmetric protocol with faster charge (b), and an asymmetric protocol with a slower charge (c). The data for each C-rate is the average of two pair cells that were tested. Cells were cycled between 3.6-4.5 V at 40 °C under low pressure with 0.6 M LiDFOB 0.6 M LiBF<sub>4</sub> FEC:DEC 1:2 electrolyte.

**Figure A.17** shows  $\Delta V$  vs cycle for cells cycled with different depths of discharge. A higher DoDs, severe resistance growth is initiated earlier, contributing to cell death.

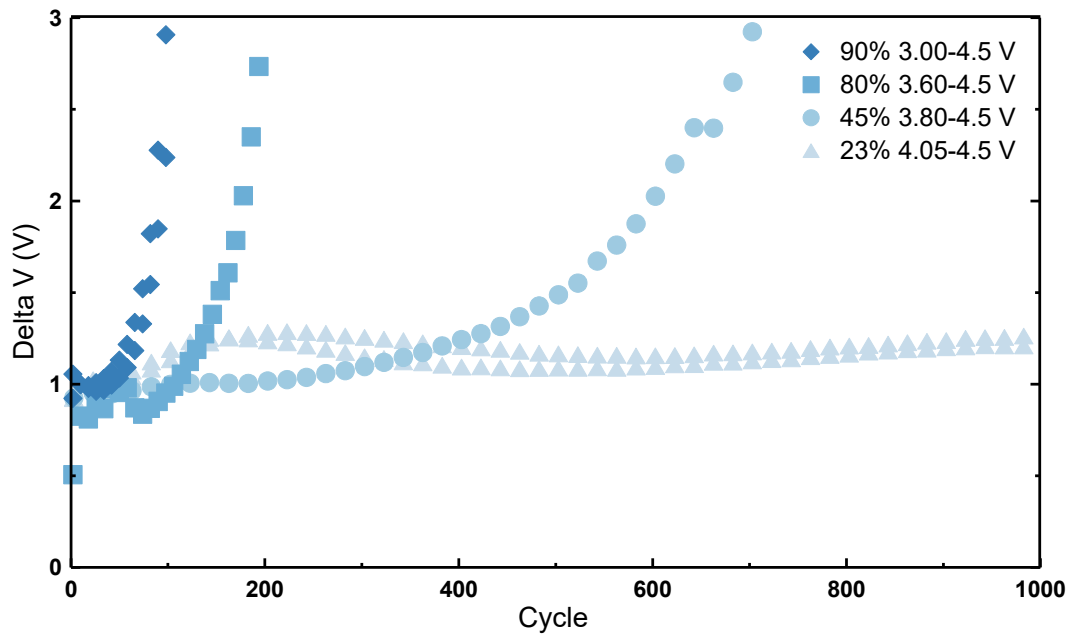


**Figure A.17 | Depth of discharge impedance growth.**  $\Delta V$  vs cycle for cells cycled with different depths of discharge. Cells were cycled at C/5 D/2 at 40°C under high pressure. The electrolyte used was 1.4 M LiDFOB 0.4 M LiBF<sub>4</sub> FEC:DEC (1:2).

### A.3 Chapter 6 Supplementary Data

**Figure A.18** shows the change in cell thickness after 100 cycles vs the number of equivalent full cycles completed.

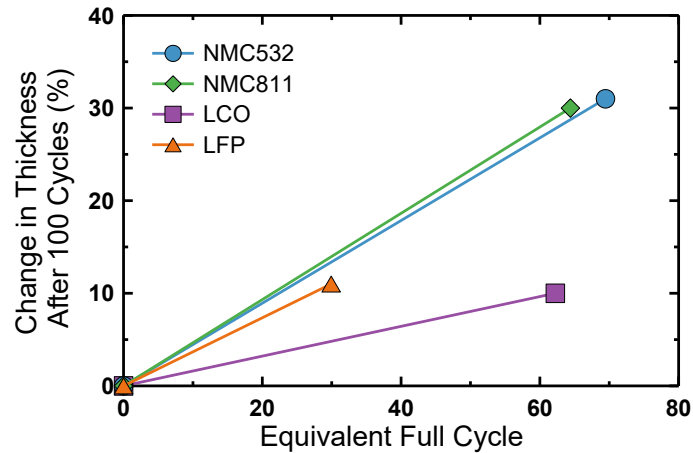


**Figure A.18 | 100 cycle thickness change.** Percentage change in cell thickness after 100 cycles vs equivalent full cycle. Cells were cycled between 3.6-4.5 V (NMC532), 3.55-4.4 V (NMC811), 3.86-4.4 V (LCO), and 2.95-3.7 (LFP) at 40 °C with 0.6 M LiDFOB 0.6 M LiBF<sub>4</sub> FEC:DEC 1:2 electrolyte.

**Figure A.19** shows results for anode-free cells with different positive electrodes tested with different charge-discharge rates. As demonstrated in Chapter 5 for NMC532 cells, the symmetric cycling protocol (C/5 D/5) performs worse than the asymmetric slower charge protocol (C/5 D/2). Slightly modifying the asymmetric slower charge protocol to a charge in 8 hours and a discharge over 3 hours does not significantly impact performance.

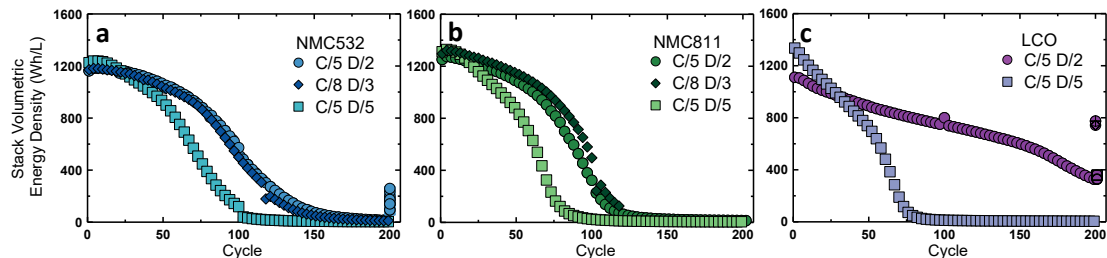


**Figure A.19 | Positive electrode rate test. a-c,** Stack volumetric energy density vs cycle for anode-free NMC532 (a), NMC811 (b), and LCO (c) cells. Cells were cycled between 3.6-4.5 V (NMC532), 3.55-4.4 V (NMC811), 3.86-4.4 V (LCO), and 2.95-3.7 (LFP) at 40 °C with 0.6 M LiDFOB 0.6 M LiBF<sub>4</sub> FEC:DEC 1:2 electrolyte.

**Figure A.20** shows the cycling results for different positive electrode anode-free cells that underwent FRA cycling for *in-situ* EIS measurements every 10 cycles. Cells were cycled between 3.6-4.5 V (NMC532), 3.55-4.4 V (NMC811), 3.86-4.4 V (LCO), and 2.95-3.7 (LFP) with dual-salt electrolyte. The corresponding EIS spectra (shown for every 20 cycles) and their fits are shown in **Figure A.21** for NMC532, **Figure A.22** for NMC811, **Figure A.23** for LCO, and **Figure A.24** for LFP. The equivalent circuit models used for these fits are shown in the bottom right of each figure; the contribution of the circuit elements to are shown in colours beneath the fitted data. These fits were performed using the RelaxIS 3 software suite.

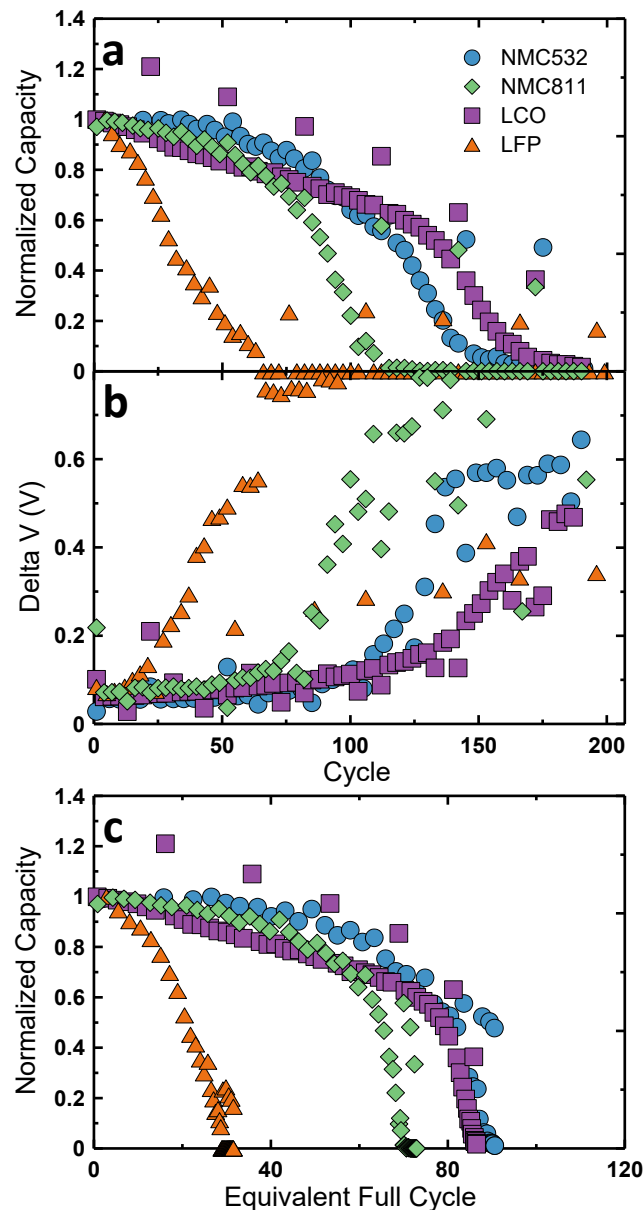


**Figure A.20 | Positive electrode FRA cycling.** Cycling data for anode-free cells with different positive electrodes tested with an FRA protocol for EIS measurements every 10 cycles. Normalized capacity (a) and delta V (b) vs cycle as well as normalized capacity vs equivalent full cycle (c) are shown. Cells were cycled nominally at C/5 D/2 and then at C/10 D/10 every ten cycles for EIS measurements—the noisiness of the data is a result of this protocol. Tests were performed at 40 °C with 0.6 M LiDFOB 0.6 M LiBF<sub>4</sub> FEC:DEC 1:2 electrolyte.

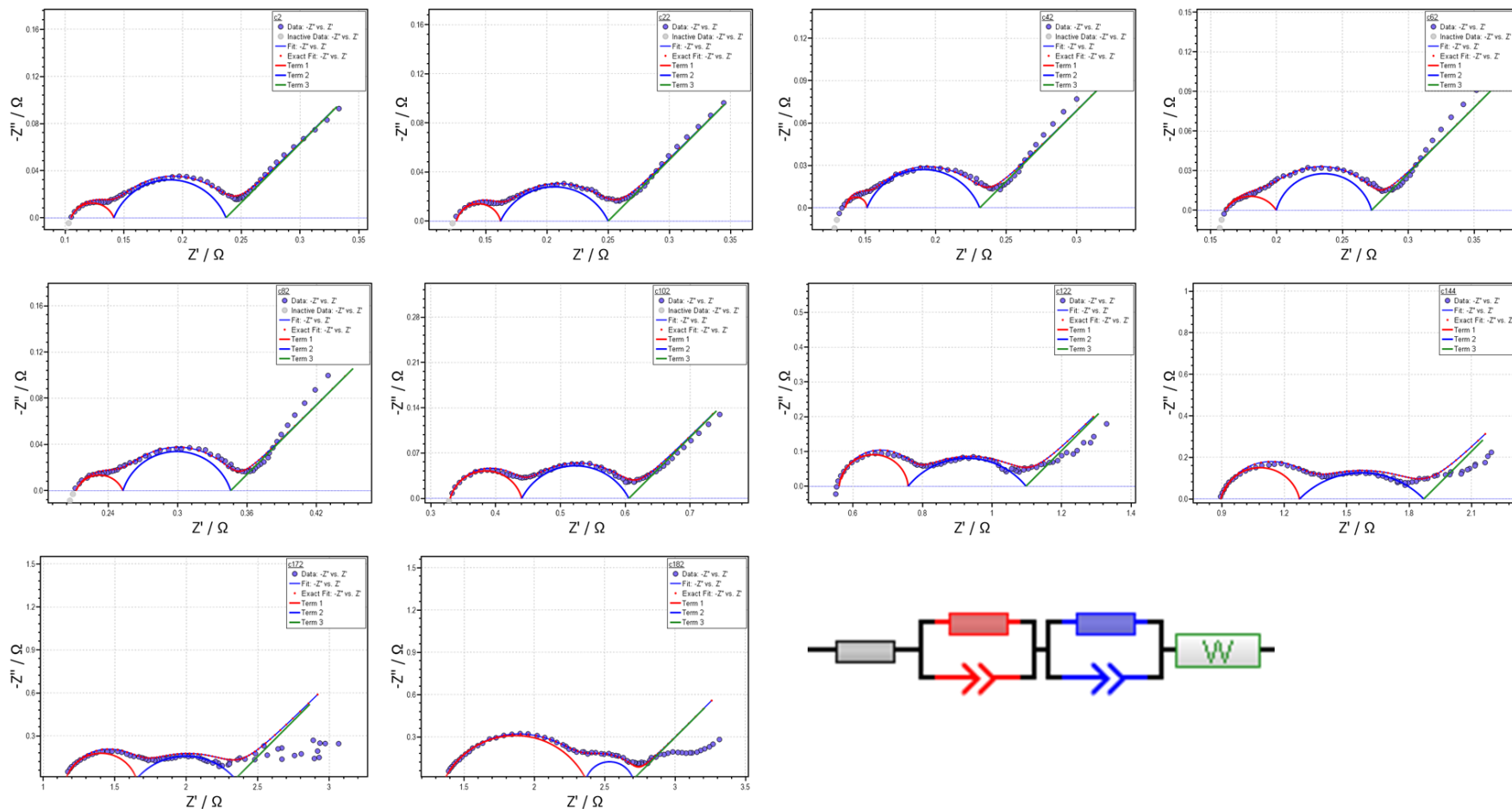


**Figure A.21 | NMC532 EIS fits.** EIS spectra (blue circles) and fits (solid lines) for anode-free NMC532 cells as a function of cycle. The circuit model for the fit is shown in the bottom right; it consists of a resistor, two R-CPE circuits, and a Warburg element. The fit contributions from the different circuit elements are shown in different colours. The fits were performed with the RelaxIS 3 software suite. EIS spectra were measured between 50 kHz to 10 mHz, and cells were cycled between 3.6-4.5 V at C/5 D/2 at 40 °C with 0.6 M LiDFOB 0.6 M LiBF<sub>4</sub> FEC:DEC 1:2 electrolyte.



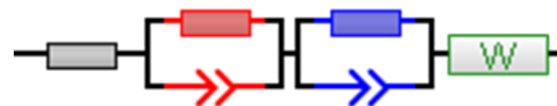
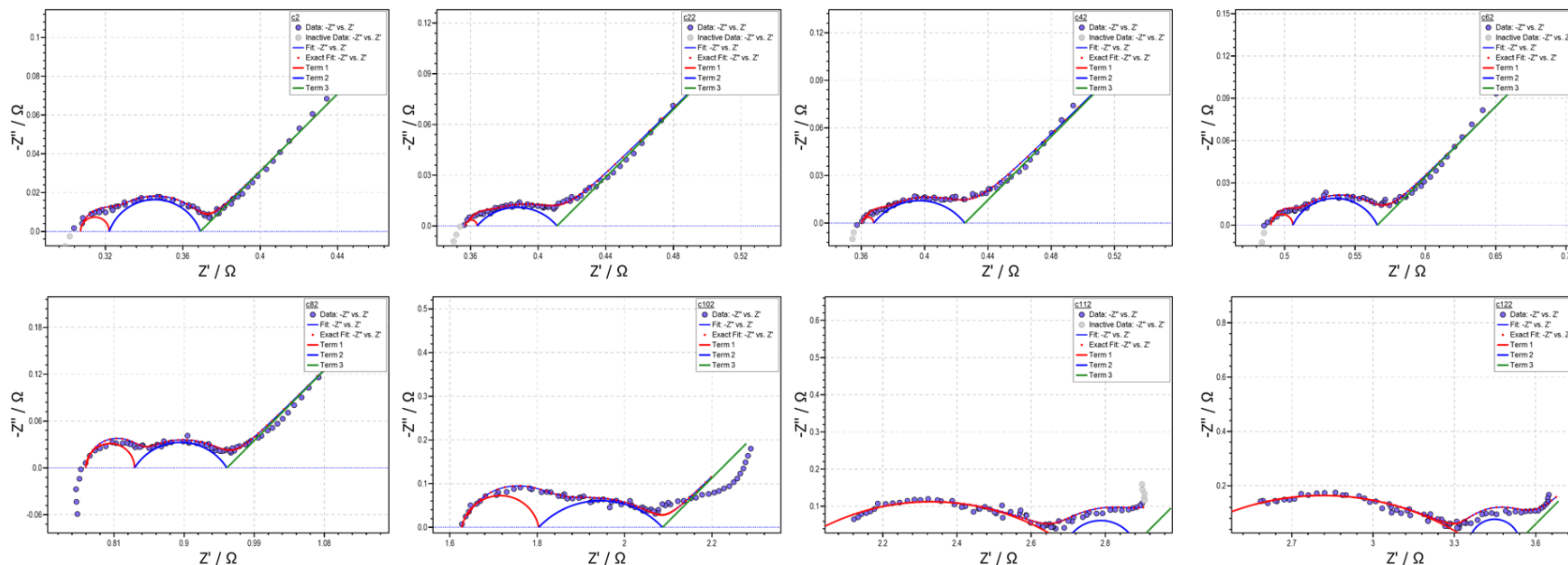


**Figure A.22 | NMC811 EIS fits.** EIS spectra (blue circles) and fits (solid lines) for anode-free NMC811 cells as a function of cycle. The circuit model for the fit is shown in the bottom right; it consists of a resistor, two R-CPE circuits, and a Warburg element. The fit contributions from the different circuit elements are shown in different colours. The fits were performed with the RelaxIS 3 software suite. EIS spectra were measured between 50 kHz to 10 mHz, and cells were cycled between 3.55-4.4 V at C/5 D/2 at 40 °C with 0.6 M LiDFOB 0.6 M LiBF<sub>4</sub> FEC:DEC 1:2 electrolyte.

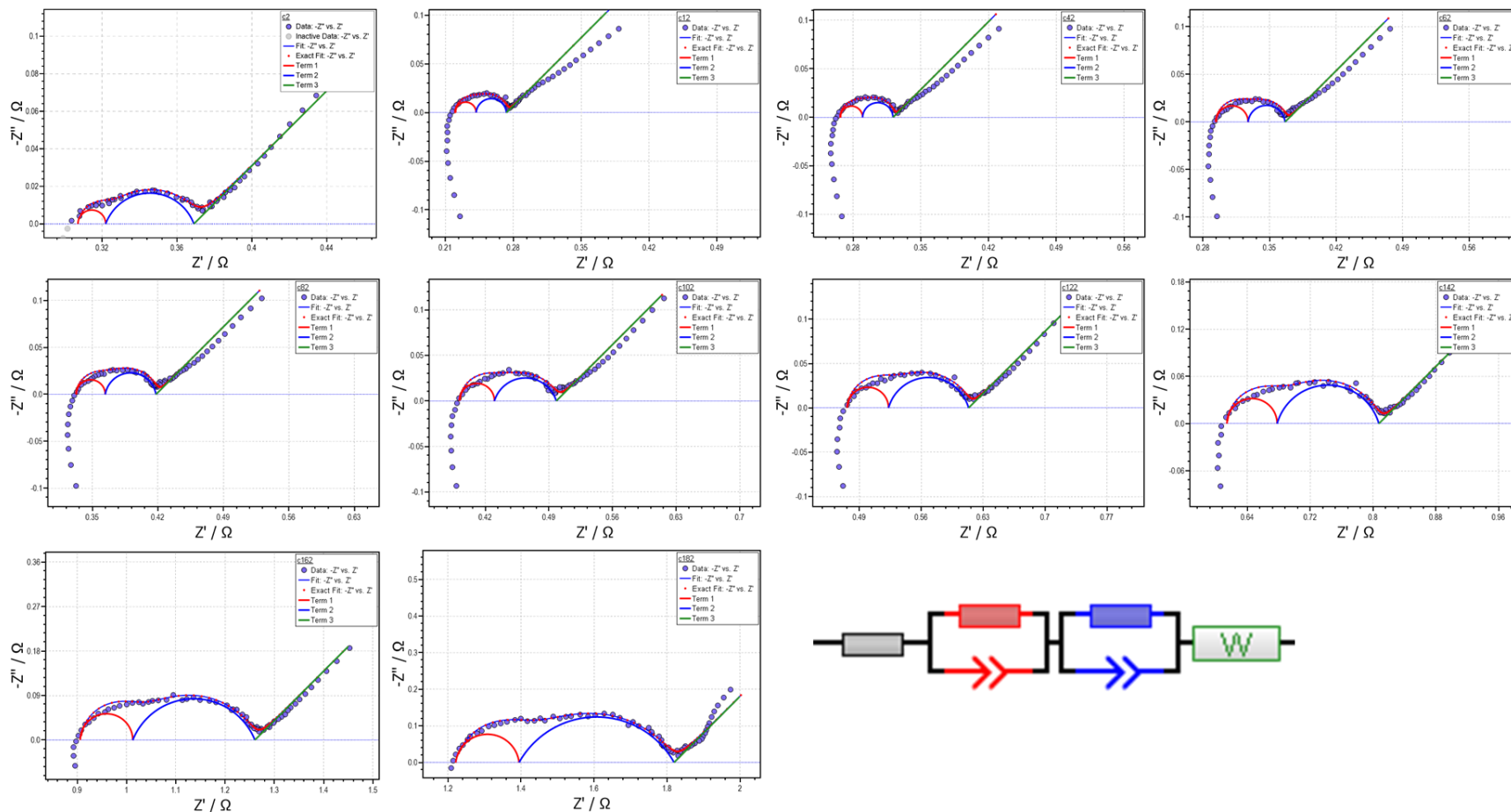


**Figure A.23 | LCO EIS fits.** EIS spectra (blue circles) and fits (solid lines) for anode-free LCO cells as a function of cycle. The circuit model for the fit is shown in the bottom right; it consists of a resistor, two R-CPE circuits, and a Warburg element. The fit contributions from the different circuit elements are shown in different colours. The fits were performed with the RelaxIS 3 software suite. EIS spectra were measured between 50 kHz to 10 mHz, and cells were cycled between 3.86-4.4 V at C/5 D/2 at 40 °C with 0.6 M LiDFOB 0.6 M LiBF<sub>4</sub> FEC:DEC 1:2 electrolyte.

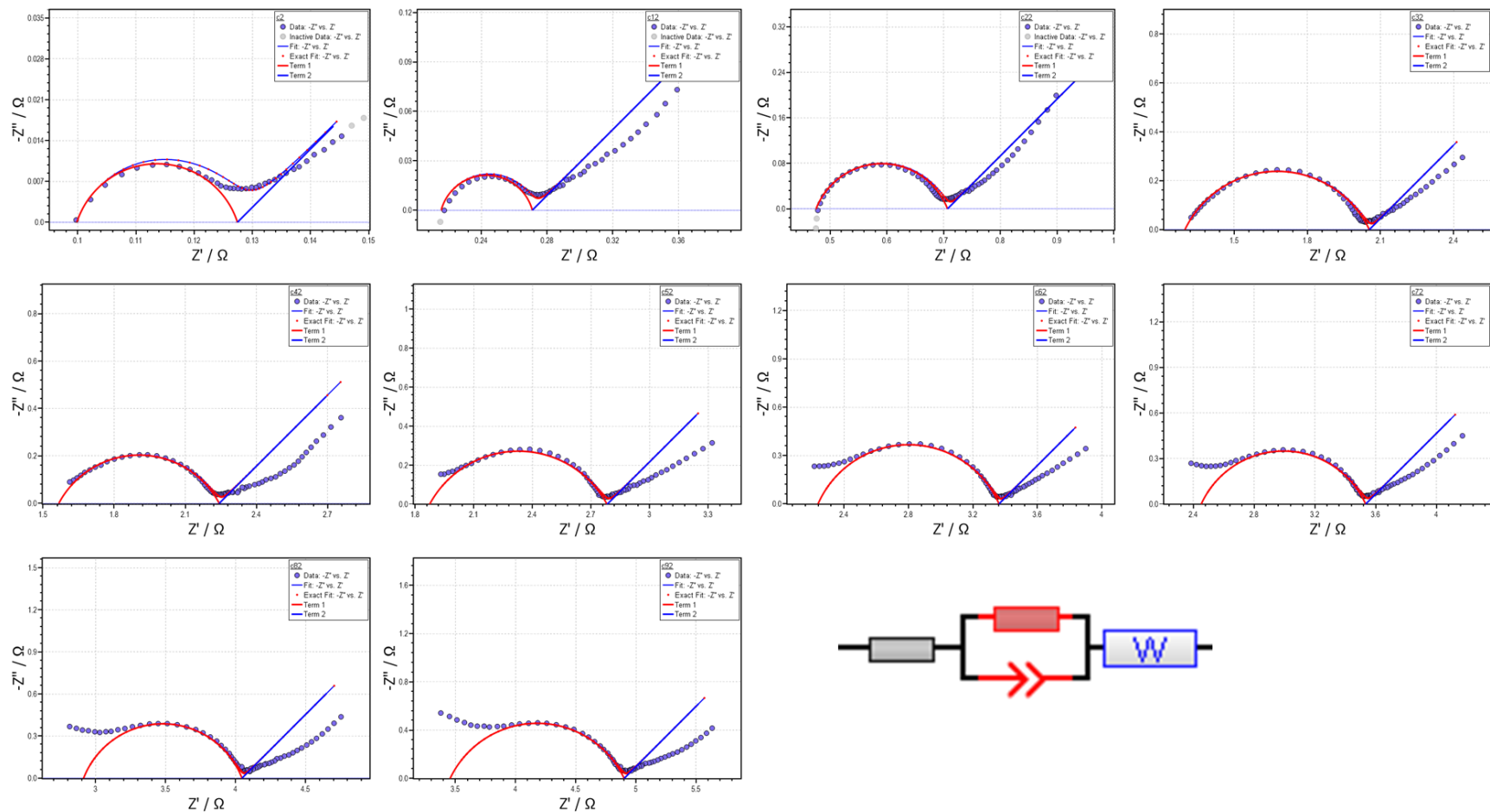


**Figure A.24 | LFP EIS fits.** EIS spectra (blue circles) and fits (solid lines) for anode-free LFP cells as a function of cycle. The circuit model for the fit is shown in the bottom right; it consists of a resistor, one R-CPE circuit, and a Warburg element. The fit contributions from the different circuit elements are shown in different colours. The fits were performed with the RelaxIS 3 software suite. EIS spectra were measured between 50 kHz to 10 mHz, and cells were cycled between 2.95-3.7 V at C/5 D/2 at 40 °C with 0.6 M LiDFOB 0.6 M LiBF<sub>4</sub> FEC:DEC 1:2 electrolyte.

**Figure A.25** shows EIS data for an aged NMC811 cell taken during *in-situ* FRA cycling from 50 kHz to 10 mHz (purple) compared to an *ex-situ* measurement taken from 700 kHz to 10 mHz (green). This *ex-situ* measurement was performed to probe higher frequencies than normally tested during FRA experiments to investigate the unexpected high frequency maximum appearing for aged NMC811 and LFP cells. The difference in size of the spectra is attributed to the measurement temperatures—*in-situ* measurements were performed at 40 °C (normal cycling temperature) while the *ex-situ* measurements were performed at 10 °C, the typical temperature we use for *ex-situ* EIS in our lab to purposely increase impedance to better resolve features that may appear in the spectra. The spectra shape below 50 kHz are mostly consistent; the *ex-situ* measurement exhibits a better resolved semi-circle. At frequencies greater than 50 kHz, the *ex-situ* measurement reveals a new high frequency semi-circle which is cutoff during normal *in-situ* FRA measurements. The cause of this emergent high frequency semi-circle is not clear. However, it appears to show up after significant cell aging and impedance growth for NMC811 and LFP cells—in other words, it's not a good sign. Since the frequency range swept during *in-situ* FRA experiments is not high enough to capture this emergent semi-circle, it was not possible to include in our fits.

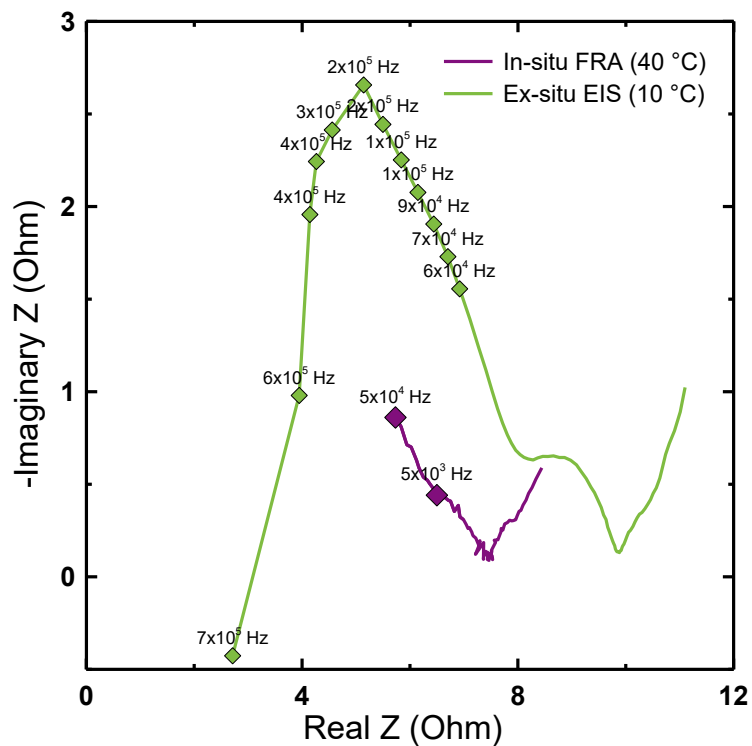


**Figure A.25 | NMC811 emergent high frequency EIS hump.** EIS spectra for an aged anode-free NMC811 cell measured *in-situ* during FRA cycling at 40 °C from 50 kHz to 10 mHz (purple) and measured *ex-situ* at 10 °C from 700 kHz to 10 mHz (green). The high frequencies are labeled.

The EIS fit parameters plotted vs equivalent full cycle are shown in **Figure A.26**.

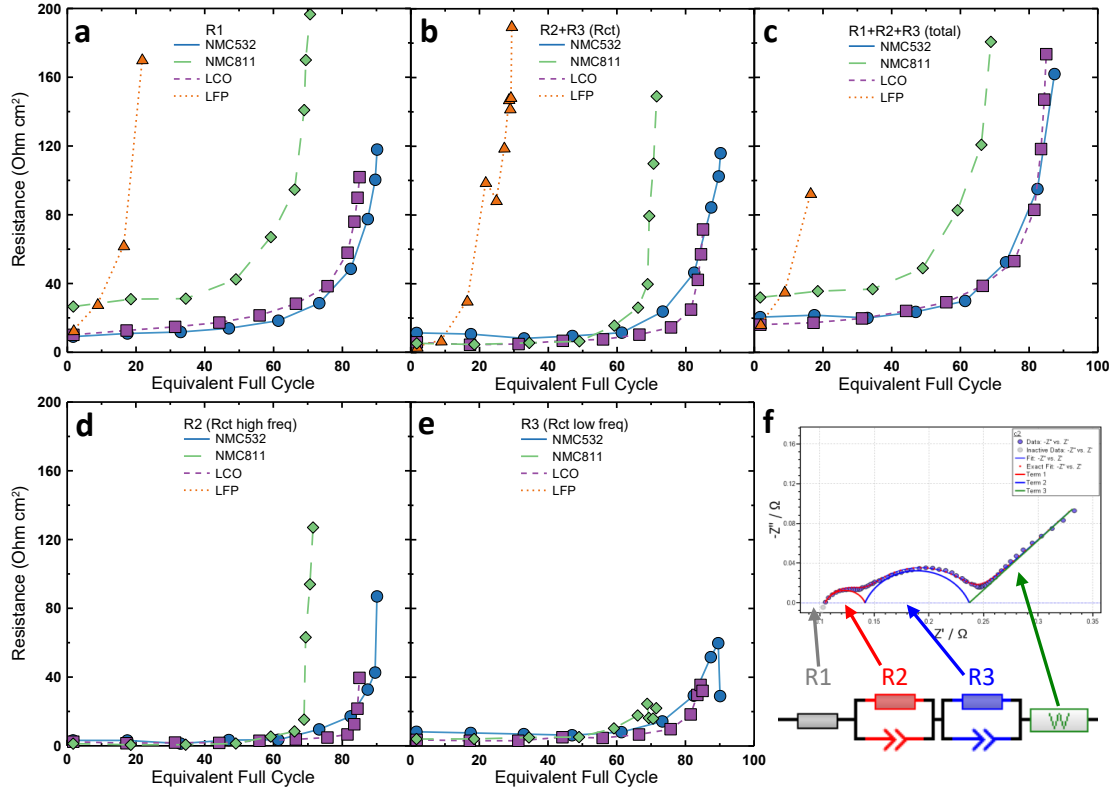


**Figure A.26 | EIS fit parameters.** a-e, Equivalent circuit fit parameters vs equivalent full cycle for EIS measurements of aged anode-free cells with different positive electrodes. The solution resistance ( $R_s = R1$ , a), charge transfer resistance ( $R_{ct} = R2 + R3$ , b), total resistance ( $R1 + R2 + R3$ , c), high frequency charge transfer resistance ( $R2$ , d), and low frequency charge transfer resistance ( $R3$ , e) are shown. f, Example EIS data (circles) that has been fit (solid lines); the individual contributions of each circle elements are shown beneath in colour. Cells were cycled between 3.6-4.5 V (NMC532), 3.55-4.4 V (NMC811), 3.86-4.4 V (LCO), and 2.95-3.7 (LFP) at  $C/5$  D/2 and 40 °C with 0.6 M LiDFOB 0.6 M LiBF<sub>4</sub> FEC:DEC 1:2 electrolyte.

To try to understand the positive and negative electrode contributions to the two charge transfer semi-circles in the impedance spectra of anode-free cells, NMC532 symmetric cells were constructed from electrodes extracted from a cell after 1 cycle. EIS measurements on these symmetric cells compared to full cells are shown in **Figure A.27**. Negative lithium symmetric cells (-/-, a) exhibit two semi-circles: a higher frequency semi-circle between 70-7 Hz and a lower frequency semi-circle between 7 Hz-60 mHz. The positive NMC532 symmetric cells (+/+, b) exhibit a single dominant low frequency semi-circle between 7 Hz-60 mHz. Comparing these contributions to the full cell impedance spectra (+/-, c), the negative lithium electrode contributes to both high and low frequency semi-circles, while the positive electrode contributes to the low frequency semi-circle. Therefore, the two semi-circles observed in the full cell spectra cannot be neatly deconvoluted into positive and negative contributes since they overlap at low frequency. However, according to this analysis, the high frequency semi-circle is solely attributed to the negative lithium electrode. This indicates that the emergent high frequency semi-circle observed for NMC811 and LFP cells may be attributed to highly porous lithium morphologies which develop after significant degradation.

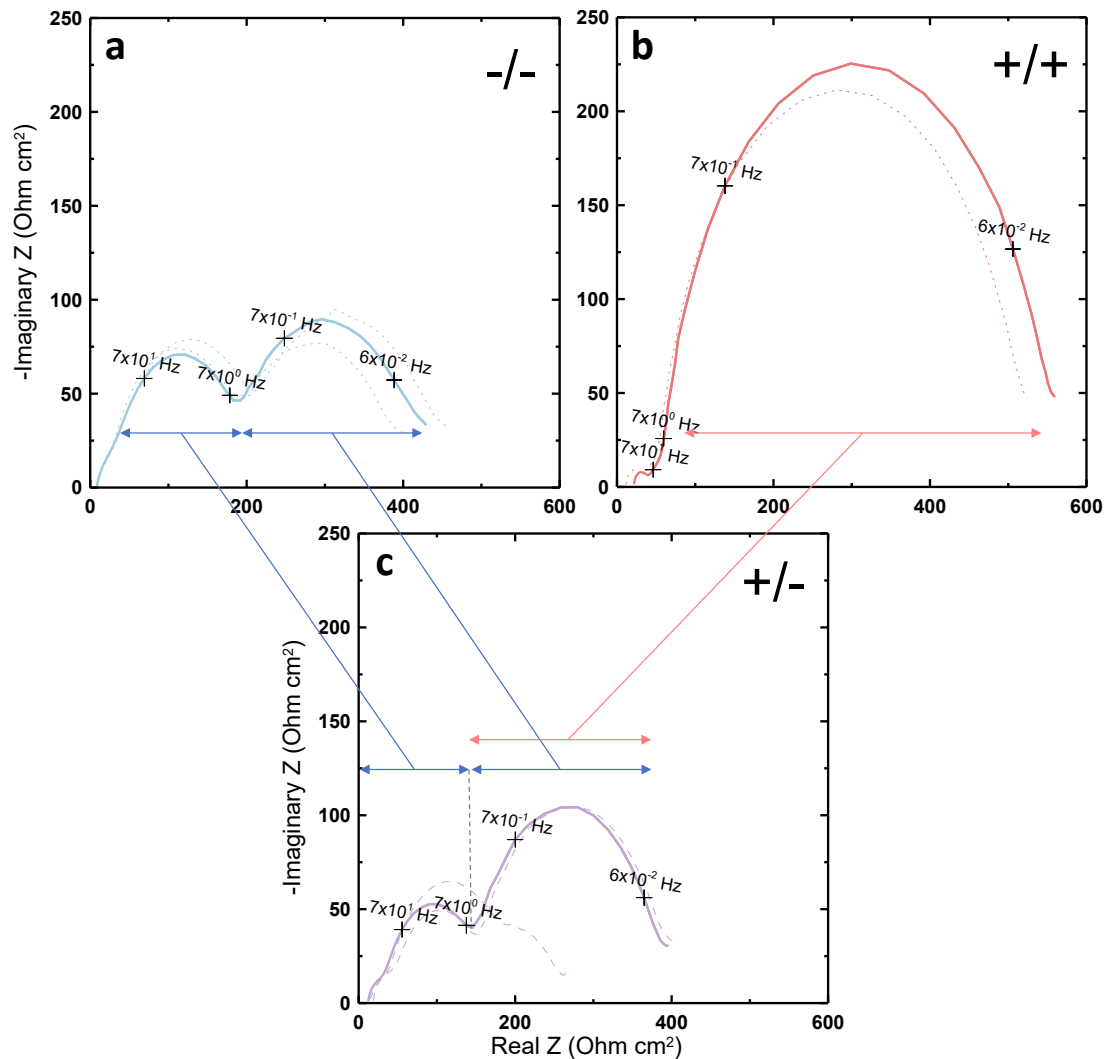


**Figure A.27 | NMC532 symmetric cells.** a-c, EIS spectra for symmetric cells built from electrodes retrieved from an NMC532 anode-free cell after 1 cycle. Negative lithium symmetric cells (-/-, a), positive NMC532 symmetric cells (+/+, b), and full cells (+/-, c) are shown. Symbols for each frequency decade are included. The negative and positive electrode contributions to the full cell impedance spectra are highlighted. EIS spectra were measured between 100 kHz to 10 mHz at 10 °C. Data for duplicate cells are shown in dotted lines.



**Figure A.28** shows the LiDFOB and LiBF<sub>4</sub> salt concentrations as a function of cycle as determined via liquid NMR analysis of extracted electrolyte from aged anode-free cells with different positive electrodes.

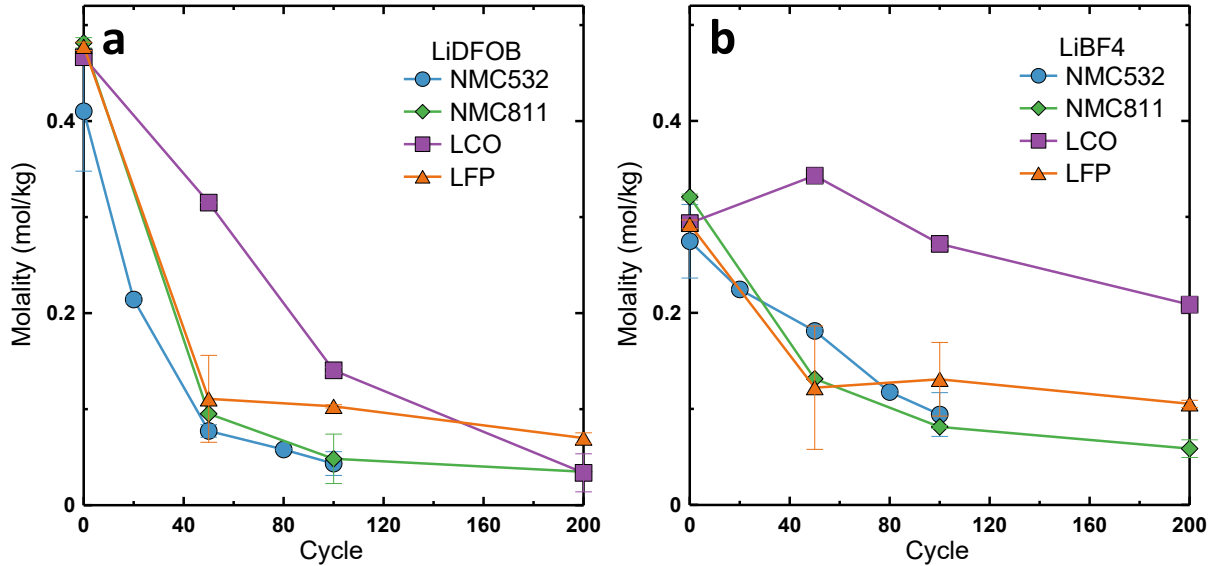


**Figure A.28 | Positive electrode salt depletion. a-b,** LiDFOB (a) and LiBF<sub>4</sub> (b) salt concentration vs cycle as measured via liquid NMR of extracted electrolyte from cycled anode-free cells. The error bars show the standard deviation of duplicate measurements. **c,** Solution resistance vs total LiDFOB + LiBF<sub>4</sub> salt concentration. The solution resistance was extracted from EIS fits. The total salt concentrations were interpolated from a and b. Cells were cycled between 3.6-4.5 V (NMC532), 3.55-4.4 V (NMC811), 3.86-4.4 V (LCO), and 2.95-3.7 (LFP) at C/5 D/2 and 40 °C with 0.6 M (0.52 m) LiDFOB 0.6 M (0.52 m) LiBF<sub>4</sub> FEC:DEC 1:2 electrolyte.

**Figure A.29** shows cycling performance of NMC811 anode-free cells tested with dual-salt electrolytes (**Figure A.29a**) and ether-based electrolyte formulations (**Figure A.29b**) cycled with different voltage ranges as detailed in the legend.

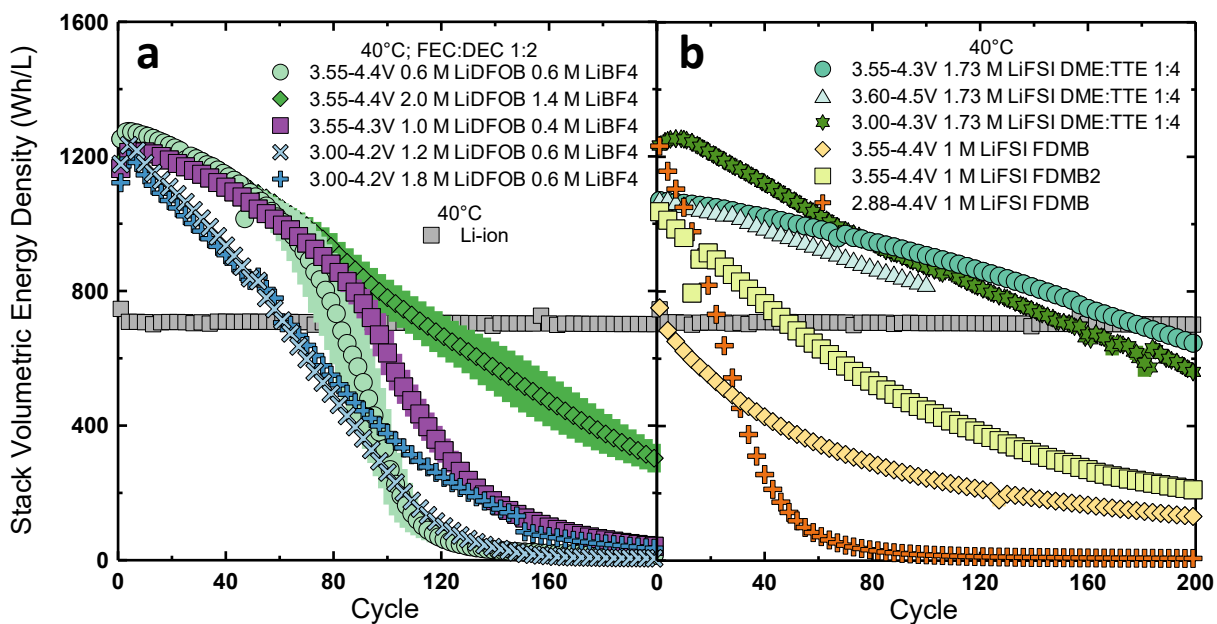


**Figure A.29 | NMC811 electrolyte study.** a-b, Cycling performance of NMC811 anode-free cells at 40 °C with NMC532 Li-ion cells. Anode-free cells were cycled between the voltage ranges listed in the legend at C/5 D/2 at low pressure (Low P, 200 kPa) and high pressure (High P, 1200 kPa). Li-ion cells were cycled between 3.0-4.3 V at C/3 D/3 with 1.2 M LiPF<sub>6</sub> EC:EMC 3:7 + 2%VC 1%DTD electrolyte. Error bars represent the standard deviation of duplicate cells.

#### A.4 Chapter 7 Supplementary Data

**Figure A.30** shows results for hybrid lithium-ion/lithium metal cells cycled at 20 °C with hot formation compared to 40 °C cycling. Similar performance is achieved at both temperatures using a conventional cycling protocol (**Figure A.30a**) and dual Li-ion mode/Li metal mode cycling (**Figure A.30b**).

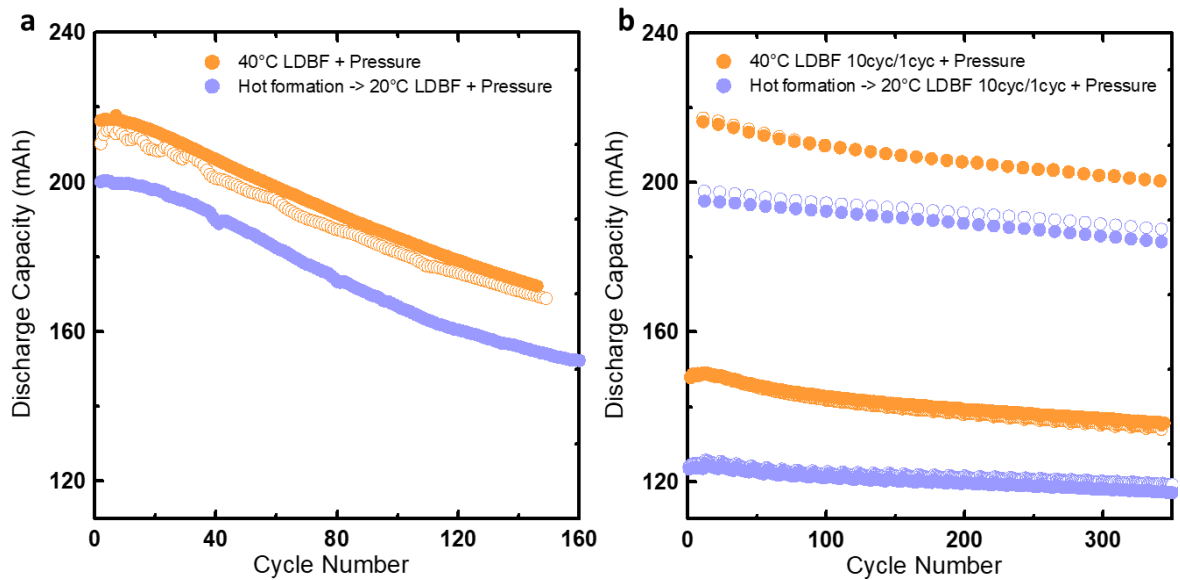


**Figure A.30 | Hot formation for hybrid cells. a-b,** Capacity vs cycle for hybrid cells with 1 M LiDFOB 0.4 M LiBF<sub>4</sub> FEC:DEC 1:2 (LDBF) electrolyte tested at 40 °C and 20 °C with hot formation with conventional cycling (a) and a dual Li-ion mode/Li metal mode protocol (b). Hybrid cells were cycled at C/5 D/2 at high pressure (1200 kPa). Pair cells are shown with open and closed circles.

**Figure A.31** shows the extracted Li metal mode cycles from the dual Li-ion mode/Li metal mode 10/5 and 10/1 cycling protocols plotted with the standard cycling protocol results. The extracted Li metal mode cycles show the same capacity fade as cells cycled over the entire hybrid capacity 100% of the time. This indicates that there are a certain number of Li metal mode cycles that are possible to cycle, regardless of being interspersed with Li-ion mode cycles.

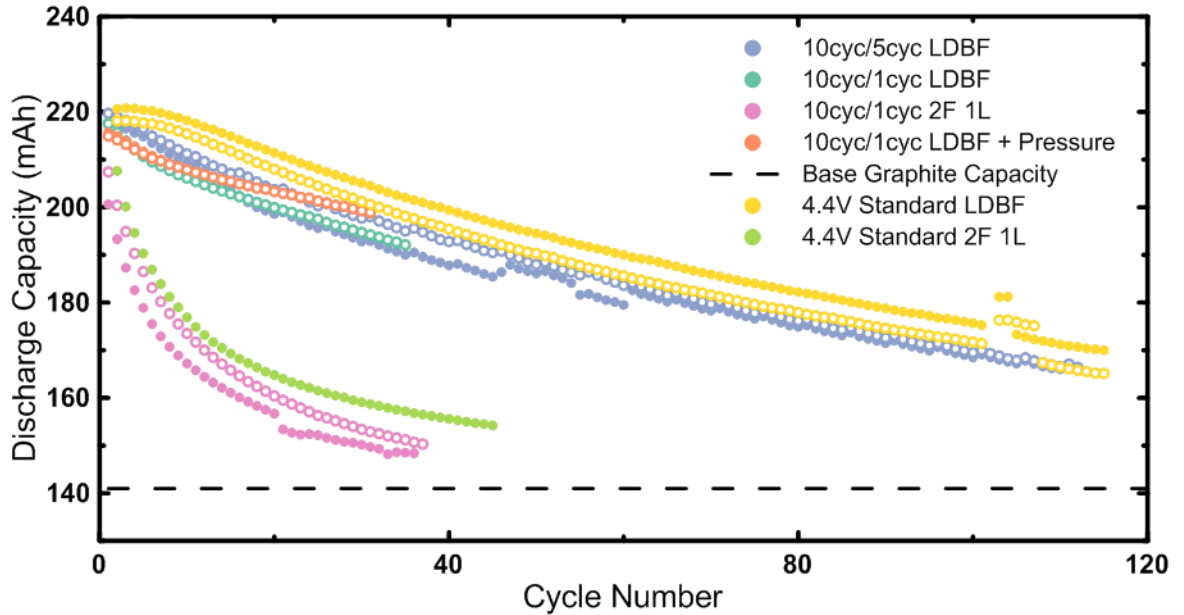


**Figure A.31 | Depth of discharge impedance growth.** Capacity vs cycle of the Li metal mode cycles from the intermittent cycling protocols (10/5 and 10/1 Li-ion mode/Li metal mode cycles) plotted with the standard cycling results. Hybrid cells were cycled at C/5 D/2, 40 °C, low pressure (200 kPa) and high pressure (+Pressure, 1200 kPa). The dotted line shows the capacity of the graphite component of the hybrid cells. Pair cells are shown with open and closed circles. The electrolyte used were 2F1L = 1.5 M LiPF<sub>6</sub> EC:EMC:DMC 25:5:70 + 2% FEC 1% LFO; LDFB = 1 M LiDFOB 0.4 M LiBF<sub>4</sub> FEC:DEC 1:2.

To demonstrate that Li-ion mode operation of hybrid cells is not impeded by Li metal cycles, hybrid cells were aged to 60 cycles while cycling the full hybrid capacity and then in Li-ion mode for a further 440 cycles, shown in **Figure A.32**.

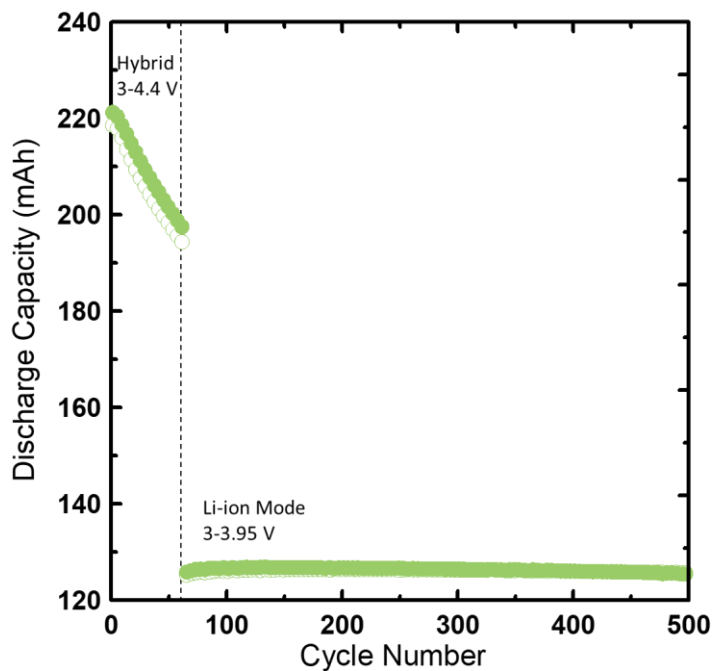


**Figure A.32 | Extended Li-ion mode operation.** Capacity vs cycle for hybrid cells aged for 60 cycles in Li metal mode and then subsequently in Li-ion mode for a further 440 cycles. Hybrid cells were cycled at C/5 D/2 and 40 °C with 1 M LiDFOB 0.4 M LiBF<sub>4</sub> FEC:DEC 1:2 (LDBF) electrolyte. Pair cells are shown with open and closed circles.

## Appendix B Rights and Permissions

### ELSEVIER LICENSE TERMS AND CONDITIONS

Jul 18, 2021

---

---

This Agreement between Dalhousie University -- Alex Louli ("You") and Elsevier ("Elsevier") consists of your license details and the terms and conditions provided by Elsevier and Copyright Clearance Center.

License Number	5112020034518
License date	Jul 18, 2021
Licensed Content Publisher	Elsevier
Licensed Content Publication	Journal of Power Sources
Licensed Content Title	Lithium–titanium disulfide rechargeable cell performance after 35 years of storage
Licensed Content Author	Nathalie Pereira, Glenn G. Amatucci, M. Stanley Whittingham, Robert Hamlen
Licensed Content Date	Apr 15, 2015
Licensed Content Volume	280
Licensed Content Issue	n/a
Licensed Content Pages	5
Start Page	18
End Page	22
Type of Use	reuse in a thesis/dissertation
Portion	figures/tables/illustrations
Number of figures/tables/illustrations	1
Format	both print and electronic
Are you the author of this Elsevier article?	No
Will you be translating?	No
Title	DEVELOPING ANODE-FREE LITHIUM METAL CELLS WITH LIQUID ELECTROLYTES
Institution name	Dalhousie University
Expected presentation date	Aug 2021

Portions	Figure 2
	Dalhousie University
	Department of Physics and Atmospheric Science
Requestor Location	Sir James Dunn Building
	6310 Coburg Road, Main office: Room 218
	Halifax, NS B3H 4R2
	Canada
	Attn: Dalhousie University
Publisher Tax ID	GB 494 6272 12
Total	0.00 CAD

SPRINGER NATURE LICENSE  
TERMS AND CONDITIONS  
Jul 18, 2021

---

---

This Agreement between Dalhousie University -- Alex Louli ("You") and Springer Nature ("Springer Nature") consists of your license details and the terms and conditions provided by Springer Nature and Copyright Clearance Center.

License Number	5112021045638
License date	Jul 18, 2021
Licensed Content Publisher	Springer Nature
Licensed Content Publication	Journal of Solid State Electrochemistry
Licensed Content Title	Lithium ion, lithium metal, and alternative rechargeable battery technologies: the odyssey for high energy density
Licensed Content Author	Tobias Placke et al
Licensed Content Date	May 17, 2017
Type of Use	Thesis/Dissertation
Requestor type	academic/university or research institute
Format	print and electronic
Portion	figures/tables/illustrations
Number of figures/tables/illustrations	1
Will you be translating?	no
Circulation/distribution	1 - 29
Author of this Springer Nature content	no
Title	DEVELOPING ANODE-FREE LITHIUM METAL CELLS WITH LIQUID ELECTROLYTES
Institution name	Dalhousie University
Expected presentation date	Aug 2021
Portions	Figure 3
Requestor Location	Dalhousie University Department of Physics and Atmospheric Science Sir James Dunn Building 6310 Coburg Road, Main office: Room 218



Total

Halifax, NS B3H 4R2  
Canada  
Attn: Dalhousie University  
0.00 CAD

SPRINGER NATURE LICENSE  
TERMS AND CONDITIONS  
Jul 18, 2021

---

---

This Agreement between Dalhousie University -- Alex Louli ("You") and Springer Nature ("Springer Nature") consists of your license details and the terms and conditions provided by Springer Nature and Copyright Clearance Center.

License Number	5112021398106
License date	Jul 18, 2021
Licensed Content Publisher	Springer Nature
Licensed Content Publication	Nature Nanotechnology
Licensed Content Title	Reviving the lithium metal anode for high-energy batteries
Licensed Content Author	Dingchang Lin et al
Licensed Content Date	Mar 7, 2017
Type of Use	Thesis/Dissertation
Requestor type	academic/university or research institute
Format	print and electronic
Portion	figures/tables/illustrations
Number of figures/tables/illustrations	1
High-res required	no
Will you be translating?	no
Circulation/distribution	1 - 29
Author of this Springer Nature content	no
Title	DEVELOPING ANODE-FREE LITHIUM METAL CELLS WITH LIQUID ELECTROLYTES
Institution name	Dalhousie University
Expected presentation date	Aug 2021
Portions	Figure 1d
Requestor Location	Dalhousie University Department of Physics and Atmospheric Science Sir James Dunn Building 6310 Coburg Road, Main office: Room 218

Total

Halifax, NS B3H 4R2  
Canada  
Attn: Dalhousie University  
0.00 CAD

ELSEVIER LICENSE  
TERMS AND CONDITIONS  
Jul 18, 2021

---

---

This Agreement between Dalhousie University -- Alex Louli ("You") and Elsevier ("Elsevier") consists of your license details and the terms and conditions provided by Elsevier and Copyright Clearance Center.

License Number	5112030024177
License date	Jul 18, 2021
Licensed Content Publisher	Elsevier
Licensed Content Publication	Joule
Licensed Content Title	Advancing Lithium Metal Batteries
Licensed Content Author	Bin Liu, Ji-Guang Zhang, Wu Xu
Licensed Content Date	May 16, 2018
Licensed Content Volume	2
Licensed Content Issue	5
Licensed Content Pages	13
Start Page	833
End Page	845
Type of Use	reuse in a thesis/dissertation
Portion	figures/tables/illustrations
Number of figures/tables/illustrations	1
Format	both print and electronic
Are you the author of this Elsevier article?	No
Will you be translating?	No
Title	DEVELOPING ANODE-FREE LITHIUM METAL CELLS WITH LIQUID ELECTROLYTES
Institution name	Dalhousie University
Expected presentation date	Aug 2021
Portions	Figure 2
Requestor Location	Dalhousie University Department of Physics and Atmospheric

Science  
Sir James Dunn Building  
6310 Coburg Road, Main office: Room 218  
Halifax, NS B3H 4R2  
Canada  
Attn: Dalhousie University  
GB 494 6272 12  
0.00 CAD

Publisher Tax ID  
Total

ELSEVIER LICENSE  
TERMS AND CONDITIONS

Jul 18, 2021

---

---

This Agreement between Dalhousie University -- Alex Louli ("You") and Elsevier ("Elsevier") consists of your license details and the terms and conditions provided by Elsevier and Copyright Clearance Center.

License Number	5112030207790
License date	Jul 18, 2021
Licensed Content Publisher	Elsevier
Licensed Content Publication	Joule
Licensed Content Title	Ultrasonic Scanning to Observe Wetting and “Unwetting” in Li-Ion Pouch Cells
Licensed Content Author	Zhe Deng,Zhenyu Huang,Yue Shen,Yunhui Huang,Han Ding,Aidan Luscombe,Michel Johnson,Jessie E. Harlow,Roby Gauthier,Jeff R. Dahn
Licensed Content Date	Sep 16, 2020
Licensed Content Volume	4
Licensed Content Issue	9
Licensed Content Pages	13
Start Page	2017
End Page	2029
Type of Use	reuse in a thesis/dissertation
Portion	figures/tables/illustrations
Number of figures/tables/illustrations	2
Format	both print and electronic
Are you the author of this Elsevier article?	No
Will you be translating?	No
Title	DEVELOPING ANODE-FREE LITHIUM METAL CELLS WITH LIQUID ELECTROLYTES
Institution name	Dalhousie University
Expected presentation date	Aug 2021

Portions	Figure 1, Figure 3
	Dalhousie University
	Department of Physics and Atmospheric Science
	Sir James Dunn Building
Requestor Location	6310 Coburg Road, Main office: Room 218
	Halifax, NS B3H 4R2
	Canada
	Attn: Dalhousie University
Publisher Tax ID	GB 494 6272 12
Total	0.00 CAD

ELSEVIER LICENSE  
TERMS AND CONDITIONS  
Jul 18, 2021

---

---

This Agreement between Dalhousie University -- Alex Louli ("You") and Elsevier ("Elsevier") consists of your license details and the terms and conditions provided by Elsevier and Copyright Clearance Center.

License Number	5112030283817
License date	Jul 18, 2021
Licensed Content Publisher	Elsevier
Licensed Content Publication	Journal of Power Sources
Licensed Content Title	Building a “smart nail” for penetration tests on Li-ion cells
Licensed Content Author	T.D. Hatchard,S. Trussler,J.R. Dahn
Licensed Content Date	Feb 1, 2014
Licensed Content Volume	247
Licensed Content Issue	n/a
Licensed Content Pages	3
Start Page	821
End Page	823
Type of Use	reuse in a thesis/dissertation
Portion	figures/tables/illustrations
Number of figures/tables/illustrations	1
Format	both print and electronic
Are you the author of this Elsevier article?	No
Will you be translating?	No
Title	DEVELOPING ANODE-FREE LITHIUM METAL CELLS WITH LIQUID ELECTROLYTES
Institution name	Dalhousie University
Expected presentation date	Aug 2021
Portions	Figure 3



Requestor Location	Dalhousie University Department of Physics and Atmospheric Science Sir James Dunn Building 6310 Coburg Road, Main office: Room 218 Halifax, NS B3H 4R2 Canada
Publisher Tax ID	Attn: Dalhousie University GB 494 6272 12
Total	0.00 CAD

ELSEVIER LICENSE  
TERMS AND CONDITIONS  
Jul 18, 2021

---

---

This Agreement between Dalhousie University -- Alex Louli ("You") and Elsevier ("Elsevier") consists of your license details and the terms and conditions provided by Elsevier and Copyright Clearance Center.

License Number	5112030372170
License date	Jul 18, 2021
Licensed Content Publisher	Elsevier
Licensed Content Publication	Joule
Licensed Content Title	High-Efficiency Lithium Metal Batteries with Fire-Retardant Electrolytes
Licensed Content Author	Shuru Chen, Jianming Zheng, Lu Yu, Xiaodi Ren, Mark H. Engelhard, Chaojiang Niu, Hongkyung Lee, Wu Xu, Jie Xiao, Jun Liu, Ji-Guang Zhang
Licensed Content Date	Aug 15, 2018
Licensed Content Volume	2
Licensed Content Issue	8
Licensed Content Pages	11
Start Page	1548
End Page	1558
Type of Use	reuse in a thesis/dissertation
Portion	figures/tables/illustrations
Number of figures/tables/illustrations	1
Format	both print and electronic
Are you the author of this Elsevier article?	No
Will you be translating?	No
Title	DEVELOPING ANODE-FREE LITHIUM METAL CELLS WITH LIQUID ELECTROLYTES
Institution name	Dalhousie University
Expected presentation date	Aug 2021

Portions	Figure 3
	Dalhousie University
	Department of Physics and Atmospheric Science
	Sir James Dunn Building
Requestor Location	6310 Coburg Road, Main office: Room 218
	Halifax, NS B3H 4R2
	Canada
	Attn: Dalhousie University
Publisher Tax ID	GB 494 6272 12
Total	0.00 CAD

JOHN WILEY AND SONS LICENSE  
TERMS AND CONDITIONS  
Jul 18, 2021

---

---

This Agreement between Dalhousie University -- Alex Louli ("You") and John Wiley and Sons ("John Wiley and Sons") consists of your license details and the terms and conditions provided by John Wiley and Sons and Copyright Clearance Center.

License Number	5112030510220
License date	Jul 18, 2021
Licensed Content Publisher	John Wiley and Sons
Licensed Content Publication	Advanced Materials
Licensed Content Title	High-Voltage Lithium-Metal Batteries Enabled by Localized High-Concentration Electrolytes
Licensed Content Author	Ji-Guang Zhang, Jun Liu, Wu Xu, et al
Licensed Content Date	Mar 25, 2018
Licensed Content Volume	30
Licensed Content Issue	21
Licensed Content Pages	7
Type of use	Dissertation/Thesis
Requestor type	University/Academic
Format	Print and electronic
Portion	Figure/table
Number of figures/tables	1
Will you be translating?	No
Title	DEVELOPING ANODE-FREE LITHIUM METAL CELLS WITH LIQUID ELECTROLYTES
Institution name	Dalhousie University

Expected presentation date	Aug 2021
Portions	Figure 2
	Dalhousie University
	Department of Physics and Atmospheric Science
	Sir James Dunn Building
Requestor Location	6310 Coburg Road, Main office: Room 218
	Halifax, NS B3H 4R2
	Canada
	Attn: Dalhousie University
Publisher Tax ID	EU826007151
Total	0.00 CAD

ELSEVIER LICENSE  
TERMS AND CONDITIONS

Jul 18, 2021

---

---

This Agreement between Dalhousie University -- Alex Louli ("You") and Elsevier ("Elsevier") consists of your license details and the terms and conditions provided by Elsevier and Copyright Clearance Center.

License Number	5112030585467
License date	Jul 18, 2021
Licensed Content Publisher	Elsevier
Licensed Content Publication	Joule
Licensed Content Title	Enabling High-Voltage Lithium-Metal Batteries under Practical Conditions
Licensed Content Author	Xiaodi Ren,Lianfeng Zou,Xia Cao,Mark H. Engelhard,Wen Liu,Sarah D. Burton,Hongkyung Lee,Chaojiang Niu,Bethany E. Matthews,Zihua Zhu,Chongmin Wang,Bruce W. Arey,Jie Xiao,Jun Liu, Ji-Guang Zhang,Wu Xu
Licensed Content Date	Jul 17, 2019
Licensed Content Volume	3
Licensed Content Issue	7
Licensed Content Pages	15
Start Page	1662
End Page	1676
Type of Use	reuse in a thesis/dissertation
Portion	figures/tables/illustrations
Number of figures/tables/illustrations	1
Format	both print and electronic
Are you the author of this Elsevier article?	No
Will you be translating?	No
Title	DEVELOPING ANODE-FREE LITHIUM METAL CELLS WITH LIQUID ELECTROLYTES
Institution name	Dalhousie University

Expected presentation date	Aug 2021
Portions	Figure 4
	Dalhousie University
	Department of Physics and Atmospheric Science
	Sir James Dunn Building
Requestor Location	6310 Coburg Road, Main office: Room 218
	Halifax, NS B3H 4R2
	Canada
	Attn: Dalhousie University
Publisher Tax ID	GB 494 6272 12
Total	0.00 CAD

SPRINGER NATURE LICENSE  
TERMS AND CONDITIONS

Jul 18, 2021

---

---

This Agreement between Dalhousie University -- Alex Louli ("You") and Springer Nature ("Springer Nature") consists of your license details and the terms and conditions provided by Springer Nature and Copyright Clearance Center.

License Number	5112030680071
License date	Jul 18, 2021
Licensed Content Publisher	Springer Nature
Licensed Content Publication	Nature Energy
Licensed Content Title	Molecular design for electrolyte solvents enabling energy-dense and long-cycling lithium metal batteries
Licensed Content Author	Zhiao Yu et al
Licensed Content Date	Jun 22, 2020
Type of Use	Thesis/Dissertation
Requestor type	academic/university or research institute
Format	print and electronic
Portion	figures/tables/illustrations
Number of figures/tables/illustrations	1
High-res required	no
Will you be translating?	no
Circulation/distribution	1 - 29
Author of this Springer Nature content	no
Title	DEVELOPING ANODE-FREE LITHIUM METAL CELLS WITH LIQUID ELECTROLYTES
Institution name	Dalhousie University
Expected presentation date	Aug 2021
Portions	Figure 3
Requestor Location	Dalhousie University Department of Physics and Atmospheric Science Sir James Dunn Building



6310 Coburg Road, Main office: Room 218  
Halifax, NS B3H 4R2  
Canada  
Attn: Dalhousie University  
0.00 CAD

Total

## References

- [1] G.E. Blomgren, The Development and Future of Lithium Ion Batteries, *J. Electrochem. Soc.* **164** (2017) A5019–A5025. doi:10.1149/2.0251701jes.
- [2] M. Ue, K. Sakaushi, K. Uosaki, Basic knowledge in battery research bridging the gap between academia and industry, *Mater. Horizons.* (2020). doi:10.1039/D0MH00067A.
- [3] J. Holden, N. Goel, Fast-Forwarding to a Future of On-Demand Urban Air Transportation, (2016) 1–98. <https://www.uber.com/elevate.pdf>.
- [4] A. Kasliwal, N.J. Furbush, J.H. Gawron, J.R. McBride, T.J. Wallington, R.D. De Kleine, H.C. Kim, G.A. Keoleian, Role of flying cars in sustainable mobility, *Nat. Commun.* **10** (2019). doi:10.1038/s41467-019-09426-0.
- [5] D. Etherington, Uber targets 2020 for on-demand VTOL demo flights in Dallas and Dubai, *Techcrunch.Com.* (2017). <https://techcrunch.com/2017/04/25/uber-targets-2020-for-on-demand-vtol-demo-flights-in-dallas-and-dubai/>.
- [6] K. Korosec, Uber sells air taxi business Elevate to Joby Aviation, shedding its last moonshot, *Techcrunch.Com.* (2020). <https://techcrunch.com/2020/12/08/uber-sells-air-taxi-business-elevate-to-joby-aviation-shedding-its-last-moonshot/>.
- [7] P. LeBeau, United Airlines orders electric vertical aircraft, invests in urban air mobility SPAC, *CNBC.* (2021). <https://www.cnbc.com/2021/02/10/united-airlines-orders-electric-vertical-aircraft-invests-in-urban-air-mobility-spac.html>.
- [8] F. Lambert, UPS is buying up to 150 electric Vertical Takeoff and Landing (eVTOL) aircraft, *Electrek.* (2021). <https://electrek.co/2021/04/07/ups-150-electric-vertical-takeoff-and-landing-evtol-aircraft/>.
- [9] L. Kolodny, Regent is making a flying electric ferry with a top speed of 180 miles per hour, *CNBC.* (2021). <https://www.cnbc.com/2021/04/20/regent-raises-9-million-for-flying-ferries-with-180-mph-top-speed.html>.
- [10] T. Boscarol, PIPISTREL CELEBRATES ONE YEAR SINCE TYPE CERTIFICATION OF THE VELIS ELECTRO, *Pipistrel.* (2021). <https://www.pipistrel-aircraft.com/pipistrel-celebrates-one-year-since-type-certification-of-the-velis-electro/>.
- [11] S. Weintraub, Bye eFlyer 800 will fly you and 7 of your closest friends 500NM at 320 knots, or more with solar, *Electrek.* (2021). <https://electrek.co/2021/04/22/bye-eflyer-800-will-fly-you-and-7-of-your-closest-friends-500nm-at-320-knots-or-more-with-solar/>.
- [12] T. Placke, R. Kloepsch, S. Dühnen, M. Winter, Lithium ion, lithium metal, and alternative rechargeable battery technologies: the odyssey for high energy density, *J. Solid State Electrochem.* **21** (2017) 1939–1964. doi:10.1007/s10008-017-3610-7.

- [13] K. Brandt, Historical development of secondary lithium batteries, *Solid State Ionics*. **69** (1994) 173–183. doi:10.1037/h0065589.
- [14] R.G. Selim, K.R. Hill, M.L.B. Rao, Research and Development of a High Capacity, Nonaqueous Secondary Battery, 1965.
- [15] D. Lin, Y. Liu, Y. Cui, Reviving the lithium metal anode for high-energy batteries, *Nat. Nanotechnol.* **12** (2017) 194–206. doi:10.1038/nnano.2017.16.
- [16] J. Dahn, G.M. Ehrlich, 17A.0. Section A: Lithium-ion Batteries, in: Linden’s Handb. Batter., 2019. <https://www-accessengineeringlibrary-com.ezproxy.sibdi.ucr.ac.cr/content/book/9781260115925/toc-chapter/chapter17/section/section6>.
- [17] C. Pillot, The Rechargeable Battery Market and Main Trends 2020-2030, *Avicenne Energy*. (2021). [www.avicenne.com](http://www.avicenne.com).
- [18] H.-J. Noh, S. Youn, C.S. Yoon, Y.-K. Sun, Comparison of the structural and electrochemical properties of layered Li[NixCoyMnz]O2 (x = 1/3, 0.5, 0.6, 0.7, 0.8 and 0.85) cathode material for lithium-ion batteries, *J. Power Sources*. **233** (2013) 121–130. doi:10.1016/J.JPOWSOUR.2013.01.063.
- [19] M.N. Obrovac, V.L. Chevrier, Alloy Negative Electrodes for Li-Ion Batteries, *Chem. Rev.* **114** (2014) 11444–11502. doi:10.1021/cr500207g.
- [20] J.R. Dahn, Phase Diagram of LixC6, *Phys. Rev. B.* **44** (1991) 9170–9177. doi:10.1103/PhysRevB.44.9170.
- [21] J.E. Harlow, X. Ma, J. Li, E. Logan, Y. Liu, N. Zhang, L. Ma, S.L. Glazier, M.M.E. Cormier, M. Genovese, S. Buteau, A. Cameron, J.E. Stark, J.R. Dahn, A Wide Range of Testing Results on an Excellent Lithium-Ion Cell Chemistry to be used as Benchmarks for New Battery Technologies, *J. Electrochem. Soc.* **166** (2019) A3031–A3044. doi:10.1149/2.0981913jes.
- [22] A. Yao, The Li(ttle) ion that could, *Honest Energy*. (2021). <https://honestenergy.substack.com/p/the-little-ion-that-could>.
- [23] P. Albertus, S. Babinec, S. Litzelman, A. Newman, Status and challenges in enabling the lithium metal electrode for high-energy and low-cost rechargeable batteries, *Nat. Energy*. **3** (2018) 16–21. doi:10.1038/s41560-017-0047-2.
- [24] J. Liu, Z. Bao, Y. Cui, E.J. Dufek, J.B. Goodenough, P. Khalifah, Q. Li, B.Y. Liaw, P. Liu, A. Manthiram, Y.S. Meng, V.R. Subramanian, M.F. Toney, V. V. Viswanathan, M.S. Whittingham, J. Xiao, W. Xu, J. Yang, X.-Q. Yang, J.-G. Zhang, Pathways for practical high-energy long-cycling lithium metal batteries, *Nat. Energy*. (2019) 10.1038/s41560-019-0338–x. doi:10.1038/s41560-019-0338-x.
- [25] R. Schmuck, R. Wagner, G. Hörpel, T. Placke, M. Winter, Performance and cost of materials for lithium-based rechargeable automotive batteries, *Nat. Energy*. **3** (2018) 267–278. doi:10.1038/s41560-018-0107-2.

- [26] S. Nanda, A. Gupta, A. Manthiram, Anode-Free Full Cells: A Pathway to High-Energy Density Lithium-Metal Batteries, *Adv. Energy Mater.* **2000804** (2020) 1–18. doi:10.1002/aenm.202000804.
- [27] U. von Saken, E. Nodwell, A. Sundher, J.R. Dahn, Comparative thermal stability of carbon intercalation anodes and lithium metal anodes for rechargeable lithium batteries, *J. Power Sources.* **54** (1995) 240–245. doi:10.1016/0378-7753(94)02076-f.
- [28] B.J. Neudecker, N.J. Dudney, J.B. Bates, “Lithium-Free” Thin-Film Battery with In Situ Plated Li Anode, *J. Electrochem. Soc.* **147** (2000) 517. doi:10.1149/1.1393226.
- [29] J. Qian, B.D. Adams, J. Zheng, W. Xu, W.A. Henderson, J. Wang, M.E. Bowden, S. Xu, J. Hu, J.G. Zhang, Anode-Free Rechargeable Lithium Metal Batteries, *Adv. Funct. Mater.* **26** (2016) 7094–7102. doi:10.1002/adfm.201602353.
- [30] R. V. Salvatierra, W. Chen, J.M. Tour, What Can be Expected from “Anode-Free” Lithium Metal Batteries?, *Adv. Energy Sustain. Res.* **2** (2021) 2000110. doi:10.1002/aesr.202000110.
- [31] B. Scrosati, History of lithium batteries, *J. Solid State Electrochem.* **15** (2011) 1623–1630. doi:10.1007/s10008-011-1386-8.
- [32] E. Peled, The Electrochemical Behavior of Alkali and Alkaline Earth Metals in Nonaqueous Battery Systems—The Solid Electrolyte Interphase Model, *J. Electrochem. Soc.* **126** (1979) 2047–2051. doi:10.1149/1.2128859.
- [33] M.S. Whittingham, Electrical Energy Storage and Intercalation Chemistry, *Science (80- )*. **192** (1976) 1126–1127. doi:10.1126/science.192.4244.1126.
- [34] N. Pereira, G.G. Amatucci, M.S. Whittingham, R. Hamlen, Lithium-titanium disulfide rechargeable cell performance after 35 years of storage, *J. Power Sources.* **280** (2015) 18–22. doi:10.1016/j.jpowsour.2015.01.056.
- [35] S. Basu, AMBIENT TEMPERATUR RECHARGEABLE BATTERY, *U.S. Pat.* **4,423,125** (1983).
- [36] R. Yazami, P. Touzain, A reversible graphite-lithium negative electrode for electrochemical generators, *J. Power Sources.* **9** (1983) 365–371. doi:10.1016/0378-7753(83)87040-2.
- [37] K. Mizushima, P.C. Jones, P.J. Wiseman, J.B. Goodenough,  $\text{Li}_x\text{CoO}_2$  ( $0 < x < 1$ ): A New Cathode Material for Batteries of High Energy Density, *Mat. Res. Bull.* **15** (1980) 783–789. doi:10.1016/0025-5408(80)90012-4.
- [38] A. Yoshino, The birth of the lithium-ion battery, *Angew. Chemie - Int. Ed.* **51** (2012) 5798–5800. doi:10.1002/anie.201105006.
- [39] J.W. Choi, D. Aurbach, Promise and reality of post-lithium-ion batteries with high energy densities, *Nat. Rev. Mater.* **1** (2016). doi:10.1038/natrevmats.2016.13.

- [40] R. Rodriguez, K.E. Loeffler, R.A. Edison, R.M. Stephens, A. Dolocan, A. Heller, C.B. Mullins, Effect of the Electrolyte on the Cycling Efficiency of Lithium-Limited Cells and their Morphology Studied Through in Situ Optical Imaging, *ACS Appl. Energy Mater.* **1** (2018) 5830–5835. doi:10.1021/acsaem.8b01194.
- [41] A. Rathi, The next major innovation in batteries might be here, *Quartz*. (2018). <https://qz.com/1349245/the-next-major-innovation-in-batteries-might-be-here/>.
- [42] A. Rathi, The death of a promising battery startup exposes harsh market realities, *Quartz*. (2019). <https://qz.com/1717201/khosla-ventures-pulled-the-plug-on-oppellion-technologies/>.
- [43] Y. Lee, S. Fujiki, C. Jung, N. Suzuki, N. Yashiro, R. Omoda, D. Ko, T. Shiratsuchi, T. Sugimoto, S. Ryu, J.H. Ku, T. Watanabe, Y. Park, Y. Aihara, D. Im, I.T. Han, High-energy long-cycling all-solid-state lithium metal batteries enabled by silver-carbon composite anodes, *Nat. Energy*. **5** (2020) 299–308. doi:10.1038/s41560-020-0575-z.
- [44] A.J. Louli, A. Eldesoky, R. Weber, M. Genovese, M. Coon, J. deGooyer, Z. Deng, R.T. White, J. Lee, T. Rodgers, R. Petibon, S. Hy, S.J.H. Cheng, J.R. Dahn, Diagnosing and correcting anode-free cell failure via electrolyte and morphological analysis, *Nat. Energy*. **5** (2020) 693–702. doi:10.1038/s41560-020-0668-8.
- [45] M. Genovese, A.J. Louli, R. Weber, C. Martin, T. Taskovic, J.R. Dahn, Hot Formation for Improved Low Temperature Cycling of Anode-Free Lithium Metal Batteries, *J. Electrochem. Soc.* **166** (2019) A3342–A3347. doi:10.1149/2.0661914jes.
- [46] R. Weber, M. Genovese, A.J. Louli, S. Hames, C. Martin, I.G. Hill, J.R. Dahn, Long cycle life and dendrite-free lithium morphology in anode-free lithium pouch cells enabled by a dual-salt liquid electrolyte, *Nat. Energy*. **4** (2019) 683–689. doi:10.1038/s41560-019-0428-9.
- [47] X. Ren, L. Zou, X. Cao, M.H. Engelhard, W. Liu, S.D. Burton, H. Lee, C. Niu, B.E. Matthews, Z. Zhu, C. Wang, B.W. Arey, J. Xiao, J. Liu, J.G. Zhang, W. Xu, Enabling High-Voltage Lithium-Metal Batteries under Practical Conditions, *Joule*. **3** (2019) 1662–1676. doi:10.1016/j.joule.2019.05.006.
- [48] Z. Yu, H. Wang, X. Kong, W. Huang, Y. Tsao, D.G. Mackanic, K. Wang, X. Wang, W. Huang, S. Choudhury, Y. Zheng, C. V. Amanchukwu, S.T. Hung, Y. Ma, E.G. Lomeli, J. Qin, Y. Cui, Z. Bao, Molecular design for electrolyte solvents enabling energy-dense and long-cycling lithium metal batteries, *Nat. Energy*. **5** (2020) 526–533. doi:10.1038/s41560-020-0634-5.
- [49] A.J. Louli, M. Genovese, R. Weber, S.G. Hames, E.R. Logan, J.R. Dahn, Exploring the Impact of Mechanical Pressure on the Performance of Anode-Free Lithium Metal Cells, *J. Electrochem. Soc.* **166** (2019) A1291–A1299. doi:10.1149/2.0091908jes.
- [50] T.T. Beyene, B.A. Jote, Z.T. Wondimkun, B.W. Olbassa, C.J. Huang, B.

- Thirumalraj, C.H. Wang, W.N. Su, H. Dai, B.J. Hwang, Effects of Concentrated Salt and Resting Protocol on Solid Electrolyte Interface Formation for Improved Cycle Stability of Anode-Free Lithium Metal Batteries, *ACS Appl. Mater. Interfaces*. **11** (2019) 31962–31971. doi:10.1021/acsami.9b09551.
- [51] J. Alvarado, M.A. Schroeder, T.P. Pollard, X. Wang, J.Z. Lee, M. Zhang, T. Wynn, M. Ding, O. Borodin, Y.S. Meng, K. Xu, Bisalt ether electrolytes: a pathway towards lithium metal batteries with Ni-rich cathodes, *Energy Environ. Sci.* **12** (2019) 780–794. doi:10.1039/C8EE02601G.
- [52] T.T. Beyene, H.K. Bezabh, M.A. Weret, T.M. Hagos, C.-J. Huang, C.-H. Wang, W.-N. Su, H. Dai, B.-J. Hwang, Concentrated Dual-Salt Electrolyte to Stabilize Li Metal and Increase Cycle Life of Anode Free Li-Metal Batteries, *J. Electrochem. Soc.* **166** (2019) A1501–A1509. doi:10.1149/2.0731908jes.
- [53] T.T. Hagos, B. Thirumalraj, C.-J. Huang, L.H. Abrha, T.M. Hagos, G.B. Berhe, H.K. Bezabh, J. Cherng, S.-F. Chiu, W.-N. Su, B.-J. Hwang, Locally Concentrated LiPF<sub>6</sub> in a Carbonate-Based Electrolyte with Fluoroethylene Carbonate as a Diluent for Anode-Free Lithium Metal Batteries, *ACS Appl. Mater. Interfaces*. (2019). doi:10.1021/acsami.8b21052.
- [54] N.A. Sahalie, A.A. Assegie, W.N. Su, Z.T. Wondimkun, B.A. Jote, B. Thirumalraj, C.J. Huang, Y.W. Yang, B.J. Hwang, Effect of bifunctional additive potassium nitrate on performance of anode free lithium metal battery in carbonate electrolyte, *J. Power Sources*. **437** (2019) 226912. doi:10.1016/j.jpowsour.2019.226912.
- [55] M. Genovese, A.J. Louli, R. Weber, S. Hames, J.R. Dahn, Measuring the Coulombic Efficiency of Lithium Metal Cycling in Anode-Free Lithium Metal Batteries, *J. Electrochem. Soc.* **165** (2018) A3321–A3325. doi:10.1149/2.0641814jes.
- [56] Z.L. Brown, S. Heiskanen, B.L. Lucht, Using Triethyl Phosphate to Increase the Solubility of LiNO<sub>3</sub> in Carbonate Electrolytes for Improving the Performance of the Lithium Metal Anode, *J. Electrochem. Soc.* **166** (2019) A2523–A2527. doi:10.1149/2.0991912jes.
- [57] V. Nilsson, A. Kotronia, M. Lacey, K. Edström, P. Johansson, Highly Concentrated LiTFSI-EC Electrolytes for Lithium Metal Batteries, *ACS Appl. Energy Mater.* **3** (2020) 200–207. doi:10.1021/acsaem.9b01203.
- [58] X. Fan, L. Chen, O. Borodin, X. Ji, J. Chen, S. Hou, T. Deng, J. Zheng, C. Yang, S.C. Liou, K. Amine, K. Xu, C. Wang, Non-flammable electrolyte enables Li-metal batteries with aggressive cathode chemistries, *Nat. Nanotechnol.* **13** (2018) 1–8. doi:10.1038/s41565-018-0183-2.
- [59] T.M. Hagos, G.B. Berhe, T.T. Hagos, H.K. Bezabh, L.H. Abrha, T.T. Beyene, C.J. Huang, Y.W. Yang, W.N. Su, H. Dai, B.J. Hwang, Dual electrolyte additives of potassium hexafluorophosphate and tris (trimethylsilyl) phosphite for anode-free lithium metal batteries, *Electrochim. Acta.* **316** (2019) 52–59. doi:10.1016/j.electacta.2019.05.061.

- [60] Z.L. Brown, S. Jurng, B.L. Lucht, Investigation of the Lithium Solid Electrolyte Interphase in Vinylene Carbonate Electrolytes Using Cu||LiFePO<sub>4</sub> Cells, *J. Electrochem. Soc.* **164** (2017) A2186–A2189. doi:10.1149/2.0021712jes.
- [61] J.-J. Woo, V.A. Maroni, G. Liu, J.T. Vaughey, D.J. Gosztola, K. Amine, Z. Zhang, Symmetrical Impedance Study on Inactivation Induced Degradation of Lithium Electrodes for Batteries Beyond Lithium-Ion, *J. Electrochem. Soc.* **161** (2014) A827–A830. doi:10.1149/2.089405jes.
- [62] K. Xu, Electrolytes and interphases in Li-ion batteries and beyond, *Chem. Rev.* **114** (2014) 11503–11618. doi:10.1021/cr500003w.
- [63] D. Aurbach, E. Zinigrad, Y. Cohen, H. Teller, A short review of failure mechanisms of lithium metal and lithiated graphite anodes in liquid electrolyte solutions, *Solid State Ionics.* **148** (2002) 405–416. doi:10.1016/S0167-2738(02)00080-2.
- [64] E. Peled, S. Menkin, Review—SEI: Past, Present and Future, *J. Electrochem. Soc.* **164** (2017) A1703–A1719. doi:10.1149/2.1441707jes.
- [65] B. Liu, J.G. Zhang, W. Xu, Advancing Lithium Metal Batteries, *Joule.* **2** (2018) 833–845. doi:10.1016/j.joule.2018.03.008.
- [66] F. Ding, W. Xu, X. Chen, J. Zhang, M.H. Engelhard, Y. Zhang, B.R. Johnson, J. V. Crum, T.A. Blake, X. Liu, J.-G. Zhang, Effects of Carbonate Solvents and Lithium Salts on Morphology and Coulombic Efficiency of Lithium Electrode, *J. Electrochem. Soc.* **160** (2013) A1894–A1901. doi:10.1149/2.100310jes.
- [67] K.N. Wood, E. Kazyak, A.F. Chadwick, K.H. Chen, J.G. Zhang, K. Thornton, N.P. Dasgupta, Dendrites and pits: Untangling the complex behavior of lithium metal anodes through operando video microscopy, *ACS Cent. Sci.* **2** (2016) 790–801. doi:10.1021/acscentsci.6b00260.
- [68] C.M. López, J.T. Vaughey, D.W. Dees, Morphological Transitions on Lithium Metal Anodes, *J. Electrochem. Soc.* **156** (2009) A726. doi:10.1149/1.3158548.
- [69] D. Aurbach, E. Zinigrad, H. Teller, P. Dan, Factors Which Limit the Cycle Life of Rechargeable Lithium (Metal) Batteries, *J. Electrochem. Soc.* (2000). doi:10.1149/1.1393349.
- [70] I. Yoshimatsu, Lithium Electrode Morphology during Cycling in Lithium Cells, *J. Electrochem. Soc.* **135** (1988) 2422. doi:10.1149/1.2095351.
- [71] C. Fang, J. Li, M. Zhang, Y. Zhang, F. Yang, J.Z. Lee, M.H. Lee, J. Alvarado, M.A. Schroeder, Y. Yang, B. Lu, N. Williams, M. Ceja, L. Yang, M. Cai, J. Gu, K. Xu, X. Wang, Y.S. Meng, Quantifying inactive lithium in lithium metal batteries, *Nature.* **572** (2019) 511–515. doi:10.1038/s41586-019-1481-z.
- [72] W. Liu, D. Lin, A. Pei, Y. Cui, Stabilizing Lithium Metal Anodes by Uniform Li-Ion Flux Distribution in Nanochannel Confinement, *J. Am. Chem. Soc.* **138** (2016) 15443–15450. doi:10.1021/jacs.6b08730.

- [73] A. Pei, G. Zheng, F. Shi, Y. Li, Y. Cui, Nanoscale Nucleation and Growth of Electrodeposited Lithium Metal, *Nano Lett.* **17** (2017) 1132–1139. doi:10.1021/acs.nanolett.6b04755.
- [74] X. Xu, Y. Liu, J.Y. Hwang, O.O. Kapitanova, Z. Song, Y.K. Sun, A. Matic, S. Xiong, Role of Li-Ion Depletion on Electrode Surface: Underlying Mechanism for Electrodeposition Behavior of Lithium Metal Anode, *Adv. Energy Mater.* **2002390** (2020) 1–10. doi:10.1002/aenm.202002390.
- [75] A. Mistry, C. Fear, R. Carter, C.T. Love, P.P. Mukherjee, Electrolyte Confinement Alters Lithium Electrodeposition, *ACS Energy Lett.* (2018) 156–162. doi:10.1021/acsenerylett.8b02003.
- [76] K.-H. Chen, K.N. Wood, E. Kazyak, W.S. LePage, A.L. Davis, A.J. Sanchez, N.P. Dasgupta, Dead lithium: mass transport effects on voltage, capacity, and failure of lithium metal anodes, *J. Mater. Chem. A.* **5** (2017) 11671–11681. doi:10.1039/C7TA00371D.
- [77] J. Xiao, How lithium dendrites form in liquid batteries, *Science (80-. )*. **366** (2019). doi:10.1126/science.aaz5670.
- [78] F. Ding, W. Xu, G.L. Graff, J. Zhang, M.L. Sushko, X. Chen, Y. Shao, M.H. Engelhard, Z. Nie, J. Xiao, X. Liu, P. V. Sushko, J. Liu, J.G. Zhang, Dendrite-free lithium deposition via self-healing electrostatic shield mechanism, *J. Am. Chem. Soc.* **135** (2013) 4450–4456. doi:10.1021/ja312241y.
- [79] C. Fang, Y. Zhang, J.Z. Lee, Y. Yang, F. Yang, J. Li, J. Alvarado, M.A. Schroeder, L. Yang, M. Cai, J. Gu, K. Xu, X. Wang, Y.S. Meng, Quantifying Inactive Lithium in Lithium Metal Batteries, (2018). <https://arxiv.org/ftp/arxiv/papers/1811/1811.01029.pdf>.
- [80] K. Brandt, J.A.R. Stiles, Battery and methods of making the battery, *Canada Pat.* **CA1190279A** (1985).
- [81] D.P. Wilkinson, H. Blom, K. Brandt, D. Wainwright, Effects of physical constraints on Li cyclability, *J. Power Sources.* **36** (1991) 517–527. doi:10.1016/0378-7753(91)80077-B.
- [82] W.S. LePage, Y. Chen, E. Kazyak, K.-H. Chen, A.J. Sanchez, A. Poli, E.M. Arruda, M.D. Thouless, N.P. Dasgupta, Lithium Mechanics: Roles of Strain Rate and Temperature and Implications for Lithium Metal Batteries, *J. Electrochem. Soc.* **166** (2019) A89–A97. doi:10.1149/2.0221902jes.
- [83] D. Wainwright, R. Shimizu, Forces generated by anode growth in cylindrical Li/MoS<sub>2</sub> cells, *J. Power Sources.* **34** (1991) 31–38. doi:10.1016/0378-7753(91)85021-N.
- [84] T. Hirai, Influence of Electrolyte on Lithium Cycling Efficiency with Pressurized Electrode Stack, *J. Electrochem. Soc.* **141** (1994) 611. doi:10.1149/1.2054778.



- [85] C. Fang, B. Lu, G. Pawar, M. Zhang, D. Cheng, Pressure-tailored lithium deposition and dissolution in lithium metal batteries Chengcheng, *ArXiv:2008.07710v1*. (2020) 1–12.
- [86] F.C. Laman, K. Brandt, Effect of discharge current on cycle life of a rechargeable lithium battery, *J. Power Sources*. **24** (1988) 195–206. doi:10.1016/0378-7753(88)80115-0.
- [87] S. Jiao, X. Ren, R. Cao, M.H. Engelhard, Y. Liu, D. Hu, D. Mei, J. Zheng, W. Zhao, Q. Li, N. Liu, B.D. Adams, C. Ma, J. Liu, J.G. Zhang, W. Xu, Stable cycling of high-voltage lithium metal batteries in ether electrolytes, *Nat. Energy*. **3** (2018) 1–8. doi:10.1038/s41560-018-0199-8.
- [88] E. Markevich, G. Salitra, F. Chesneau, M. Schmidt, D. Aurbach, Very Stable Lithium Metal Stripping-Plating at a High Rate and High Areal Capacity in Fluoroethylene Carbonate-Based Organic Electrolyte Solution, *ACS Energy Lett.* **2** (2017) 1321–1326. doi:10.1021/acsenerylett.7b00300.
- [89] J. Zheng, M.H. Engelhard, D. Mei, S. Jiao, B.J. Polzin, J.G. Zhang, W. Xu, Electrolyte additive enabled fast charging and stable cycling lithium metal batteries, *Nat. Energy*. **2** (2017). doi:10.1038/nenergy.2017.12.
- [90] X. Fan, L. Chen, X. Ji, T. Deng, S. Hou, J. Chen, J. Zheng, F. Wang, J. Jiang, K. Xu, C. Wang, Highly Fluorinated Interphases Enable High-Voltage Li-Metal Batteries, *Chem*. **4** (2018) 174–185. doi:10.1016/j.chempr.2017.10.017.
- [91] S.K. Jeong, H.Y. Seo, D.H. Kim, H.K. Han, J.G. Kim, Y.B. Lee, Y. Iriyama, T. Abe, Z. Ogumi, Suppression of dendritic lithium formation by using concentrated electrolyte solutions, *Electrochem. Commun.* **10** (2008) 635–638. doi:10.1016/j.elecom.2008.02.006.
- [92] J. Qian, W. Xu, P. Bhattacharya, M. Engelhard, W.A. Henderson, Y. Zhang, J.G. Zhang, Dendrite-free Li deposition using trace-amounts of water as an electrolyte additive, *Nano Energy*. **15** (2015) 135–144. doi:10.1016/j.nanoen.2015.04.009.
- [93] Q. Pang, X. Liang, A. Shyamsunder, L.F. Nazar, An In Vivo Formed Solid Electrolyte Surface Layer Enables Stable Plating of Li Metal, *Joule*. **1** (2017) 871–886. doi:10.1016/j.joule.2017.11.009.
- [94] Z.L. Brown, S. Jurng, C.C. Nguyen, B.L. Lucht, Effect of Fluoroethylene Carbonate Electrolytes on the Nanostructure of the Solid Electrolyte Interphase and Performance of Lithium Metal Anodes, *ACS Appl. Energy Mater.* **1** (2018) 3057–3062. doi:10.1021/acsaem.8b00705.
- [95] Z.L. Brown, B.L. Lucht, Synergistic Performance of Lithium Difluoro(oxalato)borate and Fluoroethylene Carbonate in Carbonate Electrolytes for Lithium Metal Anodes, *J. Electrochem. Soc.* **166** (2018) A5117–A5121. doi:10.1149/2.0181903jes.
- [96] S. Jurng, Z.L. Brown, J. Kim, B.L. Lucht, Effect of electrolyte on the nanostructure

- of the solid electrolyte interphase (SEI) and performance of lithium metal anodes, *Energy Environ. Sci.* (2018). doi:10.1039/C8EE00364E.
- [97] R. Petibon, V.L. Chevrier, C.P. Aiken, D.S. Hall, S.R. Hyatt, R. Shunmugasundaram, J.R. Dahn, Studies of the Capacity Fade Mechanisms of LiCoO<sub>2</sub>/Si-Alloy:Graphite Cells, *J. Electrochem. Soc.* **163** (2016) A1146–A1156. doi:10.1149/2.0191607jes.
- [98] J. Zheng, J.A. Lochala, A. Kwok, Z.D. Deng, J. Xiao, Research Progress towards Understanding the Unique Interfaces between Concentrated Electrolytes and Electrodes for Energy Storage Applications, *Adv. Sci.* **4** (2017) 1–19. doi:10.1002/advs.201700032.
- [99] Y. Yamada, A. Yamada, Review—Superconcentrated Electrolytes for Lithium Batteries, *J. Electrochem. Soc.* **162** (2015) A2406–A2423. doi:10.1149/2.0041514jes.
- [100] J. Qian, W.A. Henderson, W. Xu, P. Bhattacharya, M. Engelhard, O. Borodin, J.G. Zhang, High rate and stable cycling of lithium metal anode, *Nat. Commun.* **6** (2015). doi:10.1038/ncomms7362.
- [101] Y. Yamada, J. Wang, S. Ko, E. Watanabe, A. Yamada, Advances and issues in developing salt-concentrated battery electrolytes, *Nat. Energy.* **4** (2019) 269–280. doi:10.1038/s41560-019-0336-z.
- [102] S. Chen, J. Zheng, L. Yu, X. Ren, M.H. Engelhard, C. Niu, H. Lee, W. Xu, J. Xiao, J. Liu, J.G. Zhang, High-Efficiency Lithium Metal Batteries with Fire-Retardant Electrolytes, *Joule.* **2** (2018) 1548–1558. doi:10.1016/j.joule.2018.05.002.
- [103] S. Chen, J. Zheng, D. Mei, K.S. Han, M.H. Engelhard, W. Zhao, W. Xu, J. Liu, J.G. Zhang, High-Voltage Lithium-Metal Batteries Enabled by Localized High-Concentration Electrolytes, *Adv. Mater.* **30** (2018) 1–7. doi:10.1002/adma.201706102.
- [104] Y. Gu, H.Y. Xu, X.G. Zhang, W.W. Wang, J.W. He, S. Tang, J.W. Yan, D.Y. Wu, M. Sen Zheng, Q.F. Dong, B.W. Mao, Lithiophilic Faceted Cu(100) Surfaces: High Utilization of Host Surface and Cavities for Lithium Metal Anodes, *Angew. Chemie - Int. Ed.* **58** (2019) 3092–3096. doi:10.1002/anie.201812523.
- [105] H. Qiu, T. Tang, M. Asif, W. Li, T. Zhang, Y. Hou, Stable lithium metal anode enabled by lithium metal partial alloying, *Nano Energy.* **65** (2019) 103989. doi:10.1016/j.nanoen.2019.103989.
- [106] S.S. Zhang, X. Fan, C. Wang, A tin-plated copper substrate for efficient cycling of lithium metal in an anode-free rechargeable lithium battery, *Electrochim. Acta.* **258** (2017) 1201–1207. doi:10.1016/J.ELECTACTA.2017.11.175.
- [107] Z.L. Zhang, Y. Jin, Y. Zhao, J. Xu, B. Sun, K. Liu, H. Lu, N. Lv, Z. Dang, H. Wu, Homogenous lithium plating/stripping regulation by a mass-producible Zn particles modified Li-metal composite anode, *Nano Res.* **12** (2021). doi:10.1007/s12274-021-

3326-y.

- [108] M. Genovese, A.J. Louli, R. Weber, R.J. Sanderson, M.B. Johnson, J.R. Dahn, Combinatorial Methods for Improving Lithium Metal Cycling Efficiency, *J. Electrochem. Soc.* **165** (2018) A3000–A3013. doi:10.1149/2.0401813jes.
- [109] V. Pande, V. Viswanathan, Computational Screening of Current Collectors for Enabling Anode-Free Lithium Metal Batteries, *ACS Energy Lett.* **4** (2019) 2952–2959. doi:10.1021/acsenergylett.9b02306.
- [110] Y.S. Meng, Recent Progress on Solid State Batteries - Challenges and Opportunities, in: ECS PRiME, 2020.
- [111] M. Armand, The history of polymer electrolytes, *Solid State Ionics.* **69** (1994) 309–319. doi:10.1016/0167-2738(94)90419-7.
- [112] C. Werwitzke, “Actually, we are the pioneer of solid-state battery,” *Electrive.Com.* (2021). <https://www.electrive.com/2021/03/03/actually-we-are-the-pioneer-of-solid-state-battery/>.
- [113] A. Rathi, Battery Startup Comes Out of Stealth to Seize On Investor Frenzy, *Bloom. Green.* (2021). <https://www.bloomberg.com/news/articles/2021-04-20/battery-startup-comes-out-of-stealth-to-seize-on-investor-frenzy?sref=jjXJRDFv>.
- [114] A. Banerjee, X. Wang, C. Fang, E.A. Wu, Y.S. Meng, Interfaces and Interphases in All-Solid-State Batteries with Inorganic Solid Electrolytes, *Chem. Rev.* **120** (2020) 6878–6933. doi:10.1021/acs.chemrev.0c00101.
- [115] K. Kerman, A. Luntz, V. Viswanathan, Y.-M. Chiang, Z. Chen, Review—Practical Challenges Hindering the Development of Solid State Li Ion Batteries, *J. Electrochem. Soc.* **164** (2017) A1731–A1744. doi:10.1149/2.1571707jes.
- [116] T. Holme, A Discussion of QuantumScape’s Battery Technology Performance Results, *QuantumScape.* (2021). <https://www.quantumscape.com/blog/a-discussion-of-quantumscares-battery-technology-performance-results/>.
- [117] H.J. Deiseroth, S.T. Kong, H. Eckert, J. Vannahme, C. Reiner, T. Zaiß, M. Schlosser, Li6PS5X: A class of crystalline Li-rich solids with an unusually high Li+ mobility, *Angew. Chemie - Int. Ed.* **47** (2008) 755–758. doi:10.1002/anie.200703900.
- [118] C. Yu, Y. Li, M. Willans, Y. Zhao, K.R. Adair, F. Zhao, W. Li, S. Deng, J. Liang, M.N. Banis, R. Li, H. Huang, L. Zhang, R. Yang, S. Lu, Y. Huang, X. Sun, Superionic conductivity in lithium argyrodite solid-state electrolyte by controlled Cl-doping, *Nano Energy.* **69** (2020) 104396. doi:10.1016/j.nanoen.2019.104396.
- [119] D.H.S. Tan, A. Banerjee, Z. Chen, Y.S. Meng, From nanoscale interface characterization to sustainable energy storage using all-solid-state batteries, *Nat. Nanotechnol.* **15** (2020) 170–180. doi:10.1038/s41565-020-0657-x.
- [120] A New Breed of Battery - Investor Presentation, *Solid Power.* (2021).

[https://s28.q4cdn.com/717221730/files/doc\\_presentations/Solid-Power-Investor-Presentation-June-2021-Final.pdf](https://s28.q4cdn.com/717221730/files/doc_presentations/Solid-Power-Investor-Presentation-June-2021-Final.pdf).

- [121] S. LeVine, Solid Power pivot, Ford wakes up, Cyber threat, *The Mobilist*. (2021). <https://themobilist.medium.com/from-the-mobilist-inbox-this-week-8813e6eef7a1>.
- [122] K. Kanamura, S. Shiraishi, Z. Takehara, Electrochemical Deposition of Very Smooth Lithium Using Nonaqueous Electrolytes Containing HF, *J. Electrochem. Soc.* **143** (1996) 2187–2197. doi:10.1149/1.1836979.
- [123] S. Jiao, J. Zheng, Q. Li, X. Li, M.H. Engelhard, R. Cao, J.-G. Zhang, W. Xu, Behavior of Lithium Metal Anodes under Various Capacity Utilization and High Current Density in Lithium Metal Batteries, *Joule*. (2017) 110–124. doi:10.1016/j.joule.2017.10.007.
- [124] A.J. Louli, J. Li, S. Trussler, C.R. Fell, J.R. Dahn, Volume, Pressure and Thickness Evolution of Li-Ion Pouch Cells with Silicon-Composite Negative Electrodes, *J. Electrochem. Soc.* **164** (2017) A2689–A2696. doi:10.1149/2.1691712jes.
- [125] Z. Deng, Z. Huang, Y. Shen, Y. Huang, H. Ding, A. Luscombe, M.B. Johnson, J.E. Harlow, R. Gauthier, Observation of the Electrolyte Wetting and “Unwetting” in Li-Ion Pouch Cells Via Ultrasonic Scanning Technology, *Joule*. **JOULE-D-20** (2020). doi:http://dx.doi.org/10.2139/ssrn.3581362.
- [126] R. Petibon, Study of the Reactivity of Electrolyte Solvents and Additives in Li-Ion Cells and Design of New Electrolyte Blends, *PhD*. (2016).
- [127] A. Lasia, Electrochemical Impedance Spectroscopy and its Applications, 2014. doi:10.1007/978-1-4614-8933-7.
- [128] D.W. Abarbanel, K.J. Nelson, J.R. Dahn, Exploring Impedance Growth in High Voltage NMC/Graphite Li-Ion Cells Using a Transmission Line Model, *J. Electrochem. Soc.* **163** (2016) A522–A529. doi:10.1149/2.0901603jes.
- [129] K. Nelson, STUDIES OF THE EFFECTS OF HIGH VOLTAGE ON THE PERFORMANCE AND IMPEDANCE OF LITHIUM-ION BATTERIES, Dalhousie University, 2017.
- [130] A.S. Keefe, PROBING CHANGES IN THE SOLID ELECTROLYTE INTERPHASE IN LI-ION CELLS, Dalhousie University, 2019.
- [131] T.D. Hatchard, S. Trussler, J.R. Dahn, Building a “smart nail” for penetration tests on Li-ion cells, *J. Power Sources*. **247** (2014) 821–823. doi:10.1016/j.jpowsour.2013.09.022.
- [132] Y. Liu, D. Lin, P.Y. Yuen, K. Liu, J. Xie, R.H. Dauskardt, Y. Cui, An Artificial Solid Electrolyte Interphase with High Li-Ion Conductivity, Mechanical Strength, and Flexibility for Stable Lithium Metal Anodes, *Adv. Mater.* **29** (2017) 1–8. doi:10.1002/adma.201605531.
- [133] K. Liu, A. Pei, H.R. Lee, B. Kong, N. Liu, D. Lin, Y. Liu, C. Liu, P. chun Hsu, Z.

- Bao, Y. Cui, Lithium Metal Anodes with an Adaptive “Solid-Liquid” Interfacial Protective Layer, *J. Am. Chem. Soc.* **139** (2017) 4815–4820. doi:10.1021/jacs.6b13314.
- [134] W. Liu, W. Li, D. Zhuo, G. Zheng, Z. Lu, K. Liu, Y. Cui, Core-Shell Nanoparticle Coating as an Interfacial Layer for Dendrite-Free Lithium Metal Anodes, *ACS Cent. Sci.* **3** (2017) 135–140. doi:10.1021/acscentsci.6b00389.
- [135] G. Zheng, S.W. Lee, Z. Liang, H.W. Lee, K. Yan, H. Yao, H. Wang, W. Li, S. Chu, Y. Cui, Interconnected hollow carbon nanospheres for stable lithium metal anodes, *Nat. Nanotechnol.* **9** (2014) 618–623. doi:10.1038/nnano.2014.152.
- [136] H. Liu, X. Yue, X. Xing, Q. Yan, J. Huang, V. Petrova, H. Zhou, P. Liu, A scalable 3D lithium metal anode, *Energy Storage Mater.* **16** (2019) 505–511. doi:10.1016/j.ensm.2018.09.021.
- [137] X. Yin, W. Tang, I.D. Jung, K.C. Phua, S. Adams, S.W. Lee, G.W. Zheng, Insights into morphological evolution and cycling behaviour of lithium metal anode under mechanical pressure, *Nano Energy.* **50** (2018) 659–664. doi:10.1016/j.nanoen.2018.06.003.
- [138] C. Niu, H. Lee, S. Chen, Q. Li, J. Du, W. Xu, J.G. Zhang, M.S. Whittingham, J. Xiao, J. Liu, High-energy lithium metal pouch cells with limited anode swelling and long stable cycles, *Nat. Energy.* (2019). doi:10.1038/s41560-019-0390-6.
- [139] D.P. Wilkinson, D. Wainwright, In-situ study of electrode stack growth in rechargeable cells at constant pressure, *J. Electroanal. Chem.* **355** (1993) 193–203. doi:10.1016/0022-0728(93)80362-L.
- [140] J. Cannarella, C.B. Arnold, State of health and charge measurements in lithium-ion batteries using mechanical stress, *J. Power Sources.* **269** (2014) 7–14. doi:10.1016/j.jpowsour.2014.07.003.
- [141] R. Jung, M. Metzger, D. Haering, S. Solchenbach, C. Marino, N. Tsiouvaras, C. Stinner, H.A. Gasteiger, Consumption of Fluoroethylene Carbonate (FEC) on Si-C Composite Electrodes for Li-Ion Batteries, *J. Electrochem. Soc.* **163** (2016) A1705–A1716. doi:10.1149/2.0951608jes.
- [142] E. Plichta, S. Slane, M. Uchiyama, M. Salomon, D. Chua, W.B. Ebner, H.W. Lin, An Improved Li / Li<sub>x</sub> CoO<sub>2</sub> Rechargeable Cell, *J. Electrochem. Soc.* **136** (1989) 1865–1869. doi:10.1149/1.2097063.
- [143] D. Aurbach, Y. Ein-Eli, O. Chusid (Youngman), Y. Carmeli, M. Babai, H. Yamin, The Correlation Between the Surface Chemistry and the Performance of Li-Carbon Intercalation Anodes for Rechargeable ‘Rocking-Chair’ Type Batteries, *J. Electrochem. Soc.* **141** (1994) 603–611. doi:10.1149/1.2054777.
- [144] L.J. Krause, V.L. Chevrier, L.D. Jensen, T. Brandt, The Effect of Carbon Dioxide on the Cycle Life and Electrolyte Stability of Li-Ion Full Cells Containing Silicon Alloy, *J. Electrochem. Soc.* **164** (2017) A2527–A2533. doi:10.1149/2.1121712jes.

- [145] T. Schedlbauer, S. Krüger, R. Schmitz, R.W. Schmitz, C. Schreiner, H.J. Gores, S. Passerini, M. Winter, Lithium difluoro(oxalato)borate: A promising salt for lithium metal based secondary batteries?, *Electrochim. Acta.* **92** (2013) 102–107. doi:10.1016/j.electacta.2013.01.023.
- [146] X. Wang, M. Zhang, J. Alvarado, S. Wang, M. Sina, B. Lu, J. Bouwer, W. Xu, J. Xiao, J.G. Zhang, J. Liu, Y.S. Meng, New Insights on the Structure of Electrochemically Deposited Lithium Metal and Its Solid Electrolyte Interphases via Cryogenic TEM, *Nano Lett.* **17** (2017) 7606–7612. doi:10.1021/acs.nanolett.7b03606.
- [147] A.J. Smith, J.C. Burns, D. Xiong, J.R. Dahn, Interpreting High Precision Coulometry Results on Li-ion Cells, *J. Electrochem. Soc.* **158** (2011) A1136–A1142. doi:10.1149/1.3625232.
- [148] S.E. Sloop, J.B. Kerr, K. Kinoshita, The role of Li-ion battery electrolyte reactivity in performance decline and self-discharge, *J. Power Sources.* **119–121** (2003) 330–337. doi:10.1016/S0378-7753(03)00149-6.
- [149] E.R. Logan, E.M. Tonita, K.L. Gering, J.R. Dahn, A Critical Evaluation of the Advanced Electrolyte Model, *J. Electrochem. Soc.* **165** (2018) A3350–A3359. doi:10.1149/2.0471814jes.
- [150] D.T. Boyle, W. Huang, H. Wang, Y. Li, H. Chen, Z. Yu, Corrosion of lithium metal anodes during calendar ageing and its microscopic origins, *Nat. Energy.* **6** (2021) 487–494. doi:10.1038/s41560-021-00787-9.
- [151] K.J. Nelson, G.L. d'Eon, A.T.B. Wright, L. Ma, J. Xia, J.R. Dahn, Studies of the Effect of High Voltage on the Impedance and Cycling Performance of Li[Ni<sub>0.4</sub>Mn<sub>0.4</sub>Co<sub>0.2</sub>]O<sub>2</sub>/Graphite Lithium-Ion Pouch Cells, *J. Electrochem. Soc.* **162** (2015) A1046–A1054. doi:10.1149/2.0831506jes.
- [152] H. Zhang, W. Qu, N. Chen, Y. Huang, L. Li, F. Wu, R. Chen, Ionic liquid electrolyte with highly concentrated LiTFSI for lithium metal batteries, *Electrochim. Acta.* **285** (2018) 78–85. doi:10.1016/j.electacta.2018.07.231.
- [153] Q. Guo, Y. Han, H. Wang, S. Xiong, W. Sun, C. Zheng, K. Xie, Flame Retardant and Stable Li<sub>1.5</sub>Al<sub>0.5</sub>Ge<sub>1.5</sub>(PO<sub>4</sub>)<sub>3</sub>-Supported Ionic Liquid Gel Polymer Electrolytes for High Safety Rechargeable Solid-State Lithium Metal Batteries, *J. Phys. Chem. C.* **122** (2018) 10334–10342. doi:10.1021/acs.jpcc.8b02693.
- [154] Q. Zhou, S. Dong, Z. Lv, G. Xu, L. Huang, Q. Wang, Z. Cui, G. Cui, A Temperature-Responsive Electrolyte Endowing Superior Safety Characteristic of Lithium Metal Batteries, *Adv. Energy Mater.* **10** (2020) 1–8. doi:10.1002/aenm.201903441.
- [155] A.J. Louli, M. Coon, M. Genovese, J. deGooyer, A. Eldesoky, J.R. Dahn, Optimizing Cycling Conditions for Anode-Free Lithium Metal Cells, *J. Electrochem. Soc.* **168** (2021) 020515. doi:10.1149/1945-7111/abe089.
- [156] A.J. Smith, J.C. Burns, X. Zhao, D. Xiong, J.R. Dahn, A High Precision Coulometry

- Study of the SEI Growth in Li/Graphite Cells, *J. Electrochem. Soc.* **158** (2011) A447–A452. doi:10.1149/1.3557892.
- [157] C. Xu, Z. Ahmad, A. Aryanfar, V. Viswanathan, J.R. Greer, Enhanced strength and temperature dependence of mechanical properties of Li at small scales and its implications for Li metal anodes, *Proc. Natl. Acad. Sci.* **114** (2017) 57–61. doi:10.1073/pnas.1615733114.
- [158] J. Zheng, P. Yan, D.H. Mei, M.H. Engelhard, S.S. Cartmell, B.J. Polzin, C.M. Wang, J.G. Zhang, W. Xu, Highly Stable Operation of Lithium Metal Batteries Enabled by the Formation of a Transient High-Concentration Electrolyte Layer, *Adv. Energy Mater.* **6** (2016) 1–10. doi:10.1002/aenm.201502151.
- [159] C. Brissot, M. Rosso, J.-N. Chazalviel, S. Lascaud, Dendritic growth mechanisms in lithiumrpolymer cells, *J. Power Sources.* **81–82** (1999) 925–929. doi:10.1016/S0378-7753(98)00242-0.
- [160] P. Bai, J. Li, F.R. Brushett, M.Z. Bazant, Transition of lithium growth mechanisms in liquid electrolytes, *Energy Environ. Sci.* **9** (2016) 3221–3229. doi:10.1039/c6ee01674j.
- [161] P. Dan, E. Mengeritsky, D. Aurbach, I. Weissman, E. Zinigrad, More details on the new LiMnO<sub>2</sub> rechargeable battery technology developed at Tadiran, *J. Power Sources.* **68** (1997) 443–447. doi:10.1016/S0378-7753(97)02591-3.
- [162] J. Li, A.R. Cameron, H. Li, S. Glazier, D. Xiong, M. Chatzidakis, J. Allen, G.A. Botton, J.R. Dahn, Comparison of Single Crystal and Polycrystalline LiNi<sub>0.5</sub>Mn<sub>0.3</sub>Co<sub>0.2</sub>O<sub>2</sub> Positive Electrode Materials for High Voltage Li-Ion Cells, *J. Electrochem. Soc.* **164** (2017) A1534–A1544. doi:10.1149/2.0991707jes.
- [163] J.R. Mueller-Neuhaus, R.A. Dunlap, J.R. Dahn, Understanding Irreversible Capacity in Li<sub>x</sub>Ni<sub>1-y</sub>Fe<sub>y</sub>O<sub>2</sub> Cathode Materials, *J. Electrochem. Soc.* **147** (2000) 3598–3605.
- [164] S.H. Kang, W.S. Yoon, K.W. Nam, X.Q. Yang, D.P. Abraham, Investigating the first-cycle irreversibility of lithium metal oxide cathodes for Li batteries, *J. Mater. Sci.* **43** (2008) 4701–4706. doi:10.1007/s10853-007-2355-6.
- [165] S. e. Sheng, L. Sheng, L. Wang, N. Piao, X. He, Thickness variation of lithium metal anode with cycling, *J. Power Sources.* **476** (2020) 228749. doi:10.1016/j.jpowsour.2020.228749.
- [166] J. Smart, W. Powell, S. Schey, Extended range electric vehicle driving and charging behavior observed early in the EV project, *SAE Tech. Pap.* **2** (2013). doi:10.4271/2013-01-1441.
- [167] E. Logan, A. Louli, M. Genovese, S. Trussler, J.R. Dahn, Investigating Parasitic Reactions in Anode-Free Li Metal Cells with Isothermal Microcalorimetry, *J. Electrochem. Soc.* (2021). doi:10.1149/1945-7111/ac0947.

- [168] J. Li, H. Li, W. Stone, S. Glazier, J.R. Dahn, Development of Electrolytes for Single Crystal NMC532/Artificial Graphite Cells with Long Lifetime, *J. Electrochem. Soc.* **165** (2018) A626–A635. doi:10.1149/2.0971803jes.
- [169] B.K. Sovacool, A. Hook, M. Martiskainen, A. Brock, B. Turnheim, The decarbonisation divide: Contextualizing landscapes of low-carbon exploitation and toxicity in Africa, *Glob. Environ. Chang.* **60** (2020) 102028. doi:10.1016/j.gloenvcha.2019.102028.
- [170] V.L. Chevrier, L.J. Krause, L.D. Jensen, C. Huynh, M. Triemert, E.L. Bowen, J. Thorson, Design of Positive Electrodes for Li-Ion Full Cells with Silicon, *J. Electrochem. Soc.* **165** (2018) A2968–A2977. doi:10.1149/2.0351813jes.
- [171] C. Martin, M. Genovese, A.J. Louli, R. Weber, J.R. Dahn, Cycling Lithium Metal on Graphite to Form Hybrid Lithium-Ion/Lithium Metal Cells, *Joule.* **4** (2020) 1296–1310. doi:10.1016/j.joule.2020.04.003.
- [172] I. Bloom, A.N. Jansen, D.P. Abraham, J. Knuth, S.A. Jones, V.S. Battaglia, G.L. Henriksen, Differential Voltage Analyses of High-Power, Lithium-Ion Cells 1. Technique and Application, *J. Power Sources.* **139** (2005) 295–303. doi:10.1016/j.jpowsour.2004.07.021.
- [173] H.M. Dahn, A.J. Smith, J.C. Burns, D.A. Stevens, J.R. Dahn, User-Friendly Differential Voltage Analysis Freeware for the Analysis of Degradation Mechanisms in Li-Ion Batteries, *J. Electrochem. Soc.* **159** (2012) A1405–A1409. doi:10.1149/2.013209jes.
- [174] L. Ma, L. Ellis, S.L. Glazier, X. Ma, Q. Liu, J. Li, J.R. Dahn, LiPO<sub>2</sub>F<sub>2</sub> as an electrolyte additive in Li[Ni<sub>0.5</sub>Mn<sub>0.3</sub>Co<sub>0.2</sub>]O<sub>2</sub>/graphite pouch cells, *J. Electrochem. Soc.* **165** (2018) A891–A899. doi:10.1149/2.0381805jes.
- [175] A.J. Louli, L.D. Ellis, J.R. Dahn, Operando Pressure Measurements Reveal Solid Electrolyte Interphase Growth to Rank Li-Ion Cell Performance, *Joule.* **3** (2019). doi:10.1016/j.joule.2018.12.009.
- [176] A.J. Louli, Probing the Reversible and Irreversible Volume Expansion Observed in Li-Ion Pouch Cells, Dalhousie University, 2017.
- [177] R. Weber, J.-H. Cheng, A.J. Louli, M. Coon, S. Hy, J.R. Dahn, Surface area of lithium-metal electrodes measured by argon adsorption, *J. Electrochem. Soc.* **166** (2019). doi:10.1149/2.1181913jes.
- [178] C. Peabody, C.B. Arnold, The role of mechanically induced separator creep in lithium-ion battery capacity fade, *J. Power Sources.* **196** (2011) 8147–8153. doi:10.1016/j.jpowsour.2011.05.023.
- [179] Y. Qiao, H. Yang, Z. Chang, H. Deng, X. Li, H. Zhou, A high-energy-density and long-life initial-anode-free lithium battery enabled by a Li<sub>2</sub>O sacrificial agent, *Nat. Energy.* **6** (2021) 653–662. doi:10.1038/s41560-021-00839-0.



- [180] J. Betz, G. Bieker, P. Meister, T. Placke, M. Winter, R. Schmuch, Theoretical versus Practical Energy: A Plea for More Transparency in the Energy Calculation of Different Rechargeable Battery Systems, *Adv. Energy Mater.* **1803170** (2018) 1803170. doi:10.1002/aenm.201803170.